Low Temperature DeNOx Technologies for Power and Waste Incineration Plants

A dissertation presented by
Peter Westergaard Jakobsen, M. Sc.
to
The Department of Chemistry
in partial fulfilment of the requirements
for the degree of Doctor of Philosophy

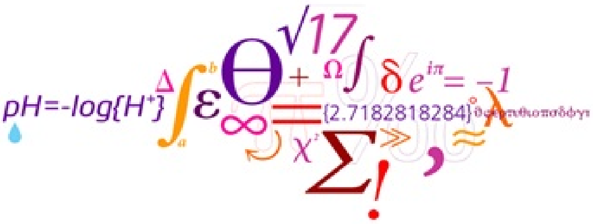

Kongens Lyngby 2017

Technical University of Denmark
Department of Chemistry
Kemitorvet, Building 207,
2800 Kongens Lyngby, Denmark
Phone +45 45 25 24 19
www.kemi.dtu.dk

Abstract

Formation of NO_x is inevitable during high temperature combustion processes in air. NO_x is of increasing environmental concern due to its participation in detrimental photochemical reactions, which lead to ozone layer depletion. NO_x emissions also cause acid rain, contributes to smog formation and induces respiratory diseases in humans.

There is no doubt that anthropogenic effects are contributing to the global climate change. The largest contributor to anthropogenic greenhouse gas emissions is CO_2. Over the past decades, a transition from fossil fuels into more CO_2 efficient fuels have been of great interest as a method to decrease global CO_2 emissions. Some of the fuels that have drawn particular interest over the past decade is biomass and municipal waste. While the CO_2 emissions are decreased by a transition to these fuels, other problems are caused by it. Potassium present in many of the alternative fuels lead to severe deactivation of the catalyst used for NO_x abatement. Consequently, NO_x abatement is currently not possible when these are used exclusively. Since NO_x gasses are strong pollutants, the increased emission caused by using these alternative fuels is highly undesirable and hinders a more widespread use of alternative fuels.

The work presented here has primarily been concerned with finding an alternative solution to NO_x abatement for biomass and waste incineration. The optimal solution to this would be a tail-end deNO$_x$ unit, which operates at low temperatures (60-140 °C).

Previous work has shown that ionic liquids (ILs) are promising absorbers and can selectively absorb flue gas constituents such as CO_2, SO_2 and NO. Utilisation of ILs is severely limited by high viscosities, which hinders mass transfer across phase boundary layers. Dispersion of the IL onto a porous support has been suggested as a possible solution to this problem.

In the present work, a vast variety of supported ionic liquid phase (SILP) materials have been tested in NO breakthrough experiments. Based on the obtained results, an attempt was made to understand the chemical and physical properties governing the SILP performance. Based on these investigations, characteristics of the optimal support were suggested.

It was found that hollow-sphere silica (HS) had properties close to what was considered optimal, therefore it was decided to investigate this support material further. Synthesis of the support material and subsequently SILP formulations utilising the HS-support material were carried out in collaboration with Prof. Dai at Oak Ridge

National Laboratory. The resulting HS-SILP performed significantly better than any other SILP formulation tested in NO breakthrough experiments. Based on this performance, it was suggested that the HS-support could be ideal for selective absorption of other gasses using SILP absorbers.

Some SILP formulations were found to have significant oxidative capabilities, willingly oxidising NO to higher NO_x species. It was found that the observed effect was due to alcohol residuals in the SILP material from the impregnation process, despite careful evaporation and drying.
In order to investigate this effect further, the effect of several alcohols were screened and showed promising results. Therefore, an experimental setup was built to investigate if the oxidation would occur under continuous flow conditions, and to determine the steady state oxidation rates. Significant steady state conversions were found under continuous flow conditions, with a high turn over number for methanol. The reaction proceeded over all porous surfaces, but the use of a SILP material seemed to increase the rate of oxidation significantly.

Resumé

Dannelse af NO_x gasser i forbindelse med forbrændingsprocesser ved høj temperatur, i luft, er stort set uundgåeligt. Udledning af NO_x er et stort miljøproblem da disse kan indgå i skadelige fotokemiske reaktioner i troposfæren og stratosfæren, og derved medvirke til nedbrydelse af ozonlaget. Ydermere kan udledning af NO_x gasser føre til syreregn og smogdannelse, samt foranledige celleforandringer og luftvejssygdomme hos mennesker.

Der er ingen tvivl om, at menneskeskabt udledning af drivhusgasser bidrager til klimaforandringerne der opleves over hele verden. Udregnet i CO_2 ækvivalenter, overgår bidraget fra menneskabt udledning af CO_2 det samlede bidrag fra alle andre drivhusgasser.
Over de seneste årtier har man forsøgt at imødekomme denne udvikling ved i større grad at overgå fra fossile brændsler til mere CO_2-effektive alternativer, såsom biomasse og brændbart affald. Dette sænker CO_2 udledningen markant, men medfører desværre andre problemer. Især er deaktivering af den katalysator, der benyttes til at fjerne NO_x et stort problem. Deaktiveringen skyldes primært tilstedeværelsen af store mængder alkalimetaller i nogle af de alternative brændsler, som bliver til ødelæggende aerosoler under forbrændingsprocessen. Derfor er det ikke, i øjeblikket, muligt at fjerne NO_x når disse brændsler benyttes alene. Dette begrænser kraftigt muligheden for en fuldstænding omstilling af energiproduktionen til disse alternative brændsler.

Dette projekt har primært omhandlet udvikling af en alternativ løsning til NO_x fjernelse i biomasse og affaldsforbrændingsprocesser. Målet har været, at gøre dette ved at udvikle en proces der muliggør en flytning af deNO_x enheden, så denne er den sidste røggassen passerer, en såkaldt "tail-end"løsning. Når røggasen kommer til "tail-end"positionen har den passeret en vådscrubber som udover at fjerne SO_2 også fjerner størstedelen af de elementer der kan skade katalysatoren. Den største udfordringer for at få processen til at virke, er at luftfugtigheden er høj (ofte over 10%) og temperaturen lav (mellem 60 og 140°C).

Tidligere studier har vist, at ioniske væsker (ILs) selektivt kan fjerne skadelige røggaskomponenter som CO_2, SO_2 og NO. Den praktiske anvendelse af ioniske væsker hindres dog markant af en høj viskositet der vanskeliggør masseoverførslen i gas/væske grænselaget. Det er tidligere blevet påvist, at man ved at suspendere den ioniske væske på et porøst bæremateriale kan lette masseoverførslen og dermed løse problemet,

dette kaldes også "supported ionic liquid phase", eller SILP.
Formålet med dette projekt har især været at udvikle og afprøve forskellige SILP materialer, for at bestemme hvor længe de kan fjerne alt NO fra en simuleret røggas, såkaldte "breakthrough"eksperimenter. Grundet en stor forskel i præstation for ellers sammenlignelige bærematerialer, blev det forsøgt at opnå en dybere forståelse af bærematerialets fysiske og kemiske egenskaber, og deres indvirkning på reaktionen. På baggrund af disse studier, var det muligt at foreslå en formulering af det mest optimale bæremateriale.
Det optimale bæremateriale var en form for hule silica kugler i nano-størrelse (hollow-sphere silica, HS), som blev syntetiseret i samarbejde med Prof. Sheng Dai og hans gruppe ved Oak Ridge National Laboratory under udvekslingsdelen af projektet. HS-bærematerialet blev brugt til at formulere et SILP materiale, som blev sammenlignet med de SILP materialer der tidligere var blevet studeret. Sammenligning mellem SILP materialerne viste, at HS-SILP materialet var flere gange bedre end de hidtil bedste SILP materialer. Derudover, blev det foreslået at HS-bærematerialet kan være med til at forbedre effektiviteten af andre SILP materialer der pt. er under udvikling til selektiv absorption af andre skadelige røggaskomponenter.

Under udviklingen af SILP materialerne viste det sig at flere af materialerne kunne oxidere NO til højere NO_x specier. Det viste sig dog, at den oxidative effekt skyldtes alkoholrester fra imprægneringen, dette til trods for at SILP materialerne blev tørret grundigt under vakuum, inden brug.
For at undersøge dette nærmere blev effekten af en lang række alkoholer analyseret ved at dryppe dem ned på SILP reaktoren og dernæst lede en gas med NO, ilt og vand hen over reaktoren. Resultaterne fra disse foreløbige forsøg var så lovende at der blev bygget en forsøgsopstilling for at undersøge om oxidationen også kunne opnås under kontinuært flow.
Det var muligt at replikere den høje omdannelse der tidligere var blevet vist. Derudover viste det sig at oxidationen forløber over alle porøse materialer, men at tilstedeværelsen af en ionisk væske øger reaktionshastigheden.

Preface and Acknowledgements

This dissertation is submitted in partial fulfillment of the requirements for obtaining the degree of philosophiae doctor (ph.d.) from the Technical University of Denmark (DTU). The work was supervised by Prof. Rasmus Fehrmann and Assoc. Prof. Susanne Mossin, and carried out primarily at DTU. Part of the work was carried out in collaboration with Prof. Sheng Dai at Oak Ridge National Laboratory.

First and foremost I would like to thank my supervisors for excellent discussions and input throughout the full project period, as well as for giving me the opportunity to do research within an area that I find very interesting.
I would like to thank Assoc. Prof. Susanne Mossin for her time and devotion to the project, and for the help Susanne has provided me in all matters of scientific communication, I have learned a lot from working with her. I would also like to thank Prof. Rasmus Fehrmann for his excellent counsel and his willingness to share his extensive knowledge within the fields of ionic liquids and heterogeneous catalysis. Furthermore, I am sincerely thankful for the warm welcome I received in Oak Ridge from Prof. Sheng Dai. His progressive vision in the application of chemistry across several technical disciplines is truly impressive, and I thank him for sharing some of his thoughts with me.

I would like to thank my friends and co-workers at DTU for making this project period worthwhile socially. Especially, Jonas Andersen, Frederick Stappen, Amalie Modvig and Andreas Boeg for numerous interesting discussions during break periods - some even included scientific topics.
Lastly, but most importantly I would like to thank my family, and especially my lovely wife, Sara, for putting up with me. Despite the odd working hours and the inevitable cancellations to family events, I always had their full support, which has helped keep me motivated.

Peter Westergaard Jakobsen, M. Sc.
Kongens Lyngby, Denmark, 31-May-2017

List of Publications

Enclosed Peer-Reviewed Journal Publications

1. **Absorption and Oxidation of Nitrogen Oxide in Ionic Liquids**, A. Kunov-Kruse, P. Thomassen, A. Riisager, S. Mossin and R. Fehrmann, *Chemistry - A European Journal*, **948**, 11745-11755 (2016)
2. **Selective Reversible Absorption of the Industrial Flue Gas Components CO_2 and NO**, P. Kaas-Larsen, P. Thomassen, L. Schill, S. Mossin, A. Riisager and R. Fehrmann, *Electrochemical Society Transactions*, **75**, 3-16 (2016)
3. **Absorption of Flue Gas Components by Ionic Liquids**, H. Kolding, P. Thomassen, S. Mossin, A. Riisager, J. Rogez, G. Mikaelian and R. Fehrmann, *Electrochemical Society Transactions*, **64**, 97-108 (2014)

Enclosed Unpublished Work

1. **Methanol Promoted Low Temperature Oxidation of Nitric Oxide**, P. W. Jakobsen, S. Mossin and R. Fehrmann, Unpublished due to patent restrictions

Patent Applications

1. **Combined Oxidation and Absorption of NO_x by an Ionic Liquid Tandem Process**, P. Thomassen R. Fehrmann, A. Riisager, S. Mossin, A. Madsen and A. Kunov-Kruse, EP2015058309, 2015
2. **Patent Application: Methanol promoted low temperature oxidation of NO, promotional technique for use in tail-end, low temperature fast SCR**, P. W. Jakobsen, S. Mossin and R. Fehrmann, in-progress

List of Conference Contributions

Oral Conference Contributions

International Conferences

1. **Synthesis of Poly Ionic Liquids in Nano-Sized Hollow-Sphere Silica**; Co-authors: S. Dai, S. Mossin and R. Fehrmann, *Presented at: 26th EuChem Conference on Molten Salts and Ionic Liquids in Vienna, Austria* - July 2016
2. **Advances in Gas Phase Separation of NO_x with Supported Ionic Liquid Phase Using Hollow-Sphere Silica**; Co-authors: S. Dai, S. Mossin and R. Fehrmann, *Presented at: 251st ACS National Meeting in San Diego, United States of America* - March 2016
3. **Absorptio and Oxidation of NO_x to Nitric Acid - An Atom-Efficient Method for NO_x Removal Using Ionic Liquids**; Co-authors: R. Fehrmann and S. Mossin, *Presented at: EuropacatXII in Kazan, Russia* - September 2015

National Conferences

1. **Atom-Efficient Strategy for NO_x Removal Using Ionic Liquids**; Co-authors: R. Fehrmann, S. Mossin, *Presented at: 7th Annual ph.d. Symposium of the Department of Chemistry, Technical University of Denmark in Hillerød, Denmark* - November 2016
2. **Elucidation of the Reaction Mechanism Involved in Absorption and Oxidation of NO in Ionic Liquids**; Co-authors: S. Mossin, R. Fehrmann, *Presented at: 1st Inorganic Graduate Student Seminar in Odense, Denmark* - June 2015

Poster Contributions

1. **Atom-Efficient NO_x Removal Using SILP Absorbers**; P. W. Jakobsen*, S. Dai, S. Mossin, R. Fehrmann, *Presented by A. Riisager at: 26th EuChem Conference on Molten Salts and Ionic Liquids in Vienna, Austria* - July 2016
2. **Advances in Absorption and Oxidation of NO in flue gas to form Nitric Acid**; Co-authors: S. Mossin, S. Dai and R. Fehrmann, *Presented at: 17th Nordic Symposium on Catalysis in Lund, Sweden* - June 2016
3. **NO_x Absorption and Oxidation in Ionic Liquids**; Co-authors: R. Fehrmann and S. Mossin, *Presented at: 5th Annual ph.d. Symposium of the Department of Chemistry, Technical University of Denmark in Frederiksdal, Denmark* - November 2014
4. **NO_x Absorption and Oxidation in Supported Ionic Liquid Phase (SILP)**; Co-authors: S. Mossin, A. Riisager and R. Fehrmann, *Presented at: 25th EuChem Conference on Molten Salts and Ionic Liquids in Tallinn, Estonia* - July 2014
5. **Absorption and Catalytic Conversion of NO to HNO_3 Using Ionic Liquids**; Co-authors: S. Mossin, A. Riisager and R. Fehrmann, *Presented at: 16th Nordic Symposium on Catalysis in Oslo, Norway* - June 2014
6. **NO Absorption and Oxidation in Supported Ionic Liquid Phase Materials**; Co-authors: A. Madsen, S. Mossing, A. Riisager and R. Fehrmann, *Presented at: 247th ACS National Meeting in Dallas, United States of America* - March 2014

Contents

CHAPTER 1

Introduction

The harmful effects of NO_x gasses are well documented and include, but are not limited to: Induction of respiratory diseases in humans, ozone layer depletion, town smog formation and acid rain.

Several excellent methods for removing NO_x from flue gasses have been developed over the years, the most important of these is selective catalytic reduction (SCR), which is used for NO_x abatement in most stationary installations today.

The anthropogenic contributions to the emission of greenhouse gasses (GHG) cause significant climate change. CO_2 is by far the most emitted GHG. In fact, CO_2 emissions constitute around 65% of the annual, global GHG emissions calculated in CO_2 equivalents. An increased use of biomass, municipal waste, and other CO_2 efficient fuels in energy production has been proposed as a possible way to mitigate global CO_2 emissions. However, a high alkaline content in some of the alternative fuels causes irreversible poisoning of the currently used SCR catalyst, which in turn makes NO_x abatement unviable when these fuels are used.

Finding a viable deNO_x method for alternative fuels is paramount for further use of these in energy production. In the literature, the two most discussed solutions are: Development of a catalyst that is not deactivated when exposed to the alkaline aerosols, or development of a deNO_x catalyst which is placed as the last step in emission control, a so called tail-end deNO_x unit.

The work presented here seeks to further advance the work on finding a suitable method for tail-end NO_x abatement. Under tail-end conditions, the most challenging factors are low temperatures and high water content. Potential catalyst poisons are expected to be insignificant at this point in the emission control process, because the gas has been passed through a wet scrubber.

Furthermore, development of a tail-end deNO_x solution will allow for retro-fitting in existing power plants where space limitations do not allow for installation of the more commonly used high-dust deNO_x unit. Expanding the deNO_x portfolio to include a tail-end solution should lead to NO_x abatement becoming a more readily available process, which in turn is expected to greatly increase the global amount of installations.

In this work, two different solutions are explored; one is the complete removal of NO through absorption and oxidation in ionic liquids (ILs) and the other is a novel, complimentary method for low temperature oxidation of NO in the presence of water. Oxidation of NO facilitates NO_x abatement under "fast-SCR" conditions, which significantly increases the activity and selectivity, especially at lower temperatures.

In Chapter 2, the motivation for NO_x abatement is presented, along with a review of the existing methods used for NO_x abatement. This is done to give a better understanding of the advantages and disadvantages of current in-use methods. A thorough understanding of current methods is paramount in knowing which limitations are important to overcome, when attempting to expand the $deNO_x$ portfolio.

Chapter 3 presents the concept of ILs and reviews state-of-the-art literature on gas absorption in ILs. Difficulties in application of ILs in wet scrubbers are also discussed. In Chapter 3, preliminary findings on absorption and oxidation of NO in ionic liquids is presented, along with a comprehensive *in-situ* study on the reaction mechanism and reaction kinetics of the reaction.

In Chapter 4, applying the IL to a porous support, forming a supported ionic liquid phase (SILP) material, is discussed as a possible method for overcoming the mass transfer limitations of ionic liquids. Current state-of-the-art literature on both technical applications of SILP and gas absorption using SILP materials are reviewed. Results from experimental work in utilising the SILP concept to improve the reaction dynamics in NO absorption and oxidation is also presented in Chapter 4, along with general considerations on the role of the support material and possible support material formulations that could help increase the absorption capacity, as well as the rate of the reaction.

Chapter 5 presents the results obtained from synthesis and subsequent application of an optimised support material. Synthesis of the support material was carried out during the external research stay, in collaboration with Prof. Sheng Dai and his group at Oak Ridge National Laboratory.

In Chapter 6, a novel method for promoted low-temperature oxidation of NO is presented. In order to assess the importance of the findings, the state-of-the-art literature on NO oxidation is also reviewed in this chapter.

CHAPTER 2

Project Background

In 2014, the Intergovernmental Panel on Climate Change (IPCC) concluded that anthropogenic effects are clearly affecting the climate, and that recently, emissions of greenhouse gasses are the highest it has ever been. The report concludes that it is virtually certain these effects have led to a global increase in temperature in the troposphere and lower stratosphere. Furthermore, it was concluded that CO_2 and N_2O levels in the atmosphere have reached the highest concentration in 800,000 years [1]. The findings in the latest IPCC report primarily consider the consequences of emissions on a global scale. And whereas CO_2 emissions are only detrimental on a global scale, several flue gas constituents are also of concern locally.

Two of the most prominent local pollutants are SO_x and NO_x gasses. Both of these contribute to acid rain and smog formation while also having severe detrimental effects on human health [2–5]. Furthermore, NO_x gasses partake in detrimental photochemical reactions in both the troposphere and the stratosphere [6, 7], and is the primary reason for ozone layer depletion [8].

The severe health effects and visible structural and plant deterioration caused by acid precipitation is well exemplified by the great smog of London in 1952. The detrimental effects observed here, quickly led to stricter regulation on sulfur content in fuels, especially in denser populated areas. In Los Angeles around the same time, visible yellow smog was observed daily due to NO_x emissions from the rapidly expanding need for personal transportation and the accompanying increase in NO_x emissions.

While SO_x constituents of a flue gas exclusively originate from sulfur in the fuel, this is not the case for NO_x gasses. NO_x gasses may also originate from the fuel, but fuel NO_x rarely constitutes the majority of NO_x in the flue gas from fossil fuel combustion. Here, flue gas NO_x primarily originates from oxidation of nitrogen from the air caused by the high temperatures exhibited during the combustion process [9, 10], NO_x formed in this process is often denoted as thermal NO_x. Since the formation of NO_x gasses in combustion processes is inevitable, finding efficient methods for NO_x abatement is of the utmost importance.

This chapter reviews some of the known methods used for NO_x abatement today and the challenges that are faced when transitioning towards more CO_2 efficient fuels.

The main focus of this work has been on NO_x removal from alternative combustion sources such as biomass and waste incineration. Through the project period, input from various collaborators, especially DONG Energy A/S and LAB A/S has been used in an attempt to best accommodate the current needs of the industry, as well as the expected future challenges that needs to be overcome in order for CO_2 alternatives to become viable on a larger scale.

2.1 Emission Control in Power Plants

In modern coal fired power plants, it is common practice to remove dust and other particulate matter as well as SO_x and NO_x gasses. Appendix B shows a schematic overview of the three most common emission control units in stationary plants denominated with respect to the selective catalytic reduction (SCR) unit positioning: High-dust, Low-dust and Tail-end.

In principle, the best practice is to remove dust from the flue gas prior to the catalyst being exposed to it, to reduce abrasion and clogging of catalyst pores. At the temperatures found in a power plant, there are no suitable dust filters to allow for placing the SCR unit at the low-dust position. Consequently, an abrasion resistant catalyst is normally used, and placed in the high-dust position [11].

In all of the schematics presented, a wet flue gas desulphurisation (FGD) unit is used. Here, the flue gas is scrubbed with an aqueous limestone slurry to remove SO_2 and SO_3. Wet limestone scrubbing is discussed in greater detail in Section 3.1.1. The temperature of the gas when exiting the FGD unit is to be expected around 60-80 °C. The gas is reheated to 120-150 °C prior to release to stack, in order to prevent condensation of residual SO_x as sulfuric acid in the chimney.

2.2 Current Methods in NO_x Abatement

In Section 6.1, the governing thermodynamic equilibria of flue gas NO_x constituents is discussed. It is shown that at high combustion temperatures, nitric oxide (NO) is the predominant NO_x species, meaning only NO is formed in thermal NO_x formation. Oxidation of the kinetically hindered NO molecule is slow and thus, flue gas NO_x abatement must be targeted at NO in order to be effective.

Some of the earliest accounts of selective NO reduction by ammonia were published in the early 1950's [12,13]. These studies were fundamental and mechanistic studies on ammonia oxidation with NO at high temperatures, at the time NO_x abatement was not considered as a use. In the early 1980's, when the necessity for NO_x reduction in flue gas arose, direct injection of ammonia at high temperatures was suggested [14].

This gave rise to the process of selective non-catalytic reduction of NO (SNCR). There are several disadvantages to SNCR, apart from requiring high temperatures to proceed. Temperature control is paramount in SNCR, both for controlling the selectivity, and maintaining reasonable reaction rates; at temperatures below 600 °C, the reaction is much too slow to obtain satisfying NO_x abatement, while at temperatures above ca. 750 °C, the selectivity of the reaction quickly moves towards partial reduction of NO and excess oxidation of ammonia. Thus, at temperatures exceeding ca. 750 °C the end products are N_2O, a potent GHG, and excess NO.

The disadvantages of SNCR strongly limit the potential applications and further improvement of the process was necessary for wide spread use, especially in power plants.

2.2.1 Selective Catalytic Reduction

Due to the strong limitations in SNCR, it was quickly identified that use of a suitable catalyst would greatly increase the applicability of the process. Some of the earliest accounts of selective catalytic reduction (SCR) used vast excess of ammonia as well as high concentrations of oxygen to obtain satisfactory NO reduction [15]. Despite the disadvantageous early reaction conditions (ammonia is also a strong pollutant), the SCR process was quickly identified as the most promising method for NO_x abatement in power plants and V_2O_5 was identified as one of the possible catalyst formulations [16]. The SCR reaction proceeds according to Reaction 2.1 below.

$$4\,NO + 4\,NH_3 + O_2 \longrightarrow 4\,N_2 + 6\,H_2O \tag{2.1}$$

Numerous different catalyst formulations were tested in the early stages of development, including several noble metal catalysts. In all cases the reaction proceeded according to Reaction 2.1. Janssen and Bosch *et al.* carried out several important preliminary studies of the reaction [17–20]. For instance they found that anatase, as the only investigated support, had a promotional effect on the reaction rate, compared to the pure V_2O_5. Later, in a series of publications, Topsøe *et al.* [21–24] investigated the reaction mechanism over the V_2O_5 catalyst supported on anatase. The proposed reaction mechanism included a redox cycle and an acid/base cycle, which were combined. The proposed catalytic cycle is shown in Figure 2.1. From Figure 2.1 it is observed, that in the proposed reaction pathway, ammonia is adsorbed on a vanadium hydroxyl group. Upon bridging with a vanadyl ($V^{5+}{=}O$) from a second vanadium, the ammonia is activated and can react with a NO molecule. Thus forming an N-N bond directly, in an Eley-Rideal type reaction mechanism. Oxygen plays a vital role in regenerating the active vanadyl species, as can be seen from the redox part of the reaction cycle. Under oxygen-starved conditions, the reaction still occurs but at much lower rates.

Under flue gas conditions oxygen is in vast excess and reoxidation occurs rapidly

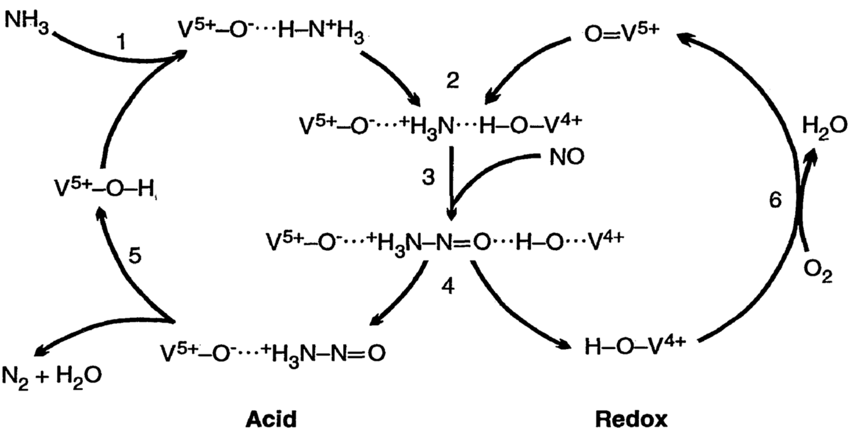

Figure 2.1: Proposed catalytic cycle by Topsøe [24].

enough for this not to be rate-determining. The N-N=O reaction intermediate denoted as 4 was not observed experimentally, suggesting that desorption of the products occurs rapidly. Thus, the rate determining step is expected to be found in reactions 1 through 3.

The rate of the reaction can be expressed using the equation presented in Equation 2.2 [25].

$$-\frac{d\mathrm{NO}}{dt} = k \cdot [\mathrm{NO}] \tag{2.2}$$

From Equation 2.2 it can be seen that the only reactant which is rate determining under flue gas conditions is NO. This, coupled with the expected fast adsorption of NH_3 on Brønsted acidic sites, suggests that the associative adsorption of NO is rate limiting.

Today, the most widely used catalyst for industrial SCR applications, is a V_2O_5 catalyst supported on anatase and promoted by addition of tungsta (WO_3). This catalysts operates optimally at temperatures between 300-375 °C [26].

During the emergence of the SCR process, several zeolites, especially metal-exchanged zeolites were discussed as potential catalysts in the reaction [27–29]. However, due to low stability at higher temperatures with water present in the gas, as well as low availability and relatively high production costs, they were not introduced at first.

Recently, SCR catalysts based on primarily Fe and Cu-exchanged zeolites have become commercially available, and are especially used for NO_x abatement in diesel exhaust systems. The emergence of metal-exchanged zeolites is primarily due to their significantly better performance under the changing conditions observed in diesel exhaust gasses.

Very recently Janssens *et al.* [30] proposed a consistent mechanism for the SCR reac-

tion over Cu-exchanged chabazite. In this case, formation of a nitrate intermediate through adsorption of NO and O_2 is proposed to be rate limiting. With a feed gas containing equimolar amounts of NO and NO_2, this rate-determining step is avoided. Avoiding the rate-determining step significantly increases the reaction rate, and thus gives a satisfactory explanation to the higher rates observed under these conditions, which are commonly referred to as "fast-SCR" conditions.
Under fast-SCR conditions the reaction proceeds according to Reaction 2.3:

$$2\,\mathrm{NO} + 2\,\mathrm{NO_2} + 4\,\mathrm{NH_3} \longrightarrow 4\,\mathrm{N_2} + 6\,\mathrm{H_2O} \tag{2.3}$$

The fast-SCR reaction occurs readily over all known SCR catalyst formulations [30–32]. While oxidation of NO to NO_2 is important for this reaction to occur, it is equally important that the molar ratio of NO_2:NO does not exceed 1, as this leads to excess NO_2 being reduced via Reaction 2.4 below:

$$8\,\mathrm{NH_3} + 6\,\mathrm{NO_2} \longrightarrow 7\,\mathrm{N_2} + 12\,\mathrm{H_2O} \tag{2.4}$$

Reaction 2.4 is significantly slower than the regular SCR reaction. Furthermore, this reaction has been proposed to significantly decrease the N_2 selectivity, thus leading to formation of the potent greenhouse gas N_2O [33].

2.2.2 Low Temperature Selective Catalytic Reduction

Over the past 15-20 years, significant work has gone into developing a low-temperature SCR catalyst [34–36]. Decreasing the temperature of the SCR reaction has several advantages, chief among which is the possibility of transitioning to a tail-end application. This is especially important for retrofitting of a $deNO_x$ unit in older plants with limited space available, and for waste and biomass incineration, where the flue gas contains aerosols with a strong deactivating effect on the SCR catalyst. SCR catalyst deactivation is discussed in greater detail in Section 2.3.1.
The low-temperature SCR activity of a vast variety of catalyst formulations has been investigated in the literature. These include chromium, copper, iron, and manganese oxides supported on titania, carbon, ceria, alumina, and various zeolites [36–39]. In order to achieve sufficient activities at low temperature, the metal loading is often very high (10-20%). The most widely studied and most efficient catalyst formulations use MnO_x as the active phase, often as a mixed oxide with iron [40]. Recently, several authors have reported a promotional effect of doping with smaller amounts of other transition metals such as chromium or nickel [41–43].
Several of these new low-temperature SCR catalysts operate at significantly lower temperatures, often reaching satisfactory activity around 200-250 °C, which is 100 °C lower than the commonly used catalyst formulation. There are several obstacles in using these catalysts that have yet to be fully addressed, including very low sulphur tolerance. The most important of these, however, is the low N_2 selectivity.

Very recently, Yang and *et al.* [44] reported a high-selectivity manganese catalyst supported on Fe-Ti spinel. Despite it being a "high selectivity" catalyst, the N_2 selectivity is still only around 95% at 225 °C. The selectivity appeared to increase in the presence of water and SO_2. Both constituents were present in concentrations that are relevant to tail-end NO_x abatement (8% and 60 ppm respectively). However, the presence of water and SO_2 seemed to decrease the activity of the catalyst considerably.

In order for these catalyst to become truly viable, the selectivity must be increased, to avoid increased emissions of N_2O. One possible way to increase the selectivity is by using the catalysts for fast SCR. However, in order to do this, a low-temperature method for oxidation of NO to NO_2 is required. Current methods for NO oxidation is discussed in greater detail in Chapter 6.

2.3 Use of Alternative Fuels in Combustion Processes

As mentioned previously, anthropogenic emissions of CO_2 are of increasing concern. The total anthropogenic emissions of GHGs is steadily increasing, and CO_2 constitutes an increasing portion of the total anthropogenic GHG emissions. Calculated in terms of CO_2 equivalents, 65% of anthropogenic GHG emissions in 2010 were from CO_2, with industrial emissions contributing with the largest portion of this [1]. These numbers do not include the negative effect of deforesting and agriculture, which add another 11 perventage points.

Biomass and other alternative fuels are attractive because they are in essence CO_2 neutral. While waste incineration is not CO_2 neutral, modern waste incineration constitutes a significantly higher degree of global energy efficiency than previously. Previously, waste was either incinerated without utilising the excess energy, or it was buried in land fills causing considerable GHG emissions and ground pollution.

In order for the introduction of alternative fuel sources to be successful, it is paramount that it does not lead to an increase in emissions of other pollutants.

Alternative fuels have a significantly different composition than fossil fuels. Fossil fuels primarily consist of carbon, hydrogen and to some extent sulphur. Alternative fuels vary significantly in composition, but generally have a considerably higher amount of alkaline metals and chloride, while the sulphur content is often lower, especially compared to bituminous coal and lignite. Table 2.1 summarises some of the literature composition values for different types of biomass and municipal solid waste (MSW), compared to coals. As can be seen from Table 2.1, the fuel compositions vary significantly between the different types of fuel. As mentioned, coals generally have higher sulphur contents and significantly lower alkali metal content, but it is important to note that these vary significantly depending on the origin of the fuel [46]. It is not possible to describe the general fuel composition of MSW, as this varies considerably. However, alkali content is generally significantly higher than in coals.

Table 2.1: Averaged literature values for fuel composition reported as weight percentage of fuel.

Fuel	K	Cl	S	Na	Ref.
Bituminous Coal	0.06	0.23	1.24	0.05	[45]
Brown Coal/Lignite	0.02	0.025	0.4	0.02	[45, 46]
MSW[a]	1[b]	0.25	0.3	2.2	[47]
Wood Chips	0.1	0.02	0.05	0.015	[48, 49]
Straw	1.0	0.4	0.15	0.05	[48, 49]

[a] Calculated from bottom ash [b] Varies from 0.075 to 1.9

This is also the case for the amount of trace metals such as lead, chromium, copper and zinc. Calcium and magnesium are also found in considerable amounts along with iron, aluminium and silicium [47].

The significant difference in fuel composition leads to other challenges in catalyst design. For instance, the V_2O_5 catalyst was, among other reasons, chosen for the high sulphur tolerance. In flue gasses where the sulphur content is low, or if the SCR unit is placed in the tail-end position after an FGD, sulphur poisoning becomes less of an issue.

The presence of alkali and alkaline earth metals decrease the V_2O_5-based SCR catalyst, as is discussed below in Section 2.3.1. The presence of alkaline aerosols in conjunction with chloride in the fuel cause deposition of highly corrosive chloride salts on the boiler and heat exchangers [50–52]. This further complicates the use of biomass and waste incineration in energy production.

2.3.1 Deactivation of Commonly Used SCR Catalyst

One of the most important challenges to overcome in order to successfully transition into using biomass and waste incineration in energy production, is deactivation of the most commonly used V_2O_5 SCR catalyst. The high-dust positioning of the SCR unit means the catalyst is exposed to trace amounts of possible catalyst poisons generated in the boiler. Mercury has been mentioned as a possible catalyst poison along with zinc, arsenic, copper and chromium [53–56]. The latter two compounds only moderately deactivate the catalyst, however they reduce the N_2 selectivity considerably, especially at high temperatures [57]. While trace metal poisons may pose a problem for high-dust deNO$_x$ units in waste incineration plants, it is unlikely they will cause detrimental effects in biomass firing plants [49].

From the SCR reaction mechanism presented in Section 2.2.1, it can be seen that adsorption of Brønsted basic ammonia onto the Brønsted acidic sites of the catalyst is an important reaction step. When other basic compounds are present, these can be irreversibly adsorbed onto the acidic sites, thus decreasing the catalyst activity by hindering ammonia adsorption.

It is well established that alkaline alkali earth aerosols present in the gas can act as Brønsted bases and adsorb onto the acidic sites, causing strong deactiviation [58, 59]. The basicity of the aerosol determines the degree of deactivation caused, the stronger the base, the higher the degree of deactivation. This means the order of deactivation for the 4 most relevant species becomes: $K > Na >> Ca > Mg$ [60, 61].

The degree of deactivation is also affected by interactions between different relevant gaseous species. For instance, the presence of SO_2 mitigates the effect of calcium and magnesium to some extent, due to precipitation as the corresponding sulfate. On the other hand, the presence of SO_2 increases the deactivation caused by zinc. The deactivation caused by zinc is further increased by the presence of calcium sulfate [54, 61].

While the potassium deactivation is widely studied, the deactivation mechanism has yet to be fully understood [62].

Upon reaction between potassium and the active phase of the catalyst, the reducibility of the redox active vanadyl ($V^{5+}=O$) is decreased [54, 63]. And thus, potassium decreases the activity of the catalyst through two detrimental interactions. Furthermore, it has been found, that the potassium can migrate into the catalyst wall after deposition on the outer catalyst surface and thus extend the degree of poisoning [62].

It is unfortunate that potassium is both the most potent catalyst poison, and also present in the highest amounts in several of the alternative fuels that are of little other value (e.g. straw and municipal waste). Therefore, potassium poisoning is generally considered the most important challenge that must be overcome in order to remove NO_x from biomass/waste incineration flue gasses.

It has been found that the high amounts of potassium present in the flue gas when straw is used as fuel, leads to severe deactivation of the catalyst within a few hundred operating hours [64]. Within the first two hundred operating hours under normal conditions, the activity of the catalyst is halved when straw is used as the primary biomass constituent. Complete deactivation of the catalyst occurs within the first 1,000-2,000 operating hours. With the current methods, the deactivation caused by potassium poisoning prevent NO_x abatement in biomass and waste incineration plants altogether, when straw is used as the only biomass constituent.

2.3.2 Avoiding NO_x Slip in Biomass/Waste Incineration Plants

As mentioned above, avoiding NO_x slip is paramount for biomass and waste incineration to become truly viable, long term solutions. If incineration of biomass and waste leads to significant NO_x slip, then one problem is simply substituted for another.

Today, there are two widely studied strategies suggested to circumvent potassium poisoning. One is development of a low-temperature catalyst for use in tail-end SCR without substantial reheating. The other possibility is development of a poison-resistant SCR catalyst for use in the high-dust position. An alternative to the poison-resistant catalyst is finding a regeneration method. Regeneration of the catalyst is, however, very undesirable unless it can be done while on-stream. Although complicated, Peng *et al.* [65] have suggested a regeneration method using electrophoresis, which could, to some extent, be used on-stream. However, avoiding a regenerative step altogether is preferred and thus development of a poison-resistant SCR catalyst has received the most attention in literature.

Several studies on copper- and iron-exchanged zeolites, alternative formulations of the active phase, alternative support materials, and sacrificial heteropoly acid (HPA) sites on the catalyst have been performed [66–72].

Copper- and iron-exchanged zeolites show very high SCR activities and also a high resistance towards poisoning with alkali metals. However, the light-off temperature for the zeolites is often significantly higher compared to the V_2O_5 catalyst. Dealumination of the zeolites due to hydrothermal ageing, which leads to a risk of aggregation of the active phase, makes metal-exchanged zeolites undesirable for flue gas after treatment in stationary sources [73]. The reason that these deactivation mechanisms are less of a concern in diesel $\mathrm{deNO_x}$ is due to the significantly lower required lifetime of the catalyst.

Use of HPA as sacrificial acid sites has been proposed as a way to increase the potassium tolerance of the regular V_2O_5 catalyst. In these instances, HPA is used as a promoter instead of WO_3 and can effectively promote the SCR reaction on supports other than titania [74]. When coupled with a high vanadia loading, the use of HPA as a promoter on a V_2O_5 catalyst can help it retain most of the SCR activity at 225 °C, after loading of a 0.3 molar ratio (K:V) onto the catalyst [75]. For comparison, the activity of the regular WO_3 promoted V_2O_5 catalyst is nearly 0 at a molar ratio of 0.3 (K:V) [67, 68]. There is some concern about the thermal stability of the HPAs at temperatures exceeding 225 °C, but the effect has yet to be fully investigated [75].

Very recently, the use of highly sulfated supports has been proposed by Gao *et al.* [76] as a way to mitigate alkali poisoning. The authors show promising results for a 10 wt% Ce/V catalyst supported on sulfated zirconia. High NO conversions (almost 100%) were maintained at 350 °C in the presence of SO_2 and only a small decrease in activity was observed after loading the catalyst with 1.2 wt% K. In the studies presented, the long term effects have yet to be determined, but the results seem promising.

Another way to mitigate the deactivation pathways described above, is to place the $\mathrm{deNO_x}$ unit in the tail-end position after a wet FGD. At this point, the wet scrubber is expected to have removed all relevant catalyst poisons. If any poisons are left, it will only be in insignificant amounts.

As mentioned in Section 2.1, the temperature after a wet scrubber is expected to be around 60-80 °C, with very high water concentrations. This temperature is too low for emission of the gas because trace amounts of SO_x together with water can form a sulfuric acid condensate in the chimney. Therefore, the gas is heated to 120-150 °C prior to emission. This means, that the optimal low temperature $\mathrm{deNO_x}$ solution should work in these temperature intervals, and not be deactivated by the presence of water.

The low temperature catalysts presented in Section 2.2.2 mostly operate at temperatures around 200-250 °C to achieve satisfactory activity. This temperature can be lowered if a suitable method for low temperature oxidation of NO is found. However, as is shown in Chapter 6, a suitable method has yet to be reported in the literature.

Chapter 3

Gas Absorption in Ionic Liquids

Ionic liquids (ILs) are a class of molten salts that are liquid at or below an arbitrary limit of 100 °C [77]. There are a vast array of advantages obtained by using molten salts as solvents, these include, but are not limited to; low or immeasurable vapour pressure [77], high ionic conductivity and ionic strength [78], large electrochemical window and high thermal stability [79]. These advantages have led to an explosive development in applications of ILs, especially in the developmental stage, over the past 20 years. This trend is reflected in the number of publications within the field. A graph showing the number of publications within the field since 1943 is shown in Figure 3.1. This work primarily considers room temperature ionic liquids (RTILs), which is a subclass of ILs defined by being liquid at or below room temperature.
The research field of ILs is not new. In 1914, Walden [80], [81] was the first to report a quarternary ammonium salt with a melting point below room temperature; $[EtNH_3][NO_3]$, which melts at 13 °C. In 1928, Sugden and Wilkins [82] further expanded the list of low melting salts, to include several other quarternary ammonium salts as well as some aniline salts. From Figure 3.1 it can be seen that the field of ILs did not take off until the early 90's. This can however, to some extent, be attributed to the IL terminology not being clearly defined early on. Another reason for the increase in interest was the introduction of air and water stable RTILs first reported by Wilkes and Zaworotko [83] in 1992. This discovery significantly extended the range of possible applications and with it, the interest from researchers.

If not considering chloroaluminate ILs that were discovered in 1951 [84] and extensively researched from the late 1970's through to the 1990's [85], most early formulations of ILs and RTILs relied on quarternary ammonium and -phosphonium, or N-containing aromatic systems as cations. For instance, the ILs presented by Wilkes and Zaworotko [83] were based on the 1-ethyl-3-methylimidazolium ([EMIM]) cation which is still used extensively today. For future reference, Figure 3.2 presents the structure and abbreviations for some of the most commonly used cations, some of which have been used during this study. Anions can often be selected from a wide

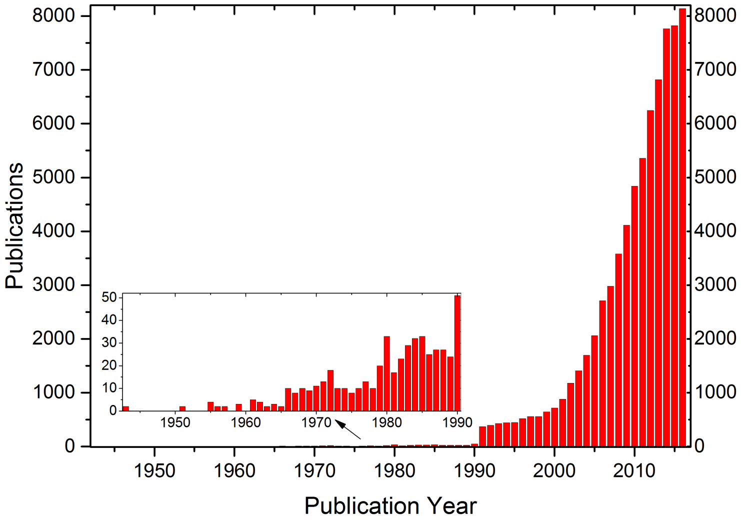

Figure 3.1: Development in publications with keywords related to ionic liquids per year, presented as an average over several multidiscipline scientific search engines; DTU Findit, SciFinder, and Web of Science. The zoom shows publications prior to 1991, in which case the highest amount was 52 (in 1990).

range including simple organic and inorganic anions as well as halides [86]. Over the past 20 years, a wide range of possible applications for ILs have emerged. Some of these utilise the tunable physical properties of the ILs to use them for e.g lubrication [87], [88]. In the following work, only the use of ILs as reaction media will be considered further.

One of the first reported uses in a catalytic process was by Chauvin *et al.* [89]. Here, a [BMIM] based IL (with various anions) was used to heterogenise the rhodium-catalysed hydroformylation of olefins with excellent yields. Several other similar applications have been reported, including hydrogenation [90] carbonylations [91] and Heck reactions [92] [93].

These biphasic systems combine some of the advantages of homogeneous catalysis, such as high atom efficiency, with the easier separation of heterogeneous catalysis [85]. However, using ILs to form a biphasic systems introduce significant mass transfer limitations and leaching of catalyst due to partial solvation of the IL [94]. A possible solution to the mass transfer limitations in the boundary layer is to disperse the IL onto a high area porous support to form a supported ionic liquid phase (SILP) or solid catalyst with ionic liquid layer (SCILL). This method is discussed in greater detail in Chapter 4.

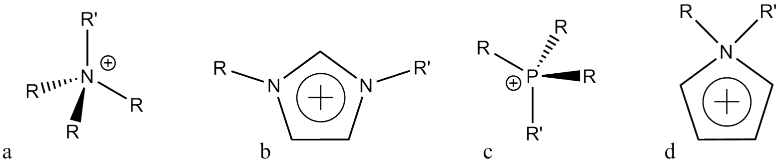

Figure 3.2: Chemical formula for several common cations. a: N,N,N,N-Tetraalkylammonium, abbreviation: $[N_{RxRxRxRx}]$ where Rx denotes the chainlength of the alkyl chain, b: 1-alkyl-3-alkylimidazolium, abbreviation: [RRIM], c: P,P,P,P-Tetraalkylphosphonium, abbreviation: $[P_{RxRxRxRx}]$ where Rx denotes the chainlength of the alkyl chain, d: 1-alkyl-1-alkylpyrrolidinium.

As the number of possible IL formulations increase, the specific sets of physical and chemical properties follow. This has led to the expansion of possible applications of IL systems, also outside of being alternative solvents in chemical synthesis. One of the applications that has emerged is the use of ILs as absorbers in natural gas sweetening, or as absorbers in flue gas after treatment systems. This was first reported by Brennecke *et al.* [95], showing how CO_2 was dissolved to a surprisingly high extent in [BMIM][PF_6]. This was the first report of relevant flue gas constituents showing high solubility in ILs.

3.1 Gas Absorption in Ionic Liquids

Since the breakthrough of Brennecke *et al.* [95] ILs have been investigated as possible sorbents for a wide variety of gasses. Several gasses have been shown to have a high solubility in ILs, including flue gas constituents, but also H_2S, ethane, O_2 and others [96].

This section will be dedicated to discussing absorption of relevant flue gas components in ionic liquids with emphasis on the absorption and oxidation of NO, which has been the main focus of this project.

3.1.1 SO_2 Absorption in Ionic Liquids

SO_2 is of concern, because it leads to smog formation and acidic precipitation. It is one of the major constituents of flue gas, especially when low quality fuels are used. In coal fired power plants, the sulphur content in the fuel is rarely above 1% and thus the resulting concentration in the flue gas is around 0.1-0.2% [97]. Despite the rather low concentration SO_2 constitutes a major environmental risk [97]. Today, most flue gas desulphurisation (FGD) is based on wet scrubbing of the acidic SO_2 with a ba-

sic aqueous solution/slurry, often comprised of limestone ($CaCO_3$). The scrubbing product, gypsum ($CaSO_4$), can in theory be used for construction. This is, however, rarely the case because the gypsum quality and purity is too low. Thus, the scrubbing generates a significant amount of waste. Other wet scrubbing alternatives have been tested, as well as solid elemental absorbers of various compositions [98]. All of these SO_2 abatement methods are seeing use on an industrial scale and remove SO_2 efficiently from the flue gas [99]. However, alternative methods are sought in order to accommodate the waste generation and possibly add value to the flue gas. This can be done by concentrating the SO_2, allowing for efficient conversion to valuable bulk chemicals such as sulfuric acid [100]. The use of ionic liquids for this separation process was first suggested by Wu *et al.* in 2004 [101].
Wu *et al.* found a molar absorption capacity of 1:1 (mol SO_2/mol IL) for 1,1,3,3-tetramethylguanidinium lactate ([TMG][L]). Since then, interest in the field has increased steadily. In a recent publication by Wang *et al.* [102], molar ratios above 4.5 were reported, with excellent reversibility. The ILs used in this study were P,P,P-trihexyl-P-tetradecylphosphonium imidazole and tetrazole ([P_{66614}][Im] and [P_{66614}][Tetz] respectively). In these formulations the anion is a functionalised azole, which is believed to increase the Lewis base strength of the nitrogen atoms considerably. Absorption is expected to occur at these sites through strong interactions with the moderately Lewis acidic sulphur on SO_2. It is important to note, that most of the maximum absorption values presented in the literature are obtained by exposing the pure IL to a SO_2 gas at 1 bar. In other studies, a SO_2/N_2 mixture with SO_2 concentrations between 2 and 10% (v/v) is used. Capacities obtained under these reaction conditions do not necessarily reflect the expected capacities in a flue gas, because of the significant discrepancy in concentration (or partial pressure) of the flue gas constituent.

There are two primary absorption interaction, which primarily governing gas uptake in an IL: Chemisorption and physisorption. Physisorption can to some extent be considered as a strong form of dissolution effect, as the interaction between the gas and the IL is weak. Thus, the capacity increases significantly with increasing partial pressure of the gas [103].
Increasing the pressure in a flue gas stream is very undesirable, as this requires a massive amount of energy, while complicating the gas treatment significantly. Consequently, increasing the SO_2 partial pressure through compression is not viable when processing several hundred cubic meters of gas per second.
Since the SO_2 concentration in the flue gas is low, the primary absorption route must be chemisorption, in order for the separation process to be efficient. In chemisorption, a chemical bond is formed between the gas component and the IL. Consequently, the interaction between the IL and the gas component is significantly stronger, making separation possible even at lower partial pressures. At higher partial pressures of the absorbent gas, reported capacities may be influenced by a high contribution from physisorption, which will also be reflected in the reported total capacity. General solvation is also dependent on the gas partial pressure [98]. The effect that these

different phenomena have on the absorption outcome are of vital importance and not conclusively tested at high SO_2 partial pressures.

One of the major advantages of absorption in ionic liquids is the reversible nature of the absorption, paired with the none-volatile sorbent. This should result in a long life span of the IL absorber. If the absorption is selective as well, this means that a high purity gas can be obtained directly from the flue gas. This high purity gas could be used for further reactions downstream to form a useful product such as sulfuric acid [100].

In order for reversible gas absorption with ILs to be applied industrially, it is important that the association energy between the gas and the IL is not too high, as this would lead to a high energy cost in the desorption process. Under optimal conditions, the association energy is only exactly high enough to absorb the gas in the desired quantities, and a small increase in temperature would lead to full desorption. Obviously, this is nearly impossible to achieved in practise.

The most efficient IL absorbers described in the literature use base functionalised anions to reach the high molar capacities reported [102, 104]. The anion can interact with the gas molecules through Lewis acid/base interactions, as most of the target gasses interact as weak Lewis acids. The Lewis acid strength of the gas species decreases as follows: $H_2S > SO_2 > CO_2 > NO$. Since the Lewis acid/base interactions are not necessarily selective, there is a risk of competitive absorption by other molecules which also possess Lewis acidic properties, such as water.

Several of the ILs presented in the literature have been shown to be very selective towards SO_2 compared to CO_2 [105], however, another major constituent of a flue gas is water. Water has very versatile acid/base properties and may act as an acid in this case, competitively absorbing on the basic sites also used for SO_2 absorption. Often, the selectivity with respect to water is not reported. Absorption of SO_2 is known to depend strongly on the anion of the IL [106]. It has also been shown previously, that water coordinates strongly with the IL anion [107]. Consequently, if water is absorbed into the IL, this coordination is likely to decrease the Lewis basicity of the anion, thus hindering absorption of acidic gasses. In some instances, water has been shown to form hydrogen bond bridges coordinating two anions; [A–H-O-H–A] [108]. Thus, even small quantities of water may be detrimental to the gas uptake.

Recently, the absorption capacity at lower partial pressures of SO_2 has been investigated. Significant absorption was found even at low SO_2 partial pressures, with a reported uptake of 0.4 mol/mol at 0.3% SO_2 for [TMG][L] [109]. However, at these molar uptakes, regeneration of the IL becomes an issue, because the SO_2 is too strongly bound. In order to reach full desorption of the SO_2, the IL had to be heated above the decomposition temperature. Consequently, the reversible molar uptakes found were significantly lower than 0.4, close to 0.05.

Very recently Murphy *et al.* [110] showed that dissolving diethylenetriamine (DETA) in a phosphonium based IL forms a system which retains its absorption capacity towards SO_2 with water present in the gas. When water is present, the SO_2 reacts to form sulfite (SO_3^{2-}) without negatively impacting the desorption capability. However, in the presence of oxygen, which is present in significant amounts in a flue gas, the sulfite is readily oxidised to form sulfate, which cannot be desorbed. Apart from this work by Murphy *et al.*, the influence of water has mostly been investigated in SILP materials.

The introduction of SILP materials is likely a necessity for most industrial applications of IL gas absorbers. Thus, it is more relevant to consider possible applicational challenges for SILP materials. Formulation of SILP materials are likely especially important for absorption of SO_2, since the viscosity of the already highly viscous IL increases upon absorption of SO_2 [111]. The use of SILP in gas absorption is discussed in detail in Section 4.2.1.

3.1.2 CO_2 Absorption in Ionic Liquids

Of the three gasses discussed here, CO_2 has by far got most attention in literature. There are several reasons for this: CO_2 levels in the atmosphere are increasing exponentially and CO_2 emissions contributes with around 65% of the total anthropogenic greenhouse gas emissions, counted in CO_2 equivalents [1]. Currently, there are no truly viable options to remove CO_2 from the biggest anthropogenic sources.

CO_2 is formed in a wide range of processes. In the U.S. the largest contributors to anthropogenic CO_2 emissions are electricity production, transportation and industry (not accounting for power usage), accounting for over 75% of total emissions [112]. As mentioned in Chapter 2, CO_2 is a more benign gas both long term and short term when emitted to the atmosphere compared to other flue gas pollutants. However, it also constitutes a significantly higher percentage of a regular flue gas, often around 10-15%, whereas the concentration of NO_x and SO_x, rarely exceeds 500 ppm (0.05%). Today, the most commonly used method for CO_2 removal is the storage/release method found in gas sweetening, in which both CO_2 and H_2S (both acidic gasses) are removed from the gas stream by scrubbing with a basic amine solution (often around 30% monoethanolamine in water) at low temperatures [113]. CO_2 is chemically absorbed in the basic solution, forming a carbamate adduct upon reaction with two monoethanolamine molecules. Upon heating of the solution, the carbamate decomposes, releasing CO_2 and simultaneously restoring the amine. It is important to keep in mind, when considering application of this method in a power plant, that the gas sweetening process is conducted at CO_2 partial pressures which can be upwards of two orders of magnitude higher than in the power plant. Furthermore, gas sweetening adds value to the final product, while there is no direct economic incentive to remove CO_2 from flue gasses.

Wet scrubbing with an amine solution has been implemented in several test facilities at power plants, but with limited success [114]. The energy required to run the reaction increases the power load of the plant by around 40% [115]. The significant added cost associated with the increased power load makes absorption with MEA undesirable. The volatility and basicity of the amine, constitutes an added risk due to emission/leaching of the amine and corrosion of materials in contact with the solution.

As mentioned previously, Brennecke *et al.* [95] were the first to report the high solubility of CO_2 exhibited by ILs. Although the purpose of their study was not removal of CO_2 from a process gas, it is still referred to by many authors as the start of studies concerning the use of ILs in CO_2 removal.
While the CO_2 partial pressure in the flue gas is significantly higher than the SO_2 partial pressure, it is still rather low. Since increasing the total pressure of the flue gas is not a possibility, an absorber primarily based on chemisorption of CO_2 is likely necessary for CO_2 removal in flue gasses.
Since the first reports of CO_2 solubility in ILs, much research has gone into improving the absorption capacity of the ILs, both by testing a wide variety of ion combinations, but also by introducing functionalisations in the ILs [104]. When paired with commonly used cations such as imidazolium, pyridinium, quaternary amines, and quaternary phosponium, the highly basic anions based on tri-flouromethanesulfonyl (TfO^-, Tf_2N^- and Tf_3C^-) yielded the highest absorption capacities [116]. This suggests that physisorption can be increased by utilising the acidic properties of CO_2. However, in a very recent publication by Carvalho *et al.* [117] this observation is suggested to be exclusively caused by formation of voids in the IL which have the correct dimensions for CO_2 absorption. In fact, the authors state that physisorption of CO_2 in almost all ILs is controlled by this void size.
Use of base-functionalised amino acid anions such as prolinate ([Pro]) and methioninate ([Met]) or base-functionalised aromatic amines such as triazole ([Triz]) and tetrazole ([Tetz]) have been shown to increase the uptake significantly at low partial pressures [104, 118].
Gurkan *et al.* [119] obtained high molar absorbtivity of CO_2 in a [P_{66614}][Pro] IL at CO_2 partial pressures relevant to flue gas conditions. A molar ratio of 0.85 (mol CO_2/mol IL) was obtained at a partial pressure of CO_2 around 50 mbar and 25°. The observations were suggested to be due to CO_2 reacting as a lewis acid, forming a carboxyl adduct with the anion. The absorption capacity was compared to a [P_{66614}][Met] and the initial absorption capacity was found to be higher for the [Pro] anion compared to [Met]. This was suggested to be due to a higher reactivity, or rather Lewis basicity, of the secondary amine [Pro] compared to the primary amine [Met].
The two ILs converged at the same equimolar ratio with no discernible difference in absorption capacity above 800 mbar. Concurrent studies by Brennecke and Gurkan [118] confirmed these observations and compared the [P_{66614}][Pro] to a known physisorbing IL ([HMIM][TF_2N]) and confirmed that the absorption capacity was several order of magnitude higher at low CO_2 partial pressures.
Functionalisation of the anion appears to be the most promising method for increasing CO_2 uptake in ILs, but functionalisation of the cation can also increase the CO2 uptake. Bates *et al.* [120] were the first to report functionalisation markedly improving absorption of CO_2 in a [BPIM] based IL. The functionalisation was an amination

on the terminal end of one of the alkyl groups (in this case propyl) of the [BPIM] cation, thus forming 1-butyl-3-aminopropylimidazolium. This IL functions through the same type of 1:2 molar ratio reaction seen for conventional chemisorption reaction with MEA. The CO_2 coordinates to the terminal amine of 2 cations, forming a coordinated ammonium carbamate dication. For this type of reaction, it was found that weakly interacting anions worked the best.

Bates *et al.* [120] also discussed the inability for most "off the shelf" ILs to absorb CO_2 without addition of other chemicals. Surprisingly, [BMIM] acetate ([OAc]) goes against this general observation and displays significant CO_2 absorption [121].

Rogers *et al.* [122] suggested this observation was caused by chemical complexation between IL and CO_2. The suggested mechanism for the reaction was a deprotonation of the C2 position on the [EMIM] cation forming a carbanion. Subsequent reaction of this with CO_2 allows for formation of a carboxylate species in the C2 position. This was suggested to be stabilised by hydrogen bonding to the C2 hydrogen of another cation, essentially forming a [EMIM-CO_2-EMIM][AcO-H-OAc] dimeric species. The maximum uptake for this type of reaction is 1:2 (mol CO_2/mol IL). And indeed, the molar ratio was found to converge on this 0.5 value at higher pressures or longer reaction times.

The effects of other types of functionalisations have also been investigated. For instance, etherification of the cation was proposed to increase CO_2 solubility, due to a higher flexibility of the long alkyl chains. The moieties created by this flexibility combined with Van der Waals complexes formed with the ether groups increases the absorption [123]. As with amination of the cation, the absorption rate and capacity increase with weaker coordinating anions.

With regards to absorption of CO_2 in ILs, the technology is improving as well as the understanding of several of the dominating factors in the absorption [124]. However, one of the major concerns with this process is the high viscosity of the current IL formulation, as well as the relatively high molecular weight (when maximum uptake is equimolar, molecular weight and density become important factors). The high viscosity may be circumvented by the use of SILP formulations which significantly increases the mass transfer, independent of the viscosity of the liquid [94]. Some reports of successful SILP absorbers can be found in the literature [104, 125, 126], suggesting that it is possible to use this technique in application in a possible absorber unit. The use of SILP absorbers is discussed in greater detail in Section 4.2.2.

Another important aspect with regards to application of the technology is the possible competitive adsorption of water. Similar to what was discussed for SO_2, water may absorb competitively or coordinate the active sites hindering the reaction. Very few authors have reported on this, other than Stevanovic *et al.* [127] reporting a significant decrease in CO_2 absorption capacity for the IL when water was present. At very low water concentrations, the decrease in capacity is somewhat negated by a decrease in viscosity. However, at 5-6 wt% of water in the IL, the capacity decreased by 83%, strongly suggesting that the high water concentrations in the flue gas are paramount to address in order for this method to become truly viable.

3.1.3 NO Absorption in Ionic Liquids

As with the other harmful emission gasses, nitric oxide solubility and absorption capacities in ILs have been investigated, but to a lesser extent than the other two mentioned above. It is unknown if this is because of lower relevance for coal fired power plants, due to the excellently working selective catalytic reduction (SCR) discussed in Section 2.2.1. It may also be that the affinity is simply lower in most liquids because NO interacts to a lesser extent than SO_2 and CO_2, thus yielding low absorption/dissolution ratios. The first reports on high capacity NO absorption in ILs are from our group [128]. An apparent uptake molar ratio of almost 4 (mol NO/mol IL) was obtained by letting a [BMIM][OAc] equilibrate with a gas containing 10% NO in N_2 for several days at 20 °C, while monitoring the gravimetric uptake. The contribution from physisorption was predicted by COSMO-RS to be negligible.

The solubility of NO in ILs was also tested by Duan *et al.* [129] and the initial findings by our group of very low physisorption was confirmed. Very recently, Chen *et al.* [130] reported a molar absorption capacity of over 4 in a [P_{66614}][Tetz] IL. This is the first superstoichiometric NO uptake reported, and the experimental results were supported by density functional theory (DFT) calculations showing a small, yet negative association energy even for the fourth associated NO molecule. Excellent reversibility was shown, regaining the absorption capacity after desorption in N_2 at 80 °C for 1 hour.

It is important to note that the experiments were conducted at high NO partial pressures compared to flue gas conditions, and the authors do not distinguish between physisorption and chemisorption. From the DFT calculations it appears, that absorption of the first two NO molecules is highly favourable, suggesting a type of chemisorption. While the association energy may be too high to use this exact type of IL for reversible absorption, the results are very intriguing.

The initial findings by our group, reported in [128], sparked several ensuing investigations. It was quickly found that the initially reported superstoichiometric uptakes based on gravimetric analysis were erroneous. The mass increase was actually caused by absorption and subsequent oxidation of the NO to nitric acid, due to a small leak of atmospheric air into the sealed container supplying both the water and oxygen needed for the oxidation to occur. Furthermore, a complete substitution of the $[OAc]^-$ anion to $[NO_3]^-$ was found.

These initial observations led to a more thorough study of the reaction, the results of which will be presented in this section. The *in-situ* attenuated total reflectance Fourier-transform infrared spectroscopy (ATR-FTIR) studies presented herein were concluded prior to the beginning the project period and performed in collaboration with Andreas Kunov-Kruse. Spectral analysis was performed during the project period along with follow-up experiments and publication of the results [131].

3.2 Experimental

Experiments with the neat ILs presented in this chapter were conducted in two different ways; bulk absorption experiments (gravimetric uptake experiments coupled with titration) and *in-situ* ATR-FTIR experiments. A more detailed description of the *in-situ* ATR-FTIR experimental setup along with reference data can be found in Appendix C.2.

3.2.1 *In-situ* ATR-FTIR experiments

The *in-situ* ATR-FTIR experiments were all conducted on a Thermo Scientific Nicolet iS5 FTIR spectrophotometer with a high temperature Specac Golden Gate ATR cell extension. The ATR-cell uses a single-reflection diamond and has golden mirrors for reflection of the IR beam inside the ATR-cell. A small IL droplet was placed on the diamond. Then a sealed gas cap was placed over the sample area. This allows for a continuous, controlled, flow of gas over the sample. The reaction gas was mixed from pressurized air, 1% NO in He (AGA) or 10% NO in N_2 (AGA). The gas flow was controlled using N_2 calibrated mass flow controllers (Bronkhorst), all were manually recalibrated for each specific gas. Two streams of air were used; one was saturated with water by bubbling through a water reservoir at room temperature. The water concentration in this stream is assumed to be 2.4 %, and the total water concentration is calculated based on this.

The earliest experiments were conducted by first fitting the gas cap over the sample and equilibrating in a stream of pure air. At time zero in the experiments the NO containing stream was shifted from bypass to join the air stream. This means there is a short period where the pure air is displaced. In this period the NO concentration is lower than the target value and may also fluctuate at the position of the IL droplet. In the experiments used for kinetic studies and temperature studies, the gas mixture was allowed to reach the target concentration before the gas cap was attached over the IL film, which was in equilibrium with the atmosphere at room temperature. Since the experiments with [BMMIM][NO_3] and the experiment with [BMIM][NO_3] in Figure 3.3 are completely comparable, the deviation resulting in the difference in the methods can be assessed by comparison of these two curves.

As expected the apparent reaction rate was lower when the gas was not allowed to equilibrate in the cap before the experiment started. Conclusions drawn on the amount of HNO_3 present at steady state as well as comparisons between the ILs measured under the same conditions are not influenced by the shift in *in-situ* methodology used. For future reference, Figure 3.3 below shows the spectral development during absorption of a gas containing 2% NO, 16% O_2, 2% H_2O and balance N_2. The gas is in vast excess and high relative flow (50 mL/min), thus absorption in the small IL droplet is not expected to influence the gas total concentration. The spectral

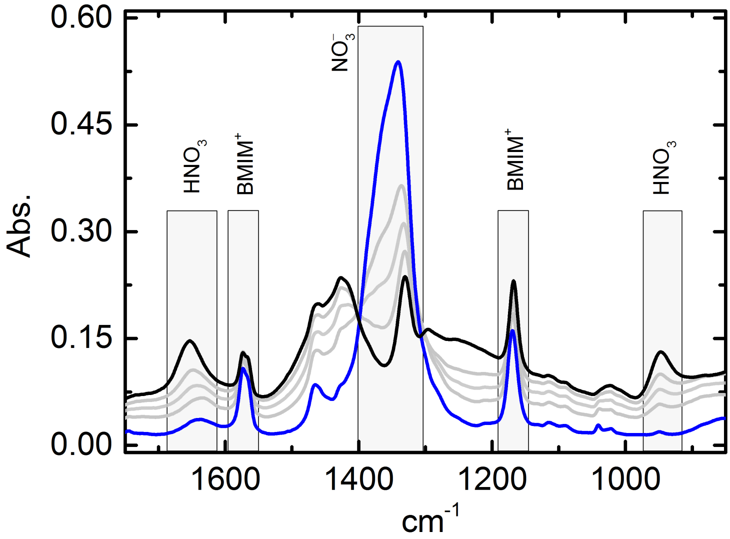

Figure 3.3: *in-situ* ATR-FTIR spectra obtained during absorption of a gas containing 2% NO, 16% O_2, ca. 1% water and balance N_2 at RT, in a [BMIM][NO_3] IL. Most relevant species are marked in the spectrum. The blue line is the starting spectrum, the grey spectra were obtained during absorption, the black spectrum was obtained after saturation.

development found in Figure 3.3 is generally descriptive of the spectral changes observed during *in-situ* ATR-FTIR experiments. Consequently, most of the species denoted here are observed throughout the *in-situ* ATR-FTIR experiments, for all IL compositions.

3.2.2 Quantification of HNO_3

In order to evaluate the rate of reaction with NO, a quantification method was developed based on spectral deconvolution. The concentration of the HNO_3 in the sample was determined by deconvolution of the spectrum around the HNO_3 band at 948 cm^{-1}. An example of such a deconvolution is shown in Figure 3.4 below. Batch deconvolution of the spectral data was carried out in `GnuPlot 4.6` by first performing a full deconvolution in `PeakFit 4.12` to determine peak positions and peak width of the Gaussian curves in the saturated spectrum. It was assumed that no relevant species appeared during the absorption, that were not present in the saturated sample.

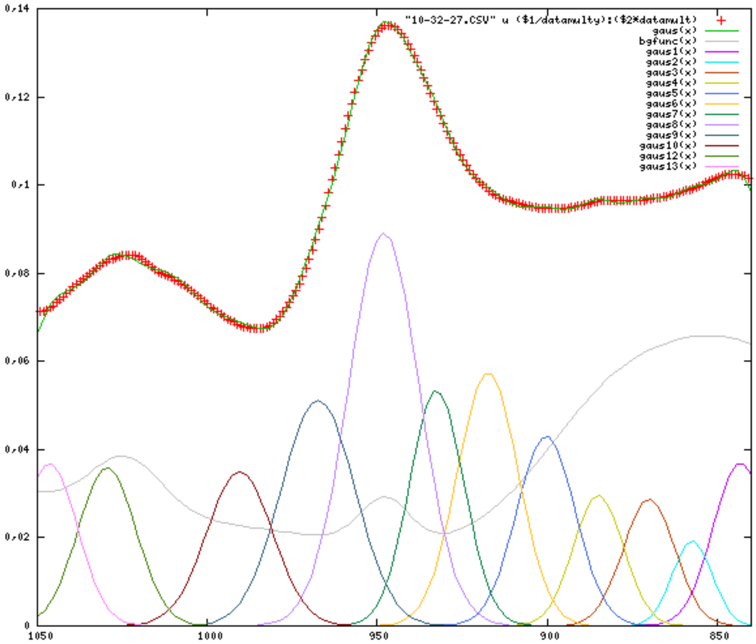

Figure 3.4: Example of output file from deconvolution of the IR spectrum around the HNO_3 band. The grey line is the background spectrum and the highest of the Gaussian peaks (purple) is the one used for HNO_3 quantification. The red dots constitute the simulated spectrum and the green line is the experimental target value.

`GnuPlot 4.6` was then used to deconvolute the spectra by changing the amplitude of the Gaussian curves, optimising the fit (least squares method). This was done by fitting the saturated spectrum, then the second to last spectrum and so forth. From Figure 3.4 it can be seen that a high number of Gaussian curves were required to obtain a satisfying fit of the experimental data. In order to assure the best possible continuity in the quantification, the peak positions and widths of the peaks were kept constant for the deconvolution of each IL. Furthermore, every single output file was examined to ensure the quality of the fit was maintained.

Unfortunately, the absolute HNO_3 concentration was derived from a standard curve with rather few points, and the equipment broke before we had a chance to redo the experiments. Therefore, there is an uncertainty on the exact HNO_3 concentration in the ILs, which is unlikely to exceed 10%. The standard curves for this experiment are found in Appendix C.2.

The potential inaccuracy of the standard curve is only expected to influence the reported molar ratio at saturation. Comparative rates found between individual ILs should be unaffected.

3.2.3 Bulk Absorption of NO in [BMIM][NO_3]

Bulk absorption experiments were conducted using a glass cylinder. A glass reactor was designed for absorption in both neat ILs and SILP materials, the reactors are shown in Appendix B.3. For absorption in bulk IL, the gas was administered through a fine glass frit. For SILP absorption experiments, the gas was instead passed through the SILP bed, which was situated on a sintered glass frit.
Approximately 1 g of IL, dried under vacuum at 60 °C for 2 days and subsequently kept in an oven at 110 °C, was loaded into the glass reactor and the reactor was sealed from the atmosphere. The full reactor was then weighed, gas lines were fitted to the reactor via SwageLock couplings and the desired gas was administered. Unless otherwise noted, the administered gas in the gravimetric experiments contained 5% NO, 10.5% O_2, 1% H_2O and balance N_2. When weighing the samples during the experiments, the reactor was sealed and the gas couplings were disconnected. The time for each measurement was recorded in order to subtract this from the total absorption time noted in experiments.
For comparison, an aqueous solution of $NaNO_3$ was exposed to the same gas as the IL. The concentration of this solution was 6.1 mol/L, which is comparable to the volumetric nitrate concentration found in [BMIM][NO_3], based on density measurements carried out on the dried IL. $NaNO_3$ was chosen because it was the only readily available nitrate salt with sufficient solubility to reach these concentrations.
For titration experiments, the dried IL or $NaNO_3$ solution was added to the reactor and weighed as explained above. The gas was then administered for the desired exposure time before the reactor was sealed and gas lines disconnected. The content of the reactor was then carefully transferred to a 250 mL volumetric flask. In order to ensure everything was transferred, the reactor including the glass frit was washed carefully with water several times. The washing water was transferred directly into the volumetric flask.

Titration was carried out using a 0.010 M NaOH solution issued from a 25 mL burette. Three standard experiments were carried out, measuring the pH with a Fisher Orion Star pH-meter. An example of the titration curve from an absorption sample is shown in Appendix A.3, showing a typical titration curve for a strong acid when the IL had been exposed to the NO containing gas. The pure IL was found to have a pH of 5.5, which increased to above 7 after addition of 1 drop of NaOH solution.
The results obtained from continuous pH measurements were compared to results obtained at equilibrium using a methyl red indicator solution. The results were found to be comparable and therefore, subsequent titrations were carried out using the methyl red solution. The methyl red solution was prepared by dissolving 0.100 g in 200 mL ethanol and 300 mL deionised water in a 500mL volumetric flask. In all titrations, triple determination of the H^+ concentration was performed with little variance ($\pm$ 0.05 mL = $\pm$ 0.25%).

3.3 Results and Discussion

This section discusses the results obtained from studying the reaction of neat ILs with NO in the presence of oxygen and water. The absorption capacity of different IL compositions was investigated along with the reaction kinetics using an *in-situ* ATR-FTIR method developed for the purpose. Studies on the bulk absorption of the IL was used to investigate the selectivity of absorption and to compare the absorption capacity to that of a sodium nitrate solution with similar nitrate concentrations.

3.3.1 *In-situ* ATR-FTIR Investigations: Influence Ionic Liquid Composition

In order to determine if NO absorption capacity was unique to a specific anion/cation combination, or if other ILs displayed the same activity, the effect of changing anions and cations was determined. The absorption capacity for choline acetate [Ch][Ac] was investigated, and both the absorption capacity and absorption rate was found to be comparable to that of [BMIM][Ac]. This suggested that there was little to no influence on the absorption from the cation. Later, a 1-butyl-2,3-dimethylimidazolium ([BDMIM]) cation was tested and yielded comparable rates as well. The rate of HNO_3 formation in some of the different ILs studied is shown in Figure 3.5. The ILs were tested in a simulated flue gas containing 6% NO, 8% O_2, ~1% water and balance N_2. Figure 3.5 shows the rate of HNO_3 formation for several different ion pairs, as determined by the deconvolution method described in the experimental section above. It appears there is a limited effect of changing the cation, as both [BMIM],[BDMIM] and [Ch] have comparable rates of HNO_3 formation.

The apparent difference in rate for the [BMIM][NO_3] sample can be explained by a change in experimental procedure, which allowed for immediate exposure of the IL to the target NO concentration. In the other experiments, the gas concentration gradually increased from 0-6%.

The figure shows an apparent molar uptake ratio capped at 1:1 in most cases, with only the triflate IL showing a lower capacity. It appears that once the equimolar molar ratio is reached the reaction proceeds, but at a significantly lower rate. This rate likely corresponds to the absorption rate of a concentrated nitrate or nitric acid solution, which is known to absorb a non-negligible amount of NO, converting it to HNO_3 in the presence of water and oxygen [132].

When the anion is changed, there appears to be a significant difference in both maximum HNO_3 formation rate and overall capacity. For the triflouromethanesulfonate (triflate, [OTf]) anion, the molar ratio appears to converge at 0.5 before reaching the slow steady state accumulation. The rate of formation also appears to be lower than for the other ILs.

For the chloride anion, the progression of the accumulation follows a different trend

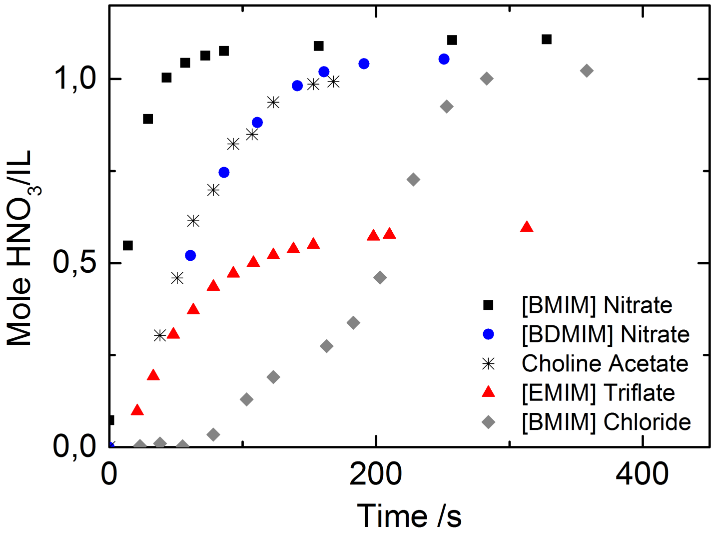

Figure 3.5: Approximate HNO_3:IL molar ratios estimated by deconvolution of *in-situ* ATR-FTIR spectra obtained during exposure of the ILs to a gas mixture containing: 6% NO, 8% O_2, ca. 1% H_2O and balance N_2 at RT. The [BMIM][NO_3] data were obtained after the experimental procedure was optimised to allow for exposure to a stabilised premixed gas. In the other experiments, there was a more gradual increase in NO concentration in the gas mixture.

than the other ILs. Here, the difference in rate may have been caused by a high water concentration in the IL prior to the experiments, because the maximum rate of formation (obtained around the 0.4 molar ratio and onwards) seems to be the same as for the other ILs, despite the reaction taking significant time to develop. The reaction was investigated further by looking at the *in-situ* ATR-FTIR spectra obtained during absorption, some of these are presented in Figure 3.6. From Figure 3.6 it appears that nitrate is formed rapidly after exposure to the gas. This can be seen from the emergence of a band at approximately 1315 cm^{-1}. Immediately after exposure, the nitric acid bands at 1660 cm^{-1} and 948^{-1} do not appear to increase significantly. Not until a significant amount of NO_3^- has formed, does the HNO_3 formation rate increase to the rate observed in Figure 3.5.
Prior to the reaction, the water band (O-H bend) at 1640 cm^{-1} is rather broad, but when the reaction starts, the band is red-shifted slightly and narrows significantly. After the initial change, the water band does not change further until it disappears after the equilibrium molar ratio of HNO_3 is reached. This effect is not observed for [BMIM][NO_3], see Figure 3.3. In [BMIM][NO_3], the band centre for the water

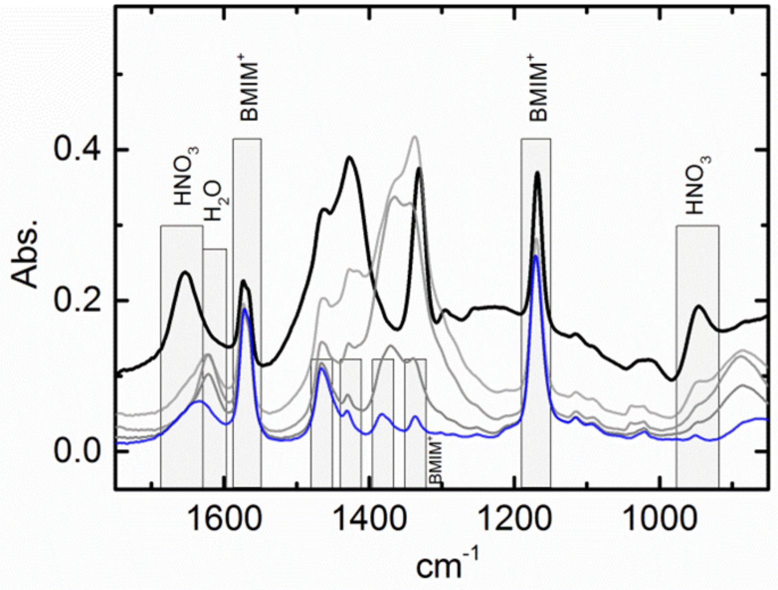

Figure 3.6: *in-situ* ATR-FTIR spectra obtained during exposure of [BMIM]Cl to a gas containing 6% NO, 8% O_2, ca. 1% H_2O and balance N_2, at RT. The blue spectrum was measured prior to exposure to the gas, the grey spectra during absorption and the black spectrum after saturation. Most relevant species are marked in the spectrum, apart from NO_3^-, which is located around 1315 cm^{-1}. The blue line is the starting spectrum, and the three grey spectra are from the initiation phase.

is unaffected, and a gradual shift of the water signal at approximately 1640 cm^{-1} to HNO_3 at approximately 1660 cm^{-1} is observed, as HNO_3 is formed and water consumed.

The change observed for the water band at 1640 cm^{-1} during reaction suggests that the hydrogen-bonding state of water changes. This change may be because the water is "activated" by the bonding state with the Cl^- anion, and acts as the reaction site for gaseous NO. The reaction between water and NO is likely significantly slower than reaction between NO and the pure anion, and would thus explain the slow initial uptake observed for [BMIM]Cl.

The chloride anion has no bands in the IR spectral region, thus the fate of the Cl^- anion is unknown. In [BMIM][OAc], the carbonyl stretching band of the acetate anion is located at approximately 1590 cm^{-1}, making it easy to follow during the reaction. *In-situ* spectra from the absorption of NO in [BMIM][OAc] are shown in Figure 3.7. From the grey and black spectra in Figure 3.7, it is seen that during absorption all acetate is transformed into acetic acid, which then slowly disappears from the IL during the reaction, as can be seen from the decreasing signal of the

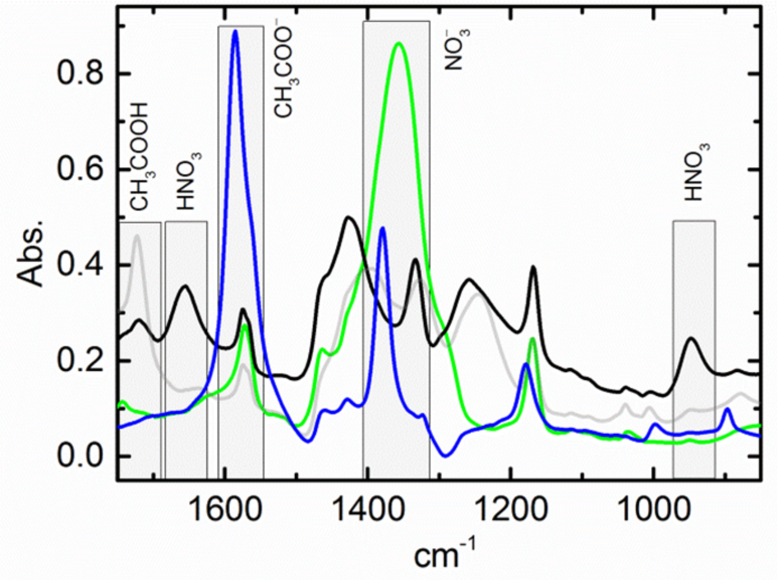

Figure 3.7: *in-situ* ATR-FTIR spectra of [BMIM][OAc] during exposure to a gas containing 6% NO, 8% O_2, ca. 1% H_2O and balance N_2, at RT. The blue spectrum was measured prior to exposure to the gas, the grey spectra during absorption, the black spectrum after saturation and the green spectrum after absorption and subsequent desorption under dry N_2 at 120 °C and for 30 min, the IL was cooled to RT prior to the measurement.

acetic acid band at 1720 cm^{-1}.

As with chloride, acetate is a stronger base than nitrate and the corresponding acid should evaporate more willingly from the IL, compared to nitric acid. It is noted, that a small amount of acetic acid still appears to be present after saturation, suggesting that the two acids can co-exist without it having a negative influence on the reaction rate.

As shown in Figure 3.5, the acetate based IL and the nitrate based IL had similar reaction rates. The presence of a small amount of acetic acid may also, in part, explain the slightly super-stoichiometric uptake in the gravimetric analysis reported in [128], even when accounting for the conversion to HNO_3. After desorption at 120°C, the acetic acid is completely removed, yielding pure [BMIM][NO_3] as the only product.

Triflate ([OTf]) is the corresponding base to the super acid triflic acid and thus, the base strength of this anion is significantly lower than nitrate. As discussed previously, the maximal capacity of the triflate IL is around half of that observed for the nitrate based ILs, while the reaction rate is significantly lower. Since it has been determined that the cation has a negligible effect on the absorption rate, this must be due to the triflate anion. Figure 3.8 shows the *in-situ* ATR-FTIR experiments from

NO absorption in the triflate IL. From Figure 3.8 it is seen that HNO_3 is still formed

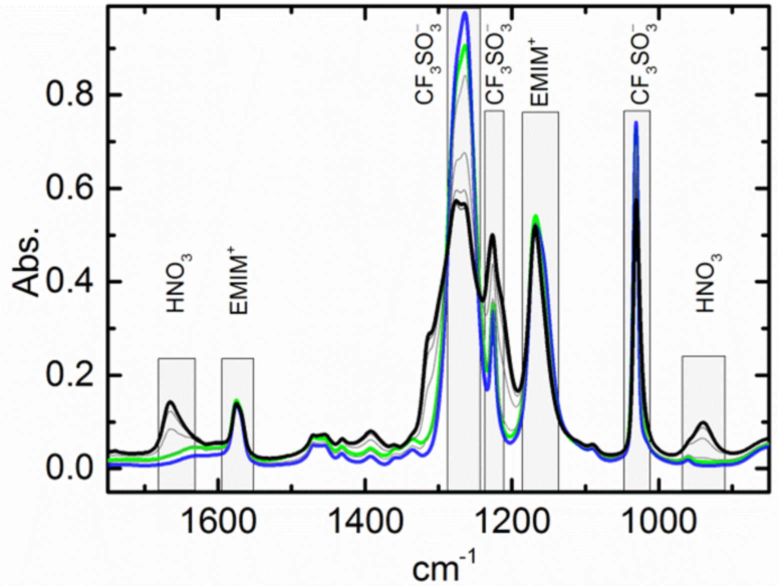

Figure 3.8: *In-situ* ATR-FTIR spectra of [EMIM][OTf] during exposure to a gas containing 6% NO, 8% O_2, ca. 1% H_2O and balance N_2, at RT in a [BMIM][OTf] IL. The blue spectrum was measured prior to exposure to the gas, the grey spectrum during absorption, the black spectrum after saturation and the green spectrum after absorption and subsequent desorption under dry N_2 at 120°C and for 30 min, the IL was cooled to RT prior to the measurement.

in the triflate, but the area of the 948 cm^{-1} peak at saturation only corresponds to a molar uptake of approximately 0.55:1. The observed splitting and decrease in intensity of the sulfonyl (S=O) band around 1270 cm^{-1} is likely caused by interaction between the anion and the nitric acid formed. This interpretation is supported by the apparent correlation with the HNO_3 band at 948 cm^{-1}. Furthermore, the strong nitrate bands around 1310 cm^{-1} and more pronounced at 1420 cm^{-1} are not observed, suggesting that no nitrate is formed during the reaction, other than that of the HNO_3. From the desorbed spectrum (green) it is seen that the anion of the IL is not changed to nitrate after absorption. After desorption, the IL returns to the former state of neat [EMIM][OTf].

Based on the presented results, the anion appears to have a significant effect on the absorption, while the cation does not. Thus, it was decided to base all future experiments on the [BMIM] cation, as this is commercially available in high purity and analytically well-defined. For larger scale operations, in case this ever becomes relevant, the research presented here shows that it should be possible to instead use

the cheaper, biodegradable choline cation.
The anion appears to have a significant effect on the absorption rate. Therefore, one could be led to believe that the basicity of the anion is an important factor for activating the kinetically hindered NO. While this is likely the case, large differences in reaction rates have not been observed in this work, other than for the triflate anion. This may be due to water coordinating strongly to the anion, decreasing the basicity. It may also be because more basic anions are quickly protonated and replaced by nitrate, under subsequent evaporation of the corresponding acid. Thus, the reaction rate will most likely not exceed the reaction rate for the corresponding nitrate IL, and even if it does, the increased reaction rate will not be maintained for long.

In all cases where the basicity of the anion exceeded that of nitrate, the resulting IL after desorption at 120 °C, always contained the nitrate anion. This means that for application in continued absorption/desorption process cycles, the IL should always be based on the nitrate anion. Incidentally, this method can also be used to synthesise nitrate based ILs from their halide counterparts. An example of this is shown in Chapter 5.

As mentioned above, Chen *et al.* [130] investigated NO absorption in azole based ILs. Upon comparison of the data presented by Chen *et al.*, with the results presented here, there is some risk they have misinterpreted their results due to formation of nitric acid. They may have accidentally formed nitric acid, as was the case in the first gravimetric experiments presented by our group. There are several indications of this in the reported FTIR spectra, with significant absorption bands at both 1313 cm^{-1} and 1411 cm^{-1}, which are consistent with nitrate bands. The authors attribute these to N-O stretching bands from absorbed NO. Their predictions are based on DFT calculations, predicting them at 1360 cm^{-1} and 1404 cm^{-1} respectively. Furthermore, absorption bands of increasing signal strength are observed at both 1650 cm^{-1} and 948 cm^{-1}, which is consistent with the presence HNO_3. The absorption band at 1650 cm^{-1} is attributed to NO dissolved in the IL, but this seems highly unlikely, as there are no reports in the literature of any IL with significant solvation effect towards NO. The absorption band at 948 cm^{-1} is not discussed.
The increase in peak intensity is not linear, but increases significantly more towards the end of the experiment. This could mean, that if the peak can indeed be attributed to dissolution of NO, this must be due to an increased solubility induced by the absorption of NO.
The reported H1-NMR data does not show the spectral region in which one would expect a strongly acidic proton, and is thus inconclusive with regards to the formation of HNO_3. It is important to note, that even if these authors have slightly misinterpreted the results (which we also did previously) their findings are still of immense importance, because their reported gravimetric uptake ratio of 4.5 corresponds almost perfectly to a molar uptake of 2:1 if the gravimetric increase is considered to be HNO_3 instead of NO. Coupled with our findings that the cation plays a minor role in determining the total capacity, this suggests that using the rather small tetrazolate

anion ([Tetz]) could possibly be coupled with a smaller cation while still maintaining the 2:1 molar capacity.

3.3.2 Bulk Absorption of NO in Ionic Liquids

Under the reaction conditions utilised in the *in-situ* experiments, the mass transfer limitations caused by reaction of a gas with an IL was avoided because the IL was a thin droplet on a plate, thus resembling a SILP which is known to increase mass transfer substantially [94]. This is not the case with the bulk absorption experiments, where a larger volume (1 mL) of IL was subjected to a gas flow. Even though the gas was submitted through a fine sintered glass frit, the bubbles formed were still large, revealing that mass transfer is poor in the gas/IL interface. This observation is further supported by viscosity measurements for the IL. The viscosity at 25 °C was larger than 200 mPa·s and thus outside the range of our equipment in the current configuration. The viscosity was estimated to be between 240-260 mPa·s, extrapolated from a series of measurements on the dry IL at elevated temp, and from a series of measurements with varying water content. For comparison, this estimated viscosity is around 300 times higher than that of water at the same temperature.

The bulk absorption experiments were largely carried out to confirm the capacities measured in the *in-situ* experiments, as well as to compare the IL to an aqueous solution with a similar nitrate concentration. Bulk absorption is likely an unfit method to directly compare the rate of the reaction because the reaction rate is strongly hindered by the viscosity of the IL. However it was the best method available since the *in-situ* investigations were found to cause irreversible damage to the ATR plate.

Figure 3.9 shows the gravimetric uptake and the corresponding acid concentration determined by titration. It is seen from Figure 3.9 that there is an increasing discrepancy between the gravimetric amount measured and the titrated amount except for the last point at 10h. The formation of HNO_3 appears to continue, albeit at a lower rate after 1:1 molar ratio has been reached. This is not unexpected as nitrate solutions have been shown capable of doing this [132]. From the *in-situ* ATR-FTIR data presented in figure 3.3 it is seen that no water is present in the IL when it has been saturated with HNO_3. This may explain the lower observed discrepancy between the gravimetric uptake and the titrated amount after 10 hours.

Figure 3.10 compares the absorption capacity of [BMIM][NO_3] to $NaNO_3$(aq) with similar nitrate concentrations. The viscosity of the almost saturated $NaNO_3$ aqueous solution was found to be 2.5 mPa·s, which is more than two orders of magnitude lower than the estimated value for [BMIM][NO_3]. It can be seen from Figure 3.10 that the absorption rate is considerably higher in the IL compared to the aqueous solution. This is despite formation of crystalline $NaNO_3$ forming around the sintered frit, increasing the local NO_3 concentration around the frit. It was not possible to analyse the uptake in the $NaNO_3$ solution gravimetrically, as there was no apparent correlation between mass increase and HNO_3 concentration, most likely due to

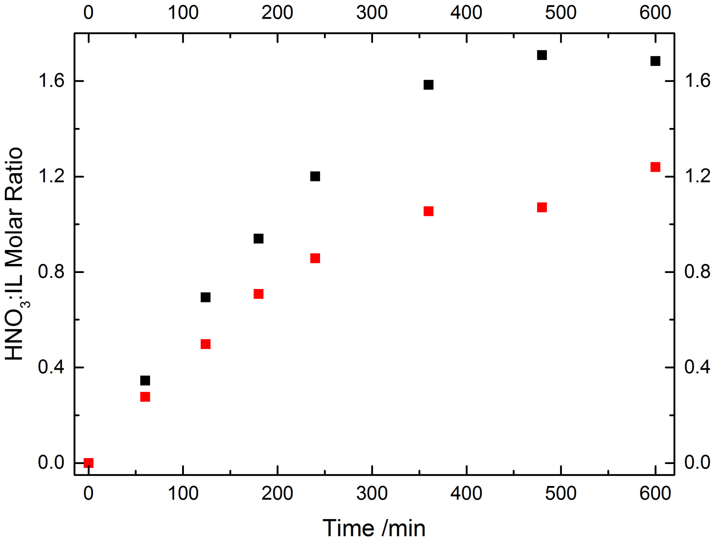

Figure 3.9: HNO_3 accumulation as a function of time calculated from gravimetric (black) and titration (red) data in a [BMIM][NO_3] IL being subjected to a gas containing 5% NO, 10.5% O_2, 1% H_2O and balance N_2.

water evaporation. It can also be seen from Figure 3.10, that despite the significantly hindered mass transfer in the IL, the rate of HNO_3 formation is significantly higher compared to an aqueous nitrate solution with comparable volumetric nitrate concentration.

3.3.3 Reaction Kinetics

In order to better understand the reaction dynamics, a more elaborate study of the reaction kinetics was carried out by the same *in-situ* ATR-FTIR method mentioned above. The maximum linear rate observed over a minimum of 7 measurements was determined at varying NO concentrations. Figure 3.11 shows the maximum linear rates obtained at varying NO concentrations. The results are presented in the form of a log/log plot, from which a linear regression of the points should yield the reaction order with respect to NO. When determining the rates presented in Figure 3.11 it was found, that at NO concentrations higher than 5%, the reaction rate decreased slightly compared to the rate observed at 5%, therefore, these data points have been excluded.

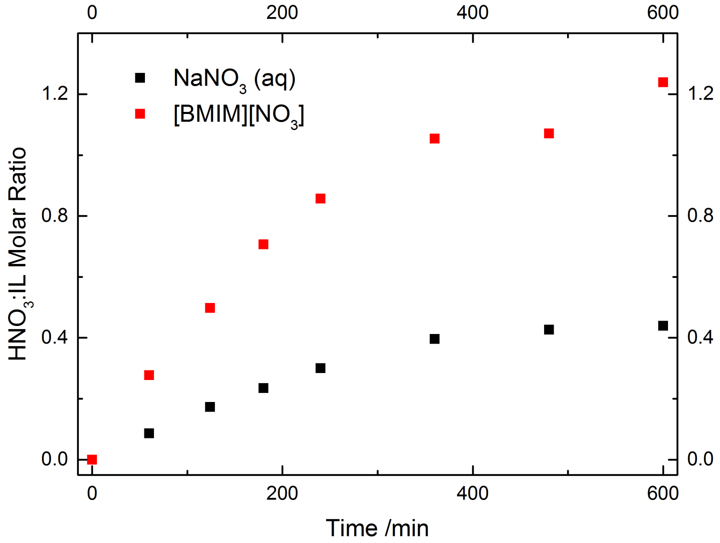

Figure 3.10: HNO_3 accumulation as a function of time calculated from titration data in a [BMIM][NO_3] IL (red) and a $NaNO_3$ aqueous solution (black) being exposed to a gas containing 5% NO, 10.5% O_2, 1% H_2O and balance N_2.

From Reaction 3.1 below it is seen that the stoichiometric ratio of NO to water is 2:1. For experiments conducted at high NO concentrations, the feed ratio (NO:H_2O) is close to 10:1. Under these conditions, water likely becomes a limiting factor, explaining the observed decrease in overall reaction rate.

$$4\,\mathrm{NO} + 3\,\mathrm{O_2} + 2\,\mathrm{H_2O} \longrightarrow 4\,\mathrm{HNO_3} \tag{3.1}$$

The slope of the red line presented in Figure 3.11 is 2.0, thus suggesting a second order dependence on NO in the formation of HNO_3. This rate of oxidation is similar to what is observed in aqueous solutions, such as in the Ostwald process [133], and also in the autoxidation of NO in air. In both of these cases, the reaction is also first order with respect to O_2, yielding the rate expression shown in Equation 3.2 below.

$$-\frac{d\mathrm{NO}}{dt} = k \cdot [\mathrm{NO}]^2 \cdot [\mathrm{O_2}] = k \cdot p_{\mathrm{NO}}^2 \cdot p_{\mathrm{O_2}} \tag{3.2}$$

When investigating the reaction kinetics, it is customary to do an Arrhenius plot to determine the activation energy of the reaction, as this yields a lot of information about the reaction and also helps in modelling at a larger scale. Figure 3.12 shows the maximum linear rates of HNO_3 formation at varying temperatures from 25 C° to 60 °C. From Figure 3.12 it can be seen that the reaction does not follow regular

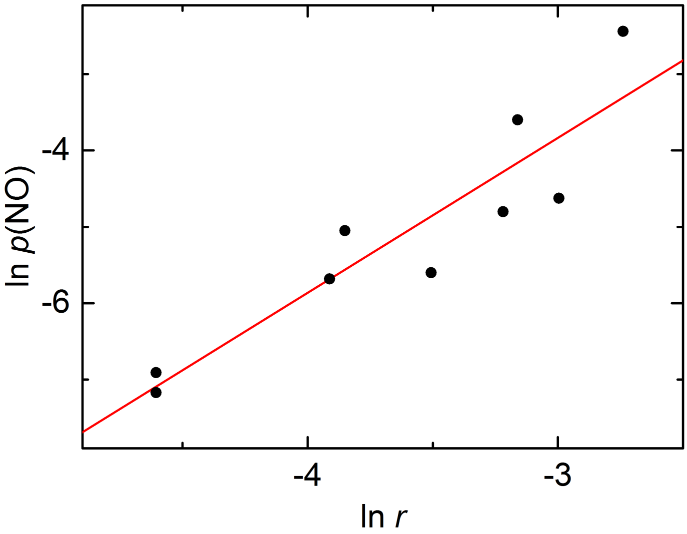

Figure 3.11: Log-log plot of the maximum linear rate of HNO_3 formation at varying NO concentrations as determined by deconvolution of the 948 cm^{-1} peak in *in-situ* ATR-FTIR spectral data. The red line shows the best fitted linear regression, the slope of this line is 2.0.

Arrhenius kinetics, in which the reaction rate increases with temperature. There does however, appear to be a significant increase in the reaction rate when increasing the temperature to slightly above room temperature. At 34 °C, the rate increases by a factor of 4 compared to room temperature. When the temperature is increased further, the reaction rate decreases again. These observations suggest two competing, rate limiting factors.

The solubility of gasses in ILs (and liquids in general) decreases with increasing temperature. Assuming the reaction occurs in the IL media between dissolved species; this decrease in solubility would effectively decrease the concentration of reactants and in turn lead to a lower observed rate. The lower rate observed at higher temperatures thus suggests that the reaction primarily occurs between dissolved species.

Several factors could play a role in increasing the reaction rate at slightly elevated temperatures. Duan *et al.* [134] reported higher NO solubility in ILs with increasing temperatures. However, with a rate increase of this magnitude, slightly higher solubility is unlikely to be the only explanation. Another explanation may be, that the increased temperature increases the mobility of the dissolved species, e.g. through lowering of the IL viscosity. A higher mobility would also lead to a higher reaction

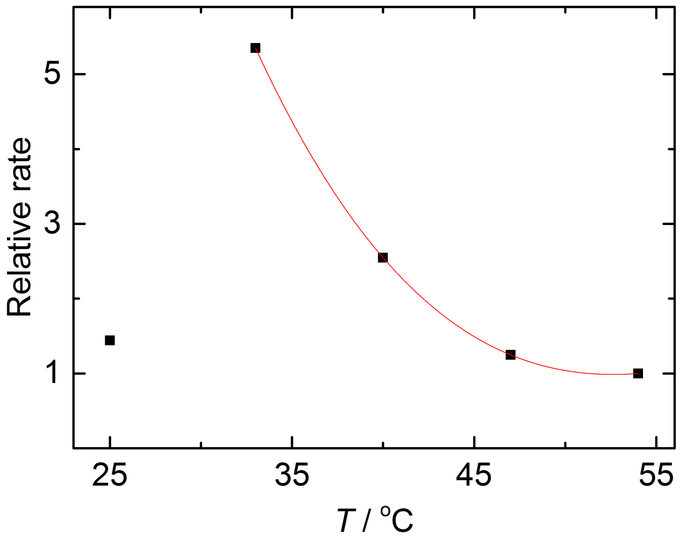

Figure 3.12: Maximum linear rates of HNO_3 formation relative to the observed rate at 327 K. Analysis was performed with a gas mixture containing 2% NO, 16% O_2, 1.5% H_2O and balance N_2. The red line is meant as a guideline to see the approximate trend of the development in reaction rate after the maximum has been achieved.

rate towards formation of HNO_3.

3.3.4 Reaction Mechanism

In order to gain a better understanding of the active species involved in the reaction, an attempt was made to determine intermediates in the reaction from the *in-situ* spectral data along with a few supporting experiments. All the results presented in this section were obtained using [BMIM][NO_3]. In one experiment, the [BMIM][NO_3]was subjected to a dried NO_2 gas formed by dissolving copper in concentrated nitric acid and drying the effluent gas with P_2O_5 before leading it over the IL. An attempt was made to dry the IL prior to the experiment, but a small residue of water was still present. Figure 3.13 shows the spectra obtained from these experiments. From Figure 3.13 it is seen, that due to the presence of water (small band at 1640 cm^{-1}) in the IL prior to the experiment, both nitric and nitrous acids were formed. Nitrous acid can be identified by the presence of characteristic bands at 1260 cm^{-1} and 1290

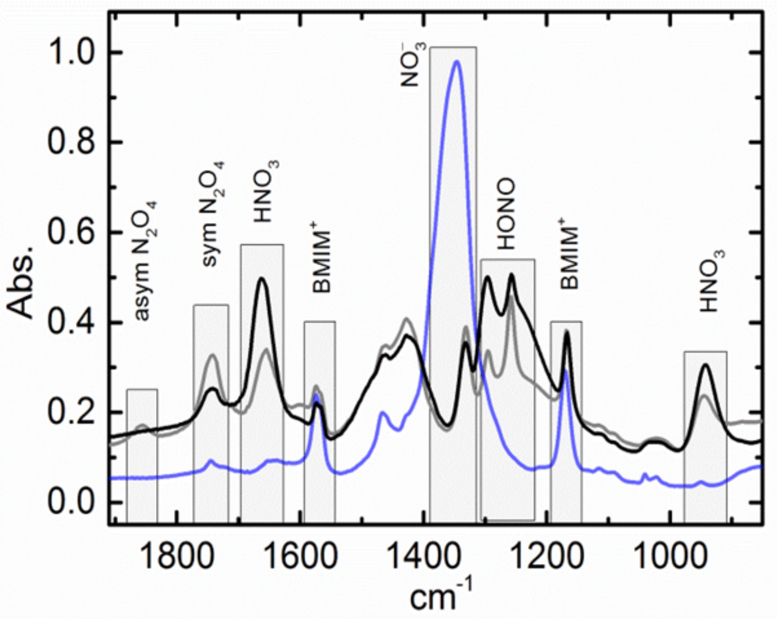

Figure 3.13: ATR-FTIR spectra of a [BMIM][NO_3]IL after being exposed to a dried NO_2 gas. The blue spectrum constitutes the dried IL prior to exposure. The grey spectrum is after 3 min exposure to the dried NO_2 gas and the black spectrum is after exposure to an N_2 gas stream saturated with water for 1 min.

cm^{-1}, corresponding to the cis- and trans- variations respectively. The characteristic HNO_3 bands discussed previously are observed at 1660 cm^{-1} and 948 cm^{-1} respectively.

There appears to be a significant excess of the cis-HONO at low water concentrations which may be due to stabilisation through a cyclic complex when H_2O is only available in limited amounts. This cyclic complex could be either dimeric or formed with a nitric acid species. Furthermore, signals attributable to dimerised NO_2 (N_2O_4) and NO_2 are observed at 1858 cm^{-1}, 1750 cm^{-1} and 750 cm^{-1}, corresponding to the asymmetric N=O stretch (only in N_2O_4), symmetric N=O stretch (also present in NO_2) and symmetric N-N stretch (only present in N_2O_4) respectively. The band at 750 cm^{-1} is not shown here.

When water is added to the NO_2 saturated IL, most of the N_2O_4 is transformed into nitric and nitrous acids immediately. This can be seen from the significant increase in band intensity of both the nitric and nitrous acids while the characteristic N_2O_4 band disappears. Furthermore, the nitrous acid conformers appear to be of equal and rather high concentrations. Unfortunately, the experimental setup used at the time did not allow for subsequent exposure to a wet gas containing oxygen. Had this been the case, addition of the oxygen with excess of water would likely have led to fast oxidation of the HONO species.

While it is likely that N_2O_4 is an intermediate formed during reaction, spectroscopic evidence of the species with excess water and oxygen may be hard to find as the concentrations are expected to be very low. A deeper spectral analysis was performed to find evidence of likely reaction intermediates. This was done by looking at spectral data in the relevant regions of the *in-situ* spectra at different points along the reaction curve. The experiment was carried out on [BMIM][NO_3] at 2% NO with excess water and oxygen. Figure 3.14 shows the spectral region relevant for HONO, at roughly 50% conversion. Figure 3.14 strongly indicates the presence HONO during reaction, the intensity of the HONO bands appeared somewhat constant during the period of maximum linear rate. Upon converging at 1:1 molar ratio (HNO_3:IL), the intensity of the bands decrease slightly, suggesting that HONO is an intermediate in the reaction.

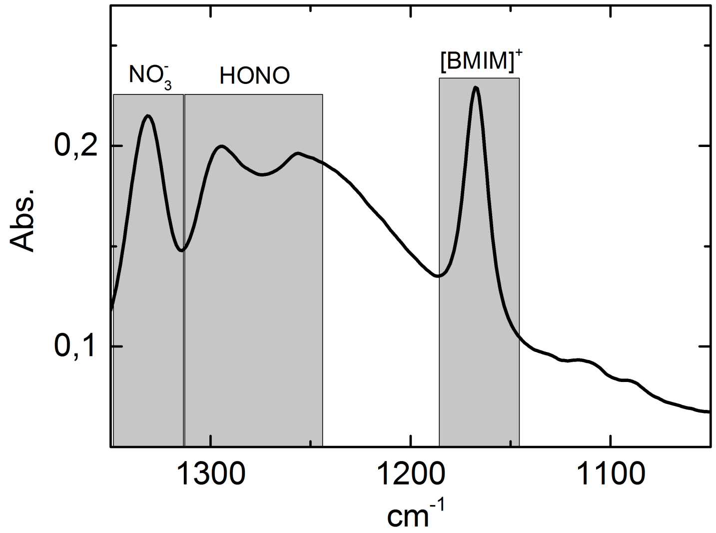

Figure 3.14: *in-situ* ATR-FTIR spectrum of [BMIM][NO_3] from 1350 cm^{-1} to 1050 cm^{-1}, during exposure to a gas containing 2% NO, 16% O_2, 1.5% H_2O and balance N_2, at RT. This spectrum was obtained at roughly 50% conversion.

As determined previously, the reaction likely occurs between species dissolved in the IL, meaning the oxidation is most likely carried out by molecular oxygen. The 4 oxidation equivalents provided by molecular oxygen correspond to either a nitrogen in oxidation state 1 or a dimeric species with nominal oxidation state 3.

The presence of N(I) in an oxidative environment is highly unlikely, and no spectroscopic evidence was found of this. Thus, oxidation is expected to occur on a dimeric species of N(III), which is consistent with the presence of HONO. The end product of this oxidation is HNO_3, which corresponds to the final absorption product, as shown in Reaction 3.3 below.

$$(HONO)_2 + O_2 \longrightarrow 2\,HNO_3 \tag{3.3}$$

Previously it was suggested that the anion of the IL largely determines the reactivity. Thus, the initiation reaction likely includes the anion, which is this case is nitrate. The expected adduct formed by reaction between NO and nitrate would be expected to form a bond between a nitrate oxygen and the NO nitrogen, yielding an adduct with the formal notation of $[O_2NONO]^-$ or $[N_2O_4]^-$. Such an adduct would be expected to have two characteristic N-O-N absorption bands, one from a cis-conformation and one from the trans-conformation. According to the literature, the band center of the N-O-N bending mode of the adduct would be in the 600-650 cm^{-1} region [135]. Gaseous NO_2 or N_2O_4 dissolved in the IL would not show this N-O-N bending mode, but instead have a symmetric N-O bending mode, which is located in the same spectral region. The ATR-FTIR spectrum from the relevant region is shown in Figure 3.15, with notations of the relevant spectral bands. Figure 3.15 indicates the presence of small amounts of NO_2, traces of N_2O_4, and the expected adduct of reaction between nitrate and NO. Assuming that contributions from gas

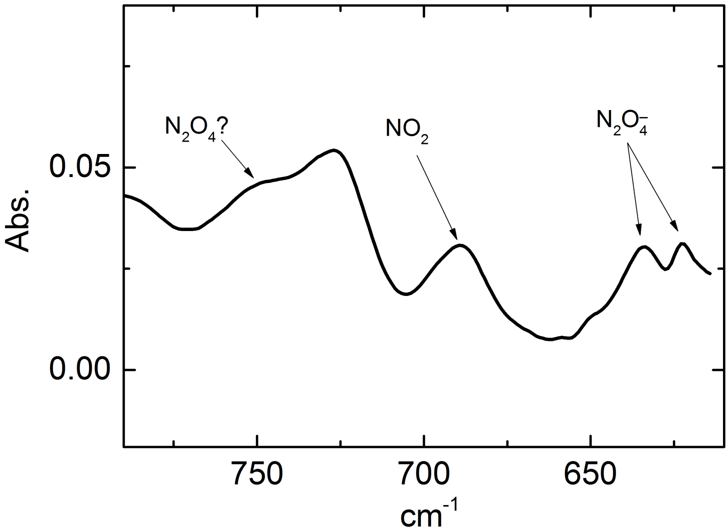

Figure 3.15: *in-situ* ATR-FTIR spectrum of [BMIM][NO_3] from 610 cm^{-1} to 790 cm^{-1}, during exposure to a gas containing 2% NO, 16% O_2, 1.5% H_2O and balance N_2, at RT. This spectrum was obtained at roughly 50% conversion.

phase reactions are negligible, as suggested previously, the most likely source of the observed NO_2 is splitting of the nitrate-NO adduct. This would form NO_2 and nitrite ($[NO_2]^-$).

All the expected reactions are presented in Table 3.1 along with the reaction coefficient necessary to yield the overall reaction presented in Equation 3.1. As discussed above, spectroscopic evidence for most of the reactions presented in Table 3.1 have been found by *in-situ* ATR-FTIR spectroscopy. The progression of the reaction is somewhat similar to that proposed in aqueous media, suggesting that the role of the IL in this reaction is mostly to provide a more favourable reaction environment for the kinetically hindered NO molecule. A combination of the reactions can be used to obtain a catalytic cycle based on the nitrate anion of the IL, this is presented in Figure 3.16. The catalytic cycle proposed in Figure 3.16 suggests a rate limiting step of two nitrogen species reacting with oxygen, which is consistent with the reaction order of 2 and 1 respectively. As it was shown, there are several other factors determining the rate of the reaction. These other factors have been hard to distinguish, but gas solubility along with anion activity have been suggested to be of importance.

Table 3.1: Reactions assumed to be involved in the absorption and oxidation of NO to HNO_3 in a nitrate IL. If the reactions are multiplied by the reaction coefficient and added up, the total reaction becomes the same as presented in Equation 3.1

Reference number	Reaction	Reaction coefficient
(1)	$NO + NO_3^- \rightleftharpoons N_2O_4^-$	6
(2)	$N_2O_4^- \rightleftharpoons NO_2 + NO_2^-$	6
(3)	$2\,NO_2 \rightleftharpoons N_2O_4$	4
(4)	$N_2O_4 + H_2O \rightleftharpoons NO_3^- + HNO_2 + H^+$	4
(5)	$H^+ + NO_2^- \rightleftharpoons HNO_2$	6
(6)	$2\,HNO_2 \rightleftharpoons (HNO_2)_2$	5
(7)	$(HNO_2)_2 + O_2 \longrightarrow 2\,NO_3^- + 2\,H^+$	3
(8)	$(HNO_2)_2 \longrightarrow H_2O + NO_2 + NO$	2

3.3.5 Selectivity and Low Concentration Experiments

In order to ensure that the protons observed in the titration were from nitric acid, the absorption capacity of CO_2 and SO_2 in the presence of air and water were also investigated (50% CO_2 and 1% SO_2). The absorption was followed gravimetrically and compared to absorption of a gas only containing water. Subsequent titration was performed to determine the amount of acidic protons present. The results from these absorption experiments are presented in Figure 3.17. It is seen from Figure 3.17 that there is little discrepancy between the gravimetric uptake of the gas solely contain-

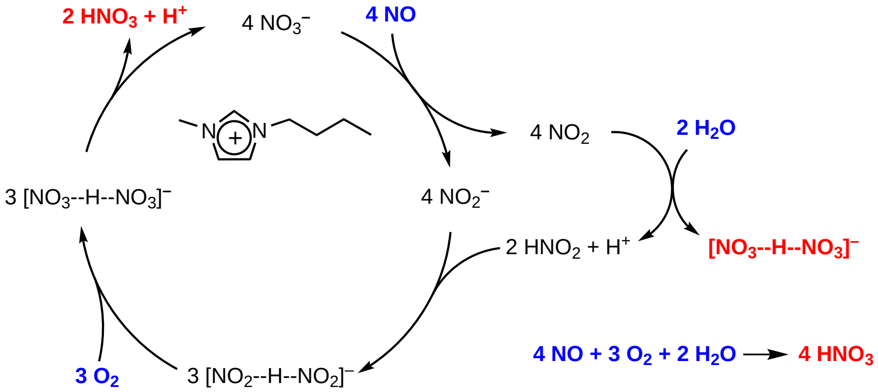

Figure 3.16: Proposed catalytic cycle for the absorption and oxidation of NO to HNO_3 by $[BMIM][NO_3]$. Blue species are reactants, red species are the products, and black species are intermediates. Each nitrate anion can undergo one absorption resulting in a 1:1 molar ratio. The IL can be regenerated (last step of the cycle) by desorption at elevated temperatures.

ing water compared to the gasses containing SO_2 and CO_2. The initial gravimetric uptake appears to be slightly higher when dilute NO is present in the gas, but the uptake seems to stagnate and converge to a gravimetric uptake comparable to the other gasses. The exposure to low concentration NO was stopped after 36 hours because the sample weight was constant.

From the titration of the exposed IL, it is seen that acidic protons are only formed when the IL is exposed to a gas containing NO. Furthermore, it is seen that a significant amount of acidic protons are still formed at low NO concentrations. This is despite the reaction being second order with respect to NO, as established previously in this work. Since the reaction is second order with respect to NO, the rate of reaction for the gas containing 5% NO is expected to be around 2500 times higher than for the gas containing 0.1% NO. This is clearly not the case here, which strongly suggests that NO uptake, especially at higher concentrations, is severely limited by mass transfer.

Despite the gravimetric increase stagnating quickly in the low concentration experiment, a significant amount of HNO_3 was formed. This suggests that the IL quickly equilibrates with the substantial amount of water present in the gas. The absorbed water can then slowly be expelled from the IL during continued absorption of NO. It is likely that NO was still being absorbed from the gas after the 36 hours at which the experiment was stopped, despite the apparent stagnation. Otherwise, the H^+ concentration would likely have been significantly lower. This observation is consistent with the *in-situ* ATR-FTIR experiments showing no water being present in the IL after saturation with NO.

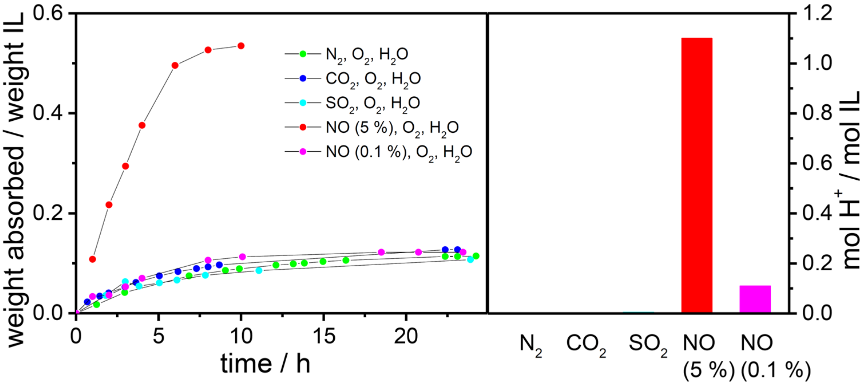

Figure 3.17: (left): Absorption of several relevant flue gasses in the presence of 10.5% O_2 and 1.5% water. For reference, the same experiment was carried out with N_2. (right): Corresponding acid concentrations as determined by titration with NaOH of the IL after absorption.

3.4 Conclusions

Ionic liquids have been found to react willingly with NO, forming HNO_3 when water and oxygen is present. NO is absorbed and oxidised in the ionic liquid, up to a molar ratio of 1:1.

It was established that the reaction rate depends strongly on the anion of the IL, while no apparent effect of the cation was observed.

Absorption experiments in bulk liquids showed that the reaction rate is significantly higher in the IL compared to an aqueous solution with a similar anion concentration, despite the IL having a dynamic viscosity which was 2 orders of magnitude higher than the aqueous solution.

When the anion of the IL is a stronger base than nitrate, the anion is replaced by nitrate during absorption, by evaporation of the corresponding acid.

Investigation of the reaction kinetics showed that the reaction is second order with respect to NO and likely first order with respect to oxygen. Several similarities between this reaction and the reaction occurring in aqueous phase were observed, suggesting that the IL is primarily providing a high ionic strength to help activate/coordinate the kinetically hindered NO molecule.

A strong dependence on temperature was found, with a maximum rate of reaction around 34 °C. The presence of a maximum in the rate of reaction was suggested to originate from two competing limiting factors for the reaction; reactant mobility at low temperature and gas solubility in the IL at higher temperatures. This in turn suggests that the reaction largely occurs between dissolved species in the IL.

Furthermore, it was determined that application of ILs in a wet scrubber type of absorber is unlikely to be feasible for flue gas cleaning in larger plants due to the enormous volumes of gas that needs to be treated and the poor mass transfer in the liquid/gas interface.

CHAPTER 4

Absorption and Oxidation of NO in Supported Ionic Liquid Phase

Promising new technologies for flue gas cleaning based on ionic liquids have emerged. In Chapter 3 several of these were reviewed. It was also explained that application of ILs in a typical wet scrubbing process of a flue gas is unlikely to be feasible on an industrial scale, due to heavy mass transfer limitations in the IL/gas interface. The mass transfer limitations are primarily due to the high viscosities observed in all ionic liquids, which also makes it hard to administer the IL to the gaseous species in e.g. a liquid spray absorption column.

In a recent review, Wasserscheid and Steinrück [94] state that the lowest known viscosity of an IL is 14 mPa·s, while the average is 40-800 mPa·s. For a dried [BMIM][NO_3] sample, an extrapolated viscosity of around 250 mPa·s was found, experimental details are discussed in Chapter 3. For comparison, a 60 wt% aqueous limestone slurry has a relative viscosity of around 3 mPa·s at 25 °C [136], which is still too high for wet flue gas desulphurisation (FGD). In wet FGDs, a solution of around 10 wt% is used to ensure that the primary mass transfer limitation for the scrubber is in the gas phase [97].

Dissolution in water to decrease viscosity is not a possibility for ionic liquids. For absorption and oxidation of NO in an IL, the anion has been established as the active agent (see Section 3.3.1). Diluting the IL this much would in essence yield an aqueous nitrate solution, which is not nearly as active as the pure IL, as shown in Section 3.3.2, despite a significantly lower viscosity.

Absorption of CO_2 and SO_2 also depends on association with the anion of the IL [100, 106, 119], with which water is known to interact strongly [77, 107]. There are no studies on the absorption capacity of these ILs in aqueous solution, but it is unlikely that any significant absorption will be observed under these circumstances. Furthermore, several of the ILs used for absorption of CO_2 and SO_2 are immiscible in water. Using a different solvent could also be a possibility, but this would lead to significant solvent evaporation, which is likely to induce other, possibly greater environmental concerns than emission of flue gasses.

Since using the ionic liquid in a wet scrubber system is insufficient for treating flue gasses, an alternative solution is required. Supported ionic liquid phase (SILP) has been suggested as a possible method for overcoming this. In SILP, the ionic liquid is suspended on a porous support, thus utilising the surface area of the support to increase the IL surface area and reduce mass transfer limitations in the gas/IL boundary layer. Figure 4.1 shows a schematic overview of a SILP particle. SILP is synthesised by dissolving the ionic liquid together with the support in a suitable solvent, which is subsequently evaporated slowly to allow for the liquid to be dispersed evenly. The resulting SILP appears completely dry even at high IL loadings (>50%). In the present work, SILP formulations with up to 50% v/v loadings were tested.

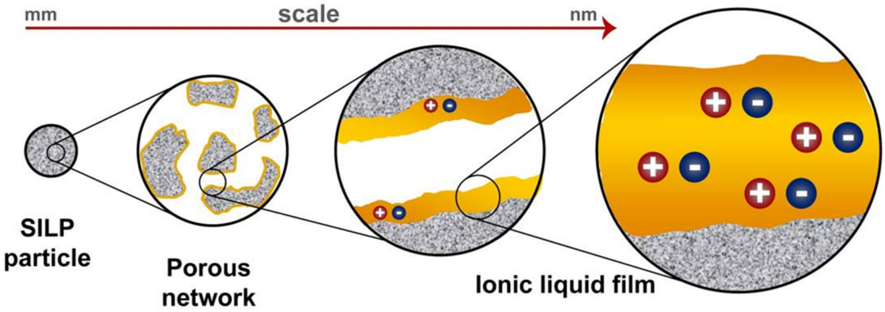

Figure 4.1: Schematic overview of a SILP particle [125].

Wasserscheid and Steinrück have proposed that when using the SILP concept, the mass transfer limitations in the IL/gas interface becomes negligible [94]. This means that the SILP concept should be a prime candidate for solving the problems associated with gas/IL interactions. Reducing the mass transfer limitations should help overcome one of the biggest obstacles in transitioning gas absorption with ILs into becoming more broadly applicable on an industrial scale.

In this chapter, some of the recent literature on the use of SILP is reviewed, especially with an emphasis on the use of SILP in gas absorption. This is presented along with the development in absorption and oxidation of NO in SILP absorbers.

4.1 Industrial Relevance of the SILP concept

The SILP concept was first introduced by Mehnert *et al.* in 2002 [137] under the name SILC (supported ionic liquid catalyst). Here, a Rh catalyst was suspended in the IL which was anchored to the support. The SILP particles were used in a slurry type reaction for hydroformylation of 1-hexene. Leaching of the Rh catalyst was found in these early SILP formulations due to partial dissolution of the IL into the liquid solvent, meaning the SILP formulation was not ideal for reactions in the liquid phase. It was instead suggested that introduction of the SILP concept could help towards heterogenising the reaction, allowing for gas phase reaction over a fixed bed reactor in later applications.

This type of heterogeneous gas phase reaction is preferred as it allows for easier product separation. Riisager *et al.* [138] were the first to demonstrate this use; SILP particles with a Rh catalyst suspended in the IL were used for hydroformylation of propene in a continuous gas flow over a fixed bed SILP reactor.

Since these promising early results, large steps have been taken towards industrialisation of SILP processes within several fields including hydroformylation [139, 140] and water-gas shift [141]. ROMEO, a large European joint project with collaborators from academia as well as industry, from five European countries, is currently working towards industrial realisation of both hydroformylation and water-gas shift. Construction of pilot-scale plants for testing both processes are already underway [142].

4.2 Gas Absorption Using SILP absorbers

In Section 3.1, ILs which can absorb large quantities of gasses were reviewed. While industrial application of SILP absorption in a flue gas has yet to be realised, important steps are being taken towards developing SILP systems that are efficient enough to be used industrially. This section will review some of the recent literature on reversible absorption of SO_2 and CO_2 from flue gasses using state-of-the-art SILP formulations, as well as describe a recently developed SILP absorption method for removal of mercury from natural gas.

4.2.1 Absorption of SO_2 Using SILP Materials

In Section 3.1.1, the affinity of several ILs in selective absorption of SO_2 was reviewed. The first report of significant absorption capacity in a SILP type absorber for SO_2 was presented by Zhang *et al.* [143]. They showed that at 1 bar, 1,1,3,3-tetramethylguanidinium lactate ([TMG][L]) suspended on a silica (SiO_2) support was able to absorb up to 0.8 gram SO_2 per gram [TMG][L]. Significant absorption was also observed for the pure silica support.

It was shown that using the SILP method led to significantly increased absorption rates compared to the neat IL. Saturation was obtained around 4 times faster for the SILP material compared to IL in the bulk phase. Furthermore, the SILP and the IL converged at roughly the same mass ratios (SO_2:IL). It is important to note that this ratio does not appear to be corrected for absorption of the support, but this is not fully specified in the publication.

Zhang *et al.* [143] also showed that [TMG][L] exhibits excellent selectivity towards SO_2, by testing absorption of several other gasses including N_2, H_2 and CO_2. No significant absorption was found for any of the gasses tested other than SO_2. Although a molar absorption ratio of 0.88 was found for H_2, this was deemed to be because of experimental error in the gravimetric experiments, since the mass increase was no larger than when testing the absorption of other gasses. Even if the IL absorbs some quantities of H_2, this is not relevant in a flue gas. The researchers also showed excellent reversibility for the SILP. At 1 bar of SO_2 pressure, it was possible to absorb SO_2 and subsequently regenerate SILP at slightly elevated temperatures by passing N_2over it. This was done 3 times with no apparent capacity loss.

The SO_2 concentration in a flue gas from a coal fired power plant rarely exceeds 500 ppm[4]. For heavy duty maritime vessels, which would be expected to have the highest flue gas concentrations of SO_2, this number may be as high as 3000 ppm, but will typically be around 1000 ppm (calculated from undisclosed engine data supplied by MAN Diesel and Turbo) with a high relative humidity. These numbers are provided under the assumption that the engine is operated in compliance with international fuel regulations.

Consequently, in order for the SILP absorber to be relevant in industrial flue gas applications, a high activity must be obtained at significantly lower partial pressures than the 1 bar tested. It is also paramount that it works in the presence of substantial amounts of water. Zhang *et al.* [143] tested these factors as well and found that water had a significant negative impact on the absorption. The total gravimetric uptake for the gas containing water was lower than for the dry gas, despite significant amounts of water being absorbed by the SILP. Furthermore, high water concentrations seemed to cause leaching of the IL, the nature of this leaching is not further specified by the authors.

At lower concentrations (2160 ppm SO_2, no water), the SILP removed most of the SO_2 from the gas stream for some time, but the equilibrium absorption capacity was found to be 0.13 (g SO_2/g IL) compared to the 0.88 (g SO_2/g IL) observed at high SO_2 concentrations. Also, it was not possible to fully regenerate the SILP after use in low concentration absorptions, only around 25% of the low concentration absorption capacity was regained by desorption. Thus, subsequent absorptions at low SO_2 concentration only reached an equilibrium uptake of 0.04-0.05 g SO_2/g IL.

Shortly after the results presented by Zhang *et al.*, similar results were obtained by our research group [128], using [TMGH]Cl supported on silica (20 wt%). Complete removal of dilute SO_2 (3%) from a dry gas stream was found. The absorption capacity at saturation was found to be 0.1 (g SO_2/g absorber), but decreased significantly when the temperature was increased. Excellent reversibility was observed with no apparent decrease in capacity after 10 absorption/desorption cycles.

In a later study [125], the optimal IL loading was determined, as well as the equilibrium absorption capacity at different SO_2 concentrations. The equilibrium capacity was found to be strongly dependent on concentration; a 0.1 molar ratio (mol SO_2/mol IL) was found at 5000 ppm while this molar ratio was 0.05 at 1000 ppm. The optimal IL-loading was determined to be 20 wt%.

More recently [126], the 20 wt% [TMGH]Cl on SiO_2 SILP absorber was found to have significant absorption capacity even at low SO_2 concentrations and in the presence of water. From a gas stream containing 1500 ppm SO_2 and 3% water, the SO_2 was completely removed for a significant amount of time. The molar uptake at the point of SO_2 breakthrough was determined to be 0.05 (mol SO_2/mol IL). The high reversibility observed in previous experiments was still retained under these conditions.

A recent study by Li *et al.* [144] compares a SILP of [TMG][L] supported on MCM-41 prepared by the authors, to several SILP formulations and neat IL absorption data obtained from the literature. This study confirms most of the observations above; decent molar uptakes (0.1-0.7 mol SO_2/mol IL) which decrease at low SO_2 concentrations. Uptakes are hindered by higher temperatures and the presence of water. Excellent reversibility is observed, especially for some SILP materials. Gas absorption rate is increased significantly in SILP compared to neat IL. A thorough investigation of the effects of IL loadings was carried out and some very interesting observations were made: Li and co-workers found that the molar efficiency of the IL was highest at very low loadings, but sharply decreases. This contradicts what would be expected, since a very small portion of the ionic liquid layer displays the same characteristics as a neat IL at low loading percentages. The authors suggest that this effect is caused by adsorption in the support material because the IL is not distributed on all surfaces of the support at these low loadings.

The optimal loading percentage was found to be 40%, above which the absorption dynamics appeared to change, likely because of pore blockage. This claim is supported by observation that at IL loadings above 50%, no microporosity is observed while both the surface area and pore volumes have decreased to less than 10% of the starting value of the pure support. The desorption efficiency was also found to depend heavily on IL loading with almost 100% desorption efficiency at 10% loading, but only around 65% at 40% loading. A series of recycling experiments were carried out, and it appears that after some time, the absorption/desorption rate becomes constant, meaning the absorption capacity is retained in subsequent absorptions. This state-of-the-art publication by Li *et al.* excellently outlines both the advantages of SILP absorbers in gas phase and also the numerous parameters that can affect performance, many of which are not yet fully understood. Molar capacities upwards of 4.5 which have been reported for neat ILs [102]. Unfortunately, the highest reported molar absorption capacity for SILP absorbers is close to 1 [145, 146].

4.2.2 Absorption of CO_2 Using SILP Absorbers

Post-combustion removal of CO_2 is of vital concern. Today, the commercially available state-of-the-art method uses an aqueous solution of monoethanolamine (MEA) to chemically bind the CO_2 as carbamate at ambient temperatures [147]. To decrease evaporation of the MEA, the concentration of the aqueous solution is 20-30%. Amine scrubbings is already widely applied for natural gas sweetening and also for some highly specific applications in confined space where removal of CO_2 from recirculating air is of importance [148].
Wet scrubbing with aqueous MEA is undesirable for post combustion flue gas treatment due to several disadvantages: Because the CO_2 is bound chemically to the amine solution, the association energy is high. Consequently, high temperatures (around 100 °C) are required during desorption. During desorption, the solvent (water) also has to be heated. This constitutes unnecessary consumption of a significant amount of energy.
Davison estimates that running an MEA scrubber increases the fuel consumption by around 30% for a coal fired power plant, while decreasing the net power output and net efficiency of the plant. This in turn increases the production price by around 40% [149].
While dissolving the MEA in water decreases evaporation significantly, evaporation still constitutes a major loss of MEA [150]. Of the evaporated MEA, a non-negligible amount is emitted to the atmosphere. The impact of these emissions are unknown and must be analysed to a greater extent before wide spread industrial scale implementation of the technology is possible [151].
Other deactivation processes such as precipitation of heat-stable salts, polymerisation and especially oxidative degradation by other oxidising flue gas constituents are also a concern. Loss of absorbent can be circumvented to some extent by using other, more complex amine absorbents instead. However, the molar absorption capacity of the more complex amines is either the same or lower than for MEA, meaning the absorption capacity per weight is significantly lower. Furthermore, introduction of more complex amines also constitutes a significant increase in capital cost and are often associated with other applicational difficulties as well [152].

Despite the drawbacks discussed above for MEA scrubbing, it is still considered the most promising available method for post combustion removal of CO_2 [148]. As mentioned in Section 3.1.2, several ILs show promising absorption of CO_2 through various absorption methods. The optimal absorption mechanism depends on the application. Generally, association between the absorber and the target molecule should be just strong enough for the target molecule to be retained. Stronger association than this just increases the energy required during desorption. For absorption at high partial pressures weak interactions are often enough, while stronger interactions are required for the low partial pressures found in a flue gas.

Recently, Niedermayer *et al.* [148] studied the characteristics of an amine-functionalised IL during absorption of CO_2. They found that two apparent pressure regimes led to two different products upon absorption of CO_2 in the IL. At lower partial pressure of CO_2, the molar absorption capacity was roughly 0.5 (mol CO_2/mol IL), which is consistent with formation of a carbamate dianion similar to that found for the MEA systems. At higher CO_2 partial pressures, the mechanisms seems to shift towards formation of carbamic acid, which yields a ratio of 1:1.

Another very important observation from this study with regards to application in flue gasses is the presence of carbamic acid on the surface of the IL at lower CO_2 partial pressures (0.9 bar). This observation suggests that the absorption capacity in the surface layers of the IL may be higher than what is observed in the bulk. The authors suggested that this indicates the absorption proceeds through formation of carbamic acid in the surface layer. This carbamic acid is then transported into the bulk to form carbamate and an ammonium zwitterion, which is the equilibrium absorption product at lower CO_2 partial pressures. The high absorption capacity found at the IL surface suggests that the capacity of the IL will be retained when increasing the surface area, also at low CO_2 concentrations.

Previous studies performed by our group have shown that amino acid functionalised ILs supported on silica can reversibly absorb CO_2 from a flue gas [104, 125]. At relevant flue gas concentrations (9%), a SILP with a 40 wt% loading of N,N,N,N-tetrahexylammonium glycine [N_{6666}][Gly] was found to completely remove CO_2 from a gas stream for a significant period of time [126, 153]. Similar trends were observed for several other amino acid anions including prolinate and taurinate. Furthermore it was found, that the SILP materials were able to delay breakthrough of CO_2, also when exposed to a CO_2 concentration of 1%. Breakthrough of CO_2 occurred at a molar uptake of 0.1 (mol CO_2/mol IL). Saturation absorption capacities for the SILP materials based on amino acid functionalised ILs was found to be very high, with molar ratios exceeding 1 (mol CO_2/mol IL) for several SILP formulations.

Very recently, Romanos *et al.* [154] have investigated the effect of using inverse SILP materials for CO_2 absorption. The inverse SILP uses the same concept as regular SILP, but instead of suspending the IL onto the surface of a support, the IL is instead encapsulated by a small layer of silica nanoparticles. As described above, there may be a significant difference between characteristics and reaction pathways observed in surface molecular layers compared to bulk IL. This method of encapsulation allows for the IL to retain a much higher degree of the bulk properties.

Wettability of the surface has been mentioned as an important factor in determining the activity of a SILP formulation, because insufficient wetting of the surface leads to pore blockage and poor IL surface distribution, which in turn yields a poor utilisation of the IL [125]. Inverse SILP may help circumvent these factors, and thus expand the portfolio of ILs that can be heterogenised by use of the SILP/inverse SILP method.

Romanos *et al.* [154] also found, that by using the inverse SILP method, signifi-

cant absorption capacity was observed for all the ILs investigated. These were all tetra-alkyl substituted ammonium cations (alkyl = various combinations of methyl and ethyl) with functionalised amino acid anions (prolinate and taurinate).
Although the capacities varied slightly between the SILP formulations, several general observations apply: All SILP formulations removed most if not all CO_2 from a flue gas during breakthrough experiments with excellent selectivity. A significant drop in absorption capacity at breakthrough was found after regenerating the SILPs, while the equilibrium absorption capacity remained constant, even at lower partial pressures of CO_2. A very small temperature difference between absorption and desorption was observed. Absorption was carried out at 40 °C and full desorption was obtained at 60 °C. A small temperature difference between absorption and desorption optimises energy consumption, but may also suggest that the interaction between the IL and CO_2 is rather weak at 40 °C.
Karousos *et al.* [146] have later addressed the breakthrough absorption capacities and found that they appear to stabilise after the first absorption. Furthermore co-absorption of SO_2 and CO_2 was carried out to determine the selectivity of these amine functionalised ILs. It was found that significant competitive absorption by SO_2 occurs, but that this can be limited by introducing a terminal alcohol on one of the cation carbonyls.

The effect of dissolving chitosan into the IL in the inverse SILP was investigated by Pohako-Esko *et al.* [155]. They found that addition of chitosan, which is a renewable and environmentally friendly polyamine, increased the CO_2 absorption capacity in most of the inverse SILP it was tested in. Furthermore, chitosan as an additive can be used to tune the selectivity towards CO_2 [146,155].

4.2.3 Industrially Applied SILP Absorber for Removal of Mercury from Natural Gas

In the sections above, several processes utilising the SILP method to combine the advantages of using ILs as solvents, with the increased applicability of heterogeneous absorption/catalysis were presented. And while some of these processes are close to commercialisation and several of them significantly outperforms commercially available methods in lab scale, only one SILP process has been fully commercialised to date: The removal of mercury from natural gas.

Mercury is a toxic pollutant, which is present in natural gas in quantities ranging from 0.1-5000 $\mu g/m^3$ [156]. Although these concentrations are rather low, more than 25,000 m^3 gas is treated each day in a typical plant, leading to a significant cumulative amount if emitted. When present in process streams, mercury is corrosive and cause structural damage as well as post-treatment catalyst deactivation [53]. Consequently, removal of mercury from natural gas is necessary for the gas to be of industrial use.

The commercially available SILP absorber for mercury removal utilises oxidative dissolution of elemental mercury from the gas stream to form Hg(II) in the IL. This is carried out by an IL with a chlorocuprate anion. The commercial absorber uses 1-butyl-3-methylimidazolium chlorocuprate, nominally; $[BMIM]Cl[CuCl_2]$ but the actual form is dimeric: $[BMIM]_2[Cu_2Cl_6]$.
It was found that high amounts of mercury can be absorbed from the gas stream ($>$99.9%) even with very low residence times (8-16 ms). The residence time in commercial plants are 5-20 s [157]. High quantities of mercury was absorbed in the SILP material ($>$20 wt%), with molar equilibrium absorption values of 1:2 (mol Hg/mol Cu). This is consistent with oxidative dissolution of elemental mercury, Hg(0) to Hg(II), by reaction with a dimeric Cu(II) IL species, described by Reaction 4.1 below.

$$\mathrm{Hg\,(g/l)} + [\mathrm{Cu_2Cl_6}]^{2-} \longrightarrow [\mathrm{HgCl_3}]^{-} + [\mathrm{CuCl_2}]^{-} + \mathrm{CuCl\,(s)} \tag{4.1}$$

The fact that a commercially available process based on SILP is available for selective absorption of such a low concentration gas phase component proves that industrialisation of processes using SILP is well within reach. It is also an excellent example, showing that flue gas cleaning using SILP is possible. Concentrations of typical flue gas components SO_x, NO_x and CO_x far exceed the concentration of mercury, showing that intelligent design and the right components can yield an extremely efficient process. It is however, important keep in mind that the absorption of mercury in the gas is irreversible. Irreversible absorption is not an economically viable option for flue gas treatment.

From the state-of-the-art literature presented in this section it is clear, that full understanding of the variables that go into developing the optimal SILP formulation has not yet been achieved. A better understanding of the phenomena governing SILP performance, coupled with an increased industrial use of ILs and ensuing decrease IL prices, should further increase the odds of several SILP becoming industrially viable in the coming years.

4.3 Experimental

Some of the materials used for absorption measurements were synthesised prior to the project period. Breakthrough absorption experiments were conducted using two different experimental setups following roughly the same schematic, thus only one schematic overview is shown.

4.3.1 Synthesis of Materials

All SILP materials were synthesised using the same impregnation procedure: A known amount of dried IL ([BMIM][NO_3] (Io-Li-Tech, >98%),[BMIM]Br (Fluka, >98%), [BMIM]Cl (Io-Li-Tech, >98%)) was added to an appropriate solvent in vast excess. Solvents used were: deionised water, methanol (Sigma-Aldrich, 99.8%), ethanol (Sigma-Aldrich, 99.5%), acetone (Sigma-Aldrich, 99.9%), diethyl ether (DEE) (Sigma-Aldrich, >99%) dichloromethane(Sigma-Aldrich, >99.8%), chloroform (Sigma-Aldrich, >99%), tetracholoromethane (Sigma-Aldrich, 99%), tetrahydrofurane (THF) (Sigma-Aldrich, 99.9%). Upon vigorous stirring with the solvent, the IL was either dissolved or formed a homogenous suspension. The support material (see Table 4.1 for data on support materials) was then added to the mixture in an amount corresponding to the desired pore filling, to yield a total amount of no less than 3 g. After mixing for 1 hour, the solvent was evaporated slowly (>3 hours) on a rotary evaporator at a pressure of 10-20 mbar and temperatures from 20-60 °C to ensure even distribution in the pores of the support.
The end product was a white, or in some cases slightly yellow, dry powder. Appropriate solvents were chosen to avoid interactions with the support material and a screening of the effect of using different solvents was performed. For most SILP syntheses, methanol or dichloromethane were used depending on the support.

An example of synthesis for one of the most used SILP formulations, 30% pore filling [BMIM][NO_3] on calcined silica (Saint-Gobain SS61138) is as follows: 3.227 g [BMIM][NO_3] (density = 1.17 g/mL, measured on Anton Paar Lovis 2000 M/ME combined densitometer and rolling ball viscometer) was dissolved in 100 mL of methanol in a 250 mL round bottomed flask. After complete dissolution (less than a minute at room temperature), 9.892 g calcined silica (180-355 μm/45-80 mesh fraction) was added and the mixture was stirred on a magnetic stirrer hot plate (IKA RCT Basic) for 1 hour at room temperature. After stirring for 1 hour, the round-bottomed flask was transferred to a rotary evaporator (IKA RV 10 Control). For the first hour, evaporation was conducted at room temperature, after this, the temperature was increased to 40 °C and evaporation was continued for another 3 hours to yield a completely dry white powder with the same size fraction (180-355 μm) as the pure support. For the silica gels (60, 90 and 100) and the carbon supports, fractioning (180-355μm/45-80 mesh) was performed on the materials as received. All other support materials were pelletized and crushed in a mortar before being fractioned (180-355μm/45-80 mesh). All non-carbonaceous support materials were calcined at 550 °C in air for 8-12 hours and left to cool in an exicator unless otherwise noted.

Table 4.1: BET results and list of support materials used for SILP formulations during this work. Most of the BET experiments were carried out by Bodil Holten. Supplier denoted in parenthesis: S-G = Saint Gobain, S-A = Sigma Aldrich.

Support material	BET area (m^2/g)	Pore volume (cm^3/g)
Carbon Black (Cabot Pearl 1400)	580	0.71
Carbon Black (Cabot Pearl 2000)	775	1.82
Silica gel 100 (Fluka)	355	0.98
Silica gel 90 (Fluka)	257	0.93
Silica gel 60 (Fluka)	352	0.87
Silica SS61138 (S-G, Uncalcined)	257	0.93
Silica SS61138 (S-G, Calcined)	251	0.93
Spinel (Fluka)	60	0.27
Ceria (S-G)	82	0.29
Zirconia (S-G)	82	0.27
Gamma-Alumina (S-G)	250	0.79
Anatase ST3119 (S-G)	150	0.38
Extruded anatase	199	0.5
Anatase (S-A)	299	0.29
Mordenite	556	0.29
Spherical Supelco (4 types)	1050	0.51
Sepiolite	280	-

4.3.2 NO Breakthrough Absorption Experiments

For the breakthrough experiments, a glass reactor (Ø=10mm, L = 300 mm) with a porous glass frit was placed in a Carbolite tubular oven, insulated with porous insulation casts at both ends. The SILP was subjected to varying mixtures of NO (AGA, 1% in He and Linde, 10% in N_2), O_2 (AGA) and air (AGA), H_2O and NO_2 (AGA, 1% in He and Linde, 10% in N_2).

Flows were controlled by mass flow controllers (MFCs), which were changed when the setup was rebuilt. In early experiments Bronkhorst EL-FLOW MFCs were used, these were manually calibrated for each specific gas, but showed excellent stability during the experiments. When the setup was rebuilt, new MKS Instruments GE50A MFCs were installed instead. These had automatic calibration for individual gasses. The flow was verified at three different flow rates when the MFC was moved to control another gas, in all cases the automatic calibration was found to work excellently. A schematic overview of the setup is found in Figure 4.2. The schematic overview shown in Figure 4.2 depicts the general flow chart used in all setups that tested breakthrough absorption capacity. During the project period, the setup was rebuilt. Experiments were continued during this time by using a temporary setup. The reactors remained

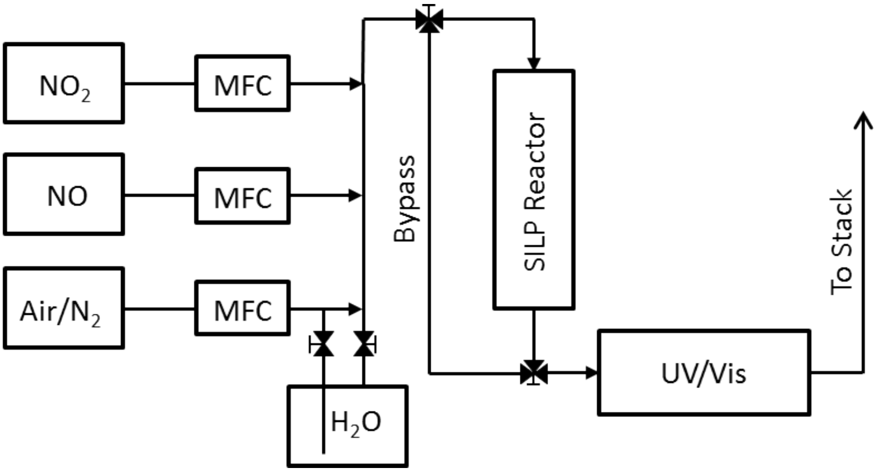

Figure 4.2: Schematic overview of the experimental setup used during the breakthrough experiments.

the same, and so did the analytical tools. No changes were observed when using different setups and the results are regarded as fully comparable. Consequently, there will be no notation of which setup was used for individual experiments when results are presented.

Water was added to the flue gas by bubbling the air/O_2 stream through a wet bubble flask prior to mixing with the NO stream. For experiments with higher NO concentrations, pure O_2 was used in some experiments. When this was the case, the air bottle was exchanged with an O_2 bottle.

4.3.3 NO Quantification Based on Spectral Deconvolution

The UV spectrum of NO_x species is well documented in the literature. NO has 4 specific and narrow bands in the UV-region at approximately 226.5, 215.1, 204.9 and 195.7 nm [158,159]. NO_2 has 1 broad band in the UV-region and another very broad band stretching far into the visible spectrum, with significant vibrational fine structure [160,161].

The NO band at 195.7 nm was not used for analysis due to experimental uncertainty introduced by the spectrophotometer in the spectral range below 200 nm. Consequently, spectra were obtained from 200-600 nm, which covers the remaining 5 bands for the two dominant NO_x species. In order to quantify the amount of each species, spectral deconvolution was performed using `PeakFit`. Figure 4.3 shows an example of spectral deconvolution using `PeakFit` in the 200-250 nm spectral range. It can be seen from the cumulative spectrum that excellent fits can be obtained. This is

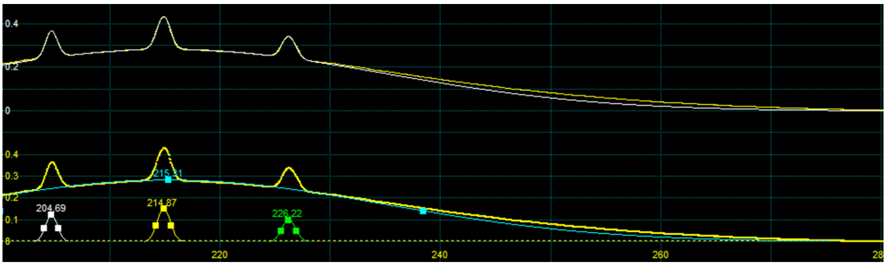

Figure 4.3: Spectral deconvolution in the 200-280 nm spectral range using PeakFit. Manual optimisation has been performed to achieve the best possible fit (least squares method). The individual spectral components can be seen from the bottom half of the screen, whereas the top half shows the cumulative simulated spectrum (white) and the experimental spectrum (yellow).

especially true for the pure NO gas, which is not shown here. It is also seen, that the peaks are asymmetric, tailing off on the towards the lower energy region. This effect is more pronounced for NO_2 peak compared to NO.

Manual fitting to both the high and low energy side of the experimental signal was performed. It was found that deconvolution of the high energy side of the spectral signal gave the lowest standard deviations. Despite the manual fitting of each spectrum, the overall standard deviation for quantification of NO was very low. Standard deviation for individual concentrations were found to be below ± 0.5%. Standard deviation found for the obtained standard curve was around ± 1%. Standard curves are presented in Appendix A.1.

The vibrational fine structure of NO_2 makes it hard to determine the exact area beneath the NO_2 curve without using a high number of Gaussian functions. Using a high number of Gaussian functions risks interfering with the quantification of NO, and is thus undesirable. Therefore, only one peak was used to deconvolute the complex NO_2 signals, after some refinement, this could be done without affecting the standard deviation for the NO_2 quantification. Using only one Gaussian function makes it impossible to get an optimal fit of the asymmetric NO_2 signal, as can be seen from figure 4.3. However, because either half of the curve is almost perfectly symmetric, the asymmetric shape did not further increase the standard deviation. When using this method, the standard deviation for quantification of NO in mixed spectra was unaffected as well.

4.4 Results and Discussion

Prior to the project period, it was shown that several SILP formulations were able to significantly delay the breakthrough time for the setup shown in Figure 4.2 [125]. Excellent reversibility was observed for the breakthrough experiments. It was possible to reproduce the breakthrough time more than 60 times for the same SILP material, with no considerable decrease in capacity. The breakthrough time and reversibility can be seen from Figure 4.4 below which shows the breakthrough curve for 4 g of anatase ST3119 SILP (30% v/v) exposed to a gas containing 2000 ppm NO, air and 2% water. Between absorptions, the SILP was regenerated by heating the reactor to 130 °C and passing wet air through the reactor. In the following, this SILP formulation will be denoted anatase SILP. From Figure 4.4 it can be seen that the anatase SILP is able to remove all NO from the gas stream for several minutes. It is also seen that when the reactor is loaded with an equivalent amount of anatase, only a modest effect is observed. This must mean that the presence of IL on the support is the reason for the increased breakthrough time.

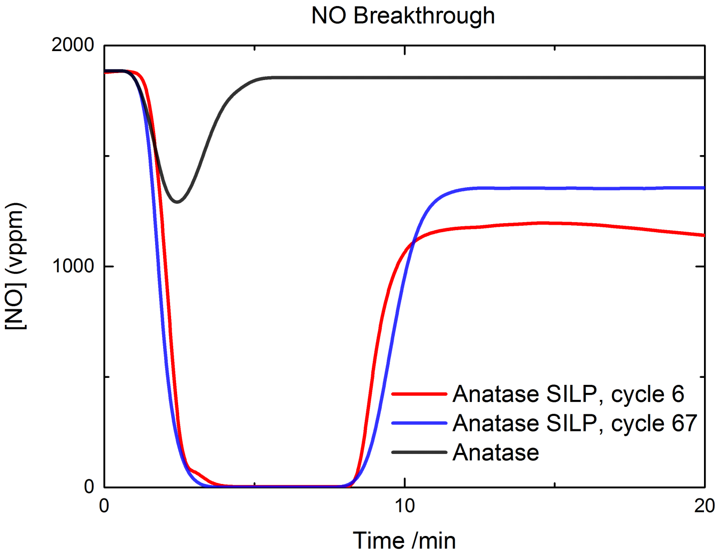

Figure 4.4: NO breakthrough curves for 4 g of anatase SILP (30% v/v) subjected to a flow of 50 mL/min of a flue gas containing 2000 ppm NO, 15% O_2, 2% water, 20% He and balance N_2.

At breakthrough, 0.8 NmL of pure NO gas has been absorbed, which corresponds to a molar uptake of roughly 0.011 (mol NO/mol IL). This value is significantly lower than what was observed for the IL both in the bulk and in the thin film experiments presented in Section 3.3.2. After breakthrough some absorption is observed, but less than 40% of the NO is removed. The reason for higher apparent absorption capacity of cycle 6 is formation of NO_2 due to residue solvent still present in the SILP. This observation is discussed in length in Chapter 6.

The anatase SILP used in these experiments had the highest molar uptake at breakthrough and thus became the benchmark for other SILP formulations going forward.

In order to determine whether this much lower observed molar ratio was due to the support material limiting the absorption capacity, the gravimetric flow setup explained in Section 3.2 was used for a 30% v/v silica SILP. Figure 4.5 shows the gravimetric uptake for the SILP during exposure to a gas containing 5% NO, 10.5% O_2, 1.2% H_2O and balance N_2. Based on the results obtained in similar experiments

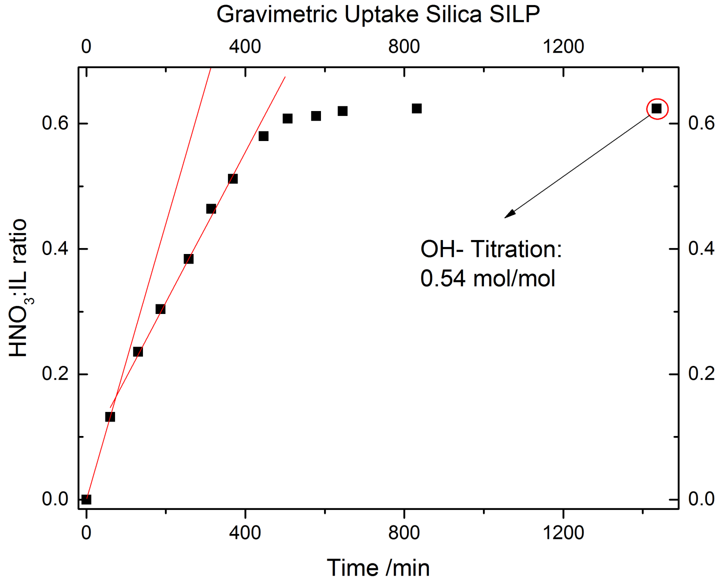

Figure 4.5: Gravimetric uptake was followed on 0.4g SILP with 30% v/v loading of [BMIM][NO_3] exposed to a gas containing 5% NO, 10.5% O_2, 1% H_2O and balance N_2 at a flow of 50 mL/min. The two red lines are fitted curves added to guide the eye; corresponding to a linear fit from origo to the first point, and for points 2 through 6 respectively.

with the neat ILs, presented in Section 3.3.2, it is known that all NO is absorbed as nitric acid. From Figure 4.5 it is seen that significant amounts of NO is absorbed by the SILP. The amount does not reach the 1:1 molar ratio (mol HNO_3/mol IL) obtained for the bulk liquid, but instead converges at a ratio of around 0.6, assuming that the full gravimetric increase is HNO_3. This is substantially higher than the 0.01 ratio observed at breakthrough.

In order to determine the molar amount of NO absorbed, the SILP was dissolved in water and a titration with aqueous NaOH was performed to determine the amount of acidic protons present. As shown in Figure 4.5, the amount of acidic protons corresponds to 0.54 mol per mol IL. The method used is similar to the one used for titration of the neat ILs presented in Section 3.2. The silica support was allowed to settle into the bottom of the flask prior to samples being taken out for titration. This was done using a pipette to avoid silica being transferred with the sample. This was done to ensure the acidic silica did not lead to an overestimation of the acid concentration.

Furthermore, it is seen that the initial absorption appears to be faster than the subsequent linear absorption. When looking back at the bulk absorption experiments with the IL (see Section 3.3.2), the same trend appears in all cases. This observation may be caused by the reaction occurring slowly and primarily on the surface of the IL, with transportation of products into the bulk phase, similar to what was observed by Niedermaier *et al.* [148]. If this is the case, surface coverage at the IL/gas interface becomes a limiting factor for the reactivity towards NO. This observation is in accordance with the ATR-FTIR results presented in Section 3.3.1, in which dissolved NO gas is not observed.

In Section 3.3.3 it was suggested that solubility of gaseous species becomes a limiting factor at higher temperatures. This is not contradicted by these observations since the final oxidation is likely to occur in the bulk phase. In that case, oxygen solubility and likely also NO_2 solubility becomes rate limiting.

An explanation as to why this high initial rate is not observed in the ATR-FTIR experiments could be that it is only the bulk phase that is observed, due to the low penetration depth of the IR beam. Consequently, some degree of product diffusion is required before it is observed in the spectrum. In the *in-situ* measurements, it is also only the product concentration that is followed.

The results from the gravimetric experiments clearly indicate that the breakthrough time is not determined by absorption capacity of the SILP material but rather by a combination of factors determining the available surface for reaction and the recovery rate of these surface sites.

An attempt was made to study the effluent NO concentration from the reactor at high NO concentrations. Therefore, experiments were conducted with a gas containing 6.67% NO, 33% O_2 and 0.8% water and balance N_2. Under these conditions water may become a limiting factor. In order to avoid this, or at least postpone the effect, the SILP was saturated with water in a stream of pure O_2 for 1 hour prior to NO being mixed into the gas. A significant amount of NO was removed during the first two minutes. Complete removal was not achieved, but a decrease in concentration to less than 1000 ppm was observed. NO quantification was limited at high concentrations because of a severe and increasing deviation from linearity for the standard curve. This deviation from linearity is especially pronounced for concentrations exceeding 2000 ppm.

Consequently, it was not possible to determine the uptake other than in the first two minutes in which the concentration was within the quantifiable range. During these two minutes, the molar uptake was around 0.033 (mol NO/mol IL). This suggests that while the surface availability of the IL plays an important role, the breakthrough at lower temperatures is unlikely to be caused by a saturation of the surface by NO, but rather by insufficient surface - NO interaction at these low concentrations.

4.4.1 Investigating the Role of the Support Material

For most applications in heterogeneous catalysis, the effective surface area of the catalyst is one of the most important properties for selecting the optimal support material. Many factors play into this, such as interactions between the catalyst and the support surface, surface availability etc. [162]. Other secondary effects such as bulk properties may also be of importance, this is well illustrated by the oxygen storage/release capacity of ceria/zirconia mixed oxide used as support in the three way catalysts [163, 164].

Therefore, it was a natural extension of the work presented above, to examine the effect of various support materials on the breakthrough time. A wide range of supports were tested with IL liquid loadings varying from 2.5% to 50%. For absorption experiments, SILP formulations with rather high IL loadings were preferred, the formulations tested are found in Table 4.2. Figures 4.6 and 4.7 show a comparison of the best performing SILP materials and the corresponding breakthrough curves. The difference between the figures is the reference used for comparison. In Figure 4.6 the breakthrough time is compared in terms of reactor volume, while in Figure 4.7 the breakthrough is normalised with respect to the amount of IL loaded. From Figures 4.6 and 4.7 it is seen that the best IL materials have significant breakthrough times, reproducing the observations from previously. However, the IL utilisation still remains low. The molar ratio does not exceed 0.011 (mol NO/mol IL) at breakthrough in either of the presented cases. From figures 4.6 and 4.7, it also becomes apparent that the support material plays an important role in determining the activity of the SILP material. This is further underlined in Table 4.2 below, showing the complete list of SILP formulations that have been tested, along with the breakthrough time for the best performing SILP formulation of the given support material. From Table 4.2 it is seen that anatase, silica and alumina SILP formulations have the highest breakthrough times. It is also observed that there is a marked difference between the best performing SILP materials and the worst. SILP formulated on ceria, zirconia and carbon black supports, are not able to remove all NO from the flue gas stream. The best performing SILP under similar conditions removed all NO from the gas stream for several minutes. These observations strongly indicate that the support plays a vital role in determining the efficiency of the SILP.

It is also noted that there is a significant difference between the calcined and uncalcined silica from Saint-Gobain (SS61138). This suggests that surface hydroxyl groups are important for the SILP performance as well, since the morphology of the support is not expected to change during calcination.

There is some difference between the silica gel supports which, but it does not appear to be caused by a difference in highest surface area. For example, silica gel 100

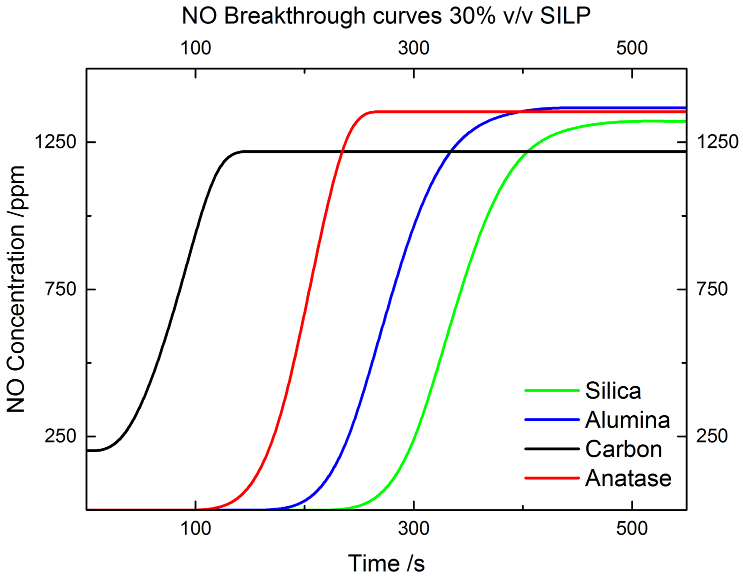

Figure 4.6: Comparison of NO breakthrough times for different SILP formulations at comparable reactor volumes. Gas composition: 2000 ppm NO, 16% O_2, 2% H_2O, 20% He and balance N_2, at a flow of 100 mL/min, GHSV = 1750 h^{-1}. SILP materials tested: Silica SS61138, Anatase ST3119, gamma-Alumina and carbon black 2000.

and silica gel 90 perform similarly. These have close to similar pore sizes but vastly different surface areas, while the silica gel 60 has a higher surface area than silica gel 90, but does not perform as well. The same trend is observed for anatase. For the two pure anatase SILP formulations, similar breakthrough times are observed despite a 100% difference in surface area. These observations suggests that pore size distribution may play a role in determining the activity of the SILP, while the surface area may be less important. The differences in performance are, however, small and trends are unclear, if any exist.

Unpublished work performed by our group, suggests hierarchical pore filling for a silica support. These findings are in agreement with observations made by Lemus *et al.* [165]. This suggests that the nature of the porous network inside the support is very important for achieving full utilisation of the loaded IL. This may also explain the observation that similar supports show similar breakthrough times, despite significantly different BET surface areas.
High BET surface areas may not necessarily lead to a high IL surface area: One could imagine a porous support in which a vast amount of the surface area and void volume is only accessible through a network of micropores, which are blocked by the IL upon

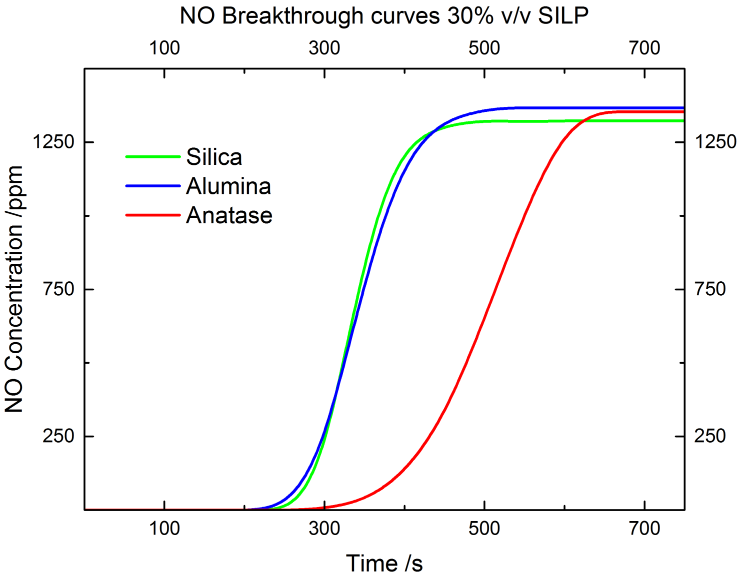

Figure 4.7: NO breakthrough curves for the same SILP formulations shown in Figure 4.6, carbon excluded, normalised with respect to total reactor IL volume. The curvature of the anatase spectrum has visibly flattened, this is due to the significantly lower IL loading on the anatase compared to the other two. Thus, the normalisation factor is by far the highest for anatase.

impregnation. In this case, the BET surface area does not matter because the vast majority of the surface is inaccessible, thus the effective IL surface area is low. This leads to poor utilisation of the surface area and also of the IL. Pore blockage is likely also the reason why higher IL loadings lead to lower absorption rates. This can be seen from the bold numbers in Table 4.2 presenting the best performing IL loading. None of these are higher than 30% v/v.

Another important factor in obtaining a high effective surface area is wettability of the support, which can be obtained through interaction with the ions in the IL. This is a likely reason for the poor performance of especially the carbon black materials. The butyl group of [BMIM][NO_3] is likely not large enough to create sufficient hydrophobic interactions with the carbon surface. Consequently, the wettability is decreased significantly. Assuming this is the case, droplets would likely form on the surface leading to pore blockage and low IL surface area.

Hydroxyl groups on the surface of the support are likely to increase the wettability, leading to a more uniform distribution of IL across the surface of the support. The difference obtained by calcination of the otherwise identical silica supports suggests that there is an optimal surface coverage of hydroxyl groups. Uncalcined silica is

Table 4.2: Full list of SILP formulations tested in NO absorption experiments. IL loadings in bold denote the best performing liquid loading, but only for SILP formulations that completely removed NO. Breakthrough times are noted in minutes, for SILP formulations that did not remove all NO, the highest achieved conversion is shown instead.

Support material	IL loading (%)	Time (min)
Carbon Black (Cabot, Pearl 1400)	20, 30, 40	85%
Carbon Black (Cabot, Pearl 2000)	10, 20, 30, 40, 50	85%
Silica gel 100 (Fluka)	10, 15, 20, 25, **30**, 40, 50	3.5[b]
Silica gel 90 (Fluka)	10, 15, 20, 25, **30**, 40, 50	3[b]
Silica gel 60 (Fluka)	20, **30**, 40	2.5[b]
Silica SS61138 (S-G, uncalcined)	20, **30**, 40	4
Silica SS61138 (S-G, calcined)	10, 15, 20, **30**, 40, 50	7.5/3.5[b]
Spinel (Fluka)	10, 20, **30**, 40	2
Ceria (S-G)	10, 20, 30, 40	70%
Zirconia (S-G)	10, 20, 30, 40	70%
Gamma-Alumina (S-G)	10, 15, 20, **30**, 40, 50	2.5[b]
Anatase ST3119 (S-G)	20, **30**	6/2.5[b]
Sepiolite extruded anatase	10, **20**, 30, 40, 50	1.5[b]
Anatase (S-A)	10, 20, **30**, 40, 50	2.5[b]
Spherical Supelco (4 types)	10, **20**, 30	1
Sepiolite	20, **30**	5[a]

[a] Sepiolite granulate was dissolved by impregnation process resulting in an enormous pressure drop and increased residence times, this breakthrough time is likely to be very inaccurate. [b] SILP formulations only tested at flows of 100 mL/min.

expected to have a higher amount of hydroxyl groups than calcined silica, but the two materials are otherwise identical.

The difference in hydroxyl-group coverage/surface acidity may also be the explanation for the observed difference between the silica, anatase and alumina supports when normalising based on IL loading. Surface acidity is expected to vary in the order of: $SiO_2 > TiO_2 > Al_2O_3$. Since the anatase SILP has the highest degree of IL utilisation, this suggests there is an optimal surface acidity.

As presented in Section 3.3.1, the absorption is expected to be highly dependent on the anion. Consequently, a high surface acidity may cause the anion activity to decrease. It is important to note, that the observed differences may also be caused by other factors such as morphology, pore size distribution, etc.

In order to promote the activity of the anion as much as possible, magnesium aluminate spinel was tested as support. This mixed magnesium/aluminium oxide should be an example of a basic support. From Table 4.2 it is seen that the breakthrough time is 2 min, which is low compared to several of the other supports. However, the spinel investigated here has poor support characteristics: Low surface area (30 m^2/g)

and low porosity (0.27). In both cases these values are the lowest of any support investigated in this work, which may be the reason for the poor performance. Considering that concentrated nitric acid is formed during the absorption, a basic support is likely unfit for industrial applications, but it would yield a lot of information about other possibly suitable support materials.

The inconclusive data obtained by screening a vast array of possible support materials for SILP formulations shows that a better understanding of IL-surface interactions on the SILP is required, along with a better understanding of e.g. pore filling phenomena. For the purpose of NO gas absorption, it appears that some interaction with the surface is required. Minimising the amount of micropores in the support likely decreases pore blockage and in turn yields a better IL and surface utilisation. Furthermore, based on the not insignificant difference in performance for the silica gel 100 SILP compared to the silica gel 60 SILP of otherwise comparable surface characteristics, it appears that incorporation of pores with optimal but narrowly distributed pore sizes may increase the absorption efficiency.

The effect of the solvent used during impregnation was also tested. This was done by impregnating silica gel 100 by the method described in Section 4.3. In most solvents [BMIM][NO_3] was fully dissolved, but for tetracholormethane, THF and DEE, only a suspension was obtained. The obtained SILP materials were then loaded into the reactor and subjected to a gas containing 2000 ppm NO, 16% O_2, 2% H_2O, 20% He and balance N_2 for 1 hour (100 mL/min). After this, the NO flow was stopped and the reactor was heated to 130 °C for 1 hour under wet air flow (100 mL/min). After cooling to 35 °C, the procedure was repeated three more times, giving a total of four absorption/desorption cycles.
On the 5th cycle, the NO breakthrough time was measured analogously to what was shown in Figure 4.6. All SILP materials showed comparable breakthrough time within the margin of experimental error, except the SILP materials that were synthesised from an IL/solvent suspension rather than solution.
The THF and tetrachloromethane SILPs was discarded, but the DEE SILP was left in the gas flow containing NO containing 2000 ppm NO, 16% O_2, 2% H_2O, 20% He and balance N_2 for a week at room temperature. After this, the DEE SILP was exposed to a flow of wet air at 130 °C for 24 hours. After this treatment, the subsequent breakthrough experiment yielded the same result as the others. This suggests that the nature of the solvent may be of importance, especially in initial distribution of the IL onto the surface of the support. This experiment also shows that under the absorption conditions, there is some degree of mobility for the IL. This may be countered by tethering the IL to the support, at least if the mobility is found to be detrimental for the performance.

4.4.2 Application Analysis

Breakthrough time is likely the best measure for activity, since an absorber with a 30-40% efficiency would not decrease the NO concentration of any flue gas to allow for compliance with the emission limits. Consequently, if a NO_x absorber of this type was to be applied with that efficiency rate, it would have to be in conjunction with another method such as SCR. Naturally, this is not a viable option unless the value addition of the nitric acid formed becomes of importance, which is highly unlikely.

The measured absorption capacities at breakthrough are not high enough to allow for continued absorption in a flue gas stream without continuous regeneration. Thus, the use of a rotating filter in which the SILP is regenerated in a smaller, hot, side stream has been proposed. This would allow the absorber to always be freshly regenerated when subjected to the gas stream, and thus run under conditions similar to those observed prior to NO breakthrough in Section 4.4.1. A schematic overview of the filter is shown in Appendix B.2.
Assuming the rate of absorption is high enough, the efficiency of such a rotating filter will largely be dependent on the rate of desorption. In order for the rotating filter to be effective, desorption must occur at a high enough rate for the absorber to be fully regenerated in the smaller side stream before it is exposed to the flue gas stream again. Figure 4.8 shows the effluent NO concentration during desorption at 160 °C. The temperature of 160 °C was chosen due to a desire to fulfill technical requirements from our collaborators. Desorption is not, however, expected to occur significantly faster at 160 °C. The higher temperature also ensured that NO was the main constituent in the effluent gas. From Figure 4.8 it is seen that desorption occurs rapidly at elevated temperature. Higher flow rates than the ones used here are expected in industrial scale application, this would likely further decrease the regeneration time. Based on undisclosed engine data supplied by collaborators in the maritime industry, the dimensions of an absorber using the rotating filter were calculated. The absorber is expected to be retrofitted as a monolith directly into the exhaust system of a Maersk Triple E class cargo ship.
For the dimensioning, it was assumed that the absorption capacity at breakthrough is directly transferrable regardless of space velocity and NO concentration. A possible decrease in capacity obtained by extrusion of the SILP onto a monolith has been disregarded, but only the anatase fraction of the extrusion is considered active. Furthermore, it is assumed that the engine is running in the low NOx emission range (500-1000 ppm) and that full regeneration of the absorber can be achieved during 1 minute of exposure in the hot side stream. Furthermore, exposure to the regenerative side stream is assumed to begin as soon as the absorber exits the flue gas duct, meaning no dead volume is calculated between the streams. It is also assumed that the absorber has a heat capacity of 0.
The assumptions described above can be considered the best case scenario, and will grossly underestimate the size of the SILP absorber. Even under these assumptions,

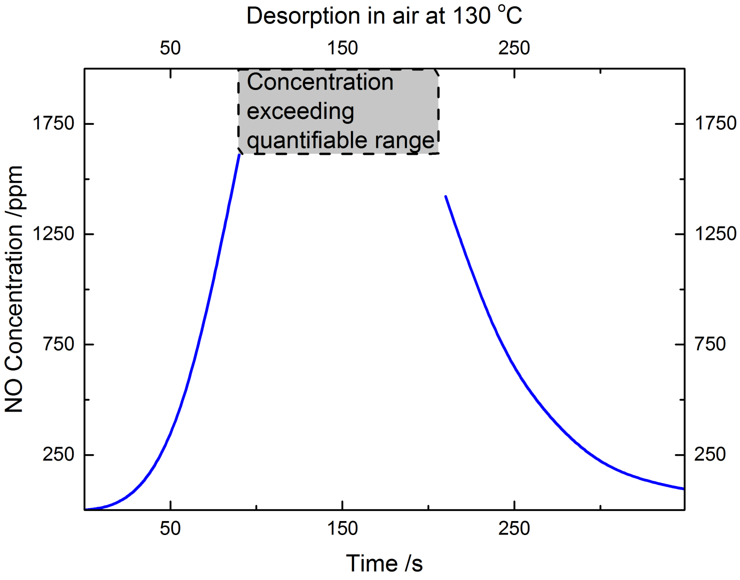

Figure 4.8: NO concentration during desorption of an anatase SILP heated to 160 °C in air with a flow rate of 100 mL/min, GHSV = 1750 h^{-1}C.

the height of a retrofitted absorber would be close to 80 m, which is far from acceptable. According to our collaborators, the height of the absorber should not exceed 2-3 m, otherwise it is hard to retrofit into the flue gas duct. Also, the pressure drop in the absorber becomes too high if it is longer than this.

Achieving this amount of improvement seems unlikely, since there is no evidence of major increments being obtained by the optimisation processes described in this work. Revisiting NO absorption by use of the inverse SILP method described above may increase the absorption capacity significantly. However, it seems unlikely this will increase the absorption capacity enough for industrial implementation to become viable, at least not for NO_x abatement in flue gasses.

During this work, a significant oxidation capacity was seen for some SILP formulations. These observations are discussed in greater detail in Chapter 6. It was also noted during the absorption experiments, that breakthrough time of NO_2 appeared to be significantly higher than for NO, since none of the NO_2 formed by autoxidation in the bypass was observed during the first hour of absorption for the most active SILP formulations. A combination of these two processes was suggested as a possible way to increase the NO_x breakthrough time significantly [166].

In order to test whether absorption of NO_2 would increase the breakthrough time, a replication of the experiments presented in Figure 4.4 was performed with NO_2

instead of NO, the result can be seen in Appendix A.2. An insignificant increase in breakthrough time was observed, while the NO_x concentration after breakthrough was significantly lower compared to when NO was administered. Few experiments were performed with no optimisation of the reaction conditions, thus it is unknown whether significant improvement of the breakthrough time can be achieved by absorption of NO_2 instead of NO. The main focus was put on utilising and optimising the apparent oxidative capability of the SILP instead, because this was believed to be of higher scientific and industrial relevance.

4.5 Conclusions

Successful application of the SILP concept in IL absorption of nitric oxide has been shown. With the best formulations of the SILP, breakthrough times of over 7 minutes were achieved for a simulated flue gas.

Initial uptakes exceeding steady state uptakes were found, suggesting that the available surface area is important for determining the rate of absorption of a given SILP material. The absorption rate and breakthrough times were found to be strongly dependent on the chosen support material. It was found that it is important for the IL to adhere to the surface through surface interactions. However, high concentrations of surface hydroxyl groups causes these interactions to become too strong, resulting in a decrease in the reactive anion activity.

A strong dependence on IL loading was also found, showing the optimal loading for most support materials is 30% v/v. It was suggested that higher IL loadings lead to pore blockage, thus significantly diminishing the available IL surface and in turn decreasing the rate of absorption.

Formulation of an optimal support was suggested. This support should have a small amount of micropores, show good gas transport properties and have narrowly distributed pore sizes of unknown optimal size.

The solvent chosen during SILP preparation was found to be of little importance when the IL could be dissolved in the solvent. Furthermore, it was found that during absorption conditions, some degree of mobility is possible for the IL. If this is a problem, tethering of the IL was suggested as a solution.

Based on calculations of absorber dimensions in a best case scenario, it was found that it is unlikely the absorption capacity of a SILP absorber can be increased enough for SILP absorbers to become of relevance in NO_x abatement from industrial flue gasses.

A surprisingly high apparent oxidative capability was observed for some of the SILP formulations. Optimising this oxidative capability was believed to have the highest immediate scientific and industrial impact. Thus, emphasis was put on investigating this further.

CHAPTER 5

Hollow Sphere Silica - An Optimised SILP Support Material

From the results presented in Chapter 4 it is apparent that significant improvements are necessary in order for absorption and oxidation of NO in SILP materials to become viable for industrial flue gas cleaning. In Section 4.4.2, it was determined, that in order for a SILP absorber to be retrofitted onto a cargo ship, the breakthrough time would have to be increased by a factor of 30-50. At breakthrough, the best performing SILP materials had absorbed a molar ratio of 0.003 and 0.011 (mol NO/mol IL). The maximum capacity was found to be a molar ratio of around 0.5. If it was possible to obtain these molar ratios at breakthrough, that would constitute an improvement of around two orders of magnitude and thus make the process industrially viable.

In Section 4.4.1 the formulation of an optimal support material for using SILP in absorption of NO was discussed. In this chapter, further investigations on formulating an optimal support material are presented. The resulting SILP materials are investigated and compared to the previously prepared SILP presented in Chapter 4.

The properties of the novel "inverse SILP", recently described by the groups of Romanos and Wasserscheid [146,154,155], were discussed as a possible way of optimising SILP formulations for NO absorption. In some practical applications, inverse SILP may give rise to problems regarding the mechanical strength of the material. since the outer shell is constructed from silica nanoparticles which adhere to the IL surface. Thus, the mechanical strength is likely to be rather low.

Inherently, the porefilling of an inverse SILP is 100%, thus, the resulting IL surface area is determined by the particle size of the inverse SILP. Romanos *et al.* [154] report particle sizes of at least 0.15μm based on LN_2 porosimetry and 0.5-1.5 μm based on scanning electron microscopy data. An average particle size of 1 μm would correspond to an IL surface area of around 3 m^2/g, which is significantly lower than the expected IL surface area for regular SILP formulations.

When the inverse SILP "droplets" are of this size, a significant amount of the loaded IL is expected to exhibit bulk-like behaviour. It is unknown how a higher degree of bulk-like behaviour will affect NO absorption in SILP materials, but it is likely to improve the capacity compared to regular supports.

For absorption and oxidation of NO in ILs, it was established in Chapter 4 that the available surface area plays an important role in determining the efficiency of the formulated SILP. The inverse SILP concept increases the available surface area significantly compared to a neat IL, but the maximum surface area is limited by the lowest obtainable particle sized formed by a mono-layer of silica nanoparticles. In Chapter 4, a high expected dependence on pore size and gas diffusivity was also mentioned, along with an assumption that the optimal support featured a low extent of microporosity.

In inverse SILP, micropores are only present in the silica nanoparticles around the IL droplets. Since these are not loaded with IL, pore blockage should be limited, meaning most, if not all, of the IL surface area is available for reaction with the gas phase. The gas diffusivity should also be high in these ordered materials compared to other SILP formulations due to the low amount of microporosity, coupled with the large interparticle voids. In general, creating a highly structured SILP material, while maintaining a high IL surface area, should be the optimal SILP formulation for gas absorption.

In a recent publication by the group of Prof. Dai [167] at Oak Ridge National Laboratory/University of Tennessee, a method for synthesis of hollow, nano-sized spheres of silica (HS) was described. Several applications, including synthesis of metal nanoparticles inside the spheres and subsequent use in size selective catalysis [168] and synthesis of porous liquids for use in gas separation processes [169] have been proposed. In the latter of the two applications, the HS is used to form voids in a liquid, to increase gas diffusion rates significantly. The liquid, a highly selective IL, is tethered to the outside of the HS allowing the resulting porous liquid to act as a high permeability membrane.

Based on this work, it was suggested that HS could function as an optimal support material for gas absorption SILP. This chapter presents some of the work that was carried out during the external research stay with Prof. Dai and his group at the Oak Ridge National Laboratory (ORNL) in Oak Ridge, Tennessee, U.S.A.

5.1 Experimental

Synthesis of the hollow-sphere silica (HS) was carried out during the external research stay, in collaboration with Prof. Dai and his group at ORNL. The HS synthesis was carried out using a designated synthesis setup, using the procedure described below.

5.1.1 Synthesis of Hollow Sphere Silica

1.0 g of triblock copolymer F127 (Fluka, MW=12000 g/mol) and 1.00 g of 1,3,5-trimethylbenzene (Sigma-Aldrich >98%) was dissolved in water and 0.87 g of K2SO4 (Sigma Aldrich >99%) was added. The solution was stirred for a minimum of 12 hours at 13.5 °C, after which 2.43 g tetramethyl orthosilicate (Sigma Aldrich >98%) was added along with 0.78 g of 3-mercaptopropyl trimethoxysilane (Sigma-Aldrich >95%).

After 24 hours of stirring, the mixture was transferred to a Teflon container, which was sealed and placed in an oven at 100 °C for another 24 hours. Hereafter, the mixtures were transferred to 40 mL Eppendorf Tubes (VWR) and centrifuged at 12,000 rpm for 10 minutes. The supernatant was discarded and the precipitate was washed with deionised water. This process was repeated 3-5 times until there was no organic solvent in the supernatant.

The precipitate was dried in an oven at 80 °C overnight (or until dry), then the dried precipitate was distributed evenly in a crucible and calcined at 550 °C for 10 hours in air; heating and cooling rates were 2 °C/min.

5.1.2 Synthesis of HS-SILP

The HS-SILP was synthesised using as-received [BMIM]Br (Io-Li-Tec 99%). 2.024 g of [BMIM] Br was dissolved in 100 mL methanol in a 250 mL round bottomed flask under vigorous stirring. 6.01 g of HS was added and the solvent was evaporated slowly over several hour using a Schlenk-line, yielding a dry, white powder. The powder was characterised by ATR-FTIR, N_2 physisorption (BET) and transmission electron microscopy (TEM). Figure 5.1 shows two TEM images of the HS-SILP. Figure 5.1 shows the uniformly sized hollow spheres of around 20 nm in size with shell thickness of around 2.5-3 nm. The IL suspended on the HS is not visible.

5.1.3 Gas Absorption Experiments

The gas absorption experiments were conducted using the absorption setup described in Section 4.3. In this case no bypass measurements were possible, but the gas composition was allowed to equilibrate by passing it through a 3-way valve at the top of the reactor. The side stream was bubbled through two aqueous solutions prior to

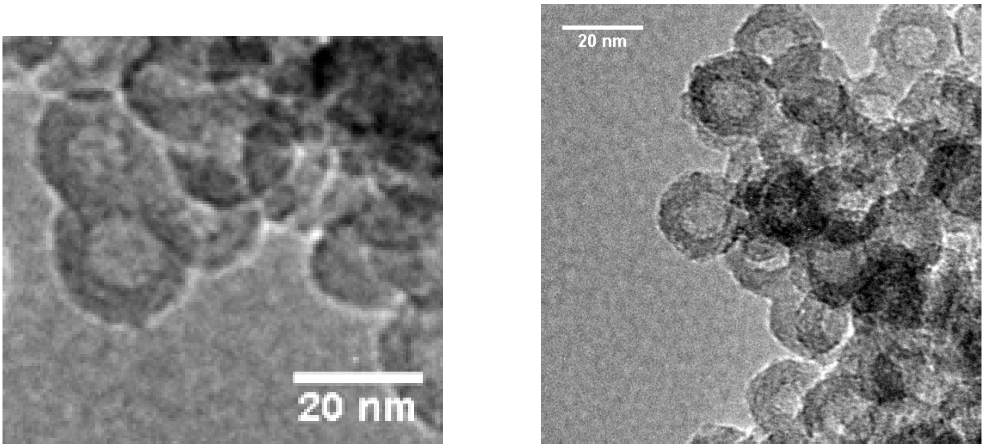

Figure 5.1: TEM images of the HS-SILP.

being released into the fume hood: The first was a nitric acid solution, the second was a NaOH solution, to oxidise and absorb the gas respectively. These breakthrough experiments were conducted at significantly higher space velocities than previously, GHSV = 12000 h^{-1}.

5.2 Results and Discussion

Prior to the beginning of the absorption experiments, surface characterisation of the HS and the HS-SILP was carried out together with Jennifer Schott. The data for the HS and the 30% v/v HS-SILP are presented in Table 5.1 below. From Table 5.1 it appears that loading of the IL onto the support still leaves a high surface area. What is not apparent from the table are the narrow pore size distributions of the HS and the HS-SILP. These were instead confirmed visually by TEM. The marked decrease in mean pore size suggests that IL is primarily loaded into the cavities of the HS material. This is supported by the measured pore filling, which is identical to the theoretical pore filling, thus suggesting there is little to no pore blockage. Further-

Sample	BET-Area (m2/g)	Porosity (cm^3/g)	Mean Pore Size (nm)
HS	895	0.98	14.7
HS-SILP	450	0.69	11.2

Table 5.1: Nitrogen physisorption data for the pure HS support and the 30% v/v [BMIM]Br HS-SILP. Data was obtained at ORNL.

more, it is noted that the surface area is roughly halved by addition of the IL, but it remains very high.

From the porosimetry data obtained, a conclusive answer to how the IL is distributed on the support cannot be given. The two most likely IL distributions for the 30% void filling of the HS are presented in Figure 5.2. From the adsorption data in Table 5.1, it appears most likely that the partial void filling formulation (HS-SILP 2) is the one formed. If the IL had filled the whole inside of the shell, the porosity of the sample would likely be significantly lower than what is observed due to the inner void of the spheres being blocked. This should also limit potential intrusion in the porosimetry measurements, which would lead to the blocked pores would not being accounted for in the measured pore sizes. With regards to the pore size, both BJH and BET pore size estimations are based on uniform and symmetric pores. Partial filling consistent with HS-SILP 2 would decrease the symmetry of the pores, leading to a higher uncertainty on the calculated pore sizes.

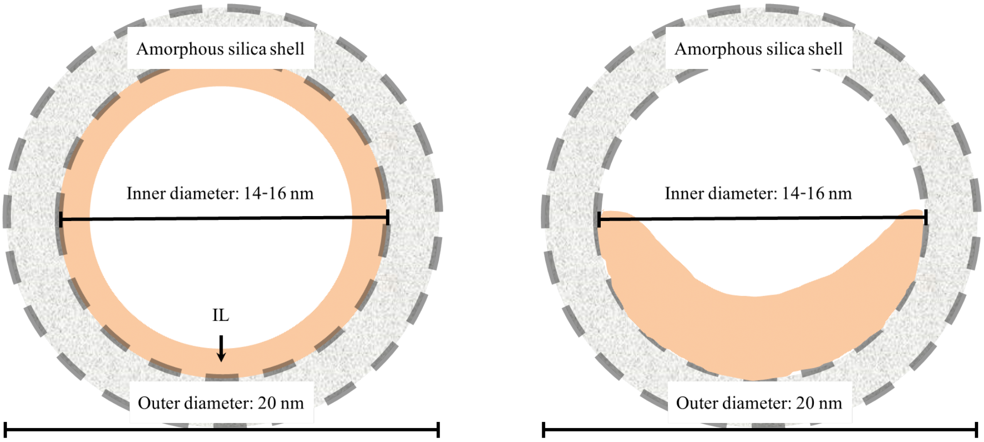

(a) HS-SILP 1

(b) HS-SILP 2

Figure 5.2: Graphic representations of the two most likely IL distributions on the HS support.

HS-SILP 2 is the most probable result of the impregnation based on the surface characterisation. This SILP formulation should also yield gas diffusion rates that are significantly higher than HS-SILP 1, since the structure in this case displays a high void volume for the gas to diffuse through. The measured surface area is halved, which may suggest that a significant amount of the micropores leading into the HS voids are filled.

In Section 3.3.1 it was described that after exposure to a gas containing NO, O_2 and H_2O, the anion of the IL is exchanged with nitrate, if the corresponding acid is more volatile than nitric acid. In order to ensure accurate data was obtained in subsequent gravimetric absorption experiments, an attempt was made to exchange the bromide anion of the HS-SILP to nitrate. Therefore, an absorption experiment was conducted using the same gas mixture and experimental setup used for the other gravimetric absorption experiments described in Section 3.2. A gas containing 5% NO, 10.5% O_2, 1% H_2O and balance N_2 was administered to the HS-SILP. Figure 5.3 shows the ATR-FTIR spectra obtained prior to exposure, after saturation and after desorption at 130 °C for 2 hours. A clear difference between the HS-SILP before and

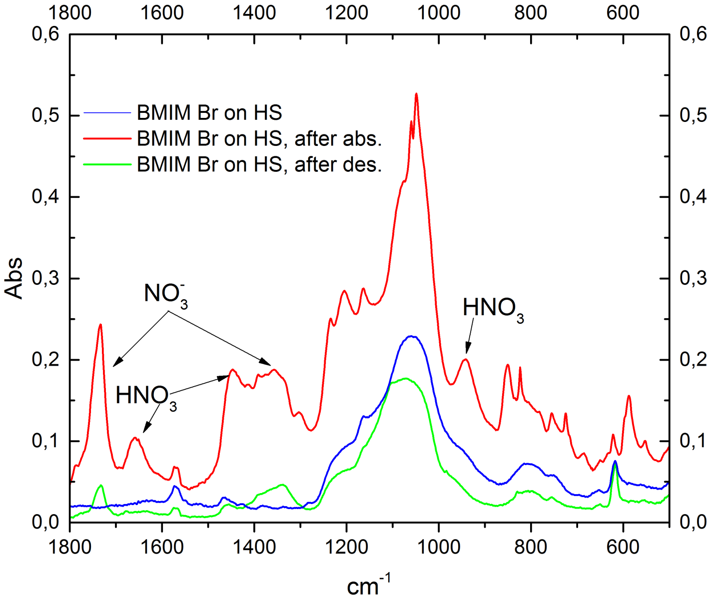

Figure 5.3: ATR-FTIR data of the HS-SILP with [BMIM]Br in experiments where the SILP was subjected to a gas containing 5% NO, 10.5% O_2 and 1% H_2O, with balance N_2. Blue spectrum was obtained prior to exposure, the red spectrum was obtained after saturation and the green spectrum was obtained after desorption at 130 °C for 2 hours under wet air flow. Expected band positions for nitrate and nitric acids species are marked in the spectrum.

after exposure to the gas mixture and subsequent regeneration at 130 °C is seen from the blue and green spectra presented in Figure 5.3.

At saturation, a number of bands assignable to HNO_3 and NO_3^- are observed, as seen from the red spectrum in Figure 5.3. After desorption the bands assignable to HNO_3 have disappeared but the nitrate bands at 1720 cm-1 and 1310 cm-1 are still clearly visible after desorption. This strongly suggests that the bromide has been, at least partly, exchanged with nitrate. The intensities may vary between samples because the reaction was followed by extracting samples from the reactor at different times. Consequently, every spectrum constitutes a new part of the sample. 3 measurements of each sample were performed to ensure the relative intensities of the observed bands were consistent.

During absorption, development of a red-brown gas which moved through the reactor bed was observed. After saturation of the HS-SILP, the red-brown gas was no longer developed. Development of a red-brown gas has not been observed previously when using a SILP material for gravimetric uptakes. The red-brown gas indicates development of bromine (Br_2) during the absorption. Formation of bromine may be caused by oxidation of hydrobromic acid formed during NO absorption. In the presence of concentrated nitric acid, oxidation of hydrobromic acid is expected to occur. It is unlikely that the gas was pure NO_2 because it had a darker and more red colour. This observation is also consistent with what was observed for the [BMIM][OAc] described in Section 3.3.1, in which acetic acid is formed quickly after exposure to the gas. The acid is then slowly released as nitric acid builds up in the IL. It is unknown if hydrobromic acid is an intermediate in this case, or if the bromide is oxidised directly by the nitric acid.

The absorption/desorption process was performed 4 subsequent times to make sure all bromide had been expelled from the sample prior to beginning the gravimetric experiments. Formation of the red-brown gas was not observed during any of the subsequent absorptions.

After anion substitution was complete, the sample was used for gravimetric absorption experiments. An average of the gravimetric increase from three absorptions with subsequent desorptions at 130 °C is shown in Figure 5.4. From Figure 5.4 it is seen that both the HS-SILP and the HS support increase significantly in weight when exposed to the NO containing gas. It is unknown which species is absorbed on the HS support, but for comparison, the uptake is presented using the same gravimetric scale as the HS-SILP: mol HNO_3/mol IL at a fictional 30% v/v pore filling

In order to not overestimate the relative absorption capacity of the HS-SILP, the reactor volume of the HS-support was around 10% higher than for the HS-SILP. The two materials appear to have a similar and high initial uptake. After around 90 minutes, the uptake for the HS stagnates and quickly converges at a molar ratio of 0.52 (mol HNO_3/mol IL, in a comparable SILP volume). For the HS-SILP, the high uptake rate continues for almost 400 minutes before decreasing, converging at a molar ratio of 1.55 (mol HNO_3/mol IL).

The high initial absorption rate for the HS support is surprising since it was established previously, that a clean IL surface shows the highest absorption rate in both SILP and bulk IL. It is however, important to keep in mind that the gravimetric analysis is unspecific and the high initial uptake is likely, in part, due to a high water uptake on the high surface area of the hydrophilic silica. The short micropores leading into the larger cavity of the HS are likely to assist this initial absorption of water due to strong capillary forces.

For the HS-SILP, the gravimetric uptake converges at 1.55, corresponding to the 1:1

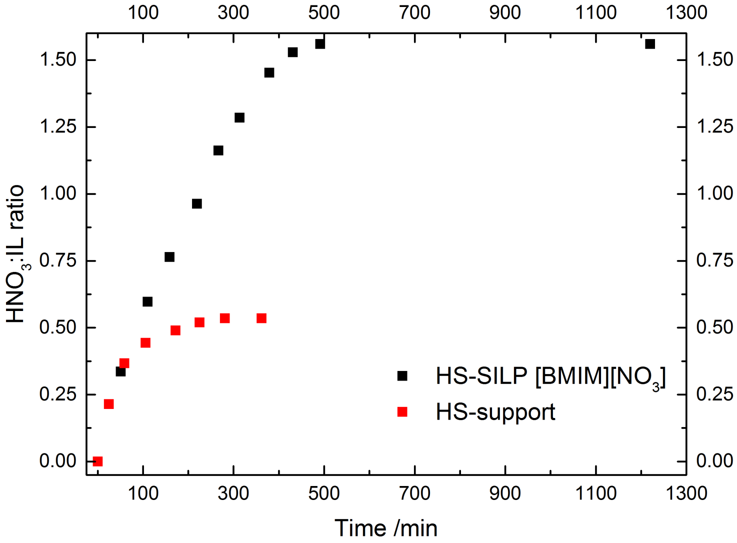

Figure 5.4: Gravimetric uptake (recalculated to HNO_3 equivalents) for 1.01 g [BMIM][NO_3] HS-SILP (black) and the pure 0.86 g HS support (red) after being subjected to a gas containing 5% NO, 10.5% O_2, 1% H_2O and balance N_2 at room temperature.

ratio found in for the pure IL, if subtracting the uptake observed for the support. While it is unknown exactly how large a part of the uptake is due to the support alone, it is highly unlikely to be higher than the 0.52 the pure support converged at. This means the HS-SILP shows a capacity which is comparable to the bulk IL. The capacity may in fact be higher than 1, depending on the contribution from the support.

The HS-SILP is the only SILP formulation that has been able to reach the full equilibrium molar ratio of 1:1 observed in bulk experiments with neat ILs. Furthermore, the equilibrium is reached significantly faster for the HS-SILP compared to the best performing silica SILP presented in Section 4.4. These findings strongly suggest that HS is a superior support material compared to the commercially available supports tested previously.

In order to further evaluate the performance of the HS support, breakthrough experiments were conducted for the HS-SILP in the new setup at flow rates that were more than an order of magnitude higher compared to previous experiments. Due to the altered reaction conditions, the best performing SILP from the previous breakthrough experiments were also tested for comparison. Results from the breakthrough experiment are shown in Figure 5.5. From figure 5.5 it is seen that the silica gel 100

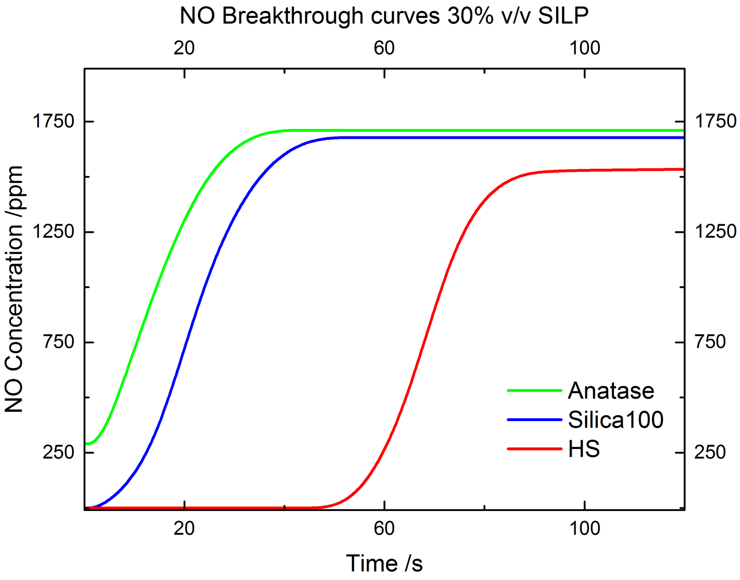

Figure 5.5: Breakthrough curves for SILP materials (30% v/v [BMIM][NO_3]) after being subjected to a gas containing 2000ppm NO, 16% O_2, 2% H_2O, 20% He and balance N_2 at 30 °C, GHSV = 12,000 h^{-1}.

SILP and the HS-SILP can both completely remove NO from the simulated flue gas, while the anatase SILP was not able to remove all NO at the tested space velocity. Thus, breakthrough occurred prior to the first measurement taken after 4 seconds. Breakthrough for the silica gel 100 SILP occurred on the second measurement after 14 seconds. For the HS-SILP the breakthrough occurred on the 7^{th} measurement, after 64 seconds.

Direct quantitative comparison between the HS-SILP and the silica gel 100 SILP is severely limited by the time resolution. A conservative estimate for comparison would be to consider the breakthrough times as 14 sec and 54 sec respectively. In this case, the absorption at breakthrough is 4 times higher for the HS-SILP compared to the silica gel 100 SILP. The molar uptake in the HS-SILP at breakthrough was 0.013 (mol NO/mol IL). This is slightly higher than the highest molar uptake reported for the SILP formulations presented in Section 4.4.1, despite these experiments being conducted at space velocities which were more than an order of magnitude higher.

Furthermore, the porosity of the HS support is 2.5 times higher compared to the anatase, thus the volumetric efficiency of the HS-SILP is significantly higher. This is also seen from figure 5.5, as the anatase and HS-SILP formulations are compared in equal volumetric amounts and a substantial discrepancy between the two is observed.

A possible limitation to the use of HS as support is the size limitations enforced by the micropores leading through the shell. The restrictions enforced by this was investigated by attempting to impregnate the HS support with $[N_{6666}][NTf_2]$. The $[N_{6666}]$ cation is currently being used for CO_2 absorption in some of the highest capacity IL formulations reported [104, 126].
The same impregnation method described for the [BMIM]Br was used, with different solvents and solvent mixtures in which the $[N_{6666}][NTf_2]$ was soluble. In all cases, the product of the impregnation was a sticky yellowish slurry, compared to the fine, dry white powder formed with [BMIM]Br. In order to test if it was possible to circumvent this size restriction, an attempt was made to synthesise $[N_{6666}]Br$ inside the HS. This was found to be unsuccessful. The experimental procedure and ATR-FTIR data of the resulting product is shown in Appendix A.8.
An attempt was also made to synthesise poly ionic liquids inside the HS-support. Anion substitution in the polymeric network was then performed to incorporate metal-containing anions, which were subsequently reduced to form nano-particles. The results from these experiments are shown in Appendix A.9.

5.3 Conclusions

Hollow sphere silica with a narrow particle and pore size distribution was successfully synthesised in collaboration with Prof. Dai and his group at ORNL, using their facilities. Surface characterisation and porosimetry results were in accordance with literature values and TEM images were found to be in agreement with the porosimetry analysis.
Supported ionic liquid phase using the hollow sphere silica as support (HS-SILP) was synthesised and analysed. Porosimetry investigations suggested most if not all of the IL was inside the HS cavities or in the microporous shells. Partial filling of the HS cavities was suggested due to the high retention of porosity and surface area, as well as the mean pore sizes found. A graphic representation was suggested and is shown in Figure 5.2.
NO absorption experiments were conducted using the HS-SILP, which was found to be the only SILP formulation to reach a molar ratio of 1 (mol HNO_3/mol IL). The HS-SILP was also tested in low concentration NO breakthrough experiments. Here, the performance was compared volumetrically to the best previous SILP formulations and found to be several times better.
NO breakthrough experiments for the HS-SILP were conducted at 10-15 times higher space velocities than previous experiments. The higher space velocities were suggested to possibly decrease the molar uptake at breakthrough. Despite the high space velocity, a molar ratio of 0.013 was found at breakthrough for the HS-SILP, which was slightly higher than the best previous SILP formulation.

Hollow sphere silica was found to substantially increase the gas absorption rate of the ILs used. A high gas diffusion rate is expected in the SILP compared to other SILP formulations. These observations and preliminary results strongly suggest that hollow sphere silica is close to being the optimal support material for gas absorption with SILP absorbers. Use of the HS support should be expanded to see if similar increases in breakthrough times are observed for other gasses such as CO_2 and SO_2. As long as the cations are not too big to enter the HS.

Chapter 6

Alcohol Promoted Oxidation of NO to NO_2

When emitted to the atmosphere, NO is converted to the more thermodynamically favoured NO_2 through a series of radical reactions often initiated by UV-light [170, 171]. As mentioned in Chapter 2 NO_2 can react further, leading to increased levels of stratospheric ozone and acid rain. Interest in these reactions arose in the late 1960s [172], and much research has been conducted in the field since. Several studies were carried out, which measured the effects of the surroundings on the rate of oxidation [173]. It was found that the rate of oxidation is readily increased by the presence of small organic compounds, especially unsaturated organic compounds [174,175]. This chapter will review some of the relevant literature in NO_x abatement, in which oxidation from NO to NO_2 is a prerequisite, as well as review current known methods for oxidising NO to NO_2. Lastly, a newly developed method for low-temperature oxidation of NO to NO_2, using a SILP catalyst and an alcohol co-catalyst is presented. The SILP catalysts are discussed in detail in chapters 5 and 4.

6.1 Thermodynamics of NO Oxidation

As mentioned above, NO_2 is the thermodynamically favoured species at ambient temperatures, but the equilibrium is highly temperature dependent, as illustrated in Figure 6.1. From Figure 6.1 it can be seen that at elevated temperatures, nitric oxide becomes the predominant NO_x species.

The rate of oxidation at lower temperatures was first studied by Bodenstein and

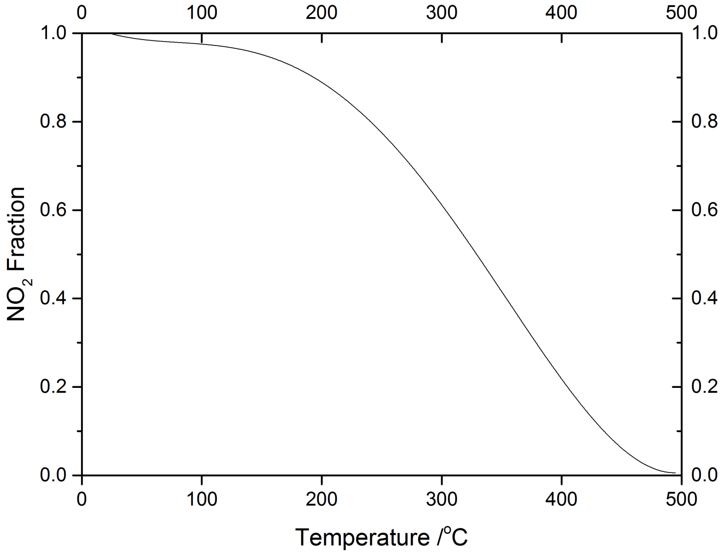

Figure 6.1: Equilibrium data calculated from the degree of dissociation as reported by Pârvulescu *et al.* [163] and presented as the expected NO_2/NOx equilibrium molar fraction in air.

Wackenheim in 1918, their studies showed that the reaction follows the rate equation shown in Equation 6.1 [176].

$$-\frac{d\mathrm{NO}}{dt} = k \cdot [\mathrm{NO}]^2 \cdot [\mathrm{O_2}] = k_p \cdot p_{\mathrm{NO}}^2 \cdot p_{\mathrm{O_2}} \tag{6.1}$$

The reaction order has since been confirmed by several authors, including Tsukahara *et al.* [177] as well as Hisatsune and Zafonte [178] who also determined the Arrhenius parameters and activation energy for the reaction. A negative apparent activation energy of -1.55 kJ/mol (-370 cal/mol) was found in the temperature range 4-56 °C [177]. Oxidation of NO to NO_2 is a fast reaction compared to other reactions occurring in the atmosphere. In chemical processing terms, however, the reaction rate is very low. This is due to NO being kinetically hindered [179]. The NO concentrations in a flue gas is very low (typically 300-2,000 ppm). This, coupled with the second order rate dependence in NO, means that the degree of autoxidation is small. Furthermore, combustion temperatures are very high making NO the prevalent NO_x species formed during combustion. Consequently, NO_x abatement in flue gas treatment must be focused on removal of NO, which is the main constituent.

As was mentioned in Chapter 2, one possible solution to the poisoning of regular

SCR catalysts is to move the $deNO_x$ unit downstream, after a wet flue gas desulphurisation (FGD) unit.
A wet FGD unit scrubs the flue gas with an aqueous $CaCO_3$ solution, removing most SO_2 from the gas. At this point the gas is almost saturated with water and the temperature of the gas is 100-150°C, far below the 300-350°C required for standard SCR to work optimally [26]. In order to avoid a costly reheating step, much effort is currently being put into developing new, low-temperature, SCR catalysts to accommodate these new reaction conditions. Most of the research is focused on manganese oxide or mixed oxides containing manganese as one of the constituents [35,37,38,42]. Several authors have reported high activity at temperatures around 200 °C even with water in the flue gas. One oft-reported disadvantage to these manganese catalysts is low N_2 selectivity. Current high selectivity state-of-the-art catalysts only show an N_2 selectivity of 90-95% [44]. Another disadvantage is very low sulphur tolerance. SO_2 from the flue gas forms sulfate species on the catalyst causing irreversible deactivation [180].
If the NO_x composition of the flue gas is an equimolar mix of NO and NO_2, it is possible to operate under fast-SCR conditions (for a more elaborate description of fast-SCR, see Chapter 2). Fast-SCR conditions increase the SCR reaction rate by around one order of magnitude, thus allowing the reaction to be carried out at even lower temperatures [181,182]. Fast-SCR has also been suggested as a way to increase selectivity [183], further mitigating the disadvantages of the low-temperature catalysts. Currently the fast-SCR method is not being employed, mostly because there are no suitable oxidation catalysts to obtain the equimolar NO:NO_2 ratio. Some of the possible solutions are reviewed in this chapter. For low-temperature applications, an optimal catalyst for oxidation of NO to NO_2 should be able to reach a conversion close to 50% at 100-150°C in a gas containing high concentrations of water, oxygen and CO_2. The target conversion should be slightly below 50%, since excess NO_2 hinders the reaction considerably [33,184].

Much research has gone into finding a suitable catalyst for low temperature oxidation of NO to NO_2 in recent years. The current research can generally be categorized as one of the four following catalyst systems; Activated carbonaceous species, siliceous compounds including zeolites, noble metal catalysts, and supported metal-oxide catalysts. Furthermore, a method for wet scrubbing with H_2O_2 has been developed and is mentioned in the literature. All of these methods be briefly reviewed and put into relevant industrial context.

6.2 High Temperature Oxidation of NO_2

Most high temperature methods for oxidation of NO to NO_2 incorporate transition metals either as oxides or nano-particles. The first formulation of catalysts used platinum nanoparticles (Pt-NP) to increase the oxidation efficiency. These catalysts were developed based on the Pt gauzes used for ammonia oxidation in the Ostwald process [133]. Today, platinum based catalysts are still the benchmark, but high cost and limited availability of platinum is driving development towards cheaper and more sustainable alternatives [185].

The first method for oxidation of NO to NO_2 specifically for implementation in flue gas treatment was developed in the early 1990's [186]. The primary objective of this catalyst was to enhance NO_x trap/storage for the newly developed NO_x storage/reduction (NSR) method [187]. NSR was developed for lean-burn diesel engines, where the traditional three-way catalyst does not work due to an overoxidising environment in a lean-burn flue gas [187]. In NSR, the NO_x is stored in a basic storage material, often containing K^+ or Ba^{2+} [188]. At appropriate intervals, the motor then shifts to rich-burn conditions, yielding an excess of reducing hydrocarbons in the flue gas, reducing the stored NO_x to N_2 in a HC-SCR step, simultaneously regenerating the NO_x trap [187].

Since then, much research has gone into the development and analysis of supported Pt-NPs for NO oxidation. A lot of the work has been focused on improving the stability and performance of the Pt catalyst, but also to analyse the oxidation reaction [188–190].

Several authors report that activity per surface platinum seems to increase with particle size, independent of the chosen support [191]. Particle sizes over 200 nm were investigated and the trend of increasing activity seems to be consistent throughout all experiments [192, 193]. This is both advantageous and disadvantageous, since sintering, which typically leads to catalyst deactivation, does not affect the activity of the platinum catalyst. Actually, most commercial catalysts require a period of activation/aging to reach optimal activities [133]. However, this heavy dependence on particle size also means that the optimal loading for the catalyst becomes rather high, significantly increasing cost[30]. Furthermore, it has been found that under oxidising conditions, the Pt catalyst is slowly oxidised, which decreases activity significantly over time. It has been found that this effect can be countered by introducing a regenerative step under reducing conditions. In NSR, and in the three-way catalyst for that matter [164, 194], the reduction obtained during rich-burn conditions also completely restores the oxidation catalyst. In stationary plants, such reducing conditions are not commonly seen; thus, a rate decrease caused by oxidation of platinum will become permanent, at least until the catalyst is regenerated externally. Consequently, Pt-based catalysts are less attractive for NO oxidation in stationary plants, even without considering possible cost limitations.

The reaction kinetics for the oxidation reaction over Pt catalysts have also been thoroughly investigated by Mulla *et al.* [190] and others [193, 195]. It has been found that water, oxygen, NO and also NO_2 influences the reaction to various extent.

The effects of oxygen have been found to depend on the support, being reported as somewhere between 0.14-1. At higher oxygen concentrations (>10%) the contribu-

tion to the rate of reaction seems to become negligible, but the dependence decreases significantly around 2-5% [189, 190, 193]. An inhibiting effect has been reported for both water and CO [195].
Most authors agree that the reaction order with respect to NO over the Pt catalyst is around 1 ±0.1, with an apparent activation energy of 80-88 kJ/mol, depending on the catalyst formulation [190, 193]. These values are significantly different from those reported in the homogenous phase, in which the reaction is second order with respect to NO and has a small but negative activation energy. Decreasing the dependence on NO to be first order provides a big improvement in expected reaction rates at the low concentrations observed in a flue gas. Another important aspect to consider in application of the catalyst for continuous oxidation is the effect of product build-up. The reaction order in NO_2 was investigated by several authors and for several different Pt catalysts formulations [190, 191, 193]. In all cases, a significant negative reaction order varying from -0.7 to -1.1 was found.
One explanation to the observed negative reaction order for water and CO, is that the oxidation reaction proceeds via an Eley-Rideal type reaction mechanism. Here, gaseous NO reacts with oxygen dispersed on the catalyst surface [196,197]. Inhibition can then be caused by competitive adsorption of CO and H_2O, reducing surface coverage of oxygen [195]. The inhibiting effect of NO_2 has been proposed to be caused by a different type of deactivation; In this case, the Pt-surface is partially oxidised, forming Pt-O species in which the oxygen is bound more strongly, thus reducing the reactivity of surface oxygen significantly [190, 193].
In NSR, the NO_2 which is formed is also removed by simultaneous absorption in the NOx trap, therefore, the negative reaction order with respect to NO_2 is negligible. This is not, however, the case for continuous oxidation, where inhibition from product build-up is a concern, since conversions close to 50% are desired.

In recent years, much research has gone into finding an alternative to the Pt based catalyst, with the primary concerns being cost efficiency and Pt availability [198], especially if a wider application range is to be considered. At the forefront of this movement is the work with mixed oxides and to some extent metal substituted zeolites. Cu-zeolites are among state-of-the-art catalysts for the SCR reaction, which has been suggested to include an oxidative step, oxidising NO to NO_2 as part of the activation cycle for NO [30]. Thus, attempting to find conditions that promote the oxidation of NO to NO_2 is a natural extension of that work.

Most recently, CuO supported on ceria and ceria-zirconia has been proposed as an active catalyst for NO oxidation at higher temperatures. This is primarily for use in the automotive industry, to further advance NSR. In a recent study by Garcia-Garcia *et al.* [199] ceria and ceria/zirconia catalysts with varying CuO loadings were characterised and the catalytic activity was determined. It was found that the optimal copper loading is around 4% and that even small amounts of copper significantly increases the rate of NO_2 formation, compared to the pure supports. Mixed oxides of zirconia and ceria have also been tested, but these materials show very low activity

in NO oxidation without the addition of metals/metal oxides [185].
In some of the earliest attempts to find a suitable oxidation catalyst Shiba *et al.* [200] used metallic copper and chromium supported on titania. Significant conversions were found with metal loadings as high as 20 wt%, but the experimental conditions were significantly different from the conditions used by more recent authors. The conditions of low space velocity and high NO and O_2 concentrations favour high conversions, which can also be seen from the blank conversion/homogenous phase conversion of 20%. This value is 0 for other authors [185, 199]. Thus, it is hard to compare conversions directly, also because NO_2 is a known inhibitor in the reaction.

When comparing these alternative oxidation catalysts to the commercially available Pt catalyst, the light-off temperature is around 120 °C higher, the maximum conversion at 30000h^{-1} GHSV is 50% obtained at 375 °C, compared to 70% obtained at 300 °C for the commercial catalyst under otherwise identical conditions [199]. Shortly after reaching the maximum conversions, all tested catalysts are limited by the thermodynamic equilibrium discussed in Section 6.1 above. In conclusion, the oxygen storage/release capacity of the ceria/zirconia support does not increase the activity of the CuO noticeably and thus, this type of catalyst is likely still some ways off of becoming commercially viable, even with increasing Pt prices.

In a recent study, Cai *et al.* [201] reported a mixed oxide of cerium, zirconium and chromium showing promising activity in the oxidation reaction. Around 10 wt% of chromium was used in the mixed oxide, which had a cerium to zirconium ratio of 1:4. The experiments were carried out with a GHSV exceeding 30000 h^{-1} and the authors achieved a conversion of up to 65% at 350 °C, with a slightly lower light off temperature than what was observed for the previously discussed CuO-ceria/zirconia catalyst. With respect to the application of such catalysts, chromium is a metal that is being phased out in industrial applications as much as possible, due to the toxicity. A catalyst with such high metal loadings will have an increased risk of leaching, which will be a profound environmental risk.
There are several similar studies testing different ratios of ceria:zirconia and different transition metal dopants, such as manganese, iron and cobalt. None of these formulations have yet to reach a satisfactory performance level when compared to the commercial Pt catalyst [180, 202]. Another concern is the absence of water in most experiments that have been conducted with the alternative oxidation catalysts, since water may adsorb more readily on some of these metals, thus influencing the reaction negatively.
The efficiency of the Pt-based catalyst for high-temperature oxidation of NO to NO_2 is really emphasised when considering all the research that has gone into finding an alternative over recent years without any truly viable alternative appearing.

6.3 Low Temperature Oxidation of NO to NO_2

Several types of zeolites have already become of industrial significance, with a rapidly expanding amount of possible applications [203, 204]. The application of metal-exchanged zeolites as catalysts in the SCR reaction was covered in Chapter 2 and it has been shown that oxidation of NO to NO_2 is an important part of this reaction [30]. In 2006, Jen and Graham [205] were the first to report the high activity of zeolites (Y and FAU zeolites in this case) in the oxidation of NO at low temperatures and propose their use as stand-alone oxidation catalysts. They showed that Ba-Y which interacts weakly with NO, was able to promote the rate of oxidation of NO with several orders of magnitude compared to homogenous oxidation rates. The zeolite also facilitated the oxidation to a slightly larger extent than the commercial Pt catalyst at these low temperatures. Furthermore the authors discovered that water hinders the reaction, and that the promoting effect is only observed at low temperatures.
A study by Halasz *et al.* [206] compared the oxidation rates for three different ZSM-5 zeolite formulations; H-ZSM-5 (Si/Al = 18), H-ZSM-5 (Si/Al = 150), and Li-ZSM-5 (Si/Al = 18) to H-Mag, a proton-exchanged form of the layered sodium silicate magadiite. All ZSM-5 samples showed similar reactivity under the reaction conditions, suggesting that lattice aluminium does not affect the reaction rate. It was proposed that Brøndsted-acidic sites may, but likely only at temperatures above 200 °C. These findings were later supported by Richter *et al.* [36] who investigated the activity of the following ammonia-substituted zeolites presented in orders of increasing acidity: ZSM-5(Si/Al = 19) > MOR (Si/Al = 5.8) > Y (Si/Al = 2.9). The authors found that the activity of NH_4-ZSM-5 and NH_4-Y were comparable while the activity of the NH_4-MOR was significantly lower than the other two, showing that neither Brøndsted acidity nor Si/Al ratio determines the activity of the zeolite.
A later study by Artioli *et al.* [207] compared high surface area silicas to siliceous zeolites (MFI, CHA and BEA) to show that the reaction proceeds willingly over both types of catalysts. The rate of the reaction depends largely on the structure of the material because there are no apparent active sites in the reaction. The authors showed that the reaction proceeds following the same rate equation (Equation 6.1) as is observed in the homogenous phase, suggesting it is an elementary reaction. This suggestion is further supported by the observation that the microporous materials show significantly higher areal reaction rates, which is likely due to a specific pore size effect. This may also help explain the large rate difference between zeolites.

Recently, Loiland and Lobo [208] made a comprehensive study of the most active zeolite catalysts for low-temperature oxidation of NO to NO_2 and compared zeolites to several types of molecular sieves based on activated carbon. Later in this section, the oxidation of NO to NO_2 over carbonaceous materials is discussed more in-depth. In the study, the authors investigated CHA (siliceous and Si/Al = 12 and 24) with H^+ and Na^+ as extra framework cations. All tested materials were very active in the oxidation and yielded oxidation rates that were several orders of magnitude higher

than in the homogenous phase. All the carbon materials were similar to the Na-CHA (Si/Al = 12) which was the zeolite that displayed the highest reaction rates. As with the studies by aforementioned authors [36, 206, 207], these studies were performed under dry conditions and the effect of water was not determined. Water has been proposed by some authors to have a significant negative effect on the reaction rate [205, 209].
The effect of formed NO_2 being present in the gas was investigated by Loiland and Lobo [208]. The reaction order was found to be -2 for both the carbonaceous materials and also for most of the zeolites, the only exception being the H-CHA for which it was -1.5. Data from some previous authors was also examined and show the same negative rate dependence for NO_2. This product inhibition is similar to what was observed for the supported Pt catalysts mentioned previously(Section 6.2), however, for the Pt catalysts the dependence on NO_2 is only -1. The significantly stronger inhibition observed is proposed to stem from NO_2 adsorbing competitively in the pores.
The effect of temperature on the rate of oxidation has been investigated by several authors [207–210]. It was found that the apparent activation energy is negative varying between -40 kJ/mol and -20 kJ/mol, as the reaction rate increases with decreasing temperature. This is consistent with what is observed for the homogenous phase oxidation, see Section 6.1.

The predominant theory is that the primary reason for the investigated materials increasing the oxidation rate significantly compared to high surface area materials, is the microporous structure. Capillary effects in the micropores lead to an increase in concentration of the reactive gas molecules. When the pore size is suitable, it can stabilise N_2O_4 which is expected to be the most important intermediate. For NO_2 to be released to the gas phase, it is important that the N_2O_4 is dissociated and desorbed as NO_2. The formation and stabilisation of N_2O_4 in the pores is likely also the reason why NO_2 has a strong inhibiting effect on the reaction rates. It has been suggested by several authors, that the final desorption step is rate determining. The presence of an inhibiting N_2O_4 species in the pores is likely also the reason why zeolites with extra framework H^+ and Na^+ show higher reaction rates than compared to their siliceous counterparts. The presence of these excess ionic sites may help dissociate the N_2O_4 through ion-stabilisation of species such as NO^+ and NO_3^- [208,210].

As with porous zeolites, carbonaceous materials can also catalyse the oxidation of NO to NO_2 [211–214]. While these carbonaceous materials are in essence very different from the zeolites, the proposed mechanism is essentially the same. It has been proposed that, the increased oxidation rate is due to pore confinement and stabilisation of an N_2O_4 transition state [210, 214, 215]. Several authors have reported that the rate of oxidation is heavily dependent on the pore structure, pore sizes and pore size distribution [214, 216]. Furthermore, it has been found that functionalised activated carbonaceous materials are more active than their unfunctionalised counterparts [217, 218]. This increased rate has been proposed to be caused by stabilisation of ionic adsorption and disproportion species on the functionalised surface. Oxidation over carbonaceous materials is extremely sensitive to both water content and temperature; no activity is observed at water contents above 0.5% v/v nor for temperatures exceeding 100 °C [214, 216]. The impact of these observations on applicability is discussed in more detail in Section 6.4.

There are two reports in the literature, where water is included in the simulated flue gas flow, without significantly decreasing the activity. In a very recent study, Ghafari and Atkinson [219] investigated the effect of using highly cross-linked polymers as catalysts in the oxidation of NO to NO_2. Based on the experimental details given in the publication, and the product data sheet for the polymers provided by DOW Chemicals [220], the space velocity has been calculated to be around 2500 h^{-1} for the experiments. This is very low compared to the low-temperature methods presented above, in which the flow rates were 10,000-35,000h^{-1}. Ghafari and Atkinson found that while highly cross-linked polymers do not show the same activity under dry conditions as activated carbon, most of the activity was retained under wet conditions (50% relative humidity at 25 °C).

The other reported method is a wet scrubbing technique where aqueous H_2O_2 is used as oxidant in a UV-catalysed process oxidising both NO and SO_2 to form the corresponding acids (sulfuric acid and nitric acid) in the solution [221]. This methods uses a vast excess of H_2O_2 at rather high concentrations (0-2.5 mol/L were tested). It has a very high efficiency towards SO_2, removing all of it under most circumstances. The highest conversions obtained for NO were around 70%, but these conversions required a high residence time to achieve. Consequently, the converted NO was trapped as nitric acid in the solution at these long residence times.

Use of a wet scrubbing method is definitely a possibility in large scale plants, as discussed in Section 3.1.1. However, the high concentration of H_2O_2 may be of concern in applications due to the risk of slip and corrosion of the equipment. Furthermore, the H_2O_2 is used in amounts that far exceed stoichiometry. Consequently it seems unlikely that this method will be broadly applicable, but it may see use for some highly specialised purposes.

6.4 Application Analysis for the Reviewed Oxidation Methods

The high temperature catalysts are mostly directed towards the automotive industry and applications in a three-way type catalyst specifically for high grade fuels. The crucial analysis of the effect of water on the oxidation rate of NO has yet to be reported for the none-Pt based high temperature catalysts. It has been shown that water significantly decreases the activity of the Pt catalyst. However, this is not a significant issue in NSR, as the catalyst is completely regenerated under rich-burning conditions, which occur often enough for this deactivation to be a non-factor. It would be interesting to see how the corresponding metal-substituted ceria/zirconia catalysts respond, but this has not been reported yet. Likewise, an assessment of the effect of NO_2 formed during reaction has yet to be fully performed for the alternative oxidation catalyst formulations. It is to be expected that NO_2 has a negative effect on the rate of oxidation, but the extent of it is hard to predict.

The purpose of this project has been to look at applications in the energy sector, where a transition to biomass and other biofuels is important to decrease the CO_2 emissions. As described in chapter 2, switching to a tail-end type of $deNO_x$ system is advantageous. After the wet-scrubbing in the FGD unit, it is to be expected that the flue gas has a low temperature (80-120 °C) and a high water content of around 35-40%, which corresponds to a relative humidity close to 100% at 70 °C. Reheating the gas is possible but costly, and should be limited as much as possible. Therefore, the aim is to run the SCR reaction at as low a temperature as possible. The best way to ensure a sufficient activity at low temperatures, is to feed an equimolar mix of NO and NO_2 into the SCR reactor, thus obtaining fast SCR reaction conditions. In order to achieve the goal of using fast SCR for tail-end $deNO_x$ applications, it is imperative to develop a catalytic system for low-temperature oxidation of NO to NO_2 with a high activity under wet conditions.

As explained above, none of the current methods fit these needs. While the carbonaceous materials show the highest activity at low temperature, this activity decreases significantly when increasing the temperature. At temperatures $>$100 °C, the activity of most of these carbonaceous catalysts is 0. The adverse effects of water are also highest with the carbonaceous materials, as even low amount of water completely negates the catalytic effect.

Different zeolite structures show the same activity as the carbonaceous materials, and are more resistant to water, while also having a larger temperature activity window. Under wet conditions the zeolites still increase the rate of oxidation significantly (several orders of magnitude) compared to the homogenous phase reaction. Another major concern for the application of either of these catalytic systems is the strong inhibition by NO_2. The exact reason for the inhibition is still debated, but it is believed to be competitive absorption in the microporous volumes where the oxidation occurs. This is compatible with the assumption that the high activity is caused by stabilisation of an N_2O_4 intermediate in the pores. If this is indeed the case, the strong inhibition caused by the presence of NO_2 is likely hard to avoid, and thus, these catalytic systems are ill-suited for continuous oxidation where the target conversion is 45-50%.

6.5 Experimental

The preliminary data for the screening process of different alcohols, presented in Section 6.6.1, was carried out by two B.Sc. students, Andreas Juul Jakobsen and David Nielsen, during their thesis work. The data analysis presented has been carried out at a later stage.

6.5.1 Synthesis of Materials

Most of the materials used in this chapter were synthesised previously and the synthesis has been described in other chapters. Impregnation of SILP materials are explained in Section 4.3 and synthesis of the hollow-sphere silica (HS) support and HS-SILP is described in Section 5.1. Alcohol solutions were prepared by mixing deionised water with the corresponding alcohol. Methanol ($>$99.8%) and ethanol ($>$99.5%) were supplied by Sigma-Aldrich, allyl alcohol ($>$98.5%) was supplied by Fluka.

6.5.2 Alcohol Screening Experiments

The first alcohol screening experiments were carried out using the same experimental setup explained in Section 4.3. The glass reactor containing a sintered frit in the middle, was packed with a small amount of quartz wool (on top of the frit), upon which 3 mL of SILP was placed. A simulated flue gas containing 2000ppm NO, 15% O_2, 1.5% H_2O and balance N_2 was passed over the reactor bed over a weekend to ensure saturation. The gas flow was then led through the bypass, the reactor was opened from the top and 3 drops of alcohol was added directly onto the SILP bed. The alcohols that were tested were all supplied by Sigma-Aldrich, 99% purity, these alcohols were: (methanol (MeOH), ethanol (EtOH), 1-propanol (n-ProOH), 1-butanol (n-BuOH), *tert*-butanol (t-BuOH), 1-hexanol (n-HexOH), 1-heptanol (n-HeptOH), 1-octanol (OctOH), 1-decanol (DecOH).
After addition of the alcohol, the top of the reactor was put back in place and the gas stream containing NO was led over the reactor. The effluent gas mixture was analysed using the same Thermo-Fisher Evolution 220s UV/Vis spectrophotometer used in previous experiments. Gas phase FTIR data were obtained on a Bruker Vertex 80v FTIR Spectrophotometer, using a 20 cm Bruker gas cell with CaF_2 windows.

6.5.3 Continuous Flow Experiments

For continuous flow experiments, the setup was rebuilt to allow for mixing of a predetermined water/alcohol solution into the gaseous phase prior to leading the flue gas into the reactor. A schematic overview of the experimental setup is shown in Figure 6.2. The flow rates in the setup shown in Figure 6.2 were controlled using MKS Instruments G50A mass flow controllers. The bottom of the reactor was fitted with a 3-way valve. One exit led directly to a frit placed in a strong NaOH solution, the other led to the gas cuvette in the UV/Vis spectrometer. The gas was led through the basic solution during startup, prior to reaching steady-state, both to reduce exposure time for the UV/Vis and avoid corrosion, but also to circumvent condensation issues which were observed at high conversions. After 2.5-3 hours, the gas was led through the spectrometer, where 15 spectra were obtained from 200-600 nm with 0.02 nm resolution. The reaction was considered to be steady state when ten consecutive spectra were identical, corresponding more than one hour of on-stream measurements.

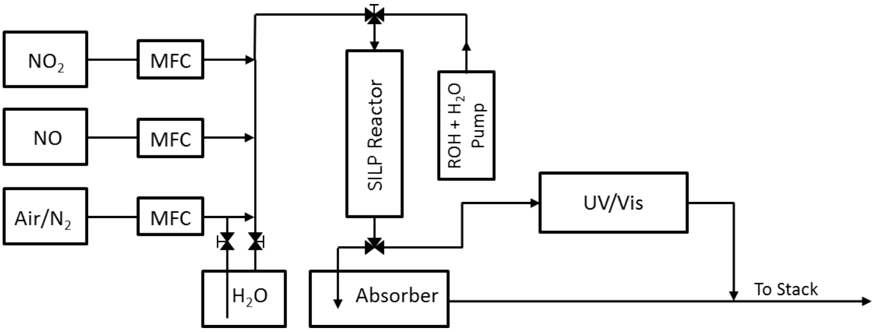

Figure 6.2: Schematic overview of the experimental setup used for addition of alcohols under continuous flow conditions.

Alcohol was administered into the system in a dilute aqueous solution using a KD Scientific 100 Legacy infusion pump to control the flow at rates between 0.2 and 0.4 mL/hour, depending on gas flow and desired alcohol concentration in the flue gas. In all cases where the alcohol concentration was changed, the pumping system and top of the reactor were removed. The top of the reactor was cleaned and put back in place and the SILP reactor was exposed to a gas mixture containing 3000 ppm NO, 14% O_2 and balance N_2, while the NO conversion was monitored. When no excess conversion compared to bypass was observed, the new alcohol solution was administered to the system and the system was allowed to equilibrate again for several hours. Same procedure was followed when testing different alcohols.

6.5.4 Quantification of NO and NO_2

Quantification of NO and NO_2 was performed by spectral deconvolution of the UV/Vis spectrum in the 200-600 nm range. Deconvolution was done using the `PeakFit 4.12` software, the deconvolution is process is described in detail in Section 4.3.

NO has three sharp peaks in this spectral range: 226 nm, 215 nm and 204 nm and NO_2 has two broader bands, one with peak band centre around 220 nm and another very broad with band centre around 405 nm [158–161]. Standard measurements in nitrogen were performed in the concentration range 500-5000 ppm for NO and 1500-5000 ppm for NO_2, standard curves are found in Appendix A.1. The higher starting concentration for NO_2 was due to limitations in the mass flow controllers. Figure 6.3 shows the spectral data obtained for the two relevant gasses. The reference data presented in Figure 6.3 above is in accordance with the literature, although a small trace of N_2O_4 is observed in the dry NO_2 spectrum, which is the reason for the apparent increase around 200 nm [161]. As expected, this peak increases with increasing NO_2 concentration. Deconvolution was performed for all peaks to determine which

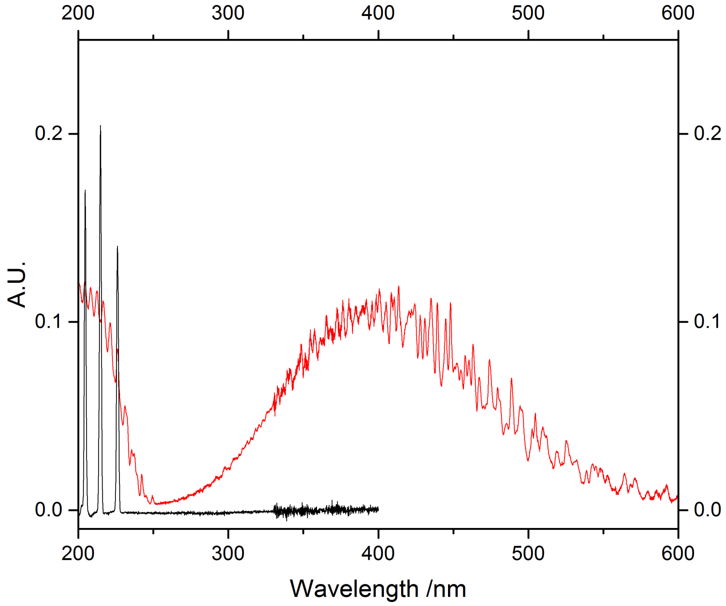

Figure 6.3: Reference spectra obtained for NO_2 (red) and NO (black) at 1500 ppm concentration with balance N_2.

was best suited for quantification analysis. It was found that the sharper of the two peaks with band centre around 217 nm yielded the lowest standard deviation for NO_2 concentration, whereas the peak at 204 yielded the lowest standard deviations for NO concentrations. Thus, the area of these two peaks were used to determine the conversion.

Almost identical standard deviations were found for the NO peaks when using the amplitude (peak height) for the corresponding Gaussian function found during deconvolution. Using the area of the peak is, however, more robust towards broadening effects from other species in multi-gas analysis, therefore, the area was used for quantification of the mixed gasses.

A mixed spectrum of NO and NO_2 was also obtained to determine if the presence of other NOx gasses affected the quantification. It was found that this was not the case for either of the species, and the resulting spectrum when mixing the two NOx species was just an addition of the individual spectra, at least within our margin of experimental uncertainty. The spectral data from these experiments are found in Appendix A.4

6.6 Results and Discussion

This section is primarily devoted to results obtained over the latter part of the project period, showing that alcohols have a strong promoting effect on the oxidation of NO to NO_2 at low temperatures. Some literature on alcohol-assisted high temperature oxidation exists and will be reviewed briefly as an introduction. The preliminary oxidation studies performed without alcohols present are also discussed.

During some of the first SILP absorption experiments conducted, a necessary induction period for the SILP absorbers that had been impregnated using an alcohol as solvent was noticed. At the time this was considered an initiation period. The product formed during this initiation period was identified as NO_2. Consequently, a wide range of SILP formulations were synthesised and tested for both absorption, as described in Chapter 4, and simultaneously for oxidation. Table 6.1 shows the SILP formulations that were tested. Bruanuer-Emmett-Teller (BET) adsorption data for the supports is shown in Section 4.3. The influence of water concentration was also screened, as the experiments were carried out with no water, a sub-stoichiometric amounts (900ppm), and vast excess ($>1.5\%$). We found that at these low conversions, there was no discernible difference between the sub-stoichiometric water concentration, and the high water concentration. It is seen from Table 6.1 that a vast variety of possible SILP formulations were screened during this work. This was done at temperatures ranging from 25 °C to 130 °C. At these temperatures, the SILP is stable, which can be seen from the TGA data in Appendix A.5. Oxidation experiments for the pure supports was never carried out in the dry gas, which likely explains why no excess conversion was observed for either silica support, which other

Table 6.1: Highest steady state NO conversions for some of the SILP materials tested. All reported values have been corrected to account for autoxidation in a corresponding system without IL. The screening was carried out at temperatures from 25 °C to 130 °C, highest steady state conversion was usually obtained at 80 °C. The SILP materials were exposed to a gas containing 2000ppm NO, 16% O_2 and balance nitrogen. GHSV = $1500h^{-1}$. Water concentrations in the gas were varied for the alumina, silica gel 100, both SS61138 and both anatase SILP materials(0ppm, 900ppm and 15,000ppm) without any notable effect.

Support material	IL Loading	SS Conversion
Carbon Black (Cabot, Pearl 1400)	5, 10, 20	5
Carbon Black (Cabot, Pearl 2000)	5, 10, 20	5
Silica gel 100 (Fluka)	0, 2.5, 5, 7.5, 10, 15, 20	3
Silica gel 90 (Fluka)	0, 5, 10, 15	3
Silica gel 60 (Fluka)	2.5, 5, 7.5, 10, 15, 20	3
Silica SS61138 (S-G, uncalcined)	0, 5, 10, 20, 30	0
Silica SS61138 (S-G, calcined)	0, 5, 10, 15, 20	2
Spinel (Fluka)	5, 10, 20	4
Ceria (S-G)	10, 20	0
Zirconia (S-G)	10, 20	0
Gamma-Alumina (S-G)	0, 5, 10, 15, 20	3
Anatase ST3119 (S-G)	5, 10, 15, 20	3
Anatase (S-A)	0, 5, 10, 15, 20	3
Spherical Supelco (4 types)	10, 20	4

authors have shown to increase oxidation significantly. The highest conversion was generally observed at 80 °C, but the difference in measured conversions is close to the experimental error. An example of a temperature series (from 25 °C to 130 °C) is shown in Appendix A.7 and clearly shows this insignificant difference.

At low IL loadings, the continuous flow experiments showed no impact of the SILP on the degree of oxidation of NO to NO_2. For most SILP materials the rate of oxidation decreased at the lowest IL loadings, compared to the pure support. At higher IL loadings, most SILP materials had a small promotive effect on the oxidation, but as can be seen from Table 6.1, the effect was modest in all cases.

Previous studies by our research group (unpublished data) showed hierarchical pore filling of the SILP material. These finding are in accordance with investigations performed by Lemus *et al.* [165]. From the literature presented in Section 6.3, it appears stabilisation of an intermediate in the micropores is the likely the reason for the added oxidation activity of the porous supports. At low IL loadings, these micropores are blocked and become unavailable thus hindering the reaction. The available surface of the IL does not compensate for the blocking of micropores, thus a significant decrease in reaction rate is observed. At higher IL loadings, the oxidative capability of the IL compensates for the loss of microporosity, leading to a slight increase in reaction

rate. However, it was found that no IL loading promoted the rate of NO oxidation by more than a few percentage points compared to the pure support.
Based on these results, it was concluded, that there was no SILP formulation which could continuously promote the oxidation of NO to NO_2, at least not in the temperature regime where the IL is stable.
It was later found, that the observed oxidation of NO to NO_2 during initiation of the SILP was caused by unremoved alcohol residues in the SILP. This was surprising since the solvent had been evaporated using a rotary evaporator at 60 °C and 10-20 mbar for 2 hours prior to use.

Very little literature is available, describing NO oxidation by use of an injection agent such as methanol. In the early 1990's Dam-Johansen *et al.* [222, 223] conducted a series of studies on the promoting effect of adding equimolar amounts of methanol to a reactor during NO oxidation. It was found that methanol increases the NO oxidation significantly at temperatures between 600 and 750 °C. At both lower and higher temperatures there was no added effect on oxidation. However, this was not tested for temperatures below 400 °C. These high temperatures are not relevant to the applications considered in this work. Also, the reaction forms considerable amounts of CO.
Other relevant literature is found within the field of atmospheric and smog chemistry. Studies conducted in the 1970's considered the effect of small organic molecules on NO oxidation under atmospheric conditions [174, 175]. Here, it was found that UV-initiation is necessary for the reaction to proceed; otherwise, the oxidation rate for NO is not affected by the presence of small organic molecules. Furthermore, it was found that unsaturated organic compounds increased the NO oxidation considerably compared to saturated compounds. It is worth noting however, that none of these early smog experiments report on the reactivity when alcohols are used as the organic molecule.
More recent studies suggest the rate of reaction between nitrate radicals and methanol in the gas phase is several orders of magnitude lower compared to the unsaturated compounds studied previously [6].

6.6.1 Screening of Different Alcohols

In order to investigate the theory that residual methanol was the cause of the increased rate of NO oxidation, a screening experiment was conducted. This was done by adding a small amount of alcohol to the SILP reactor at 30 °C, after the SILP had been saturated in a gas stream containing NO, oxygen and water for 24 hours. This process was described in the SILP absorption experiments presented in Chapter 4. Under these conditions, it was found that addition of the small amount of alcohol increased the oxidation significantly. In order to test whether the increased NO_2 concentrations were due to release of already absorbed and oxidised NO from the SILP,

a blank experiment was conducted in which alcohol was added to the saturated reactor bed, and a gas flow without NO was passed over. It was found that only an insignificant amount of NOx was released in this process, thus confirming that most of the oxidised NOx observed in the spectrum was due to oxidation occurring in the reactor bed during the analysis.
Adding the alcohol directly onto the reactor bed was the only possible method for screening at this stage. This method was not ideal since the added amount of alcohol was not quantifiable. Later, the setup was rebuilt to allow for addition of the alcohol directly into the gas stream. The results obtained from the optimised setup are presented in Section 6.6.2.

During the screening process, the NO concentration was monitored by deconvolution of the 204 nm peak in the UV-Vis spectrum. The time-resolved NO conversion estimated by this deconvolution after addition of methanol and allyl alcohol to the reactor is presented in Figure 6.4 below. When looking at the total conversion presented in Figure 6.4, it appears a maximum conversion of 75% and 90% is reached for the methanol and allyl alcohol respectively. This maximum conversion appears to be maintained for some time before rapidly decreasing to regain the conversion

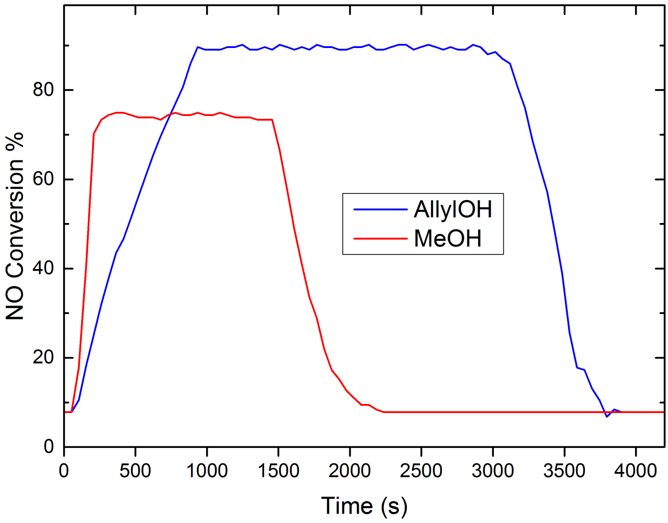

Figure 6.4: NO conversion over time after adding three drops of alcohol to the SILP (30% v/v [BMIM][NO_3] on silica gel 100) reactor and then exposing it to a simulated flue gas containing 2000 ppm NO, 1.5% H_2O, 16% O_2, balance N_2, GHSV = 4500h^{-1}. Maximum conversion is found at the plateaus.

observed prior to addition of the alcohol. The sudden drop in conversion suggests that the promoting alcohol is no longer available. The molar amount of the three drops of alcohol added to the reactor, was estimated gravimetrically for each individual alcohol by adding three drops into a weighing vial placed on a micro balance. This was repeated 5 times for each alcohol, with little variance between results.
By integration of the area beneath the curve in figure 6.4, it was found that the molar amount roughly corresponded to 1 mol of NO converted per mol methanol and 2 mol NO converted per mol of allyl alcohol. Most of the uncertainty factors, such as evaporation, pore confinement etc. point towards the quantified amount of alcohol being significantly higher than the actual amount partaking in the reaction. The results presented in figure 6.4 were obtained over a silica gel 100 SILP with 30% loading v/v. The same experiment was conducted with two other SILP formulations. These experiments yielded slightly lower conversions but showed the same difference between methanol and allyl alcohol and same high NO conversion. All subsequent screening experiments were based on the silica gel 100 SILP.

From the results presented in Figure 6.4 above, it appears the nature of the alcohol play a significant role in determining the rate of oxidation. Consequently, a screening of alcohols of varying size was conducted. The maximum conversions for each alcohol is shown in Figure 6.5 below. From Figure 6.5 it appears that allyl alcohol is significantly more active when compared to the other alcohols. This is in accordance with the observations made by atmospheric chemists that unsaturated organic compounds has a higher impact on the oxidation reaction [174,175]. There also seems to be a strong correlation between the boiling point of the alcohol and the activity. In fact, the only alcohol which does not follow this trend is allyl alcohol, which is the only unsaturated alcohol that was tested. This may be due to a vaporisation effect, but other factors such as solubility in the IL could also influence the activity. There is a discernible difference between n-Butanol and t-Butanol, this could suggest that coordination around the OH group is of importance. This could be due to a stabilising effect on an intermediate species. While there are too many unknown factors to give a quantitative understanding of the role of the alcohol, this study gives a good understanding which alcohols to use going forward. When not considering allyl alcohol, the maximum conversion follows: MeOH>EtOH>t-ButOH>ProOH>ButOH, which is consistent with the order of the boiling points of the alcohols. Considering industrial application, methanol and ethanol would likely be preferred over the other alcohols if comparable in activity on a molar basis. Both are readily available, cost efficient and are globally produced on the multimillion ton scale.

Since the results obtained in the screening process seemed promising, the reactor setup was modified substantially to investigate the reaction further under continuous flow conditions, with a known amount of alcohol in the gas stream. In order to reach alcohol concentrations in the gas stream which were low enough, the alcohol was dissolved in water and injected into the gas stream before the reactor bed. Thus

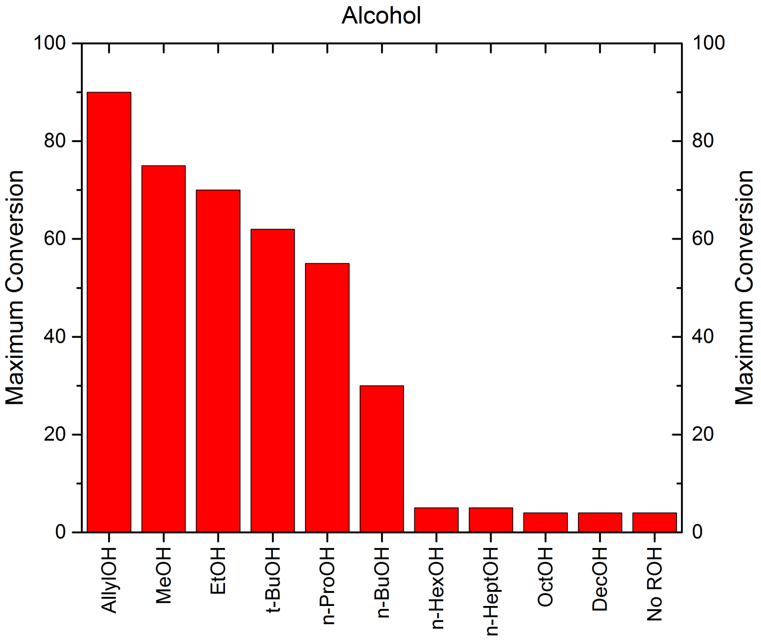

Figure 6.5: Maximum obtained NO conversion over after adding three drops of alcohol to the SILP (30% v/v [BMIM][NO_3] on silica gel 100) reactor and then exposing it to a simulated flue gas containing 2000 ppm NO, 1.5% H_2O, 16% O_2, balance N_2, GHSV = $4500h^{-1}$. In all cases, maximum conversion was obtained within the first 10 minutes.

the added alcohol/water mixture is the source of water for the reaction as well. The addition of alcohol and the other modifications are described in detail in Section 6.5

6.6.2 Continuous Flow Oxidation

In this section, results from the continuous flow experiments will be presented. The rate of oxidation is presented as NO conversion because this is believed to be the most accurate representation of the catalytic activity. For a more detailed discussion on this, see Section 6.6.3. The effect of several parameters on the NO conversion was examined. It was found that the SILP materials used were not deactivated by water, contrarily; water is likely required for the oxidation to occur. Based on the screening results presented above, methanol was chosen as the main alcohol for further investigation, since it showed higher activity than ethanol and is expected to be significantly more attractive for industrial purposes compared to allyl alcohol. The effect of both allyl alcohol and ethanol was also investigated for comparison. It is important to keep in mind, that the target NO conversion for application as preoxidation for fast-SCR should be 45-50%.

The optimal ratio of NO to alcohol, based on methanol was investigated. The results from these experiments are presented in Figure 6.6. From the data presented in figure 6.6, it is seen that even low concentrations of methanol increase the oxidation rate significantly. At the highlighted point, the NO:MeOH ratio is 75, corresponding to a methanol concentration in the gas phase of 40ppm. The conversion at this point is 40%, corresponding to a turn over number (TON) of 30 for methanol. This strongly suggests that methanol acts as a promoter in the reaction.

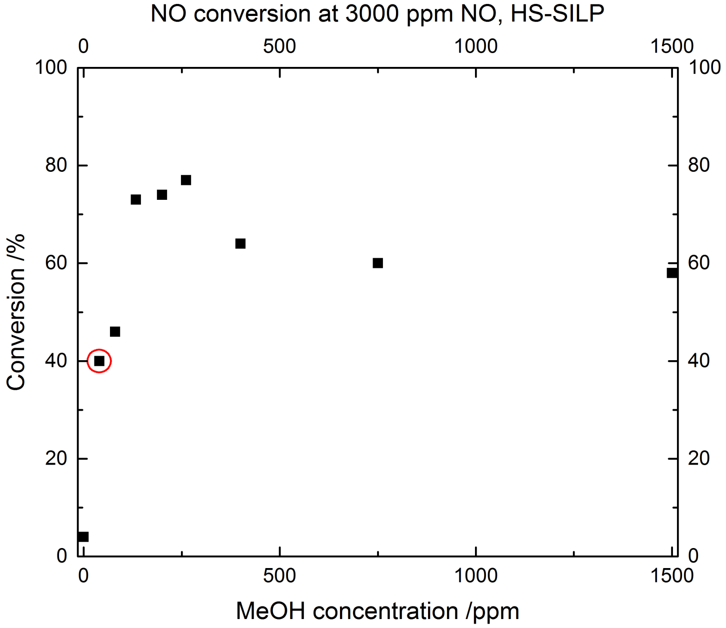

Figure 6.6: Steady-state NO conversion as a function of methanol concentration in the gas stream. The gas was comprised of 3,000ppm NO, 12% O_2, 4% H_2O and balance N_2, GHSV = 15,000h^{-1} at 30 °C. The catalyst used was a HS-SILP with 30% v/v pore filling of [BMIM][NO_3].

Previously, it was explained how similar oxidations can be initialised in the atmosphere by UV radiation from the sunlight. In order to rule out this possibility, all gas lines that were not made of steel were protected from any possible exposure to sunlight. When a reference experiment was performed, it was found that there was no significant effect of UV-light on the reaction.

Furthermore, it is noted that there appears to be a plateau upon which the methanol concentration is optimal. If the concentration becomes too high, the continuous flow conversion of NO decreases significantly. From the FTIR experiment shown in Figure 6.12, Section 6.6.3, no carbon species other than CO_2 appear to be formed during reaction, suggesting that the end product is a full oxidation of methanol to CO_2. The conversions shown in Figure 6.6 have not been corrected for empty reactor conversion, which is rather high when methanol is present, as is shown in Figure 6.8. Most of the observed oxidation in the empty reactor likely occurs in the frit upon which the reactor bed is packed under normal conditions. The frit provides a significantly higher surface area compared to the rest of the reactor.

In the literature reviewed above, it was observed that increasing the temperature leads to a significant decrease in conversion. For the scope alternative deNOx it is most relevant to achieve high conversions at temperatures between 80-150 °C, especially if it is possible with high water concentrations as well. Therefore, the reaction rate was measured over a range of temperatures from 30 °C to 120 °C. The results are presented in Figure 6.7 below. The relative NO conversions presented in Figure 6.7

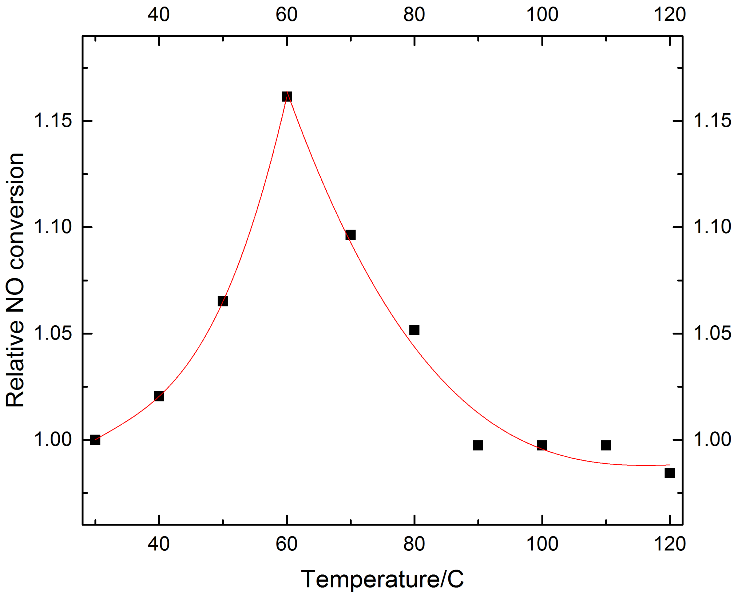

Figure 6.7: Normalised NO conversions at different temperatures. The fitted curves (red lines) are to show the trend and guide the eye. The gas was comprised of 2000ppm NO, 800 ppm methanol, 16% O_2, 4% H_2O and balance N_2, GHSV = 15,000h^{-1} at 30 °C. The catalyst used was a silica gel 100 SILP with 30% v/v pore filling of [BMIM][NO_3].

are reported relative to the conversion obtained at 30 °C. It can be seen from the relative NO oxidation, that there appears to be an optimum around 60 °C. Since the relative rate is only 1.16 compared to the value at 30 °C, temperature does not appear to have a drastic impact on the reaction rate. The presence of a temperature optimum is different from the trend reported in the literature for low-temperature oxidation over carbonaceous materials and zeolites [208, 216]. For zeolites and carbonaceous materials, the oxidation rate decreases steadily with increasing temperature. This strongly suggests that the oxidation mechanism is different when methanol is used as a promoter. The rather sharp temperature dependence is also similar to what was observed for the simultaneous absorption and oxidation in bulk IL, albeit, the temperature effect is much lower in this case. This suggests that there are two competing rate limitations.

The reaction rate is likely increased by increasing the temperature, until gas solubility in the IL becomes limiting at higher temperatures. This in turn suggests that when the IL is present, the reaction occurs between dissolved species in the IL, but this is purely speculative. A temperature series performed on the pure support would likely yield a lot of information about the limiting factors and whether gas solubility in the IL is of any importance. However, this was not within the time frame of the study.

The high TON for methanol, coupled with the observation (see Figure 6.12) that it is oxidised under the reaction conditions strongly suggests a radical reaction involving methanol occurs. During the oxidation of NO, the methanol radical species can be reformed thus yielding the high TON. Termination of the radical reaction then leads to formation of CO_2. The observed decrease in conversion at higher methanol concentrations, suggests that excess methanol provides excess termination sites and thus leads to faster termination of the active radical species.

Formation of a radical species may also be the explanation of the different behaviour of this reaction compared to the other low-temperature oxidation methods presented in the literature. Higher temperatures are expected to yield a higher amount of radical species. However, if these methanol radical species originate from initial reaction with HONO formed in the IL, this could explain the decreased rates observed at higher temperatures. These suggestions are purely speculative, but offer an explanation to the observations. Significant work is necessary in order to fully elucidate this reaction mechanism.

Figures 6.6 and 6.7 were obtained using two different SILP materials: HS-SILP and silica gel 100 SILP. The HS-SILP appears to have a significantly higher reaction rate compared to the silica gel 100 SILP. In order to investigate this further, a comparison between SILP materials on both supports was conducted. Furthermore, the oxidation capacity of the pure silica gel 100 support was tested along with the effect of changing the type of alcohol. The steady-state conversions of each experiment is summarised in Figure 6.8 below. From the data presented in Figure 6.8 it is evident that using the HS-SILP as catalyst results in higher conversion compared to the Silica gel 100 SILP. The pore filling of both the SILP materials is 30% v/v

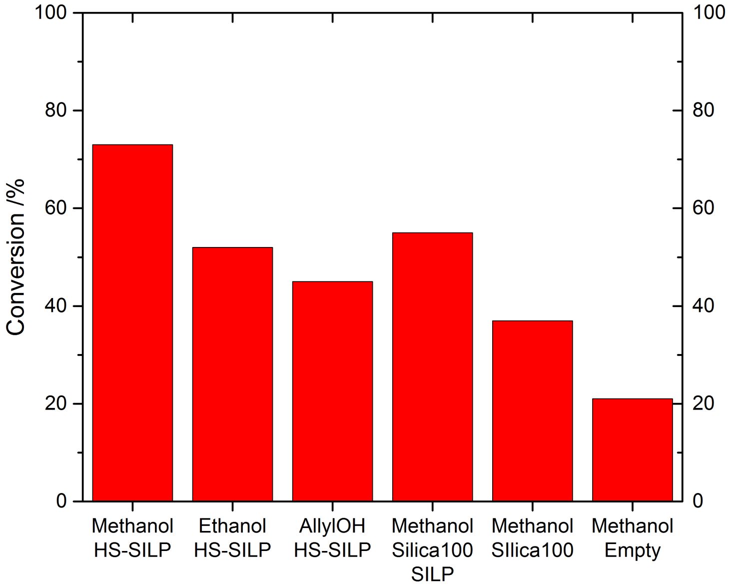

Figure 6.8: From left to right; steady-state conversions over a HS-SILP with methanol, ethanol and allylalchol. A silica gel 100-SILP, calcined silica gel 100 support (same batch used for SILP) and the empty reactor conversion (empty reactor includes quartz wool and the glass frit), all with methanol as the alcohol. In all cases, the experiments were run with a gas composition of 3000 ppm NO, 130 ppm alcohol (1:22.5), 4% H_2O, 12% O_2 and balance N_2 with a GHSV of 15,000 h^{-1} at 30 °C. GHSV for the silica support was 3750 h^{-1}, not 15,000.

and the porosity is almost identical, therefore the IL amount should be comparable at comparable reactor bed volumes. Surprisingly, the allyl alcohol is significantly worse than both methanol and ethanol under continuous flow conditions. This was unexpected considering the results obtained from the alcohol screening experiments presented in Section 6.6.1. The allyl alcohol was also tested at 60 °C and 120 °C, without any significant increase in rate. Furthermore, the allyl alcohol seemed to deactivate the HS-SILP, after it had been exposed to the gas mixture at 120 °C for 5 hours. Discoloration from white to a brownish yellow of the SILP was observed, the SILP became sticky compared to the otherwise dry appearance of the powder and the conversion obtained over the catalyst decreased significantly.

The observed deactivation was reversible, but required a 24h treatment in a dry gas at 140 °C, followed by another 24h in a wet gas at the same temperature. After this treatment, the appearance of the SILP was again back to normal and two benchmark

experiments were performed to assure there was no permanent activity loss.
It is important to note that there is significant conversion on the pure support and in the empty reactor when methanol is available. This suggests that the reaction will occur on any surface and that the IL just supplies a more reactive surface.

In order to test the compliance with demands for oxidation for alternative deNOx applications, the NO concentration was lowered to 500ppm, which is likely in the low range of what would be expected for this type of exhaust gas compositions. Furthermore, an experiment was run at higher space velocity, to also move nearer the expected values required for the reaction to be successful. Due to limitations in the mass flow controllers, the higher space velocity had to be achieved by decreasing the reactor volume. The results of these experiments are shown in Figure 6.9

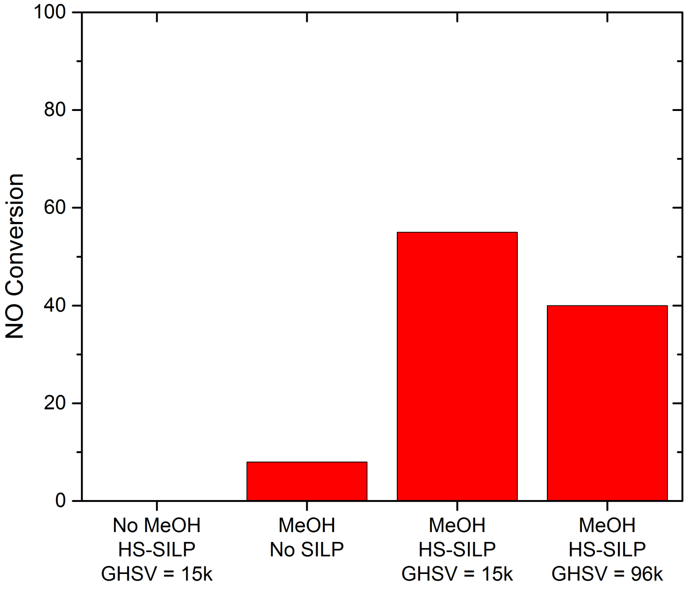

Figure 6.9: Conversions for low concentration experiments at varying reactor volumes. The GHSV is denoted in the description of the experiment. Gas composition: 500ppm NO, 17ppm methanol when present (NO:MeOH = 30), 4% H_2O, 19% O_2 and balance N_2 at 30 °C.

From Figure 6.9 it can be seen that a significant amount of oxidation capacity is still retained at the lower NO concentration. The empty reactor oxidation rate is decreased significantly by the lower NO concentration. This is fully expected, as the reaction rate is expected to depend heavily on NO concentration, regardless of phase and reaction mechanism.

An important observation is the rather small decrease in reaction rate despite the significant increase in space velocity. The volumetric rate of oxidation at GHSV = 96,000h^{-1} is $2.51 \cdot 10^{-4}$ mol·(L·s)$^{-1}$, which is 4 times higher than the highest reported value for a zeolite catalyst [208]. It is important to keep in mind that the literature values have been obtained at twice the NO concentration (1000 ppm), conversion below 15%, and without water in the flue gas. These factors are important since NO_2 and water are known inhibitors in this reaction.

The O_2 concentration during literature experiments was 5%, while it is 12-19% here. Although the reaction rate has a first order dependence on O_2, the higher O_2 concentrations in these experiments are not likely to be the sole cause of the observed discrepancies in reaction rates. This is because O_2 is already in vast excess, and the reaction order with respect to O_2 has been reported to go towards 0 at concentrations exceeding 5% [208, 209]. During the experiments presented here, no significant impact of O_2 concentrations was observed, at least not in the concentrations that were investigated. This is in compliance with the literature stating that O_2 concentrations above 5-10% do not influence the rate of oxidation.

When the observed conversion at high space velocity, presented in figure 6.9 above, are corrected for the empty reactor conversion of 8% (disregarding concentration gradient effects) the conversion still corresponds to a volumetric rate of $2.01 \cdot 10^{-4}$ mol·(L·s)$^{-1}$. These reaction rates are very promising, especially considering that little optimisation has been done to the parameters of this reaction. It is expected that further analysis of the reaction parameters and catalyst can lead to a significant optimisation of the reaction conditions.

6.6.3 In-Depth Spectral Analysis

In order to determine if NO conversion is a reasonable measure for the expected effluent NO_2 concentration, a deeper analysis of the UV-VIS spectral data was performed. Furthermore, high resolution gas phase FTIR was used to analyse the effluent gas for residuals which cannot be detected in UV-Vis. Examples of steady state UV-Vis spectra are shown in Figure 6.10, comparing the spectra for empty reactor with methanol added to the gas stream (red) and when the same gas was passed over a SILP bed with a 30% v/v [BMIM][NO_3] silica gel 100 SILP. The spectral data shown in Figure 6.10 corresponds to an NO conversion of 21% and 55% respectively. When compared to reference UV-Vis data of NO and NO_2 it becomes apparent, that under high conversions, the effluent gas does not seem to contain NO_2 in any significant concentration. This conclusion is based on the broad band with absorption maximum around 400 nm, which is absent in the black spectrum where the conversion (based on the area of the NO peaks) is significantly higher. The other broad NO_2 band, with maximum around 215 appears to increase significantly at higher conversions.

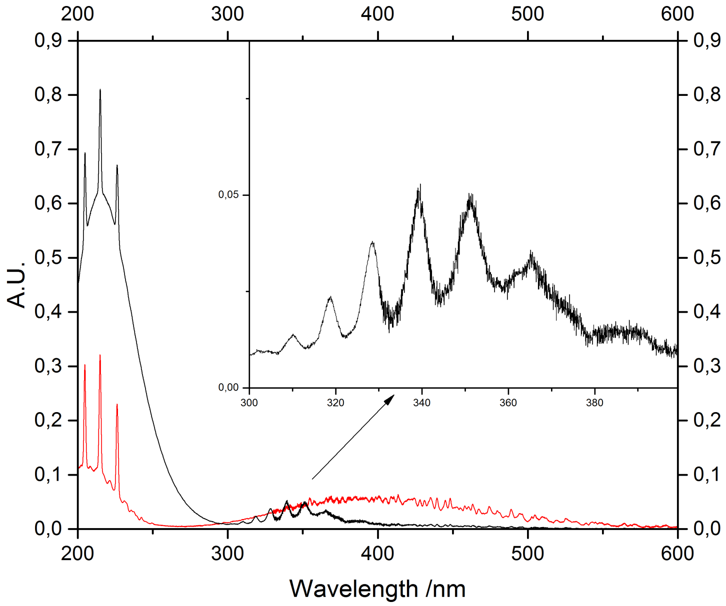

Figure 6.10: UV-Vis spectral data of effluent gas after passing the gas through the empty reactor tube (red) and a 30% v/v [BMIM][NO_3] SILP on calcined silica gel 100. Gas composition: 3,000 ppm NO, 135 ppm MeOH, 4% H_2O, 12.5% O_2 and balance N_2. GHSV = 15,000h^{-1}.

However, upon closer inspection, as is shown in Figure 6.11 below, the specific vibrational contributions from NO_2 are no longer discernible, suggesting there is little to no NO_2 in the gas phase. Another clear indication that there is no NO_2 in the gas is the marked change in line profile for the peak around 215 nm (FWHM roughly doubles), combined with a small red-shift. The resulting signals in the spectrum are consistent with HNO_3 (broad peak around 215 nm) [224–226] and HONO (sharper set of signals from 300- 380nm) [227,228]. Based on literature values of the absorption cross section of the gas phase molecules, the HNO_3 concentration is around 15 times higher than the HONO concentration [6, 226, 228]. Furthermore, it appears that the line positions and line profiles are somewhere in between the aqueous and gas states, suggesting that the acids are present as an aerosol type species. This is especially evident for the HONO bands which are narrower and slightly blue-shifted compared to an aqueous phase reference spectrum obtained by acidifying a potassium nitrite solution (see Appendix A.6).
The lines in question are slightly broader and slightly red-shifted compared to the gas phase reference data found in literature[73]. The line profiles are similar in all three

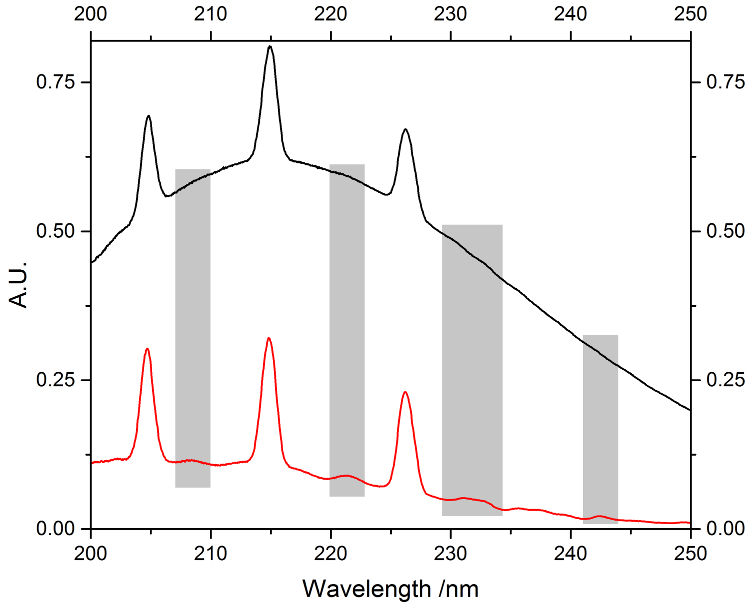

Figure 6.11: Zoom in of the 200-250 nm region of the spectrum shown in Figure 6.10 above. Red spectrum corresponds to an NO conversion of around 21%, the black corresponds to 55%. The grey areas show the individual vibrational contributions to the NO_2 UV-spectrum. These are visible in the red spectrum but not in the black.

cases, strongly indicating that it is the same species. The reason for the appearance of the acidic species is likely caused by condensation/aerosol formation due to reaction with the high amounts of water present. This likely occurs between the gas exiting the reactor and entering the gas cuvette. The condensation/aerosol formation can likely be circumvented by heating the tubing and the gas cuvette to around 120 °C. Unfortunately, this was not possible within the time frame of this study.

The formation of HNO_2 and HNO_3 introduces an uncertainty in the analysis of NO_2 content based upon the UV-Vis spectra. In order to minimise this uncertainty, all analysis should be based on NO conversion since the NO peaks in the UV spectrum are highly specific, narrow, and unaffected by the presence of water in the flue gas.

Based on the spectral analysis presented here, it is believed that reporting the catalytic performance in terms of NO conversion is the best possible solution. The presence of both HNO_3 and HONO in the flue gas suggests that NO is oxidised to NO_2, which subsequently reacts with water in the flue gas to form HNO_3 and HONO [229]. The significant discrepancy in concentration between HNO_3 and HONO suggests that a substantial part of the HONO disproportionates to form NO and NO_2, which can

further react to form more HNO_3. It is unlikely that oxidation of HONO by O_2 occurs to any significant extent under the reaction condition applied [133].
Since homogenous oxidation of NO to NO_2 is a slow process, it is unlikely that the NO formed by disproportionation will be oxidised during after the reactor due to the short residence time. In Table 6.2 an attempt is made to summarise expected the reactions. From the reaction scheme presented in Table 6.2 it can be seen that analysed NO conversions far exceeding 75% are not expected when condensation can occur, even if the initial NO_2 yield is 100%. Higher conversions of NO can be achieved depending on HONO concentration, which is reported to be significantly lower than the HNO_3 concentration. Consequently, reporting catalytic activity based on NO conversion will likely underestimate the total NO_2 yield rather than overestimate it.

Table 6.2: Reactions expected to occur in the gas-phase after passing the reactor. Expected yields indicated in percentage are based on a 100% NO conversion to NO_2 and assuming equilibrium for the highly favoured reactions are reached immediately, while unfavoured reactions are assumed not to occur at all.
Assuming reactions 1 and 3 occur immediately and are shifted completely toward the products, while reactions 2 and 4 do not occur, the total reaction becomes: $8\,NO_2 + 3\,H_2O \longrightarrow 6\,HNO_3 + 2\,NO$

Reaction	Expected Yield	Reaction no.
$2\,NO_2 + H_2O \rightleftharpoons HNO_3 + HONO$	100%	1
$2\,HONO + O_2 \rightleftharpoons 2\,HNO_3$	0%	2
$2\,HONO \rightleftharpoons NO + NO_2\,H_2O$	100%	3
$2\,NO + O_2 \rightleftharpoons NO_2$	0%	4

In order to finally assess whether it was reasonable to base the assumed NO_2 formation on the NO conversion, a gas phase FTIR analysis was performed to determine if N_2O was formed during the reaction. The FTIR should also give a qualitative understanding of what happens to the alcohol during the oxidation reaction. Figure 6.12 shows a high resolution FTIR spectrum of the steady state effluent gas after it has been passed over a 30% v/v silica gel 100 SILP, with an NO:MeOH ratio of 12.5 and a resulting conversion of around 58%. Under expected operating conditions, addition of methanol is likely to be limited as much as possible. The 12.5 NO:MeOH ratio is much lower than the expected methanol concentration under industrial operating conditions, this was chosen to determine if a methanol slip could occur. Figure 6.12 shows the high resolution gas-phase FTIR spectrum obtained for the effluent gas from these experiments, showing the ro-vibrational transitions. Literature values reported here, correspond to the vibrational band centre, which can be extrapolated from the ro-vibrational transitions. The fundamental vibrational transition (band centre) for these species is observed as the absence of a ro-vibrational transition. Since the ro-vibrational transitions otherwise have the exact same energy splitting, the band centre of the fundamental vibration is easy to distinguish.

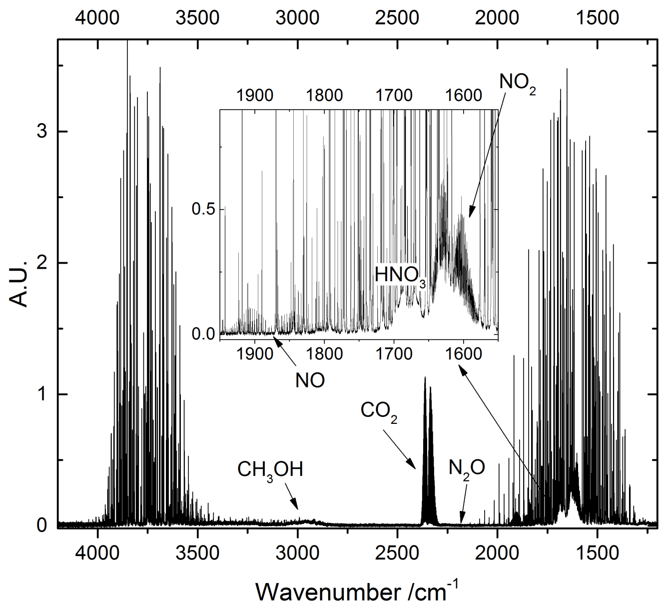

Figure 6.12: High resolution FTIR gas phase spectrum of steady-state effluent gas from the reactor. Experimental conditions: 3,000 ppm NO, 240 ppm methanol, 12% O_2, 4% H_2O and balance N_2, GHSV = 15,000 h^{-1} at 30 °C. The relevant area for NOx species has been magnified and is shown together with the full spectrum. Relevant band centres have been marked. N_2O and methanol are not found in the spectrum.

The strong signals present in the spectral region depicted in Figure 6.12 are from water (4000-3500 cm^{-1} and 2100-1250 cm^{-1}), which have coupled rotational contributions that cover most of the spectrum and CO_2 (2290-2390 cm^{-1}). There is no N_2O present in the spectrum, which would have been present around 2223 cm^{-1}. Therefore, it should be safe to assume that products from the reaction are solely oxidation products, meaning it is also safe to assume that all NO removed from the spectrum has been oxidised. Furthermore, it can be seen from Figure 6.12, that there is no apparent methanol slip based on the absence of signals in the C-H stretching region (3200-2800 cm^{-1}).

In the zoomed area of the spectrum, the signals for NO (1875 cm^{-1}), NO_2 (1617 cm^{-1}) and HNO_3 (1690 cm^{-1}) are shown, numbers in parenthesis are values simulated in HITRAN which are in concordance with literature values [230,231]. For both NO and NO_2, the peak positions correspond well with gas phase literature values, the ratio of NO to NO_2 suggests a very high conversion >70%. The time between obtaining the gas sample and recording the full spectrum is around 10 minutes, meaning a significant contribution from autoxidation is to be expected. The HNO_3 signal corresponds better with a semi-dissolved species, than with the gas phase value, as the peak position is red-shifted slightly. This is also consistent with the absence of individual rotational contributions which are normally only seen for a gaseous species.

6.7 Conclusions

SILP materials have been shown to oxidise NO to higher NO_x species efficiently at low temperatures and high water concentrations when trace amounts of alcohols are present in the flue gas. High water concentrations typically diminishes the activity of other catalytic systems. Only NO_x species with oxidation state 2 or higher were found, with HNO_3 as the primary oxidation product. Reaction rates succeeding any found in the literature have been achieved. Further optimisation of reaction conditions such as temperature, catalyst formulation and alcohol concentration are expected to further increase the activity of this catalytic system.

An initial screening process suggested that allyl alcohol would be the optimal alcohol for the reaction, but this was not the case under continuous flow conditions. Instead, methanol appears to have a superior effect on the rate of oxidation compared to the other alcohols under continuous flow conditions.

Significant reactivity is achieved by the support in conjunction with an alcohol, but addition of the [BMIM][NO_3] increases the conversion significantly. Also, it was found that the HS support is superior to regular silica gel 100 support boosting the conversion by over 100% in some cases. This is in agreement with previous absorption and oxidation experiments, in which HS is also superior to other supports.

Modest impact of temperature was found in the interval 30 °C-120 °C. The reaction seems to have a temperature optimum around 60 degrees for a NO:MeOH ratio of 2.5. The presence of a local temperature optimum is unexpected, but corresponds well with previously published literature on NO absorption and oxidation in ILs [131]. This suggests dissolution of gaseous species affects the reaction.

Conversions above 75% were not found, which suggests that NO is first oxidised to NO_2 which then reacts with water to form equimolar amounts of HONO and HNO_3. HONO was also found in the effluent gas, but in much smaller quantities than HNO_3, suggesting that it is either further oxidised to HNO_3 by excess O_2 or that it disproportionates to form NO, NO_2 and water. According to Thiemann *et al.* [133], direct oxidation of HONO is a slow process and thus unlikely to occur to any significant extent under the reaction conditions applied. Most of the NO formed from this disproportionation is likely to end up in the effluent gas, thus lowering the measured NO conversion.

Some uncertainty in the quantification of the oxidative capacity of the catalytic system was introduced by condensation in the exhaust tubing going to the gas cuvette.

It has been proposed that the condensation likely results in an under-estimation of the overall NO_2 yield under optimal conditions.

Chapter 7

Concluding Remarks and Outlook

The aim of the work presented here was to develop an alternative method for low-temperature NO_x abatement, primarily for biomass and waste incineration plants. This was to be achieved through optimisation of a novel method developed in our group, in which NO is absorbed and oxidised in an ionic liquid (IL), in the presence of water and oxygen. The rate of absorption is optimal at near-ambient temperatures and the end product of the reaction, HNO_3, is retained in the IL until it is released by heating the IL above the boiling point for the highest boiling HNO_3-H_2O azeotrope (130 °C).
The reaction mechanism and reaction kinetics were studied in detail and the reaction was found to have a second order dependence on the NO concentration. This is a considerable disadvantage for NO removal in flue gasses, since the concentration rarely exceeds 1,000 ppm, and is often around 500 ppm. In Chapter 3 the applicability of ILs in gas absorption was discussed. It was found that ILs are ill-suited for application in wet scrubbers due to the high viscosities. Therefore, optimisation of the mass transfer in the IL/gas interface is required. As discussed in Chapter 4, dispersing the IL on a porous support material is believed to decrease the mass transfer limitations in the IL/gas boundary layer, to a point where it is negligible.

Work on formulating these supported ionic liquid phase (SILP) materials had begun shortly prior to the start of this project. It was believed that a considerable improvement could be achieved through optimisation of the support material. Numerous SILP formulations were compared in breakthrough experiments with low concentrations of NO. It was found that SILP materials were able to remove all of the NO for several minutes. However, upon closer inspection, the capacity at breakthrough for the best performing SILP materials was only around 0.5% of the 1:1 molar ratio (mol NO:mol IL) observed in bulk absorption. Although the maximum capacity decreased by approximately 40% in the SILP compared to neat ILs, this cannot account for the low uptake found at breakthrough. It was suggested that the main problem was the reaction dynamics at low NO concentrations, or possibly the SILP formulation.

Saturation of a SILP material took the same amount of time as for neat ILs, suggesting the SILP does not increase reaction dynamics in the boundary layer to any significant extent. This is surprising, compared to literature reports on gas absorption in SILP materials. An attempt was made to improve the SILP formulation and understand the effects of surface chemistry of the support, porosity, pore size distribution etc. It was suggested that larger pore sizes and minimising the amount of micropores could increase the efficiency of the SILP.
Dimensioning of an absorber unit for retrofitting into a cargo ship was performed based on the obtained results, and best case scenario assumptions. It was found, that in order for the SILP absorbers to become viable for maritime applications, the absorption capacity at breakthrough had to be increased by a factor of 30-50.

In order to investigate if the necessary improvement could be achieved, formulation of a novel support material, hollow sphere silica (HS), was carried out in collaboration with Prof. Sheng Dai and his group at Oak Ridge National Laboratory, during the external research stay.
It was found that use of this optimised SILP formulation, based on HS, greatly increased the capacity at breakthrough despite space velocities which were more than an order of magnitude higher compared to previous SILP absorption experiments. An improvement with a factor of 4-6 was found when the SILP materials were compared volumetrically. This improvement is, however, still far from enough in order for absorption and oxidation of NO_x with SILP materials to become a viable solution for flue gas cleaning.
At this stage, absorption and oxidation of NO in SILP materials still needs to improve by at least a factor of 10, in order for the process to become a viable solution in flue gas cleaning of dilute NO gas.
It is believed, however, that NO_x absorption and oxidation may be applied for more specialised purposes e.g. in nitric acid production. Furthermore, it was suggested that absorption of other gasses, such as CO_2 and SO_2, with SILP absorbers, could greatly benefit from utilising the HS support.

Although great improvements have been made in the development of low temperature SCR catalysts over recent years, the required temperature is still too high for implementation in tail-end $deNO_x$. Also, the N_2 selectivity has yet to reach truly satisfactory values. Both of these issues can, to some extent, be overcome by utilising fast-SCR conditions, where NO and NO_2 are present in equimolar amounts. This can be achieved by oxidising 50% of the NO to NO_2 prior to the SCR catalyst. A catalytic system which can do this under tail-end conditions has yet to be developed.
In this work, a novel method for low-temperature oxidation was presented. It was found that alcohols have a significant promoting effect on NO oxidation at low temperatures over porous materials. The effect was increased when an IL was suspended on the porous material, especially at low (500 ppm) NO concentrations, when methanol was used as the promoter. It was found that temperature did not affect the rate of reaction significantly in the range from 30-120 °C. A temperature optimum was

found around 60 °C, which is close to the optimum temperature for positioning directly after a wet FGD scrubber.
The development of this catalytic method is still in its early stages and it is believed that significant improvement can still be achieved through optimisation of reaction parameters. Despite this, the volumetric reaction rates found in this work are significantly higher than those found in the literature. Furthermore, unlike other present low-temperature oxidation methods, this method is not affected negatively by the presence of water in the flue gas. Contrarily it is believed that some amount of water is necessary for the reaction to occur.

While there are several considerations that must be taken into account prior to implementation of the proposed methanol-promoted SILP oxidation method, the results presented here are very encouraging. The implementation of a suitable oxidation method for tail-end NO_x abatement greatly increases the likelihood of finding a suitable low-temperature SCR catalyst. This in turn makes tail-end NO_x abatement more attractive than ever, allowing for retrofitting of deNO_x units in existing plants, where this has not yet been possible. It will also allow for much more efficient NO_x abatement in biomass and waste incineration plants.

CHAPTER 8

Bibliography

---

[1] Pachauri, R. K.; Meryer, L. A., *Climate Change 2014: Synthesis Report. Contribution of Working Groups I, II and III to the Fifth Assessment Report of the Intergovernmental Panel on Climate Change*, Technical report, IPCC, Geneva, Switzerland, **2014**.

[2] Srivastava, R. K.; Jozewicz, W.; Singer, C., *Environ. Prog.* **2001**, 20, 219–228.

[3] Chang, S. G.; Liu, D., *Nature* **1990**, 343, 151.

[4] Pham K., E.; Chang G., S., *Nature* **1994**, 369, 139–141.

[5] Kanchongkittiphon, W.; Mendell, M. J.; Gaffin, J. M.; Wang, G.; Phipatanakul, W., *Environ. Health Perspect.* **2015**, 123, 6–20.

[6] Wayne, R. P.; Barnes, I.; Biggs, P.; Burrows, J. P.; Canosa-Mas, C. E.; Hjorth, J.; Le Bras, G.; Moortgat, G. K.; Perner, D.; Poulet, G.; Restelli, G.; Sidebottom, H., *Atmos. Environ. Part A.* **1991**, 25, 1–203.

[7] Chameides, W. L.; Kasibhatla, P. S.; Yienger, J.; Levy, H., *Science* **1994**, 264, 74–77.

[8] Kramlich, J.; Linak, W., *Prog. Energy. Combust. Sci* **1994**, 20, 149–202.

[9] Chorkendorff, I.; Niemantsverdriet, J., *Concepts of Modern Catalysis and Kinetics*, Wiley VCH, **2007**.

[10] Ban-Weiss, G. A.; Chen, J.; Buchholz, B. A.; Dibble, R. W., *Fuel Process. Technol.* **2007**, 88 (7), 659 – 667.

[11] European Commission on Integrated Pollution Prevention and Control, *Reference Document on Best Available Techniques for Large Combustion Plants*, Technical report, IPPC, **2006**.

[12] Wise, H.; Frech, M. F., *J. Chem. Phys.* **1954**, 22, 1463–1464.

[13] Poole, D. R.; Graven, W. M., *J. Am. Chem. Soc.* **1961**, 83 (2), 283–286.

[14] Javed, M. T.; Irfan, N.; Gibbs, B., *J. Enviro. Manage.* **2007**, 83, 251 – 289.

[15] Meier, H.; Gut, G., *Chem. Eng. Sci.* **1978**, 33, 123 – 131.

[16] Takagi, M.; Kawai, T.; Suma, M.; Onishi, T.; Tamaru, K., *J. Catal.* **1977**, 50, 441–446.

[17] Bosch, H.; Janssen, F. J.; van den Kerkhof, F. M.; Oldenziel, J.; van Ommen, J. G.; Ross, J. R., *Appl. Catal.* **1986**, 25 (1), 239 – 248.

[18] Janssen, F. J. J. G.; Kerkhof, F. M. G. V. D.; Bosch, H.; Ross, J. R. H., *J. Phys. Chem* **1987**, 91, 6633–6638.

[19] Janssen, F. J. J. G.; Kerkhof, F. M. G. V. D.; Bosch, H.; Ross, J. R. H., *J. Phys. Chem* **1987**, 11, 5921–5927.

[20] Janssen, F.; Vogt, E.; van Dillen, A.; Geus, J., *Catal. Today* **1988**, 2, 569–579.

[21] Dumesic, J.; Topsøe, N.; Topsøe, H.; Chen, Y.; Slabiak, T., *J. Catal.* **1996**, 163, 409–417.

[22] Topsøe, N.; Dumesic, J.; Topsøe, H., *J. Catal.* **1995**, 151, 241–252.

[23] Topsøe, N.; Topsøe, H.; Dumesic, J., *J. Catal.* **1995**, 151, 226–240.

[24] Topsøe, N.-Y., *Science* **1994**, 265, 1217–1219.

[25] Choi, E.-Y.; Nam, I.-S.; Kim, Y. G., *J. Catal.* **1996**, 161, 597 – 604.

[26] Busca, G.; Lietti, L.; Ramis, G.; Berti, F., *Appl. Catal. B* **1998**, 18, 1–36.

[27] Seiyama, T.; Arakawa, T.; Matsuda, T.; Yamazoe, N.; Takita, Y., *Chem. Lett.* **1975**, (7), 781–784.

[28] Long, R.; Yang, R., *J. Catal.* **1999**, 188, 332 – 339.

[29] Eng, J.; Bartholomew, C. H., *J. Catal.* **1997**, 171, 14 – 26.

[30] Janssens, T. V. W.; Falsig, H.; Lundegaard, L. F.; Vennestr??m, P. N. R.; Rasmussen, S. B.; Moses, P. G.; Giordanino, F.; Borfecchia, E.; Lomachenko, K. A.; Lamberti, C.; Bordiga, S.; Godiksen, A.; Mossin, S.; Beato, P., *ACS Catal.* **2015**, (5), 2832–2845.

[31] Bru, T. C.; Przybylski, M.-D.; Balaji, S. P.; Keil, F. J., *J. Phys. Chem. C* **2010**, 6567–6587.

[32] Grossale, A.; Nova, I.; Tronconi, E.; Chatterjee, D.; Weibel, M., *J. Catal.* **2008**, 63, 492–531.

[33] Madia, G.; Koebel, M.; Elsener, M.; Wokaun, A., *Ind. Eng. Chem. Res.* **2002**, 41, 4008–4015.

[34] Marbán, G.; Antuña, R.; Fuertes, A. B., *Appl. Catal. B* **2003**, 41, 323–338.

[35] Peña, D. A.; Uphade, B. S.; Reddy, E. P.; Smirniotis, P. G., *J. Phys. Chem. B* **2004**, 9927–9936.

[36] Richter, M.; Eckelt, R.; Parlitz, B.; Fricke, R., *Appl. Catal. B* **1998**, 15, 129–146.

[37] Reddy, P.; Ettireddy, N.; Mamedov, S., *Appl. Catal. B* **2007**, 76, 123–134.

[38] Qi, G.; Yang, R. T., *J. Catal.* **2003**, 217, 434–441.

[39] Schill, L.; Putluru, S. S. R.; Jensen, A. D.; Fehrmann, R., *Catal. Commun.* **2014**, 56, 110 – 114.

[40] Schill, L.; Putluru, S.; Fehrmann, R.; Jensen, A., *Catal. Lett.* **2014**, 144, 395–402.

[41] Thirupathi, B.; Smirniotis, P. G., *Appl. Catal. B* **2011**, 110, 195 – 206.

[42] Thirupathi, B.; Smirniotis, P. G., *J. Catal.* **2012**, 288, 74–83.

[43] Chen, Z.; Yang, Q.; Li, H.; Li, X.; Wang, L.; Tsang, S. C., *J. Catal.* **2010**, 276, 56 – 65.

[44] Yang, S.; Qi, F.; Xiong, S.; Dang, H.; Liao, Y., *Appl. Catal. B* **2016**, 181, 570–580.

[45] Gottwald, U.; Monkhouse, P.; Wulgaris, N.; Bonn, B., *Fuel Process. Technol.* **2002**, 75, 215 – 226.

[46] Oleschko, H.; Schimrosczyk, A.; Lippert, H.; Müller, M., *Fuel* **2007**, 86 (15), 2275 – 2282.

[47] Wiles, C. C., *J. Hazard. Mater.* **1996**, 47, 325 – 344.

[48] Zheng, Y.; Jensen, A. D.; Johnsson, J. E., *Appl. Catal. B* **2005**, 60, 253 – 264.

[49] Sander, B., *Biomass Bioenergy* **1997**, 12 (3), 177–183.

[50] Nielsen, H.; Frandsen, F.; Dam-Johansen, K.; Baxter, L., *Prog. Energy Combust. Sci.* **2000**, 26, 283 – 298.

[51] Frandsen, F. J., *Fuel* **2005**, 84, 1277 – 1294.

[52] Yin, C.; Rosendahl, L. A.; Kær, S. K., *Prog. Energy Combust. Sci.* **2008**, 34, 725 – 754.

[53] Kong, M.; Liu, Q.; Jiang, L.; Guo, F.; Ren, S.; Yao, L.; Yang, J., *Catal. Commun.* **2016**, 85, 34–38.

[54] Nicosia, D.; Czekaj, I.; Kröcher, O., *Appl. Catal. B* **2008**, 77, 228–236.

[55] Kröcher, O.; Elsener, M., *Appl. Catal. B* **2008**, 77, 215 – 227.

[56] Amiridis, M. D.; Duevel, R. V.; Wachs, I. E., *Appl. Catal. B* **1999**, 20, 111 – 122.

[57] Klimczak, M.; Kern, P.; Heinzelmann, T.; Lucas, M.; Claus, P., *Appl. Catal. B* **2010**, 95 (1-2), 39–47.

[58] Zheng, Y.; Jensen, A. D.; Johnsson, J. E.; Thøgersen, J. R., *Appl. Catal. B* **2008**, 83, 186–194.

[59] Kling, Å.; Andersson, C.; Myringer, Å.; Eskilsson, D.; Järås, S. G., *Appl. Catal. B* **2007**, 69, 240 – 251.

[60] Calatayud, M.; Minot, C., *J. Phys. Chem. C* **2007**, 111, 6411–6417.

[61] Nicosia, D.; Elsener, M.; Kröcher, O.; Jansohn, P., *Top. Catal.* **2007**, 42, 333–336.

[62] Olsen, B. K.; Kügler, F.; Castellino, F.; Jensen, A. D., *Catal. Sci. Technol.* **2016**, 6, 2249–2260.

[63] Peng, Y.; Li, J.; Si, W.; Luo, J.; Wang, Y.; Fu, J.; Li, X.; Crittenden, J.; Hao, J., *Appl. Catal. B* **2015**, 168 - 169, 195 – 202.

[64] Jensen-Holm, H.; Castellino, F.; White, N., *SCR DeNOx catalyst considerations when using biomass in power generation*, Technical report, Haldor Topsøe A/S, Kgs. Lyngby, **2012**.

[65] Peng, Y.; Li, J.; Shi, W.; Xu, J.; Hao, J., *Environ. Sci. Technol.* **2012**, 46, 12623–12629.

[66] Putluru, S. S. R.; Riisager, A.; Fehrmann, R., *Appl. Catal. B* **2011**, 101, 183 – 188.

[67] Putluru, S. S. R.; Jensen, A. D.; Riisager, A.; Fehrmann, R., *Catal. Commun.* **2012**, 18, 41 – 46.

[68] Kristensen, S. B.; Kunov-Kruse, A. J.; Riisager, A.; Rasmussen, S.; Fehrmann, R., *J. Catal.* **2011**, 284, 60 – 67.

[69] Putluru, S. S. R.; Kristensen, S. B.; Due-Hansen, J.; Riisager, A.; Fehrmann, R., *Catalysis Today* **2012**, 184, 192 – 196.

[70] Putluru, S. S. R.; Riisager, A.; Fehrmann, R., *Appl. Catal. B* **2010**, 97, 333 – 339.

[71] Putluru, S. S. R.; Mossin, S.; Riisager, A.; Fehrmann, R., *Catalysis Today* **2011**, 176, 292 – 297.

[72] Putluru, S. S. R.; Jensen, A. D.; Riisager, A.; Fehrmann, R., *Catal. Sci. Technol.* **2011**, 1, 631–637.

[73] Brandenberger, S.; Krøcher, O.; Tissler, A.; Althoff, R., *Catalysis Reviews* **2008**, 50, 492–531.

[74] Weng, X.; Dai, X.; Zeng, Q.; Liu, Y.; Wu, Z., *J. Colloid Interface Sci.* **2016**, 461, 9 – 14.

[75] Putluru, S. S. R.; Schill, L.; Godiksen, A.; Poreddy, R.; Mossin, S.; Jensen, A. D.; Fehrmann, R., *Appl. Catal. B* **2016**, 183, 282 – 290.

[76] Gao, S.; Wang, P.; Yu, F.; Wang, H.; Wu, Z., *Catal. Sci. Technol.* **2016**, 6, 8148–8156.

[77] Weingärtner, H., *Angew. Chem. Int. Ed.* **2008**, 47, 654–670.

[78] Noda, A.; Bin, A.; Susan, H.; Kudo, K.; Mitsushima, S.; Hayamizu, K.; Watanabe, M., *J. Phys. Chem. B* **2003**, 107, 4024–4033.

[79] Broder, T. L.; Silvester, D. S.; Aldous, L.; Hardacre, C.; Compton, R. G., *J. Phys. Chem. B* **2007**, 111, 7778–7785.

[80] Walden, P., *Bull. Acad. Imper. Sci. (St. Petersburg)* **1914**, 1800.

[81] Plechkova, N. V.; Seddon, K. R., *Chem. Soc. Rev.* **2008**, 37, 123–150.

[82] Sugden, S.; Wilkins, H., *J. Chem. Soc.* **1928**, 1291–1298.

[83] Wilkes, J.; Zaworotko, M., *Chem. Commun.* **1992**, 965–967.

[84] Hurley, F. H.; Wier, T. P., *J. Electrochem. Soc.* **1951**, 98, 207–212.

[85] Welton, T., *Chem. Rev.* **1999**, 99, 2071–2083.

[86] Wasserscheid, P.; Keim, W., *Angew. Chem. Int. Ed.* **2000**, 39, 3772–3789.

[87] Mu, Z.; Liu, W.; Zhang, S.; Zhou, F., *Chem. Lett.* **2004**, 33, 524–525.

[88] Yu, G.; Zhao, D.; Wen, L.; Yang, S.; Chen, X., *AIChE J.* **2012**, 58, 49–53.

[89] Chauvin, Y.; Mussmann, L.; Olivier, H., *Angew. Chem. Int. Ed.* **1996**, 34, 2698–2700.

[90] Monteiro, A. L.; Zinn, F. K.; de Souza, R. F.; Dupont, J., *Tetrahedron: Asymmetry* **1997**, 8, 177 – 179.

[91] Zim, D.; de Souza, R. F.; Dupont, J.; Monteiro, A. L., *Tetrahedron Lett.* **1998**, 39, 7071 – 7074.

[92] Kaufmann, D.; Nouroozian, M.; Henze, H., *Synlett* **1996**, 33, 1091–1092.

[93] Boehm, V. P. W.; Herrmann, W. A., *Chem. Eur. J.* **2001**, 7, 4191–4197.

[94] Steinrück, H.-P.; Wasserscheid, P., *Catal. Lett.* **2015**, 145, 380–397.

[95] Blanchard, L.; Hancu, D.; Beckman, E.; Brennecke, J., *Nature* **1999**, 399, 28–29.

[96] Lei, Z.; Dai, C.; Chen, B., *Chem. Rev.* **2014**, 114, 1289–1326.

[97] Kiil, S.; Michelsen, M. L.; Dam-johansen, K., *Ind. Eng. Chem. Res.* **1998**, 37, 2792–2806.

[98] Anderson, J. L.; Dixon, J. K.; Maginn, E. J.; Brennecke, J. F., *J. Phys. Chem. B* **2006**, 110, 15059–62.

[99] Ma, X.; Kaneko, T.; Tashimo, T.; Yoshida, T.; Kato, K., *Chem. Eng. Sci.* **2000**, 55, 4643–4652.

[100] Huang, J.; Riisager, A.; Wasserscheid, P.; Fehrmann, R., *Chem. Commun.* **2006**, 38, 4027–9.

[101] Wu, W.; Han, B.; Gao, H.; Liu, Z.; Jiang, T.; Huang, J., *Angew. Chem. Int. Ed.* **2004**, 43, 2415–2417.

[102] Wang, C.; Cui, G.; Luo, X.; Xu, Y.; Li, H.; Dai, S., *J. Am. Chem. Soc.* **2011**, 133 (31), 11916–9.

[103] Anthony, J. L.; Anderson, J. L.; Maginn, E. J.; Brennecke, J. F., *J. Phys. Chem. B* **2005**, 109, 6366–6374.

[104] Kolding, H.; Fehrmann, R.; Riisager, A., *Sci. China Chem.* **2012**, 55, 1648–1656.

[105] An, D.; Wu, L.; Li, B.-G.; Zhu, S., *Macromolecules* **2007**, 40, 3388–3393.

[106] Berg, R. W.; Harris, P.; Riisager, A.; Fehrmann, R., *J. Phys. Chem. A* **2013**, 117, 11364–11373.

[107] Cammarata, L.; Kazarian, S. G.; Salter, P. a.; Welton, T., *Phys. Chem. Chem. Phys.* **2001**, 3, 5192–5200.

[108] Mele, A., *ChemInform* **2005**, 36, 2–17.

[109] Jin, M.; Hou, Y.; Wu, W.; Ren, S.; Tian, S.; Xiao, L.; Lei, Z., *J. Phys. Chem. B* **2011**, 115, 6585–6591.

[110] Murphy, L. J.; McPherson, A. M.; Robertson, K. N.; Clyburne, J. A. C., *Chem. Commun.* **2012**, 48, 1227–1229.

[111] Ren, S.; Hou, Y.; Wu, W.; Liu, Q.; Xiao, Y.; Chen, X., *J. Phys. Chem. B* **2010**, 114, 2175–2179.

[112] US Environmental Protection Agency, Sources of Greenhouse Gas Emissions, URL `https://www.epa.gov/ghgemissions/sources-greenhouse-gas-emissions`.

[113] Versteeg, G. F.; Swaaij, W. P. M., *Chem. Eng. Sci.* **1988**, 43, 573–585.

[114] Rochelle, G. T., *Science* **2009**, 325, 1652–1654.

[115] D'Alessandro, D.; Smit, B.; Long, J., *Angew. Chem. Int. Ed.* **2010**, 49, 6058–6082.

[116] Aki, S.; Mellein, B. R.; Saurer, E. M.; Brennecke, J. F., *J. Phys. Chem. B* **2004**, 108, 20355–20365.

[117] Carvalho, P.; Kurnia, K.; Coutinho, J., *Phys. Chem. Chem. Phys.* **2016**, 18, 14757.

[118] Brennecke, J. F.; Gurkan, B. E., *J. Phys. Chem. Lett.* **2010**, 1, 3459–3464.

[119] Gurkan, B. E.; de la Fuente, J. C.; Mindrup, E. M.; Ficke, L. E.; Goodrich, B. F.; Price, E. A.; Schneider, W. F.; Brennecke, J. F., *J. Am. Chem. Soc* **2010**, 132, 2116–2117.

[120] Bates, E. D.; Mayton, R. D.; Ntai, I.; Davis, J. H., *J. Am. Chem. Soc* **2002**, 124, 926–927.

[121] Shiflett, M.; Kasprzak, D.; Junk, C.; Yokozeki, A., *J. Chem. Thermodyn.* **2008**, 40, 25.

[122] Gurau, G.; Rodriguez, H.; Kelley, S. P.; Janiczek, P.; Kalb, R. S.; Rogers, R. D., *Angew. Chem. Int. Ed.* **2011**, 50, 12024–12026.

[123] Muldoon, M. J.; Aki, S. N. V. K.; Anderson, J. L.; Dixon, J. K.; Brennecke, J. F., *J. Phys. Chem. B* **2007**, 111 (30), 9001–9009.

[124] Sarmad, S.; Mikkola, J.-p.; Ji, X., *ChemSusChem* **2017**, 10, 324–352.

[125] Thomassen, P.; Riisager, A.; Kunov-Kruse, A. J.; Mossin, S.; Kolding, H.; Kegnaes, S.; Fehrmann, R., *ECS Trans.* **2012**, 50, 433–442.

[126] Kolding, H.; Thomassen, P.; Mossin, S.; Riisager, A.; Rogez, J.; Mikaelian, G.; Fehrmann, R., *ECS Trans.* **2014**, 64, 97–108.

[127] Stevanovic, S.; Podgorsek, A.; Padua, A. A. H.; Costa Gomes, M. F., *J. Phys. Chem. B* **2012**, 116, 14416–14425.

[128] Shunmugavel, S.; Kegnæs, S.; Due-Hansen, J.; Gretasdottir, T. A.; Riisager, A.; Fehrmann, R., *ECS Trans.* **2010**, 33, 117–126.

[129] Duan, E.; Guo, B.; Zhang, D.; Shi, L.; Sun, H.; Wang, Y.; Duan, E.; Guo, B.; Zhang, D.; Shi, L., *J. Air Waste Manag. Assoc.* **2011**, 61, 1393–1397.

[130] Chen, K.; Shi, G.; Zhou, X.; Li, H.; Wang, C., *Angew. Chemie Int. ed.* **2016**, 55, 14364–14368.

[131] Kunov-Kruse, A. J.; Thomassen, P. L.; Riisager, A.; Mossin, S.; Fehrmann, R., *Chem. - A Eur. J.* **2016**, 22, 11745–11755.

[132] Goldstein, S.; Czapski, G., *J. Am. Chem. Soc.* **1995**, 117, 12078–12084.

[133] Thiemann, M.; Scheibler, E.; Wiegand, K. W., *Nitric Acid , Nitrous Acid , and Nitrogen Oxides*, Ullmann's Encyclopedia of Industrial Chemistry, 7th ed, **2012**.

[134] Duan, E.; Guo, B.; Zhang, D.; Shi, L.; Sun, H.; Wang, Y., *J. Air Waste Manage. Assoc.* **2011**, 61, 1393–1397.

[135] Mélen, F.; Herman, M., *J. Phys. Chem. Ref. Data* **1992**, 21, 831–881.

[136] He, M.; Wang, Y.; Forssberg, E., *Int. J. Miner. Process.* **2006**, 78, 63–77.

[137] Mehnert, C. P.; Cook, R. A.; Dispenziere, N. C.; Afeworki, M., *J. Am. Chem. Soc.* **2002**, 124, 12932–12933.

[138] Riisager, A.; Wasserscheid, P.; Hal, R. v.; Fehrmann, R., *J. Catal.* **2003**, 219, 452–455.

[139] Jakuttis, M.; Schönweiz, A.; Werner, S.; Franke, R.; Wiese, K. D.; Haumann, M.; Wasserscheid, P., *Angew. Chem. Int. Ed.* **2011**, 50, 4492–4495.

[140] García-Verdugo, E.; Altava, B.; Burguete, M. I.; Lozano, P.; Luis, S. V., *Green Chem.* **2015**, 17, 2693–2713.

[141] Werner, S.; Szesni, N.; Kaiser, M.; Fischer, R. W.; Haumann, M.; Wasserscheid, P., *ChemCatChem* **2010**, 2, 1399–1402.

[142] ROMEO Project Website, `http://www.romeo-h2020.eu/project-presentation/demonstration-plants/`, accessed on: 07-05-2017.

[143] Zhang, Z.; Wu, L.; Dong, J.; Li, B.-g.; Zhu, S., *Ind. Eng. Chem. Res.* **2009**, 48, 2142–2148.

[144] Li, X.; Zhang, L.; Zheng, Y.; Zheng, C., *Energy & Fuels* **2015**, 29, 942–953.

[145] Karousos, D. S.; Vangeli, O. C.; Athanasekou, C. P.; Sapalidis, A. A.; Kouvelos, E. P.; Romanos, G. E.; Kanellopoulos, N. K., *Chem. Eng. J.* **2016**, 306, 146–154.

[146] Karousos, D. S.; Kouvelos, E.; Sapalidis, A.; Pohako-Esko, K.; Bahlmann, M.; Schulz, P. S.; Wasserscheid, P.; Siranidi, E.; Vangeli, O.; Falaras, P.; Kanellopoulos, N.; Romanos, G. E., *Ind. Eng. Chem. Res.* **2016**, 55, 5748–5762.

[147] Wang, Z.; Mitch, W. A., *Environ. Sci. Technol.* **2015**, 49, 11974–11981.

[148] Niedermaier, I.; Bahlmann, M.; Papp, C.; Kolbeck, C.; Wei, W.; Krick, S.; Grabau, M.; Schulz, P. S.; Wasserscheid, P.; Steinru, H.-p.; Maier, F., *J. Am. Chem. Soc.* **2014**, 136, 436–441.

[149] Davison, J., *Energy* **2007**, 32, 1163–1176.

[150] K. Veltman, B. Singh, E. H., *Environ. Technol.* **2010**, 44, 1496–1502.

[151] Reynolds, A. J.; Verheyen, T. V.; Adeloju, S. B.; Meuleman, E.; Feron, P., *Environ. Sci. Technol.* **2012**, 46, 3643–3654.

[152] Notz, R.; Tönnes, I.; McCann, N.; Scheffknecht, G.; Hasse, H., *Chem. Eng. Technol.* **2011**, 34, 163–172.

[153] Kolding, H., *Catalysis and selective gas absorption in ionic liquids*, Ph.D. thesis, Technical University of Denmark, **2015**.

[154] Romanos, G. E.; Schulz, P. S.; Bahlmann, M.; Wasserscheid, P.; Sapalidis, A.; Katsaros, F. K.; Athanasekou, C. P.; Beltsios, K.; Kanellopoulos, N. K., *J. Phys. Chem. C* **2014**, 118, 24437–24451.

[155] Pohako-Esko, K.; Bahlmann, M.; Schulz, P. S.; Wasserscheid, P., *Ind. Eng. Chem. Res.* **2016**, 55, 7052–7059.

[156] Abai, M.; Atkins, M. P.; Hassan, A.; Holbrey, J. D.; Kuah, Y.; Nockemann, P.; Oliferenko, A. a.; Plechkova, N. V.; Rafeen, S.; Rahman, A. a.; Ramli, R.; Shariff, S. M.; Seddon, K. R.; Srinivasan, G.; Zou, Y., *Dalt. Trans.* **2015**, 44, 8617–8624.

[157] Boada, R.; Cibin, G.; Coleman, F.; Diaz-Moreno, S.; Gianolio, D.; Hardacre, C.; Hayama, S.; Holbrey, J. D.; Ramli, R.; Seddon, K. R.; Srinivasan, G.; Swadźba-Kwaśny, M., *Dalt. Trans.* **2016**, 45, 18946–18953.

[158] Bair, W. H., *Astrophys. J.* **1920**, 52, 301–316.

[159] Sigmund, L., *Astrophys. J.* **1926**, 63, 73–89.

[160] Harris, L., *Proc. Natl. Acad. Sci.* **1928**, 690–694.

[161] Schneider, W.; Moortgat, G. K.; Tyndall, G. S.; Burrows, J. P., *J. Photochem. Photobiol. A Chem.* **1987**, 40 (2-3), 195–217.

[162] Galan-Fereres, M.; Alemany, L. J.; Mariscal, R.; Bañares, M. A.; Anderson, J. A.; Fierro, J. L. G., *Chem. Mater.* **1995**, 7, 1342–1348.

[163] Pârvulescu, V. I.; Grange, P.; Delmon, B., *Catal. Today* **1998**, 46, 233–316.

[164] Gandhi, H.; Graham, G. W.; McCabe, R. W., *J. Catal.* **2003**, 216, 433–442.

[165] Lemus, J.; Palomar, J.; Gilarranz, M. A.; Rodriguez, J. J., *Adsorption* **2011**, 17, 561–571.

[166] Thomassen, P.; Madsen, A.; Fehrmann, R.; Riisager, A.; Mossin, S.; Kunov-Kruse, A., Patent, no:WO2015158849, *Combined Oxidation and Absorption of NO_x by an Ionic Liquid Tandem Process*, **2015**.

[167] Qiao, Z.-a.; Huo, Q.; Chi, M.; Veith, G. M.; Binder, A. J.; Dai, S., *Adv. Mater.* **2012**, 24, 6017–6021.

[168] Qiao, Z.-A.; Zhang, P.; Chai, S.-H.; Veith, G. M.; Gallega, N. C.; Kidder, M.; Dai, S., *J. Am. Chem. Soc.* **2014**, 136, 11260–11263.

[169] Zhang, J.; Chai, S.-h.; Qiao, Z.-a.; Mahurin, S. M.; Chen, J.; Fang, Y.; Wan, S.; Nelson, K.; Zhang, P.; Dai, S., *Angew. Chemie Int. Ed.* **2015**, 54, 932–936.

[170] Burkhardt, E.; Lambert, C.; Patel, C., *Science* **1975**, 188, 1111–1113.

[171] Goldsmith, P.; Tuck, A. F.; Foot, J. S.; Simmons, E. L.; Newson, R. L., *Nature* **1973**, 244, 545–551.

[172] Murcray, D.; Kyle, T.; Murcray, F. H.; Williams, W., *Nature* **1968**, 218, 78–79.

[173] Finlayson-pitts, B. J.; Saliba, N.; Wingen, L.; Barney, W.; Mochida, M.; Yang, H., *The Formation of Gaseous Nitrous Acid (Hono): A Key Determinant of Tropospheric Ozone and Fine Particles*, Technical Report 97, California Environmental Protection Agency, **2001**.

[174] Niki, H.; Maker, P. D.; Savage, C. M.; Breitenbach, L. P., *J. Phys. Chem.* **1978**, 82, 135–137.

[175] Fox, D.; Kamens, R.; Jeffries, H., *Science* **1975**, 188, 1113–1114.

[176] Bodenstein, M., *Zeitschrift für Angew. Chemie* **1918**, 1, 145–148.

[177] Tsukahara, H.; Ishida, T.; Mayumi, M., *Nitric Oxide* **1999**, 3, 191–198.

[178] Hisatsune, I. C.; Zafonte, L., *J. Phys. Chem.* **1969**, 73, 2980–2989.

[179] Tsukahara, H.; Ishida, T.; Todoroki, Y.; Hiraoka, M.; Mayumi, M., *Free Radic. Res.* **2003**, 37, 171–177.

[180] Casapu, M.; Kroecher, O.; Elsener, M., *Appl. Catal. B* **2009**, 88, 413–419.

[181] Koebel, M.; Elsener, M.; Madia, G., *Ind. Eng. Chem. Res.* **2001**, 40, 52–59.

[182] Koebel, M.; Madia, G.; Elsener, M., *Catal. Today* **2002**, 73, 239–247.

[183] Nova, I.; Ciardelli, C.; Tronconi, E.; Chatterjee, D.; Bandl-konrad, B., *Catal. Today* **2006**, 114, 3–12.

[184] Jeong, Y. E.; Anil, P.; Danh, K.; Huong, T.; Phil, H., *Top. Catal.* **2017**, Preprint.

[185] Atribak, I.; Guillen-Hurtado, N.; Bueno-Lopez, A.; Garcia-Garcia, A., *Appl. Surf. Sci.* **2010**, 256, 7706–7712.

[186] Xue, E.; Seshan, K.; Ommen, J. G. V.; Ross, J. R. H., *Appl. Catal. B* **1993**, 2, 183–197.

[187] Takahashi, N.; Shinjoh, H.; Iijima, T.; Suzuki, T.; Yamazaki, K.; Yokota, K.; Suzuki, H.; Miyoshi, N.; Matsumoto, S.-i.; Tanizawa, T.; Tanaka, T.; Tateishi, S.-s.; Kasahara, K., *Catal. Today* **1996**, 27, 63–69.

[188] Kašpar, J.; Fornasiero, P.; Hickey, N., *Catal. Today* **2003**, 77, 419–449.

[189] Burch, R.; Watling, T. C., *J. Catal.* **1997**, 169, 45–54.

[190] Mulla, S. S.; Chen, N.; Cumaranatunge, L.; Blau, G. E.; Zemlyanov, D. Y.; Delgass, W. N.; Epling, W. S.; Ribeiro, F. H., *J. Catal.* **2006**, 241, 389–399.

[191] Xue, E.; Seshan, K.; Ross, J. R. H., *Appl. Catal. B* **1996**, 11, 65–79.

[192] Schießer, W.; Vinek, H.; Jentys, A., *Catal. Lett.* **1998**, 56, 189–194.

[193] Després, J.; Elsener, M.; Koebel, M.; Kröcher, O.; Schnyder, B.; Wokaun, A., *Appl. Catal. B* **2004**, 50, 73–82.

[194] Kaspar, J.; Fornasiero, P.; Graziani, M., *Catal. Today* **1999**, 50, 285–298.

[195] Crocoll, M.; Kureti, S.; Weisweiler, W., *J. Catal.* **2005**, 229, 480–489.

[196] Olsson, L.; Westerberg, B.; Persson, H.; Fridell, E.; Skoglundh, M.; Andersson, B., *J. Phys. Chem. B* **1999**, 103, 10433–10439.

[197] Irfan, M. F.; Goo, J. H.; Kim, S. D., *Environmentalist* **2011**, 31 (1), 4–10.

[198] Fernández, J. L.; Raghuveer, V.; Manthiram, A.; Bard, A. J., *J. Am. Chem. Soc.* **2005**, 127, 13100–13101.

[199] Giménez-Mañogil, J.; Bueno-López, A.; García-García, A., *Appl. Catal. B* **2014**, 99–107.

[200] Shiba, K.; Hinode, H.; Wakihara, M., *React. Kinet. Catal. Lett.* **1996**, 58, 133–137.

[201] Cai, W.; Zhong, Q.; Zhao, W., *Chem. Eng. J.* **2014**, 246 (x), 328–336.

[202] Ren, Z.; Guo, Y.; Zhang, Z.; Liu, C.; Gao, P.-X., *J. Mater. Chem. A* **2013**, 1, 9897–9906.

[203] Davis, M. E., *Nature* **2002**, 417, 813–821.

[204] Pérez-Ramírez, J.; Christensen, C. H.; Egeblad, K.; Christensen, C. H.; Groen, J. C., *Chem. Soc. Rev.* **2008**, 37, 2530–2542.

[205] Jen, H. W.; Graham, G. W., *Catal. Lett.* **2006**, 108, 21–23.

[206] Halasz, I.; Brenner, A.; Simon, K. Y., *Catal. Lett.* **1995**, 34, 151–161.

[207] Artioli, N.; Lobo, R. F.; Iglesia, E., *J. Phys. Chem. C* **2013**, 117, 20666–20674.

[208] Loiland, J. A.; Lobo, R. F., *J. Catal.* **2014**, 311, 412–423.

[209] Loiland, J. A.; Lobo, R. F., *J. Catal.* **2015**, 325, 68–78.

[210] Zhang, Z.; Atkinson, J. D.; Jiang, B.; Rood, M. J.; Yan, Z., *Appl. Catal. B* **2015**, 163, 573–583.

[211] Mochida, I.; Kisamori, S.; Hironaka, M.; Kawano, S.; Matsumura, Y.; Yoshikawa, M., *Energy and Fuels* **1994**, 8, 1341–1344.

[212] Kircher, O.; Hougen, O. A., *AIChE J.* **1957**, 3 (3), 331–335.

[213] Mochida, I.; Kawabuchi, Y.; Kawano, S.; Matsumura, Y.; Yoshikawa, M., *Fuel* **1997**, 76, 543–548.

[214] Guo, Z.; Xie, Y.; Hong, I.; Kim, J., *Energy Convers. Manag.* **2001**, 42, 2005–2018.

[215] Zhang, W.; Rabiei, S.; Bagreev, a.; Zhuang, M.; Rasouli, F., *Appl. Catal. B* **2008**, 83, 63–71.

[216] Zhang, Z.; Atkinson, J. D.; Jiang, B.; Rood, M. J.; Yan, Z., *Appl. Catal. B* **2014**, 149, 573–581.

[217] Sousa, J. P. S.; Pereira, M. F. R.; Figueiredo, J. L., *Appl. Catal. B* **2012**, 125, 398–408.

[218] Atkinson, J. D.; Zhang, Z.; Yan, Z.; Rood, M. J., *Carbon* **2013**, 54, 444 – 453.

[219] Ghafari, M.; Atkinson, J. D., *Environ. Sci. Technol.* **2016**, 50, 5189–5196.

[220] Dow Chemical Product Data Sheet for V493 Polymer Beads, `http://msdssearch.dow.com/PublishedLiteratureDOWCOM/dh{_}0988/0901b803809885d2.pdf?filepath=liquidseps/pdfs/noreg/177-01505.pdf{&}fromPage=GetDoc`, accessed on: 29-04-2017.

[221] Liu, Y. X.; Zhang, J., *Ind. Eng. Chem. Res.* **2011**, 50, 3836–3841.

[222] Dam-Johansen, K. H.; Kim; Department, *Environ. Prog.* **1993**, 12, 300–305.

[223] Hjuler, K.; Glarborg, P.; Dam-johansen, K., *Ind. Eng. Chem. Res.* **1995**, 34, 1882–1888.

[224] B. Cleaver and E. Rhodes and A. Ubbelohde, j. . P. p. . . t. . S. v. . . y. . ., file = :C\:/Users/pett/Desktop/PhD Papers/important_HNO3_Paper.pdf:pdf .

[225] Johnston, H.; Graham, R., *J. Phys. Chem.* **1972**, 77, 62–63.

[226] Biaume, F., *J. Photochem.* **1973**, 2, 139–149.

[227] Bongartz, A.; Kames, J.; Welter, F.; Schurath, U., *J. Phys. Chem.* **1991**, 95, 1076–1082.

[228] Gratien, A.; Lefort, M.; Picquet-Varrault, B.; Orphal, J.; Doussin, J. F.; Flaud, J. M., *J. Quant. Spectrosc. Radiat. Transf.* **2009**, 110, 256–263.

[229] Kinugawa, T.; Enami, S.; Yabushita, A.; Kawasaki, M.; Hoffmann, M. R.; Colussi, A. J., *Phys. Chem. Chem. Phys.* **2011**, 13, 5144–9.

[230] Mochida, M.; Finlayson-pitts, B. J., *J. Phys. Chem. A* **2000**, 104, 9705–9711.

[231] Mochida, M.; Finlayson-Pitts, B., *J. Phys. Chem. A* **2000**, 104, 8038–8044.

Appendix A

Supplementary Experimental Data

A.1 NO and NO_2 Fitted Standard Curves

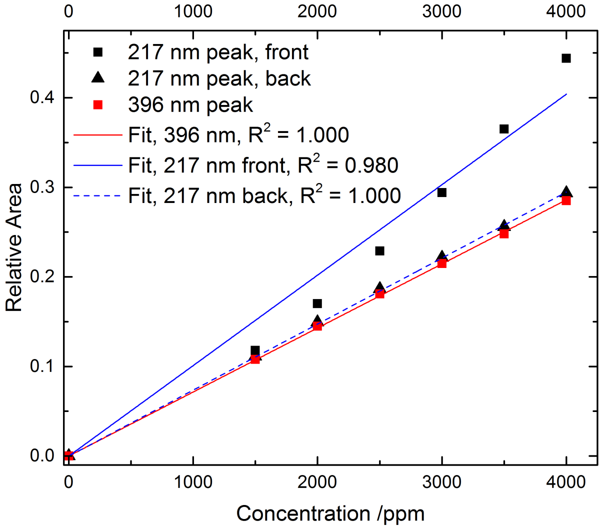

Figure A.1: Normalised area of 217 nm peak (black) and 396 nm peak (red) of NO_2 as a function of concentration. Gaussian fits were performed on the front part of the curve (squares) and the back (triangles) for the 217 nm peak. Excellent linearity was obtained by fitting the front of the 396 nm peak.
The deviation from linearity observed for the NO_2 areas is caused by the formation of N_2O_4, which would not be present had the experiments been performed under wet conditions.

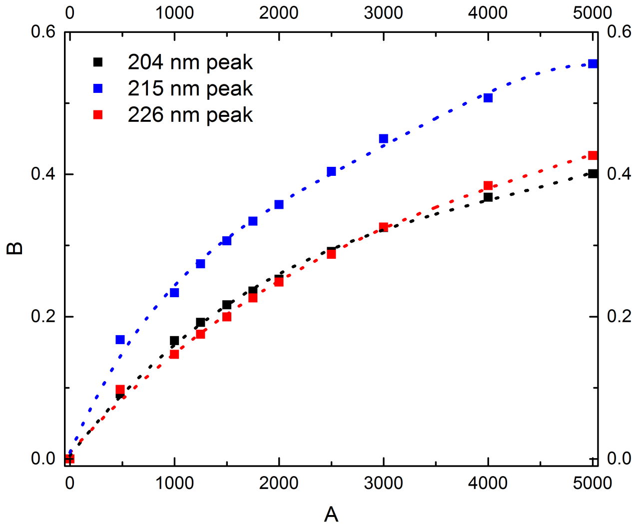

Figure A.2: Normalised area of the three NO peaks at 204 nm (black), 215 nm (blue) and 226 nm (red). Polynomial fits (third order for the 204 and 226 nm peaks and fourth order for the 215 peak) for each set of the three data sets are shown as dotted lines in the respective colours.
It can be seen that 226 nm peak shows a behaviour closest to linearity, while the 204 nm peak has the lowest deviation from the fitted curve. All NO quantification is based on the 204 nm peak due to the full understanding of the behaviour, as well as the reproducibility.

A.2 NO_2 Breakthrough Experiment

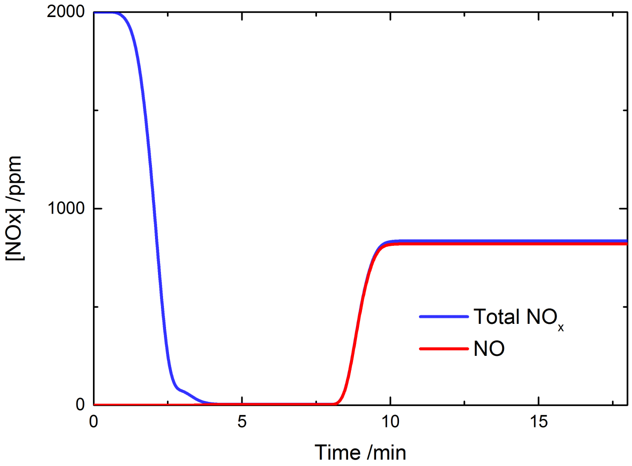

Figure A.3: Breakthrough curves for NO_2, as shown in NO concentration and total NO_x. It is noted that after passing the reactor, most NO_2 has been reduced to NO. It is believed that the small difference between NO and total NO_x is due to autoxidation in the reactor after breakthrough.

A.3 Titration Curve for [BMIM][NO_3]

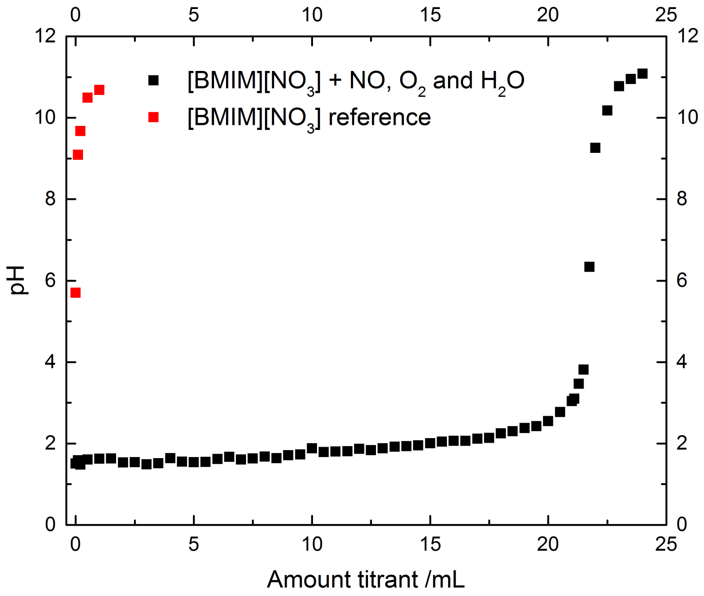

Figure A.4: Titration curves for [BMIM][NO_3] during titration with a 0.010 M NaOH solution. Titration of a reference sample (red) and of a sample that had been exposed to a gas containing NO, O_2, H_2O and balance N_2 for 6 hours. The titration curve is consistent with titration of a strong acid, and the equivalence point based on pH measurements was found to be 21.75 mL. This was exactly the same when titration was performed with methylred as acid/base indicator. The pH measurements were tedious and since the same results were obtained with a regular indicator, this method was used going forward.
It is worth noting that there is no apparent presence of HNO_2 despite the water used for dissolution was degassed. The sample was, however, exposed to the air for an extended period of time during measurements, suggesting any HNO_2 present would likely have been oxidised anyway.

A.4 Reference UV-Vis Spectrum of Mixed NO_x Species

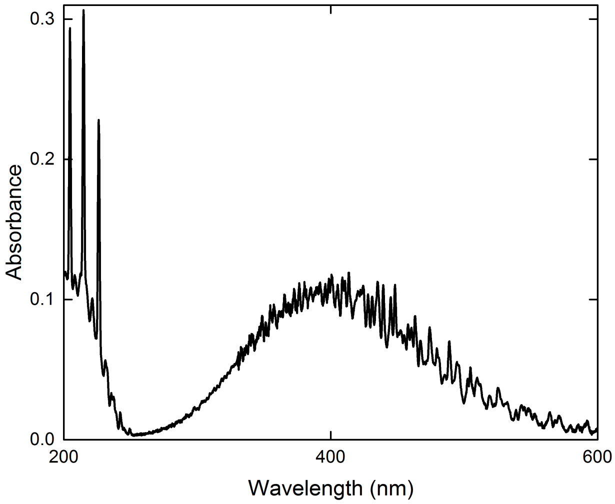

Figure A.5: Reference spectrum of NO and NO_2, both at 1500 ppm, with balance N_2.

A.5 TGA Data at 130 °C for [BMIM][NO$_3$] SILP on Silica Gel 100

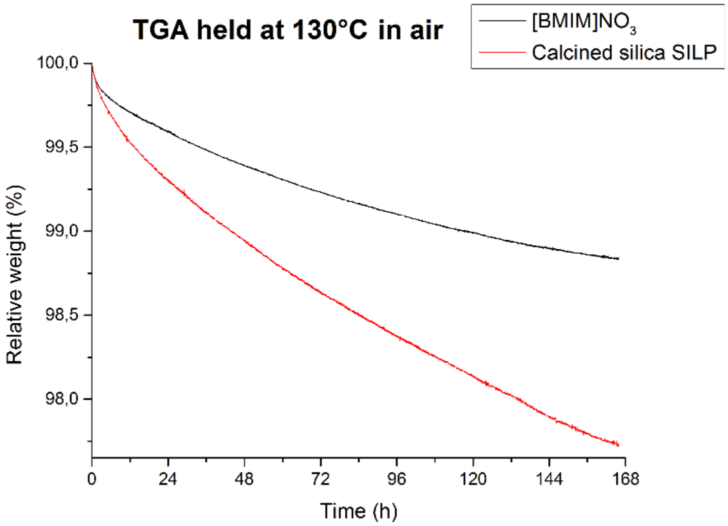

Figure A.6: Thermogravimetric analysis of SILP and neat IL at 130 °C in air. The weight percentage of water in the neat IL is around 1.2 wt% and this is believed to be the reason for the decrease in weight. The same is expected for the silica SILP, only the weight percentage of water is likely much higher, due to the hydrophilic nature of the silica support.

A.6 Aqueous HNO_2 UV-Vis Data

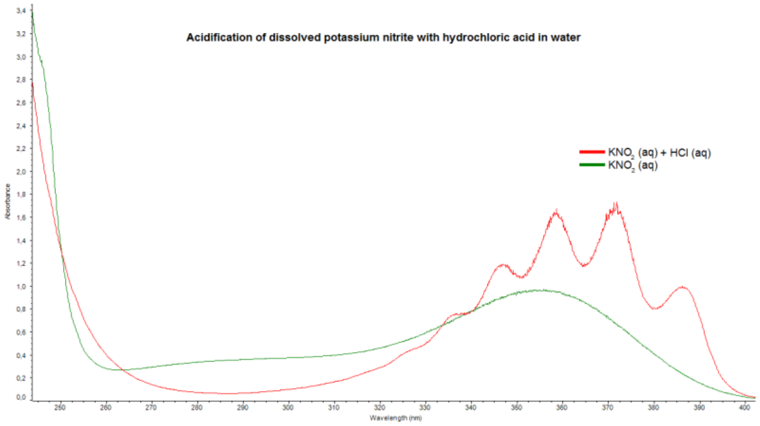

Figure A.7: UV-Vis spectra of acidification of KNO_2 to form HNO_2.

A.7 Temperature Dependence of NO Oxidation over SILP Materials

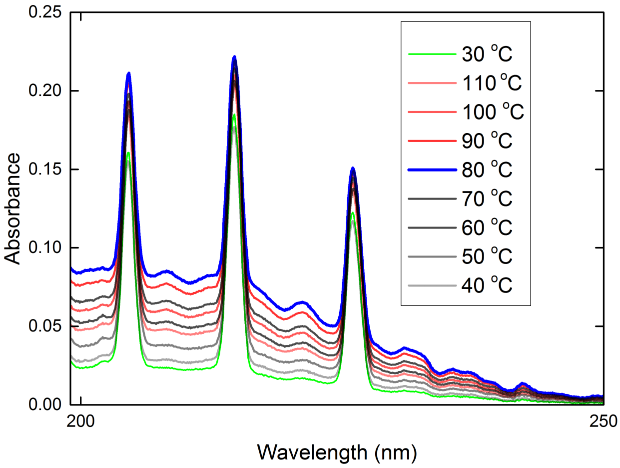

Figure A.8: UV-Vis spectra obtained after exposing a silica gel 100 SILP (30 % v/v [BMIM][NO_3]) to a gas containing 2000 ppm NO, 16% O_2, 2% H_2O and balance N_2 at temperatures from 30 °C to 130 °C. A small increase in NO_2 concentration is observed, with an optimal temperature observed around 80 °C. At this temperature, the NO conversion is around 10%.

A.8 Experimental Procedures for One-Pot Synthesis of [N_{6666}]Br in HS and Synthesis of PolyIonic Liquids in HS support

Experimental procedure for VBIM NTf_2 IL

First, 1-bromobutane (6.85 g) is added to a pre cooled round bottomed flask (50 mL) situated in an ice bath. Then, Argon is bubbled through the solvent for 20 min, to degas. Afterwards, 1-vinylimidazole is added to the 1-bromobutane and Ar is bubbled through the cooled mixture for another 10 min.

After degassing the gas nozzle was raised above the level of the mixture, the round bottomed flask was removed from the ice bath and the reaction was continued at room temperature. Laboratory film was placed loosely over the flask, while the Ar flow was maintained to secure an inert atmosphere. The solution was left for 24h to fully react, yielding a light brown, viscous liquid. The resulting liquid was washed five times with diethyl ether. Each wash significantly increased the viscosity of the liquid, one final subsequent wash with ethylacetate was performed, further increasing the viscosity to somewhere in between honey and tar.

Anion exchange: Prior to polymerisation of the IL, the bromide anion was exchanged for NTf2 (bis-(triflouromethanesulfon)imide). The anion exchanged was carried out by dissolving 1.25 equimolar amount of LiNTf2 in water (8.036 g in 20 mL). The ionic liquid from above was also readily dissolved in water (10 mL) in the same 50mL flask that was used for synthesis. The LiNTf2 solution was then added dropwise to the IL solution, under stirring, at room temperature. After one or two drops the otherwise clear solution turned pale and unclear. After a short while, a brownish liquid started precipitating at the bottom of the flask. After addition of the LiNTf2 solution, the mixture was left overnight to fully react.

Synthesis of VIM- Bu-VIM crosslinker

10.80g of 1,4-dibromobutane and 9.41g VIM, corresponding to 1:2 ratio, was added to a 125mL round bottomed flask, together with 60mL of methanol. The literature describes using a reactor at 60oC and running the reaction for 15 hours. As there was no reactor immediately available, the reaction was done under reflux, at 60oC instead.

Upon cooling, the reaction mixture was added dropwise to 500mL of diethyl ether, turning the ether milky white as fine particles were formed. An attempt was made to separate the particles from the ether through filtration, however unsuccessful. Then, the full amount of ether was evaporated using a rotavap at room temperature and 30mbar pressure, yielding a clear, slightly viscous liquid.

Polymerisation of ILs in HS (No crosslinker)

Solvent (either water (15g) or ether and THF (12g and 0.70g respectively)) is added to 1.00g of HS support in a 50mL round bottomed flask. 0.50g of VBIM Br was added to the solution and the solution was stirred for 1 hour at room temperature. After this, 50mg of recrystallized AIBN was added to the solution and the stirring was continued for 3 hours, before applying vacuum. The solvent was evaporated over a long period of time (several hours). The resulting, fine white powder is transferred to an autoclave under inert atmosphere (argon). The autoclave was then left in the oven at 120 deg C overnight. No significant difference in polymerisation was observed when comparing a 12h experiment to a 24h experiment, thus, leaving it overnight should be sufficient to complete polymerisation.

In the case of using water as the solvent, the powder after evaporation showed a slight discolouring (pinkish).

The fine white powder was transferred to an autoclave under argon atmosphere. The autoclave was then left in an oven at 120oC overnight. The fine white powder turned light brown. After cooling down, the light brown powder was transferred to a glass container in air. It was also analysed using both ATR-FTIR and TGA. In both cases it should have had more than enough time to equilibrate with moisture in the air prior to analysis. This is of relevance because it appears that the polymerised samples have significantly lower amount of moisture compared to the sample prior to polymerisation.

Polymerisation of ILs in HS (with crosslinker)

Polymerisation of IL with the crosslinker was largely carried out as described above; 1.07g of HS support was added to a 50mL round bottomed flask together with 0.47g of [VBIM]Br and solvent (13.0 g of ether, 0.78g THF). The solution was left to stir for 1 hour at room temperature, before adding the crosslinker (0.049g) and AIBN. After addition of the chemicals, the flask was submersed in an ice bath and stirred for an additional hour, after which a low amount of vacuum was applied to slowly remove the solvent over several hours, yielding a fine white powder which was treated as described above.

Attempted one pot synthesis of [N_{6666}]Br in HS

N,N-dihexylamine (4.634 g) was added to a solution of 1-bromohexane (8.621 g), together with 10 g of HS support. The solution was cooled in an icebath. N,Ndihexylamine was added in a ratio slightly below equimolar amounts since 1-bromohexane is easier to remove by evaporation. The solution was kept in the icebath for 5 hours before it was slowly heated to room temperature. Reaction was continued at room temperature for 7 days. After 7 days, the temperature was increased step wise to 120oC over 4 days, and the reaction was run at 120oC for 5 additional days. The development in the IR spectrum was followed continuously throughout, with few changes. The resulting liquid after 14 days was viscous and black.

A.9 Synthesis of Poly Ionic Liquids in Hollow Sphere Silica

As was mentioned in Chapter 5, hollow sphere silica (HS) shows great promise as a support material for several different applications.

Some poly ionic liquids (polyIL) have been mentioned as possible membrane materials for gas separation and as solid ionic conductors. The mechanical strength of polyILs is not high enough for practical application, at least for some of these suggested uses. Therefore, supporting the polyILs in the HS materials should allow for retention of the important membrane characteristics, while allowing for shaping of a solid membrane with high mechanical stability.

In this work, the primary objective was two things: One was to test if synthesis of polyILs inside the HS was possible, and the other was to utilise the charged polymeric network for anion substitution of metal-containing anions, with the purpose of reducing them later to form metal nano-particles.

The polyIL was synthesised as described in Appendix A.8 and the degree of polymerisation was investigated by ATR-FTIR. The synthesis was performed through radical initiation using azobisisobutyronitrile (AIBN), on a 1-vinyl-3-butylimidazole ([VBIM]) based IL. The first attempt used [VBIM][NTf$_2$] and showed little to no polymerisation based on the C=C double bond FTIR band at 1660 cm^{-1}.

In the two other attempts, polymerisation was done using [VBIM]Br or 90 wt% [VBIM]Br in conjunction with 10 wt% crosslinker (N,N'-butyldiimidazole). The ATR-FTIR spectral data for the two polyIL synthesis are shown in Figures A.9 and A.10.

From Figures A.9 and A.10 it is seen that a significant degree of polymerisation is

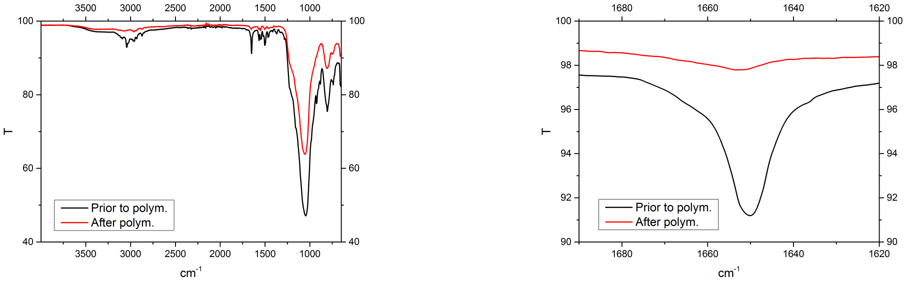

(a) ATR-FTIR data of the HS prior to and after absorption.

(b) Zoom of the spectral area relevant for the C=C band.

Figure A.9: ATR-FTIR data obtained from the synthesis of [VBIM]Br polyIL in HS, the black spectrum was obtained prior to polymerisation, the red was obtained after polymerisation. Based on deconvolution of the 1660 cm^{-1} band, the degree of polymerisation was found to be around 90-95%.

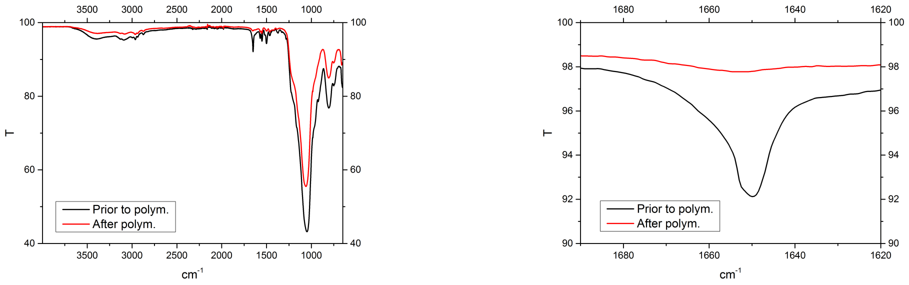

(a) ATR-FTIR data of the HS prior to and after absorption.

(b) Zoom of the spectral area relevant for the C=C band.

Figure A.10: ATR-FTIR data obtained from the synthesis of [VBIM]Br polyIL in HS, with addition of 10 wt% crosslinker. The black spectrum was obtained prior to polymerisation, the red was obtained after polymerisation. Based on deconvolution of the 1660 cm^{-1} band, the degree of polymerisation was found to be around 95-98%.

observed for both compounds. Due to uncertainty between ATR-FTIR samples and deconvolution, the error of reported data is approximately 5 percentage points.
The polyIL in HS samples were analysed through thermogravimetric analysis (TGA) in order to determine the thermal stability. TGA was performed both in air and in Ar, with little difference. Furthermore, it was found that the polyIL had a slightly higher decomposition temperature than the sample prior to polymerisation. TGA data is shown in Figure A.11. From Figure A.11 it is seen that both polyIL materials

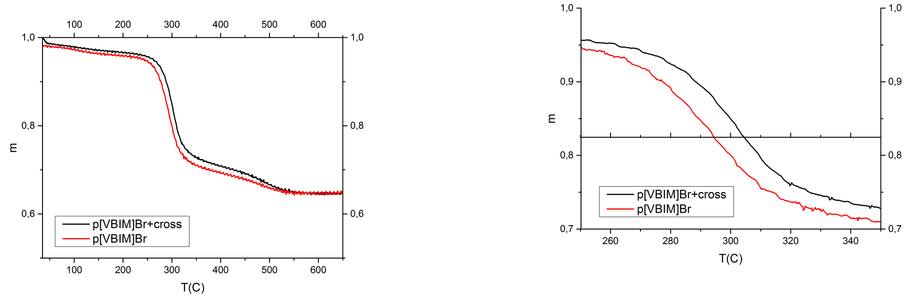

(a) Full TGA

(b) Zoom of TGA around decomposition point.

Figure A.11: TGA analysis of HS samples with and without crosslinker incorporated in the polyIL.

have a high thermal stability. It appears the crosslinked polyIL has a slightly higher decomposition temperature than the one without crosslinker, suggesting that it either has a higher degree of polymerisation or that the crosslinked polymer has a higher thermal stability.

Incorporation and Reduction of Gold-Containing Anion

Previously in this work (Chapter 6), it was briefly described that sintering of metal nano-particle catalysts can cause deactivation and poor metal utilisation. A possible way to avoid this sintering is to encapsulate the metal nano-particles in a support and thus not allowing them to interact with eachother.

Most of the metal precursors used to synthesise metal nano-particles are anionic, such as tetrachloroaurate ($[AuCl_4]^-$). Therefore, it should be possible to incorporate these metal-containing anions into the cationic polyIL framework.

In order to investigate whether this type of anion substitution was possible, an aqueous solution of chloroauric acid ($H[AuCl_4]$) was prepared corresponding to a 1.2 wt% loading of the crosslinked polyIL-HS. The crosslinked polyIL-HS was then added to the solution and stirred for 1 hour. The polyIL-HS was then filtered off and dried. After drying, the polyIL-HS had changed colour from white to orange, strongly suggesting incorporation of gold into the polyIL-HS.

The dried Au-polyIL-HS was then transferred to a crucible and reduced by exposing it to a 10% H_2 in N_2 gas mixture at 150 °C for 10 hours. After reduction, the Au-polyIL-HS had changed colour to purple. Transmission electron microscopy (TEM) images were then recorded, these are shown in Figure A.12. From Figure A.12 it is

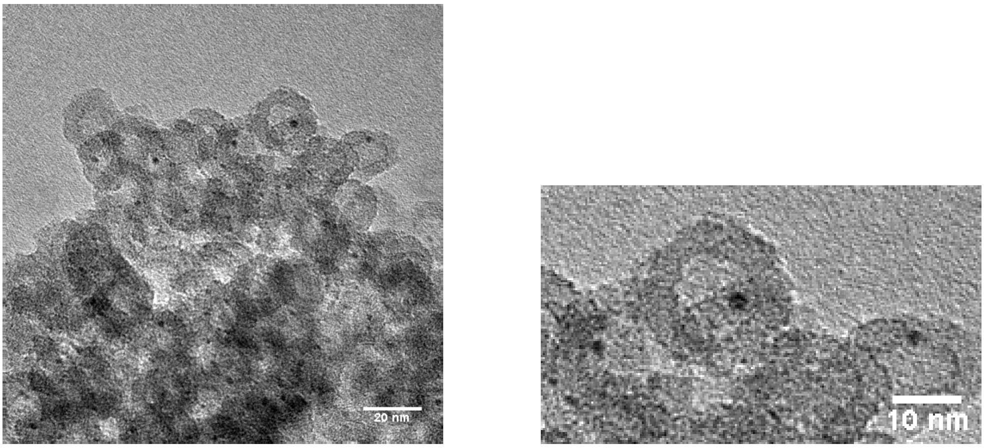

(a) Full scale TEM.

(b) Zoom of left image.

Figure A.12: TEM image of polyIL-HS after tetrachloroaurate anion exchange with bromide and subsequent reduction in H_2.

seen that gold nano-particles (AuNP) have formed in the HS material. Upon further inspection, it appears that the AuNP are uniform in size and that all are formed inside the HS shells. Based on over 50 measurements of the AuNP, the size of the AuNP is 1.5-2 nm. The narrow size distribution strongly suggests that the anion substitution is uniform. Furthermore, the placement of the AuNP inside the spheres strongly suggests that all the polyIL is formed inside the HS support material. Both of these observations are encouraging and suggests that metal nano-particle catalysts can be synthesised based on the HS-support.

Unfortunately, time has not allowed for catalytic testing of the synthesised HS-AuNP. It is expected that the HS-AuNP is highly sinter-stable, but this has not yet been confirmed experimentally. Furthermore it will be interesting to see if the HS-AuNP show any catalytic activity and if so, also to see if the expected size selectivity of the HS can be utilised.

APPENDIX B

Technical Schematics, Drawings and Pictures

B.1 Post Combustion Emission Control Schematics

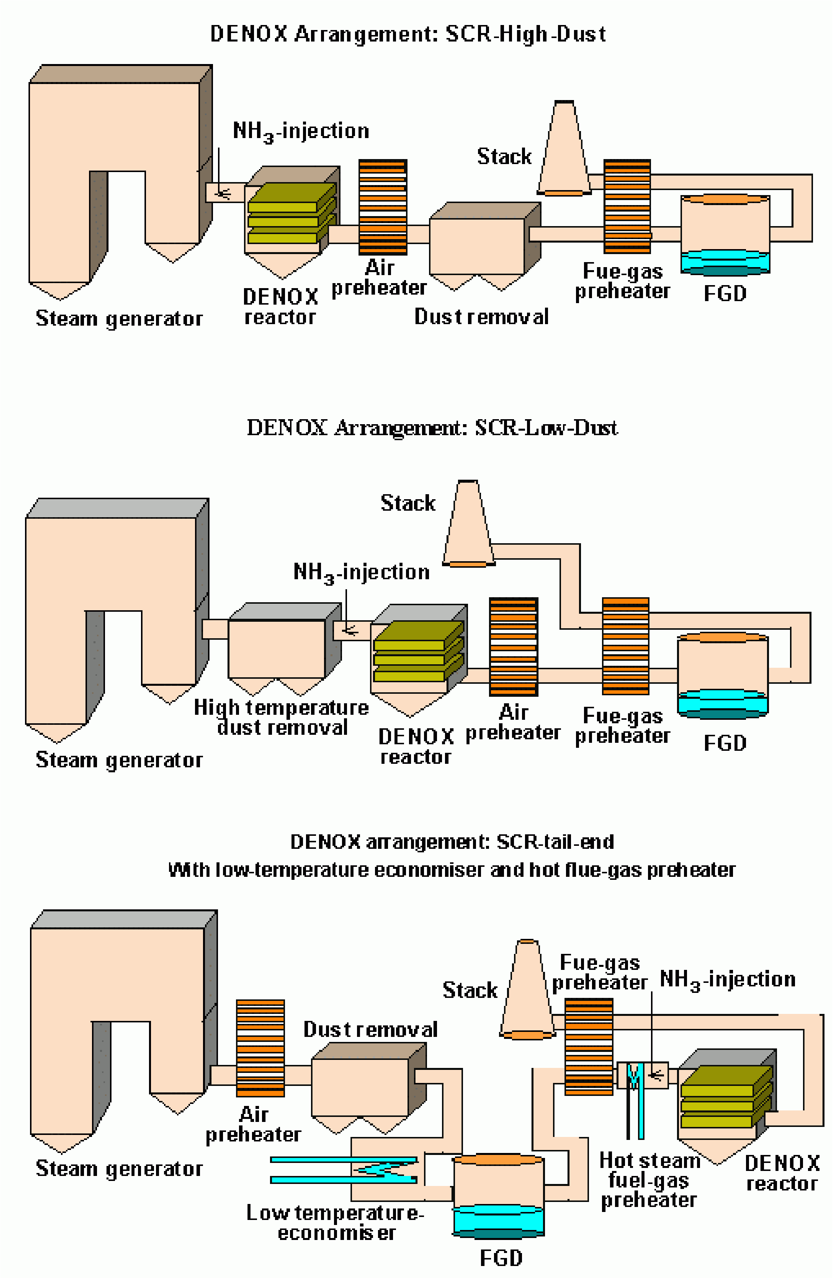

Figure B.1: Schematic overview of the three most common emission control layouts in stationary plants.

B.2 Suggested Design for Rotating Filter

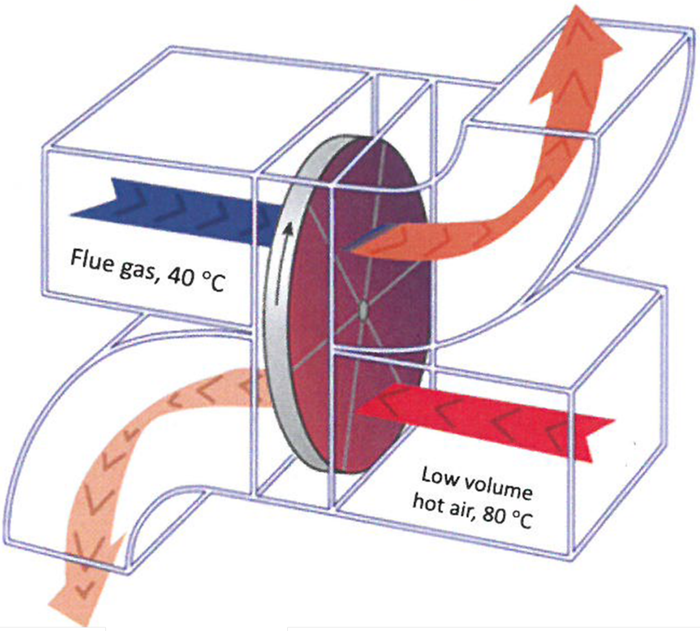

Figure B.2: Suggested design of a rotating filter, temperatures are expected to vary from the suggested in the final installation

B.3 Pictures of SILP and IL Reactors for Gravimetric Absorption

(a) IL reactor

(b) SILP reactor

Figure B.3: Pictures of the reactors used for the gravimetric uptake experiments.

APPENDIX C

Peer-Reviewed Journal Publications

C.1 Absorption and Oxidation of Nitrogen Oxide in Ionic Liquids

A. J. Kunov-Kruse, P. Thomassen, A. Riisager, S. Mossin* and Rasmus Fehrmann*

Chemistry - A European Journal, **2016**, 22, 11745-11755

ChemPubSoc Europe
DOI: 10.1002/chem.201601166
CHEMISTRY
A European Journal
Full Paper

Ionic Liquids

Absorption and Oxidation of Nitrogen Oxide in Ionic Liquids

Andreas J. Kunov-Kruse, Peter L. Thomassen, Anders Riisager, Susanne Mossin,* and Rasmus Fehrmann*[a]

Abstract: A new strategy for capturing nitrogen oxide, NO, from the gas phase is presented. Dilute NO gas is removed from the gas phase by ionic liquids under ambient conditions. The nitrate anion of the ionic liquid catalyzes the oxidation of NO to nitric acid by atmospheric oxygen in the presence of water. The nitric acid is absorbed in the ionic liquid up to approximately one mole HNO_3 per mole of the ionic liquid due to the formation of hydrogen bonds. The nitric acid can be desorbed by heating, thereby regenerating the ionic liquid with excellent reproducibility. Here, time-resolved in-situ spectroscopic investigations of the reaction and products are presented. The procedure reveals a new vision for removing the pollutant NO by absorption into a non-volatile liquid and converting it into a useful bulk chemical, that is, HNO_3.

Introduction

The man-made emission of NO_x (N_2O, NO, NO_2) is of environmental concern because NO_x participates in detrimental photochemical reactions in both the troposphere and the stratosphere.[1] NO_x reacts with hydrocarbon-containing pollutants to form health-threatening smog in densely populated areas, as well as being active in depleting the ozone layer. The end product, that is, NO_2, contributes to acid rain. To remove the NO_x from flue gases, ammonia or hydrocarbons are generally used as reductants in the excellently performing selective catalytic reduction (SCR) reaction. This technology is, however, not attractive for specialized applications, for example, for NO_x removal on ships or in biomass fired and co-fired power plants, where an end-of-pipe cleaning technology is preferred.

The unique properties of ionic liquids (ILs) include high thermal stability, practically no vapor pressure, and a large electrochemical window.[2–5] Recent research has focused on the use of ILs for selective absorption of acidic gases such as CO_2 and SO_2.[6–9] In addition a recent comprehensive review on gas solubilities in ILs concerns not only CO_2 and SO_2 but also reports on all other gases known to solubilize in ILs.[10] It is remarkable that no data on NO solubilities in ILs are reported so far. SO_2 capture by ILs is suggested to depend on the association of SO_2 with the anion of the IL.[7] This has later been confirmed by X-ray investigations of crystalline [TMGH]Cl·SO_2 (TMGH = 1,1,3,3-tetramethylguanidinium).[11] CO_2 capture by ILs similarly depends on the association between the CO_2 molecule and the anion.[8] The bonds formed are often relatively weak and therefore, the gas can be easily expelled from the IL in a regeneration step. Water is inevitably present in a flue gas and because water also interacts with the anion of the IL,[12] water is a likely inhibitor in both cases. Oxygen from the flue gas may also interfere with the absorption.[13] Here, a different strategy to remove NO and NO_2 from a gas stream is proposed, where the water and oxygen present are actively utilized to chemically convert the NO_x into nitric acid, HNO_3, which then accumulates in the IL due to the formation of strong hydrogen bonds.[14]

The current work presents in-situ attenuated total reflectance Fourier transform infrared (ATR-FTIR) spectroscopic results of the interaction between a thin IL film and a combined gas stream containing dilute NO gas, atmospheric air, and water. From time-resolved experiments mechanistic evidence for the oxidation and absorption reactions as well as the stoichiometry of the absorption have been extracted. The accumulated HNO_3 can be desorbed by heating the IL above 120 °C. The IL is completely regenerated with no trace of decomposition products observed.

Results and Discussion

A thin film of an IL was monitored with ATR-FTIR spectroscopy during exposure to a controlled gas flow containing NO. A schematic of the setup is shown in Figure S1 in the Supporting Information. The influence of the cations and anions of the IL on the reactivity was also investigated. The employed cations are depicted in Scheme 1.

The characteristic IR bands observed and monitored during the reactions were: nitrate (NO_3^-): $\tilde{\nu} = 1340\ cm^{-1}$ (vs), nitric acid (HNO_3): $\tilde{\nu} = 948$ (s), $1660\ cm^{-1}$ (s); water (H_2O): $\tilde{\nu} = 3400$ (s), $1640\ cm^{-1}$ (s); dinitrogen tetroxide (N_2O_4): $\tilde{\nu} = 1858$ (w), 1750

---

[a] Dr. A. J. Kunov-Kruse, MSc. P. L. Thomassen, Assoc. Prof. A. Riisager, Assoc. Prof. S. Mossin, Prof. R. Fehrmann
Centre for Catalysis and Sustainable Chemistry, Department of Chemistry, Technical University of Denmark, DK-2800 Kgs. Lyngby (Denmark)
E-mail: slmo@kemi.dtu.dk
rf@kemi.dtu.dk

Supporting information for this article is available on the WWW under http://dx.doi.org/10.1002/chem.201601166.

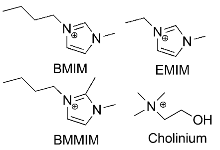

Scheme 1. IL cations used in this work. BMIM = 1-butyl-3-methylimidazolium, EMIM = 1-ethyl-3-methylimidazolium, BMMIM = 1-butyl-2,3-dimethylimidazolium, cholinium (Ch) = *N*-(2-hydroxyethyl)-*N*,*N*,*N*-trimethylammonium.

(vs), 750 cm^{-1} (w); acetate (CH_3COO^-): $\tilde{\nu} = 1550$ cm^{-1} (vs); and acetic acid (CH_3COOH): $\tilde{\nu} = 1710$ cm^{-1} (vs).[15,16] The bands corresponding to the IL cations do not change significantly during the experiments.[17]

According to calculation, the nitric acid band at $\tilde{\nu} = 948$ cm^{-1} corresponds to the symmetric O-N-O bend. The experiments are in agreement with this because the band does not shift when the water in the gas stream is exchanged with D_2O. The other characteristic peak for HNO_3 at $\tilde{\nu} = 1660$ cm^{-1} shifts to $\tilde{\nu} = 1610$ cm^{-1} with deuterium substitution (Scheme 2).

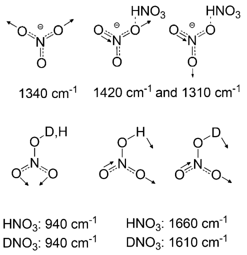

Scheme 2. Top) Assigned IR modes of NO_3^-, HNO_3, and their complexes. Assignment based on calculated frequencies of NO_3^-, $NO_3^- \cdots HNO_3$, and HNO_3. The analogous modes of DNO_3 were assigned by observation of the red shift of lines in the experimental spectra. Calculations were performed by using the B3LYP functional and the 6-31G(d,p) basis set in Gaussian 09.[18]

In-situ ATR-FTIR experiments

[BMIM][NO$_3$]

A thin film of [BMIM][NO$_3$] was applied to the diamond surface of the IR cell and exposed to a gas stream containing different concentrations of NO (1–6% v/v) in combination with O_2 (8–18% v/v), water (≈1% v/v), and balance N_2 at different temperatures. When applied, the IL forms a thin film on the diamond, thereby minimizing mass transfer limitations. Thus, the experiment is envisioned as a model for the interaction between the gas phase and a supported ionic liquid phase (SILP) material.[19]

The IR spectra obtained for the 2% v/v NO experiments at room temperature are shown in Figure 1. The characteristic very intense band at approximately $\tilde{\nu} = 1340$ cm^{-1} of the nitrate ion immediately decreases in intensity as acidic protons become available (see Scheme 2). Additionally, the nitrate band splits as less symmetric hydrogen-bonded species are generated, giving bands at $\tilde{\nu} = 1426$, 1330, 1295, and 1250 cm^{-1}, see Figure 1. Similarly, within twenty seconds of gas exposure the characteristic bands of the solvated HNO_3 molecule at $\tilde{\nu} = 940$ and 1660 cm^{-1} increase in intensity. An isosbestic point is clearly observed at $\tilde{\nu} = 1400$ cm^{-1}. Another isosbestic point at $\tilde{\nu} = 1300$ cm^{-1} is less well defined due to weak intensity bands from HONO at $\tilde{\nu} = 1260$ and 1290 cm^{-1}. The presence of isosbestic points confirms that essentially only two forms of the nitrate ion exist in the solution, that is, free as in pure [BMIM][NO$_3$] and in a strong hydrogen bond with HNO_3. A reference experiment was performed in order to assess whether the reaction proceeds without O_2. No reaction was observed when [BMIM][NO$_3$] was first left to equilibrate with the atmosphere and then exposed to NO (10% v/v) for 80 min (Figure S2 in the Supporting Information). Therefore, the disproportionation of NO and the presence of a NO_2 impurity in the gas stream are both dismissed as the reason for the observed activity. A control experiment with dry NO and O_2 on a dry IL film was also performed and we could determine that the reaction was indeed slower when water was the limiting factor. The only source for the protons in the observed HNO_3 was water present either in the IL or in the gas phase and no other type of reactivity was observed in experiments with NO gas. If NO, O_2, and H_2O are all present, the characteristic HNO_3 bands appear within minutes of exposure of the IL film to the gas mixture. Thus it was concluded that HNO_3 is only formed when all three components are present simultaneously.

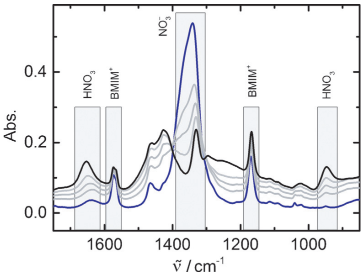

Figure 1. ATR-FTIR spectra of [BMIM][NO$_3$] exposed to a gas stream containing NO (2% v/v), O_2 (16% v/v), and water (≈1% v/v) at RT. The blue line corresponds to the spectrum of the pure IL exposed to air saturated with water and the black line to the steady-state spectrum obtained after 15 min gas exposure. Intermediate spectra are indicated with gray lines. The most intense identifiable bands are indicated.

[BMIM][CH$_3$COO]

The experiment performed using [BMIM][CH$_3$COO] is shown in Figure 2. Initially, a prominent water band at $\tilde{\nu} = 3400$ cm^{-1} (not shown) was present because [BMIM][CH$_3$COO] is hygroscopic and has a significant content of water when in equilibrium with the atmosphere. It was eroded quickly as the reaction progressed. The prominent acetate bands at $\tilde{\nu} = 1570$ and

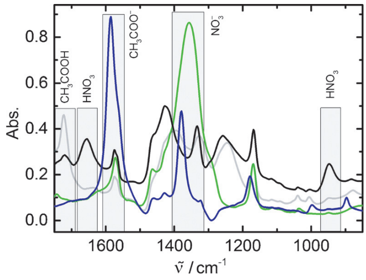

Figure 2. ATR-FTIR spectra of [BMIM][CH_3COO] exposed to a gas stream containing NO (6% v/v), O_2 (8% v/v), and water (≈1% v/v) at RT. The blue line corresponds to the spectrum of the pure IL exposed to air saturated with water, whereas the gray and black lines correspond to the spectra recorded after 7 and 12 min gas exposure, respectively. The green line corresponds to the spectrum recorded after heating to 120 °C and subsequent cooling to RT.

1380 cm^{-1} disappeared within a few minutes, whereas a band from acetic acid concurrently appeared at $\tilde{\nu} = 1710$ cm^{-1}. After longer time of exposure, the HNO_3 bands appeared and bands corresponding to both acids co-existed. After gas exposure for more than five minutes (or after gentle heating to 80 °C) the acetic acid was lost, as indicated by the disappearance of the bands assignable to both acetate and acetic acid. Hence, only the bands from nitric acid and hydrogen-bonded nitrate remained. When heated to 120 °C the nitric acid bands were finally also completely lost, and the resulting spectrum features the characteristic nitrate band at $\tilde{\nu} = 1340$ cm^{-1} corresponding to the spectrum of pure [BMIM][NO_3]. The minor differences were assigned to the different water content of the ILs. Desorption is gradual and most of the nitric acid is desorbed before 120 °C. Interestingly, the temperature of complete desorption corresponds to the boiling temperature of the azeotrope of nitric acid and water (b.p. 121 °C),[20] whereas pure nitric acid boils at 83 °C. On the other hand, water and acetic acid (b.p. 118 °C) do not form an azeotrope and the complete loss of acetic acid was accordingly observed at significantly lower temperatures.

[BMIM]Cl

A similar experiment for [BMIM]Cl is shown in Figure 3. Here, the bands from the cation are more readily identified. The final spectrum obtained after exposure to NO, O_2, and H_2O was identical to the spectrum recorded in the [BMIM][NO_3] experiments. The absence of isosbestic points, however, indicates the formation of an intermediate. The strong band at $\tilde{\nu} = 1360$ cm^{-1} identifies the intermediate as a non-hydrogen-bonding nitrate anion (see below).

[EMIM][CF_3SO_3]

[EMIM][CF_3SO_3] was investigated in the same setup (Figure 4). The oxidation reaction forming HNO_3 was observed, but at a slower rate compared to the nitrate- and chloride-based ILs.

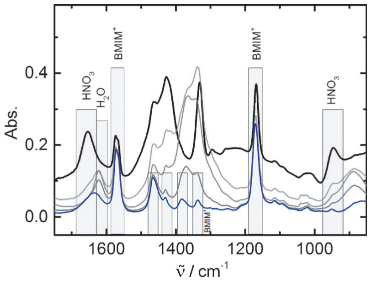

Figure 3. ATR-FTIR spectra of [BMIM]Cl exposed to a gas stream containing NO (6% v/v), O_2 (8% v/v), and water (≈1% v/v) at RT. The blue line corresponds to the spectrum of the pure IL exposed to air saturated with water, the gray lines correspond to the spectra recorded after 2, 3, and 4 min of gas exposure. The black line corresponds to the spectrum at steady state after 6 min of gas exposure.

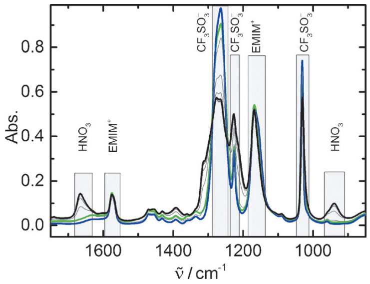

Figure 4. ATR-FTIR spectra of [EMIM][CF_3SO_3] exposed to a gas stream containing NO (6% v/v), O_2 (8% v/v), and water (≈1% v/v) at RT. The blue line corresponds to the spectrum of the pure IL, the black line corresponds to the spectrum of the saturated IL at steady state (17 min), and the gray lines correspond to intermediate spectra. The green line corresponds to the spectrum after heating to 120 °C and subsequent cooling to RT.

Notably, the strong bands from nitrate were not observed after desorption, whereas the strong bands originating from the triflate ion were observed throughout the experiment. The latter bands only changed moderately after accumulation of HNO_3 in the IL, suggesting that hydrogen bonding of HNO_3 to the anion was present but less pronounced than observed in the experiments with the nitrate IL. Hence, the strong triflate band centered at $\tilde{\nu} = 1270$ cm^{-1} (asymmetric S=O stretch) lost intensity and became broadened when HNO_3 was present but regained intensity after desorption.

[BMMIM][NO_3]

The C2-position of the IL imidazolium ring can be deprotonated when the anion of the IL is a strong base, and the formed carbene has been shown to be reactive towards CO_2.[21] In order to discard an analogous reaction path in the current study, IR experiments were also performed with [BMMIM][NO_3] having a methyl group at the C2-position of the imidazolium ring. The obtained spectral results (Figure S3 in the Supporting Information) were identical to the results for [BMIM][NO_3], validating that the carbene reaction path is not relevant. Hence, all experimental results suggested that the [BMIM]$^+$ ion does not partake in the reaction. The non-involvement of the cation was further confirmed in experiments performed with acetate- and nitrate-based ILs containing the cheap, biodegradable, and non-toxic cholinium cation (Scheme 1). The results are shown in Figures S4 and S5 in the Supporting Information and are analogous to the ones for imidazolium ILs with the same anion.

[BMIM][NO_3] and NO_2

By using dry NO_2 gas instead of NO the experiment with [BMIM][NO_3] was repeated (Figure 5). NO_2 was willingly absorbed in the IL and dimerized in the condensed phase, giving characteristic bands from N_2O_4 at $\tilde{\nu}=1858$ (w), 1750 (vs), and 750 cm^{-1} (w).[22] Bands from HONO and HNO_3 were also prominent after absorption, indicating disproportionation of N_2O_4 in the presence of water in the IL. When the gas feed was changed to dinitrogen saturated with water, the bands specific for N_2O_4 decreased immediately and the characteristic HNO_3 bands increased.

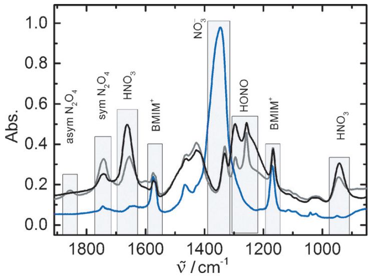

Figure 5. ATR-FTIR spectra of [BMIM][NO_3] exposed to a gas stream containing NO_2 at RT. The blue line corresponds to the spectrum of the pure IL exposed to air saturated with water, the gray line corresponds to the spectrum recorded after NO_2 exposure for 3 min, and the black line belongs to the spectrum recorded after subsequent 30 s of exposure to N_2 saturated with water.

Quantification of HNO_3

A standard curve for the determination of the HNO_3 concentration in the IL was generated by measuring IR spectra of solutions prepared by dissolving known amounts of concentrated nitric acid in [BMIM][NO_3] at RT (Figure S6 in the Supporting Information). Either of the HNO_3 bands at $\tilde{\nu}=1660$ and 948 cm^{-1} can be used to quantify the amount of HNO_3 present in the IL, but because a water band overlaps with the former band, the results obtained by using the latter were more reliable and reproducible. Importantly, all conclusions are equally valid from quantification of the $\tilde{\nu}=1660$ cm^{-1} band. The IR spectrum in the vicinity of the characteristic HNO_3 vibrations at $\tilde{\nu}=948$ cm^{-1} were deconvoluted by Gaussian functions, by using the method described previously.[23] The area under the Gaussian function fitted to the $\tilde{\nu}=948$ cm^{-1} band in the experimental spectrum can be correlated to the HNO_3 content by the use of the standard curve. The uncertainty of the total HNO_3 content determined by this method is estimated to be 10–20% based on the quality of the reference spectra and the fitting procedure.

The fitting procedure was applied to all time-resolved spectra at RT of [BMIM][NO_3], [EMIM][CF_3SO_3], [BMIM]Cl, [Ch][CH_3COO] as well as [BMMIM][NO_3] when exposed to NO (6% v/v) with O_2 and water in excess. The results are shown in Figure 6. For the cholinium-based ILs, IR bands from the cation are overlapping with the quantifiable HNO_3 bands. By careful use of the peak deconvolution method, reliable data were obtained. The steady-state saturation point approximately corresponds to a molar ratio of 1.1:1 (HNO_3/IL) for the acetate, chloride, and nitrate ILs, whereas the triflate IL converges at a ratio of approximately 0.6. The apparent difference in the absorption rate observed between [BMIM][NO_3] and [BMMIM][NO_3] was due to a difference in the absorption setup and is not considered to be significant. The time-resolved spectra of [BMIM][NO_3] were measured with an improved setup allowing the IL to be exposed to the $NO/O_2/H_2O$ mixture exactly at $t=0$, whereas the switch for the other ILs was dependent on replacement of a non-negligible volume of gas before the ATR cell, resulting in a concentration gradient during the first minutes of the experiment. Accordingly, the time line has been shifted 20 s to partially correct for this. All experiments performed under identical conditions support the conclusion that the cation does not influence the rate of absorption or the obtained molar ratio of HNO_3 to IL.

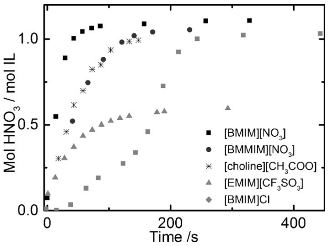

Figure 6. Integrated area of the $\tilde{\nu}=948$ cm^{-1} HNO_3 band as a function of the exposure time to a gas stream containing NO (6% v/v), O_2 (8% v/v), and water (≈1% v/v) at RT. The area is converted to mole ratios by using the standard curve obtained from Figure S6 in the Supporting Information. The experiment with [BMIM][NO_3] was performed with the gas above the IL changing immediately to the target composition. All the other experiments were performed with a more gradual change of the gas flow.

The IL anion, on the other hand, is decisive for the evolution of the spectra. The acetate IL shows conversion of NO to HNO_3

as fast as the nitrate IL, whereas the triflate IL shows a slower conversion. The slow rate of accumulation of HNO_3 in [BMIM][CF_3SO_3] is assigned to triflate being less nucleophilic towards activation of NO. Evaluation of the IR spectra of the IL suggests that HNO_3 forms hydrogen bonds to other HNO_3 molecules, weak hydrogen bonds to the oxygen atoms in the triflate ion, and no hydrogen bonds to the fluorine atoms, which are very poor hydrogen-bond acceptors. Triflate is the ion of a stronger acid than HNO_3 and is not protonated during the reaction.

Notably, the chloride IL has a significantly different overall profile with an initial induction period followed by first a slow and then a fast HNO_3 formation rate, before converging to almost the same molar HNO_3/IL ratio as the nitrate ILs. The difference is assigned to chloride being a stronger base than nitrate in ILs,[24] making strong bonds to protons. The water content of [BMIM]Cl in equilibrium with the atmosphere was determined by Karl-Fischer titration to be 5% w/w, which corresponds to a molar ratio of about 1:2 for H_2O to Cl^-. This is much higher than for any of the other ILs used ($\approx$1% w/w H_2O for [BMIM][NO_3]).

After the first minutes of gas exposure some water was likely driven out of the liquid and the reaction also consumed water resulting in the $\tilde{\nu} = 3400\ cm^{-1}$ water band decreasing fast. All protons generated in the reaction became bound to chloride leaving no protons to generate HNO_3. Accordingly, a relatively narrow band corresponding to non-hydrogen-bonded nitrate appears in Figure 3 in the time interval corresponding to 50–150 s in Figure 6 and the apparent rate of the HNO_3 generation is lower. After 150 s the rate of HNO_3 formation in [BMIM]Cl increases sharply to the same value as for [BMIM][CH_3COO], [BMIM][NO_3], [Ch][NO_3], and [BMMIM][NO_3] and the band of the non-hydrogen-bonded nitrate disappears.

The rate of accumulation of nitric acid in the IL is very dependent on the NO concentration as well as the temperature. [BMIM][NO_3] was saturated with HNO_3 at room temperature after 50 s when exposed to 6% v/v NO, excess O_2, and water. With 1% v/v NO it took 3000 s. In the in-situ ATR-IR experiments the maximal linear rate of increase in intensity of the HNO_3 band was determined. The experiment was performed multiple times with different NO concentrations at RT and the measured rates are plotted in Figure 7, top. From these experiments an apparent order of the reaction with respect to NO was determined to be 2.0 ($\pm$0.3).

Once the IL is saturated with HNO_3, the reaction cannot be followed further with IR spectroscopy performed on the IL film, but the reaction between NO and HNO_3 is likely to continue although at a significantly lower rate. The IL provides a sticky surface where NO from the gas phase can react with HNO_3 giving NO_2 and HNO_2, which are liberated to the gas stream if the IL is locally saturated. However, the liberated species might be absorbed further downstream.

The absorption of NO by the ILs is very temperature-dependent giving rise to a decrease in the absorption capacities with increasing temperature (Figure 7, bottom). The solubility of gases in ILs generally decreases with increasing temperature.[25] We expect the same to be the case for NO, NO_2, and O_2. On the other hand, the rate of NO oxidation is expected to increase with temperature. Due to the two competing effects it was not possible to generate an Arrhenius plot for the total reaction based on the experiments described here. The overall maximum rate was observed around 30 °C. We assume that the rate of the NO oxidation reaction is limiting the overall rate below this temperature and that the solubility of the reactants in the IL determines the overall rate above this temperature.

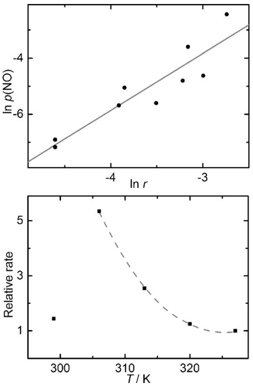

Figure 7. Top) Double logarithmic plot of maximal linear rates of HNO_3 formation (r) in [BMIM][NO_3] at RT with excess water and oxygen as function of partial pressure of NO in the gas phase. Bottom) Relative rate of HNO_3 formation in [BMIM][NO_3] with 2% v/v NO with excess water and oxygen at different temperatures. A dotted line is added as a guide to the eye. Rates are determined as the maximal linear rate of the change in intensity of the $\tilde{\nu} = 948\ cm^{-1}$ band in the in-situ ATR-FTIR spectra.

Bulk experiments

Absorption followed by gravimetric analysis

Absorption of NO in [BMIM][CH_3COO] and [BMIM][NO_3] was performed by passing the gas slowly through bulk ILs ($\approx$1 g) in two types of experiments. The gas uptake was followed gravimetrically. Series 1 was performed with 10% v/v NO in N_2 bubbling through [BMIM][CH_3COO] at 100 °C for about ten days to obtain steady state. The resulting solution was allowed to cool to RT under continuous gas exposure. $t = 0$ was chosen as the point when the temperature of the solution was at RT. The solution was left with time to equilibrate. After several days a new steady state had been reached (Figure 8). Oxygen and water was not deliberately added in this experiment, because it was originally intended as a pure NO absorption experiment. Series 2 is a reproduction of series 1 with a different batch of the IL. In series 3, pre-dried [BMIM][NO_3] was bubbled through with a gas stream of 5% v/v NO containing water and oxygen in excess (1 and 10% v/v, respectively). The weight was followed closely until steady state. Despite the difference in the conditions for series 1 and 2 compared to series 3 an identical weight increase compared to time $t = 0$ was found at steady state.

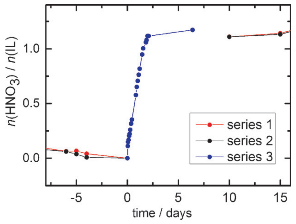

Figure 8. Increase in the mass of the bulk ILs as a function of the time by passing a gas through the IL through a sintered glass frit at RT. The gain of mass is assumed to be due to HNO_3 only and has been recalculated to a mole fraction of HNO_3 relative to the IL. In series 1 and 2 [BMIM][CH_3COO] was exposed to a gas flow of 10 % v/v NO in N_2 at 100 °C for several days before cooling to RT (at $t=0$) under a continued gas flow. In series 3, predried [BMIM][NO_3] was exposed to a gas mixture of 5 % v/v NO with excess O_2 and water at RT.

The observations are explained in the following way: In the initial stages of series 1 and 2 some water is present in the [BMIM][CH_3COO] and the precautions to keep out oxygen and water over an extended period were not sufficient. Thus, NO is being oxidized to HNO_3, which is a stronger acid than acetic acid and [BMIM][CH_3COO]+HNO_3 will give [BMIM][NO_3]+CH_3COOH. The generated acetic acid is not retained in the liquid at 100 °C and is lost to the gas phase with time. At steady state the conversion is complete. This is in correspondence with the observation of the viscosity of the IL changing drastically because [BMIM][NO_3] has a much lower viscosity than [BMIM][CH_3COO] due to a weaker hydrogen-bonding pattern between the cations and anions.[20,21] After the temperature is lowered to RT the starting point in series 1, 2, and 3 are now analogous. Series 3 reaches steady state faster because the access to oxygen and water is not limited by diffusion through tubing or the presence as impurity in the gases or setup. The end point after waiting to steady state is the same for series 1, 2 and 3. Thus, we conclude that the reactivity observed for series 1 and 2 is the same as for series 3 despite the initial difference in the IL and the reaction conditions.

Thermogravimetric analysis

Thermogravimetric analysis (TGA) performed on the pure [BMIM][CH_3COO] compared to the product at steady state after reaction with NO + O_2 + H_2O confirms the transformation of the IL (see Figure S7 in the Supporting Information). [BMIM][NO_3] decomposes at temperatures well above 240 °C, which is 60 °C higher than the decomposition temperature of [BMIM][CH_3COO].

NMR spectroscopy

^1H and ^{13}C NMR analyses (in $CDCl_3$ and [D_6]DMSO) were performed on the bulk [BMIM][CH_3COO] sample after absorption to steady state with NO at room temperature and subsequent desorption for 3 h at 100–110 °C (without gas flow). The data were compared to the NMR spectra of pure [BMIM][NO_3] (Figures S8 and S9 in the Supporting Information) and were found to be almost identical. The spectra revealed no indication of proton or carbon signals attributed to acetic acid [these would be found at $\delta(^1H)=2.1$ (3 H), 11.4 ppm (1 H); $\delta(^{13}C)=20.8$ (CH_3), 178.1 ppm (COOH)] in the sample after desorption. On the other hand, some well-defined signals at $\delta(^1H)$ ($CDCl_3$) = 13.8 and $\delta(^1H)$ ([D_6]DMSO) = 5–6 ppm (br) were observed indicating that desorption of HNO_3 was not complete. No decomposition products were observed in the NMR spectra after this absorption–desorption cycle, and the chemical shifts of the imidazolium ion signals remained essentially unchanged compared to the pure [BMIM][NO_3], except for a slight upfield shift (0.05–0.20 ppm) of the aromatic protons caused by the acidic environment.

Comparison between the IL and aqueous nitrate solution

It is relevant to compare the reaction rates of the uptake and the oxidation of NO in IL media to the one in an analogous aqueous nitrate solution in order to prove that the IL is in fact enhancing the reaction rate and not just providing a non-volatile reaction medium. Unfortunately, it is not possible to design a comparable experiment by using neither the in-situ FTIR setup nor the gravimetric analysis of absorption in a bulk sample. The water in the aqueous nitrate solution will evaporate fast leaving just the nitrate salt on the IR diamond and, in the bulk experiment, evaporation of water will change the weight of the solution. Instead the reactions were compared by quantifying the developed acidic protons by volumetric analysis as follows. In series 4, a solution of $NaNO_3$ in water having the same molar concentration of nitrate as [BMIM][NO_3] (≈6 M) was prepared. NO (5 % v/v) and air saturated with water was bubbled through 3.0 mL of the solution with a rate of 10 mL min^{-1} in a series of experiments. After 2, 4, 6, 8, and 10 h, respectively, the gas flow was stopped and the solution was diluted with degassed water. Thymol blue was added as acid/base indicator and titration was performed with a 0.10 M aqueous solution of NaOH. In series 5 the same experiments were performed on [BMIM][NO_3]. Both series 4 and 5 showed an increasing amount of acidic protons being accumulated in the liquids, as a function of the exposure time. The higher viscosity of the IL should result in a hindered mass transfer across the gas/liquid interface compared to an aqueous $NaNO_3$ solution. Despite this effect favoring the conversion in the aqueous solution it was observed that the IL had accumulated approximately three times as many acidic protons as the aqueous nitrate solution during the first couple of hours (see Figure S10 in the Supporting Information). After longer experimental times, the IL approaches saturation and reacts slower, whereas the aqueous solution continues to have a linear increase. Water evaporating from the aqueous solution during the experiment was partially avoided by using a low flow rate and the air in the flow being saturated with water. Nevertheless, some water loss could not be avoided judged by the weight change of the solution. The aqueous solution produces some precipitate of $NaNO_3$ with time because the solubility is exceeded locally. This is not a problem for the IL where no precipitates are observed. The use of a frit section at the end of the gas tube inserted in the aqueous solution provided irreproducible results as $NaNO_3$ precipitates in the frit. Therefore, an open-end (Ø = 1 mm) glass tube was used for both experiments.

Comparison between inert gas, NO, CO_2, and SO_2

In a realistic flue gas CO_2 and SO_2 are also present and can interact with the ionic liquid. In order to separately assess the interactions of these gases with the ionic liquid the following control experiments were performed: five different gas mixtures were bubbled through approximately 1 g of initially dry [BMIM][NO_3] with a rate of 40 $mL\,min^{-1}$ (see Table 1 and Figure S11 in the Supporting Information).

Table 1. Absorption of gases in [BMIM][NO_3] determined gravimetric and by titration with NaOH(aq).

Experiment	1	2	3	4	5
CO_2 [%]	–	50	–	–	–
SO_2 [%]	–	–	1	–	–
NO [%]	–	–	–	5	0.1
O_2 [%]	10	10	10	10	10
H_2O [%]	1.4	1.4	1.4	1.4	1.4
after absorption for *x* h	24	24	24	8	36
weight increase [$wt\,wt^{-1}$ IL]	0.10	0.11	0.09	0.53	0.11
mol H^+ / mol IL	0	0	0.004	1.10	0.10

In the first three experiments the weight increase is only due to water because acid–base titration reveals that the amount of acidic protons in the solutions after absorption is close to zero. For experiment 4 with 5% NO, the IL is almost saturated after 6 h and the increase in both weight and acidity of the solution is very high. For experiment 5 with 1000 ppm NO, the results show that the reaction does take place but the saturation is slow due to the low concentration of NO. The weight increase is not significantly higher than for experiments 1–3, but acidic protons corresponding to 10% of the molar amount of the IL were found after 36 h. This corresponds to approximately 15% of the NO in the total gas volume that was bubbled through 1 g of the IL for 36 h.

Discussion

The cations of the ILs do not decompose even when heated to 120 °C in concentrated nitric acid; the original IR spectra of the nitrate and triflate ILs are completely recovered after cooling to RT even after many cycles. If bulk [BMIM][NO_3] saturated with HNO_3 is kept completely dry and heated to above 120 °C for longer periods, some yellow coloration is observed, but no irreversible decomposition products have been observed. When exposing [BMIM]Cl to NO, species corresponding to both hydrochloric acid and nitric acid are present in the solution, but the IL does not decompose despite being saturated with this very potent oxidation mixture. These observations show that the ILs have excellent chemical stability towards $H_xN_yO_z$ species. This is rationalized with the imidazolium ring being well protected from electrophilic attack by NO_2^+ or similar species due to its positive charge. As seen from the proposed reaction pathway below, radicals originating from dioxygen are not believed to be part of the turnover of the reaction. The fact that the organic cations are unaffected by the harsh treatment is also a strong indication that the formation of uncontrollable reactive radical species is controlled in the IL media by the more stable radicals NO and NO_2. Uncharged organic molecules or other impurities present in the IL are likely less protected and therefore oxidized and decomposed completely to CO_2 and water giving a self-cleaning process of the IL during heating to the regeneration temperature.

NO_2 is always present to some extent in pressurized NO gas bottles due to the slow, but irreversible disproportion reaction of NO to form N_2O and NO_2.[26] However, because no HNO_3 formation was observed in the absence of dioxygen in the feed gas (Figure S2 in the Supporting Information), the disproportion reaction cannot account for the observed generation of HNO_3. Similarly, the level of autoxidation of NO by dioxygen in the gas phase before contact with the IL was monitored with gas-phase UV/Vis spectroscopy and was found to be very low and thus not responsible for the observed reactivity. Furthermore, preliminary[27] and ongoing investigations of the gas conversion reaction with supported ionic liquid phase (SILP) absorbers reveal much higher conversion dynamics over the IL phase compared to bypass experiments. So far, several absorption (at RT)–desorption (at 130 °C) cycles performed by SILP absorbers revealed a completely reversible and unchanged capacity of the absorber.

Proposed reaction cycle

The overall reaction (1) is thermodynamically favored with $\Delta_r G = -210\ kJ\,mol^{-1}$, but it is very slow under ambient conditions.

$$4\,NO(g) + 3\,O_2(g) + 2\,H_2O(l) \rightarrow 4\,HNO_3(l) \qquad (1)$$

ILs have ionic strengths, which are of course much higher than those of molecular liquids and higher than those of brine solutions as well. For ILs consisting of large organic cations and small inorganic anions, the base strength and the nucleophilicity of the anion is much higher than if the anion was solvated in water.[24] Normally, NO is kinetically inert toward many common reactants but ILs provide a condensed medium containing strong nucleophiles. The absence of a full hydration shell decreases the activation barrier for nucleophilic attack. Based on the experimental evidence given here, a mechanism for the oxidation reaction of NO in IL is suggested.

The oxidation of NO is reported in the literature to have the same rate law as given in Equation (2) in the gas phase and in aqueous solution despite the total reactions being different.[28,29] In this work, a second-order dependence on p(NO) over the IL film was also found (see Figure 7), and we expect the same rate law is relevant for the rate-determining step in this IL solution.

$$-\frac{d[NO]}{dt} = k[NO]^2[O_2] \tag{2}$$

Gas phase:

$$2\,NO(g)+O_2(g) \rightarrow 2\,NO_2(g) \tag{3}$$

Aqueous solution:

$$4\,NO(g)+O_2(g)+2\,H_2O(l) \rightarrow 4\,H^+(aq)+4\,NO_2^-(aq) \tag{4}$$

In ILs an adduct can form between the IL anion and the NO molecule capturing and activating the NO for further reactions, because the anion is a powerful base and nucleophile. In the case of a nitrate IL, the attack on NO can involve oxidation of the NO nitrogen atom, which is thermodynamically favored. The product has one negative charge and is likely to be caught in the IL phase and to participate in further reactions. The initiation step in the condensed IL phase is thus proposed to be:

$$NO(g)+NO_3^-(IL) \rightarrow N_2O_4^-(IL) \tag{5}$$

The unstable adduct $N_2O_4^-$ is then suggested to decompose into two species with the intermediate oxidation states of +III and +IV as given in reaction (6). Reactions (5) and (6) are analogous to the reaction between NO and HNO_3 in the atmosphere or on surfaces.[30–33]

$$N_2O_4^-(IL) \rightarrow NO_2(IL)+NO_2^-(IL) \tag{6}$$

It was shown (see Figure 5) that NO_2 dimerizes to N_2O_4 in the IL when insufficient water is present (reaction (7)).

$$2\,NO_2(IL) \rightarrow N_2O_4(IL) \tag{7}$$

We expect N_2O_4 to be able to disproportionate to ions in an ionic media as given in reaction (8). This corresponds to the anhydrous form of the known disproportionation reaction occurring on surfaces.[34]

$$N_2O_4(IL) \rightarrow NO_2^+(IL)+NO_2^-(IL) \tag{8}$$

Two nitrite anions from reactions (6) or (8) could hypothetically be oxidized by O_2 in one step, as given in reaction (9):

$$2\,NO_2^-(IL)+O_2(g) \rightarrow 2\,NO_3^-(IL) \tag{9}$$

However, reaction (9) is probably not very favored even in an IL phase because two anionic species have to be close together in order to allow reaction with one O_2 molecule. Under dry conditions, the final products after complete oxidation are the ionic species NO_2^+ and NO_3^-, as in the solid state of N_2O_5.

In the majority of the experiments enough water was present allowing reactions (10)–(12) to take place and several of the intermediates are observed in Figure 5.

$$N_2O_4(IL)+H_2O(IL) \rightarrow HNO_3(IL)+HNO_2(IL) \tag{10}$$

$$HNO_2(IL) \rightarrow NO_2^-(IL)+H^+(IL) \tag{11}$$

$$HNO_2(IL)+NO_2^-(IL) \rightarrow HN_2O_4^-(IL) \tag{12}$$

The protons generated will prefer NO_2^- over NO_3^- because nitrite is the stronger base. The dimeric species $HN_2O_4^-$(IL) and the nitrous acid dimer have a strong hydrogen bond keeping the two nitrogen(III) species close together. The nitrogen(III) species have thus been activated for oxidation by dioxygen in one step. The product is the analogous nitric acid nitrate dimer:

$$HN_2O_4^-(IL)+O_2(IL) \rightarrow HN_2O_6^-(IL) \tag{13}$$

This corresponds well to the observed molar ratio of approximately 1:1 between HNO_3 and the IL after gas saturation. When the IL is saturated with HNO_3 there are just enough protons to allow every proton to form a strong hydrogen bond between two nitrate anions. No free basic nitrate anions are then available for nucleophilic attack on NO, only allowing HNO_3 to accumulate very slowly in the IL after this point (see Figure 7). The nitrate–nitric acid dimer is clearly observable in the IR spectrum and is the final product until the nitric acid is desorbed by raising the temperature:

$$HN_2O_6^-(IL) \rightarrow HNO_3(g)+NO_3^-(IL) \tag{14}$$

An analogue reaction to reaction (13) has previously been suggested to explain why the rate of the oxidation of NO_x by dioxygen was observed to be several orders of magnitude faster just around 0 °C in water droplets.[35,36] The freeze-concentration effect leads the HNO_2 concentration to increase drastically in the remaining liquid phase by a factor of 240–11 000.[37] The formed HNO_2 dimers are activated towards oxidation by O_2:

$$(HONO)_2(aq)+O_2(aq) \rightarrow 2\,HNO_3(aq) \tag{15}$$

In the IL phase a single proton assures that the nitrogen(III) species are held together, activating them towards oxidation by O_2 in an analogous manner.

Reaction (13) is suggested to be the rate-determining step after a series of pre-equilibria, that is, reactions (5)–(7) and reactions (10)–(12). This is in accordance with the overall reaction order of two with respect to NO. The complete reaction pathway consisting of reactions (5)–(7) and reactions (10)–(14) is shown in the catalytic cycle in Scheme 3, having the stoichiometry of the total reaction given in Equation (1). The individual reactions with coefficients are listed in Table S1 in the Supporting Information. The appearance of the cycle is complicated by the demands of stoichiometry and the suggestion of elementary reactions but can be considered in a simple way as nitrate oxidizing NO to HNO_3 and thereby being reduced itself to nitrite. O_2 then re-oxidizes nitrite to nitrate, thereby regenerating the catalyst.

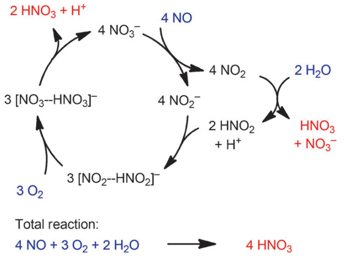

Scheme 3. Stoichiometric reaction cycle for the oxidation of NO to HNO_3 catalyzed at RT by nitrate based ILs (reactants: red, products: blue, intermediates: black).

It should be noted that the chemistry is similar to what would be expected in aqueous solution. The difference observed is due to an enhanced activity of the nitrate anions in IL solution because they are not solvated by water molecules. Also the interaction between typically large cations of ILs with the anions is significantly weaker compared to the interaction by the typically smaller inorganic cations (e.g., Na^+) with the anions.[38] Furthermore, the generation of dimeric units of N^{III} species coupled by hydrogen bonding has a favorable impact on the rate of oxidation with O_2, which is the rate-determining step.

In ILs with other anions than nitrate, a different initiation reaction for the catalytic cycle must take place: Acetate is not an oxidant but is still a good nucleophile that can capture NO in the condensed phase. The reaction mechanism for this initiation is not clear, but it is possible that a small percentage of NO_2 present in the gas can disproportionate and start the process or that O_2 could participate in radical reactions for the initiation reaction. After a while, nitrate accumulates and the reaction proceeds like in nitrate-based ILs. The ILs with anions, which are stronger bases than nitrate, will be converted to the corresponding nitrate IL after one cycle. Acetate is a very powerful Lewis and Brønsted base in a pure IL[24] and FTIR measurements performed on [BMIM][CH_3COO] (Figure 2) and [Ch][CH_3COO] (Figure S4 in the Supporting Information) show that IR features assignable to acetate at $\tilde{\nu} = 1550\ \text{cm}^{-1}$ decrease very quickly as the nitrate and acetic acid bands increases. As NO is absorbed and oxidized, nitric acid is formed but the protons are removed immediately by acetate. Judged from the decreasing intensity of the band at $\tilde{\nu} = 1715\ \text{cm}^{-1}$ with time, the acetic acid is slowly removed from the liquid even at RT. In the bulk experiments with [BMIM][CH_3COO], acetic acid was absent according to NMR analysis after one absorption–desorption cycle. When starting from a more basic anion than nitrate, it is suggested that the generated, unprotonated nitrate anion is involved in the further absorption and oxidation of NO. Furthermore, as acids accumulate in the IL, the nitric acid will be retained more strongly than the other acids due to its formation of a high-boiling azeotrope with water having a pattern of strong hydrogen bonds.

Conclusion

Nitrate is a catalyst for the oxidation of NO by O_2 to nitric acid. Nitrate is reduced to nitrite by NO and is re-oxidized by O_2, thereby restoring the catalyst. Aqueous nitrate solutions have modest activity towards this reaction. By using a nitrate-based ionic liquid, the catalyst is an integral part of the reaction medium, the reaction is at least three times faster than in aqueous solution with a comparable nitrate concentration, and, most importantly, the reaction can be run in a continuous flow without the reaction media being lost by evaporation. Under exactly the same conditions, the IL does not absorb either CO_2 or SO_2 to any measurable extent.

Interconversion between the different nitrogen species in the condensed IL phase is likely dynamic and fast and the concentrations are the equilibrium values. The most reactive species towards oxidation by dioxygen is expected to be a nitrite–nitrous acid adduct or a nitrous acid dimer. Both are poised to deliver four electrons to a dioxygen molecule and make the corresponding dimeric nitrogen(V) species without oxygen radical intermediates. The hydrogen bonds formed serve to retain the nitrogen species in the IL phase removing them from the gas phase. This method is therefore a tool to absorb exhaust NO_x species from off gases and storing them. The absorption ability can be restored in a desorption step at higher temperatures. No deterioration of the absorption properties of the IL is observed even after many absorption–desorption cycles. After saturation, all nitrate ions participate in strong hydrogen bonds and the molar ratio between NO_3^- and HNO_3 is approximately 1:1. Thus, the resulting mixture after saturation with HNO_3 can be formulated as a new IL, that is, [BMIM][$NO_3 \cdot HNO_3$]. The product after desorption is a concentrated HNO_3 stream that can be condensed with water as nitric acid of commercial grade.

The cation of the IL has no apparent influence on the absorption reaction and in most cases the anion is converted to nitrate after one absorption–desorption cycle. Thus, ILs like the non-toxic cholinium chloride used as a vitamin additive for livestock, are expected to be just as effective as traditional imidazolium-based ILs and can be obtained at a much lower cost.

In order to overcome the mass-transfer limitations for the interaction of bulk ILs with the gas phase, solid absorbers with ILs impregnated on porous silica or other porous supports can be made. The resulting SILP materials[9,27] are very promising for the application as reversible NO_x absorbers in end-of-pipe installations of industrial units emitting NO_x like, for example, power plants, ships, and cement factories. Investigations with such SILP absorbers are ongoing.

Experimental Section

[BMIM][NO_3] (>98%, IoLiTec), [BMIM][CH_3COO] (>98%, Sigma–Aldrich), [BMIM]Cl (95%, Sigma–Aldrich), [BMMIM][NO_3] (>98%, IoLiTec), [Ch][CH_3COO] (95%, Sigma–Aldrich), and [EMIM][CF_3SO_3] (>99%, IoLiTec) were obtained from commercial sources and used as received. [Ch][NO_3] was produced in situ by exposing [Ch]

[CH_3COO] to a gas mixture of NO/O_2/water in nitrogen followed by heating to 120 °C in a flow of nitrogen.

The gas streams were mixed from 10 % v/v NO in N_2, N_2, CO_2, 2 % v/v SO_2 in N_2 and air. All gases were delivered by AGA. The gas flow was controlled by mass flow controllers (Bronkhorst). To obtain a wet gas, the air or N_2 stream was led through water or D_2O (99.9 %, Sigma–Aldrich) in a bubble flask fitted with a glass frit and joined with the NO gas just before the reactor. NO and O_2 were led through stainless steel tubing (Swagelok) close to the reactor chamber in order to minimize the autoxidation of NO in the gas phase, which is facilitated by sunlight. NO_2 was generated by treating copper metal with HNO_3 (65 %, Sigma–Aldrich). Prior to subjecting the IL sample to the gas, the gas was dried through a column with activated molecular sieves (4 Å). ATR-FTIR experiments were performed on a Nicolet iS5 spectrometer equipped with a thermo-regulated (up to 300 °C) Specac golden gate high-temperature diamond ATR cell. This was fitted with an add-on cap, allowing the controlled gas mixture to flow over the diamond of the instrument at atmospheric pressure (Figure S1 in the Supporting Information). The experiments were performed with 1–6.5 % v/v NO, 8–20 % v/v O_2, 1–1.5 % v/v water with a flow rate of 50 mL min^{-1}. The IL was applied as a thin film in the center of the diamond before securing the add-on cap. For the IL screening experiments, the gas exchange was performed with a valve outside the add-on cap and a reproducible delay before the reaction was present. The time-resolved experiments with [BMIM][NO_3] were performed with the atmosphere in the cap being equilibrated before quickly adding the cap over the IL film on the ATR diamond. The reaction and absorption were followed in real time by recording spectra continuously. For each spectrum, 4–16 scans with 4 cm^{-1} resolution (approximately 5–20 s measuring time) were performed. The spectra were background- and ATR-corrected in OMNIC 8.2 assuming a refractive index of 1.5 and a reflectance angle of 90°. Gaussian deconvolution by using PeakFit[39] was performed individually in the area of the $\tilde{\nu} = 948$ and 1660 cm^{-1} bands of HNO_3. To allow for batch deconvolution, a method was developed for Gnuplot 4.1.[34] Further details on the deconvolution method can be found in the literature.[23] The shown full spectra in Figures 1–6 were all obtained at RT. Spectra (not shown) obtained at temperatures up to 60 °C were the basis for the results shown in Figure 7, bottom.

The bulk experiments were performed in five series in a 15 mL custom-made cylindrical Schlenk flask fitted with a tube (with or without a glass frit) reaching almost to the bottom and valves both on the inlet and outlet. Enough liquid is added to cover the opening of the insert so the gas is passing through the liquid. After closing the valves, the entire flask can be disconnected from the gas line and weighed.

For series 1 and 2, [BMIM][CH_3COO] (1 mL) was used. For series 3 and 5, [BMIM][NO_3] (1 mL and 0.9 mL, respectively) was used. For series 4, $NaNO_3$ (2 mL, 6 M) in degassed water was used. The gases were pure 10 % v/v NO at 10 mL min^{-1} for series 1 and 2; 5 % v/v NO, 10 % v/v O_2, and approximately 1 % v/v water at 30 mL min^{-1} for series 3; and 5 % v/v NO, 10 % v/v O_2, and approximately 1 % v/v water at 10 mL min^{-1} for series 4 and 5. All five series were followed gravimetrically by weighing several times. In series 1 and 2, the reaction vial was submerged in an oil bath at 100 °C while under the gas flow for several days to obtain steady state. Then the oil bath was removed and the flask was cooled down to RT. Still under flow, a new steady state was obtained at room temperature after several days. Series 3 was performed at RT and followed by weighing multiple times. Series 4 and 5 consists of several individual experiments at RT, which were stopped after 2, 4, 6, 8, and 10 h, respectively, by adding a total of 50 mL degassed water in several portions and transferring the resulting solution to an Erlenmeyer flask. Thymol blue was added as acid/base indicator and the amount of acidic protons was determined by titration with NaOH (0.100 M). For series 4 and 5, the experiments were reproduced with an open-end glass tube. This had little influence for the experiments with IL but problems with clogging of the frit with $NaNO_3$ in the aqueous solution bulk experiments were avoided giving more reproducible results.

NMR spectra were recorded at RT on a Bruker 300 MHz NMR instrument by using $CDCl_3$ solutions/inhomogeneous mixtures of pure [BMIM][NO_3] and [BMIM][CH_3COO] as well as of the ILs after saturation with NO gas in the bulk at RT as described above for series 3 and subsequent desorption without flow at 110 °C for 3 h.

[BMIM][NO_3]: ^{1}H NMR (300 MHz, $CDCl_3$): $\delta = 0.86$ (3 H; butyl), 1.28 (2 H; butyl), 1.78 (2 H; butyl), 3.93 (3 H; methyl), 4.16 (2 H; butyl), 7.42 (1 H; C5), 7.48 (1 H; C4), 9.62 ppm (1 H; C2); ^{13}C NMR (300 MHz, $CDCl_3$): $\delta = 13.5$, 19.5, 32.2, 36.4, 49.9, 122.5, 124.0, 137.7 ppm (impurities: 54.7, 104.6 ppm).

[BMIM][CH_3COO] after reaction: ^{1}H NMR (300 MHz, $CDCl_3$): $\delta = 0.92$ (3 H; butyl), 1.33 (2 H; butyl), 1.84 (2 H; butyl), 3.96 (3 H; methyl), 4.20 (2 H; butyl), 7.37 (1 H; C5), 7.41 (1 H; C4), 9.42 (1 H; C2), 13.52 ppm (0.5 H; HNO_3); ^{13}C NMR (300 MHz, $CDCl_3$): $\delta = 13.5$, 19.6, 32.2, 36.5, 50.1, 122.5, 123.9, 137.5 ppm (impurity: 54.7 ppm).

TGA was performed on a Mettler Toledo TGA/DSC 1 STARe system in a flow of nitrogen of 70 mL min^{-1}. Samples were heated from RT to 600 °C with a heating rate of 10 °C min^{-1}.

Determination of water contents in the ILs were performed by Karl-Fischer titration on a Metrohm 888 Titrando by analyzing three samples of 0.1 mL.

Acknowledgements

This work is financially supported by the Energinet.dk through the PSO project 10521 and the Copenhagen Cleantech Cluster (GAP project no. 91050-ko). S.M thanks the Danish Independent Research Council DFF (project no. 09-070250). The FP7 COST Action CM1306 EXIL is acknowledged for financial support for dissemination. Dr. Johannes Due Hansen, Thorey Gretarsdottir, and Anita Godiksen, Centre for Catalysis and Sustainable Chemistry, DTU Chemistry, Technical University of Denmark are acknowledged for performing preliminary investigations. LAB S.A, France and DONG Energy, Denmark are also thanked for financial support and valuable discussions.

Keywords: gas absorption · ionic liquids · IR spectroscopy · nitric acid · NO_x

[1] *Health Aspects of Air Pollution with Particulate Matter, Ozone and Nitrogen Dioxide*: Report on a WHO Working Group, World Health Organization, Regional Office for Europe, **2003**.
[2] N. Meine, F. Benedito, R. Rinaldi, *Green Chem.* **2010**, *12*, 1711 – 1714.
[3] C. P. Fredlake, J. M. Crosthwaite, D. G. Hert, S. N. V. K. Aki, J. F. Brennecke, *J. Chem. Eng. Data* **2004**, *49*, 954 – 964.
[4] A. Noda, M. A. B. H. Susan, K. Kudo, S. Mitsushima, K. Hayamizu, M. Watanabe, *J. Phys. Chem. B* **2003**, *107*, 4024 – 4033.
[5] H. Tokuda, K. Hayamizu, K. Ishii, M. A. B. H. Susan, M. Watanabe, *J. Phys. Chem. B* **2004**, *108*, 16593 – 16600.
[6] J. Huang, A. Riisager, P. Wasserscheid, R. Fehrmann, *Chem. Commun.* **2006**, 4027 – 4029.

[7] C. Wang, G. Cui, X. Luo, Y. Xu, H. Li, S. Dai, *J. Am. Chem. Soc.* **2011**, *133*, 11916 – 11919.
[8] J. F. Brennecke, B. E. Gurkan, *J. Phys. Chem. Lett.* **2010**, *1*, 3459 – 3464.
[9] P. Thomassen, A. Riisager, A. J. Kunov-Kruse, S. Mossin, H. Kolding, S. Kegnæs, R. Fehrmann, *ECS Trans.* **2013**, *50*, 433 – 442.
[10] Z. Lei, C. Dai, B. Chen, *Chem. Rev.* **2014**, *114*, 1289 – 1326.
[11] R. W. Berg, P. Harris, A. Riisager, R. Fehrmann, *J. Phys. Chem. A* **2013**, *117*, 11364 – 11373.
[12] L. Cammarata, S. G. Kazarian, P. A. Salter, T. Welton, *Phys. Chem. Chem. Phys.* **2001**, *3*, 5192 – 5200.
[13] L. J. Murphy, A. M. McPherson, K. N. Robertson, J. A. C. Clyburne, *Chem. Commun.* **2012**, *48*, 1227 – 1229.
[14] A. Riisager, A. J. Kunov-Kruse, S. Mossin, R. Fehrmann, *Absorption and Oxidation of NO in Ionic Liquids*, **2013**, WO2013079597.
[15] F. Mélen, M. Herman, *J. Phys. Chem. Ref. Data* **1992**, *21*, 831 – 881.
[16] D. C. Harris, M. D. Bertolucci, *Symmetry and Spectroscopy*, Oxford University Press, New York, **1978**.
[17] K. Noack, P. S. Schulz, N. Paape, J. Kiefer, P. Wasserscheid, A. Leipertz, *Phys. Chem. Chem. Phys.* **2010**, *12*, 14153 – 14161.
[18] Gaussian 09, Revision A.02, M. J. Frisch, G. W. Trucks, H. B. Schlegel, G. E. Scuseria, M. A. Robb, J. R. Cheeseman, G. Scalmani, V. Barone, B. Mennucci, G. A. Petersson, H. Nakatsuji, M. Caricato, X. Li, H. P. Hratchian, A. F. Izmaylov, J. Bloino, G. Zheng, J. L. Sonnenberg, M. Hada, M. Ehara, K. Toyota, R. Fukuda, J. Hasegawa, M. Ishida, T. Nakajima, Y. Honda, O. Kitao, H. Nakai, T. Vreven, J. A. Montgomery, Jr., J. E. Peralta, F. Ogliaro, M. Bearpark, J. J. Heyd, E. Brothers, K. N. Kudin, V. N. Staroverov, R. Kobayashi, J. Normand, K. Raghavachari, A. Rendell, J. C. Burant, S. S. Iyengar, J. Tomasi, M. Cossi, N. Rega, J. M. Millam, M. Klene, J. E. Knox, J. B. Cross, V. Bakken, C. Adamo, J. Jaramillo, R. Gomperts, R. E. Stratmann, O. Yazyev, A. J. Austin, R. Cammi, C. Pomelli, J. W. Ochterski, R. L. Martin, K. Morokuma, V. G. Zakrzewski, G. A. Voth, P. Salvador, J. J. Dannenberg, S. Dapprich, A. D. Daniels, O. Farkas, J. B. Foresman, J. V. Ortiz, J. Cioslowski, D. J. Fox, Gaussian Inc., Wallingford CT, **2009**.
[19] H.-P. Steinrück, P. Wasserscheid, *Catal. Lett.* **2015**, *145*, 380 – 397.
[20] M. Thiemann, E. Scheibler, K. W. Wiegand in, *Ullmann's Encyclopedia of Industrial Chemistry, Vol. 24*, Wiley-VCH, Weinheim, **2012**, pp. 177 – 223.
[21] H. A. Duong, T. N. Tekavec, A. M. Arif, J. Louie, *Chem. Commun.* **2004**, 112 – 113.
[22] R. N. Wiener, E. R. Nixon, *J. Chem. Phys.* **1957**, *26*, 906 – 908.
[23] A. J. Kunov-Kruse, A. Riisager, S. Saravanamurugan, R. W. Berg, S. B. Kristensen, R. Fehrmann, *Green Chem.* **2013**, *15*, 2843 – 2848.
[24] Z. Guo, B.-M. Lue, K. Thomasen, A. S. Meyer, X. Xu, *Green Chem.* **2007**, *9*, 1362 – 1373.
[25] J. L. Anthony, J. L. Anderson, E. J. Maginn, J. F. Brennecke, *J. Phys. Chem. B* **2005**, *109*, 6366 – 6374.
[26] H. Tsukahara, T. Ishida, Y. Todoroki, M. Hiraoka, M. Mayumi, *Free Radical Res.* **2003**, *37*, 171 – 177.
[27] H. Kolding, P. Thomassen, S. Mossin, S. Kegnæs, A. Riisager, J. Rogez, G. Mikaelian, R. Fehrmann, *ECS Trans.* **2014**, *64*, 97 – 108.
[28] P. C. Ford, D. A. Wink, D. M. Stanbury, *FEBS Lett.* **1993**, *326*, 1 – 3.
[29] S. Goldstein, G. Czapski, *J. Am. Chem. Soc.* **1995**, *117*, 12078 – 12084.
[30] B. J. Finlayson-Pitts, N. A. Saliba, L. M. Wingen, W. S. Barney, M. Mochida, H. Yang, *Rep. Calif. Air Ressources Board Calif. Environ. Prot. Agency* **2001**, 1 – 166.
[31] M. Mochida, B. J. Finlayson-Pitts, *J. Phys. Chem. A* **2000**, *104*, 9705 – 9711.
[32] J. Kleffmann, T. Benter, P. Wiesen, *J. Phys. Chem. A* **2004**, *108*, 5793 – 5799.
[33] R. Svensson, E. Ljungström, *Int. J. Chem. Kinet.* **1988**, *20*, 857 – 866.
[34] T. Kinugawa, S. Enami, A. Yabushita, M. Kawasaki, M. R. Hoffmann, A. J. Colussi, *Phys. Chem. Chem. Phys.* **2011**, *13*, 5144 – 5149.
[35] D. E. Damschen, L. R. Martin, *Atmos. Environ.* **1983**, *17*, 2005 – 2011.
[36] P. K. Mudgal, S. P. Bansal, K. S. Gupta, *Atmos. Environ.* **2007**, *41*, 4097 – 4105.
[37] N. Takenaka, A. Ueda, T. Daimon, H. Bandow, T. Dohmaru, Y. Maeda, *J. Phys. Chem.* **1996**, *100*, 13874 – 13884.
[38] Q. Yang, H. Xing, Z. Bao, B. Su, Z. Zhang, Y. Yang, S. Dai, Q. Ren, *J. Phys. Chem. B* **2014**, *118*, 3682 – 3688.
[39] *PeakFIT v. 4.11*, Systat Software Inc, **2009**.

Received: March 11, 2016

C.2 Supplementary Information to: Absorption and Oxidation of Nitrogen Oxide in Ionic Liquids

A. J. Kunov-Kruse, P. Thomassen, A. Riisager, S. Mossin* and Rasmus Fehrmann*

Chemistry - A European Journal, **2016**, 22, 11745-11755

CHEMISTRY
A European Journal

Supporting Information

Absorption and Oxidation of Nitrogen Oxide in Ionic Liquids

Andreas J. Kunov-Kruse, Peter L. Thomassen, Anders Riisager, Susanne Mossin,* and Rasmus Fehrmann*[a]

chem_201601166_sm_miscellaneous_information.pdf

Content:

Experimental methods for in-situ ATR-FTIR experiments

The in-situ ATR-FTIR experiments were all conducted on a Thermo Scientific Nicolet iS5 FTIR spectrophotometer with a High temperature Specac Golden Gate ATR cell extension. The ATR-cell uses a single-reflection diamond and has golden mirrors for reflection of the IR beam inside the ATR-cell. A small IL droplet was placed on the diamond. Then a sealed gas cap is placed over the sample area (see Figure S1). This allows for a continuous, controlled, flow of gas over the sample. The reaction gas was mixed from pressurized air, 1% NO in He (AGA) or 10% NO in N_2 (AGA). The gas flow was controlled using N_2 calibrated mass flow controllers (Bronkhorst), all were manually recalibrated for each specific gas. Two streams of air were used; one was saturated with water by bubbling through a water reservoir at room temperature. The water concentration in this stream is assumed to be 2.4 %, and the total water concentration is calculated based on this.

The experiments shown in Figures 1-5 of the main text and in Figures S3 – S6 were conducted by first fitting the gas cap over the sample and equilibrating in a stream of pure air. At time zero in the experiments the NO containing stream was shifted from bypass to join the air stream. This means there is a short period where the pure air is displaced. In this period the NO concentration is lower than the target value and may also fluctuate at the position of the IL droplet.

In the experiments underlying the data given in Figure 6 of the main text and for [BMIM][NO_3], the gas mixture was allowed to reach the target concentration before the gas cap was attached over the IL film, which was in equilibrium with the atmosphere at room temperature.

For the kinetic experiments in Figure 6 of the main text both methods were used: For [BMIM][NO_3] the gas was equilibrated before it was led over the IL sample like in Figure 7. For the remaining ILs in Figure 6 the experiment was conducted with the cap fixed like in Figure 1 – 5 of the main text. Since the experiment with [BMMIM][NO_3] and the experiment with [BMIM][NO_3] in Figure 6 is completely comparable the deviation resulting in the difference in the methods can be assessed by comparison of these two curves. As expected the apparent reaction rate is slower when the gas was not allowed to equilibrate in the cap before the experiment started. Conclusions drawn on the amount of HNO_3 present at steady state as well as comparisons between the ILs measured under the same conditions are not influenced by the shift in in-situ methodology used.

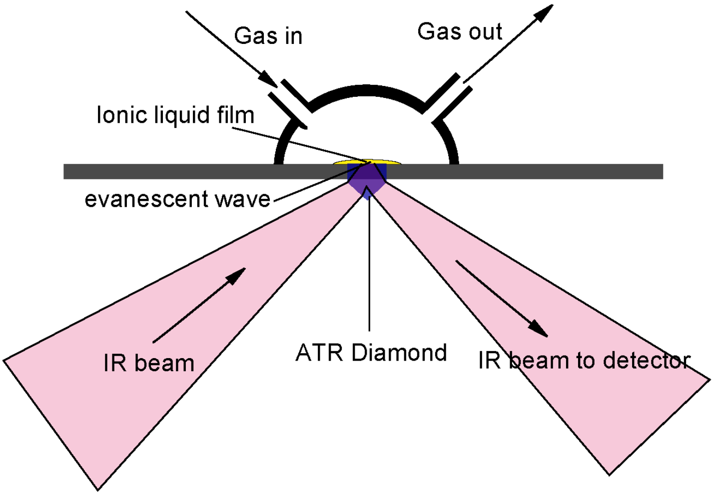

Figure S1: Setup for *in-situ* ATR-FTIR experiments.

The path of the IR beam, the sample position and the gas inlet and outlet is marked on the figure.

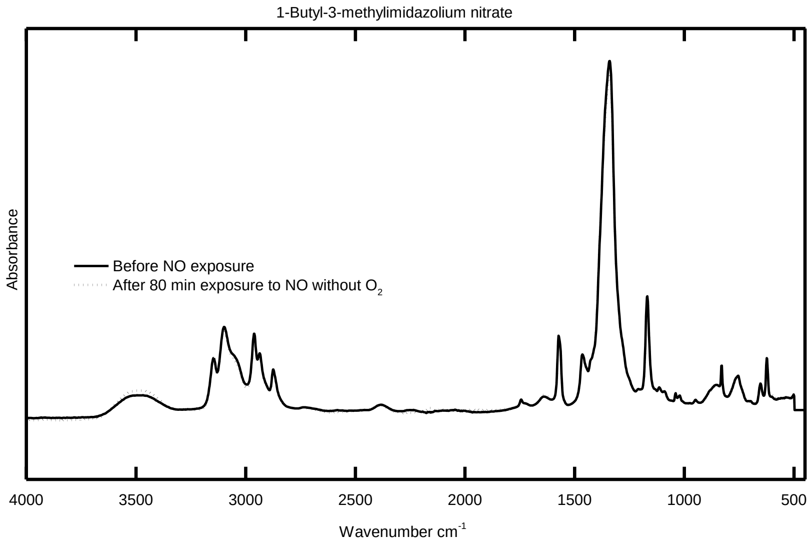

Figure S2: In-situ ATR-FTIR absorption spectra of NO absorption in [BMIM][NO_3].

A control experiment of NO absorption in [BMIM][NO_3] was performed for 80 minutes at room temperature with 10 % v/v NO in N_2 as the only gas component. The IL film is in equilibrium with the atmosphere before the experiment and therefore contains about 1 % w/w water. The band at 3500 cm^{-1} is due to water and is the only one which is not completely identical before and after the experiment.

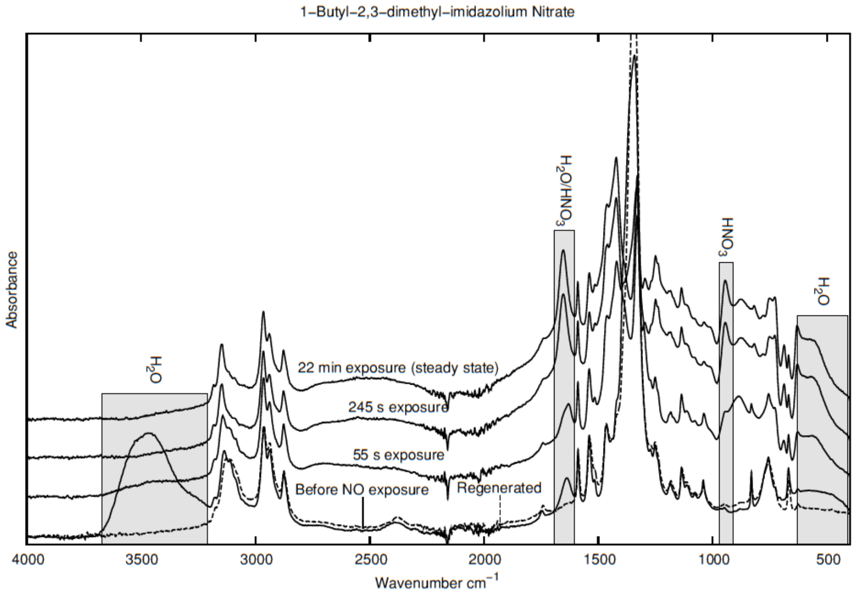

Figure S3: In-situ ATR-FTIR absorption spectra of NO absorption and oxidation in [BMMIM][NO_3].

The gas stream contained NO (6.6 % v/v), O_2 (7 % v/v), H_2O (1 % v/v) and balance N_2.The spectra are shifted on the ordinate for clarity. Bands appearing at 1660 cm^{-1} and 948 cm^{-1} indicate formation of nitric acid. The bands corresponding to water decrease quickly because water is used in the reaction. The nitric acid is driven out by heating to 180^{o}C, restoring all bands except the water bands. The only other difference between the starting spectrum and the regenerated spectrum is the intensity of the nitrate peak at 1340 cm^{-1}. This is assigned to the hydrogen bonding pattern of the nitrate ions being different when water is present in the IL.

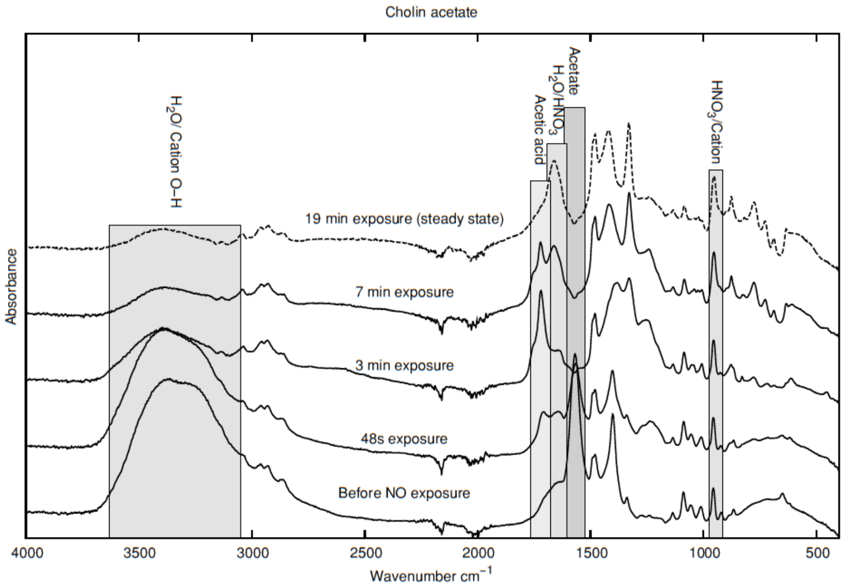

Figure S4: In-situ ATR-FTIR absorption spectra of NO absorption and oxidation in [Ch][CH_3COO].

The gas stream contained NO (6.6 % v/v), O_2 (7 % v/v), H_2O (1 % v/v) and balance N_2. The spectra are shifted on the ordinate for clarity. Characteristic bands are indicated. As is also seen in Figure S3, the water concentration is initially high but quickly decreases as the reaction occurs. In this case, the cation contains an O-H bond so bands are still found in the O-H stretch region at 3400 cm^{-1}. At 1740 cm^{-1} the band for acetic acid increases and later decreases again. This suggests that acetic acid is formed initially during the reaction but is slowly driven out of the IL as the reaction proceeds. Acetate is a stronger base than nitrate and is protonated and the corresponding acid is driven out during the reaction. According to Figure 5 and 6 in the main text, the formation and evaporation of acetic acid happens simultaneously with the formation of nitric acid, without affecting the rate of the nitric acid formation. It can be seen from the steady state spectrum that no acetate is apparently present in the IL after the steady state is obtained. Furthermore, formation of the nitrate band at 1340 cm^{-1} suggests that all acetate has been replaced by nitrate at the point of saturation. The final spectrum in this figure is closely related to the final spectrum found in Figure S5, showing the same reaction performed on choline nitrate.

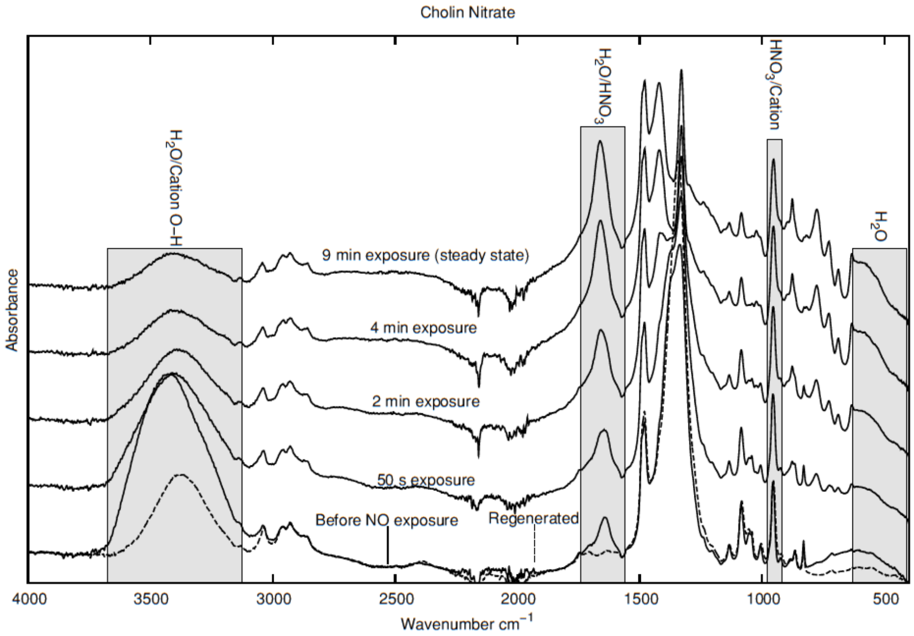

Figure S5: In-situ ATR-FTIR absorption spectra of NO absorption and oxidation in [Ch][NO_3].

The gas stream contained NO (6.6 % v/v), O_2 (7 % v/v), H_2O (1 % v/v) and balance N_2. The spectra are shifted on the ordinate for clarity. Water quickly disappears as observed from both the band at 1640 cm^{-1} and 3400 cm^{-1}. Nitric acid is formed as seen from the bands at 948 cm^{-1} and 1660 cm^{-1}, as they increase in intensity with the reaction. The band at 948 cm^{-1} also contains significant contribution from the choline cation. However, when comparing the individual spectra, an increase in intensity is observed during the reaction. This can also be seen from the increase in intensity of the 1660 cm^{-1} band. The nitrate band from the IL at 1340 cm^{-1} is again split due to hydrogen bond formation. See Chart 2 in the main text.

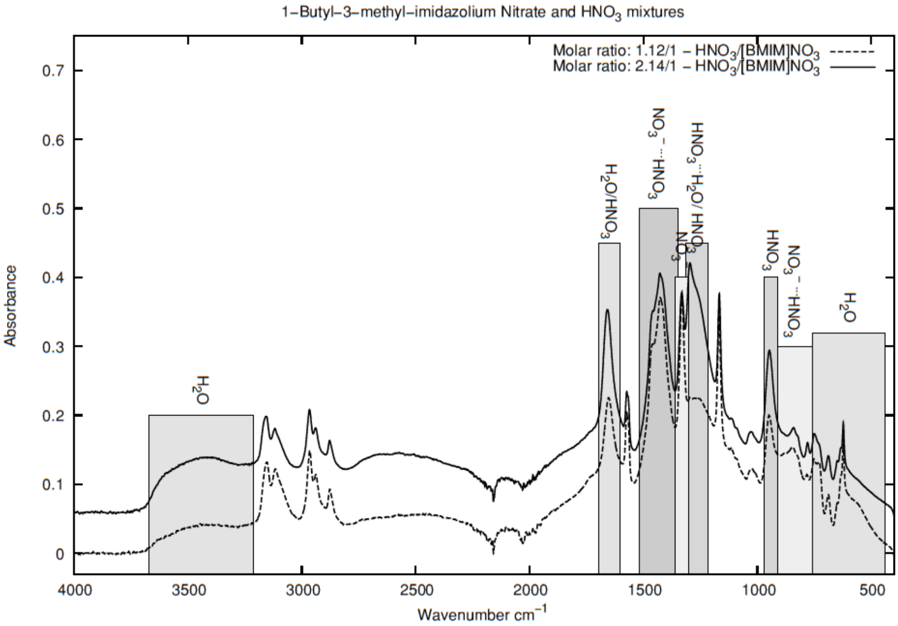

Figure S6: ATR-FTIR data of different HNO_3/IL molar ratios.

Ex-situ spectra of solutions of HNO_3 (67 %) in [BMIM][NO_3] with known concentrations. The area of the 948 cm^{-1} and 1660 cm^{-1} bands were determined and used as reference in later determination of the HNO_3 concentrations. The areas were determined by the deconvolution method developed by Kunov-Kruse et. al. [1].

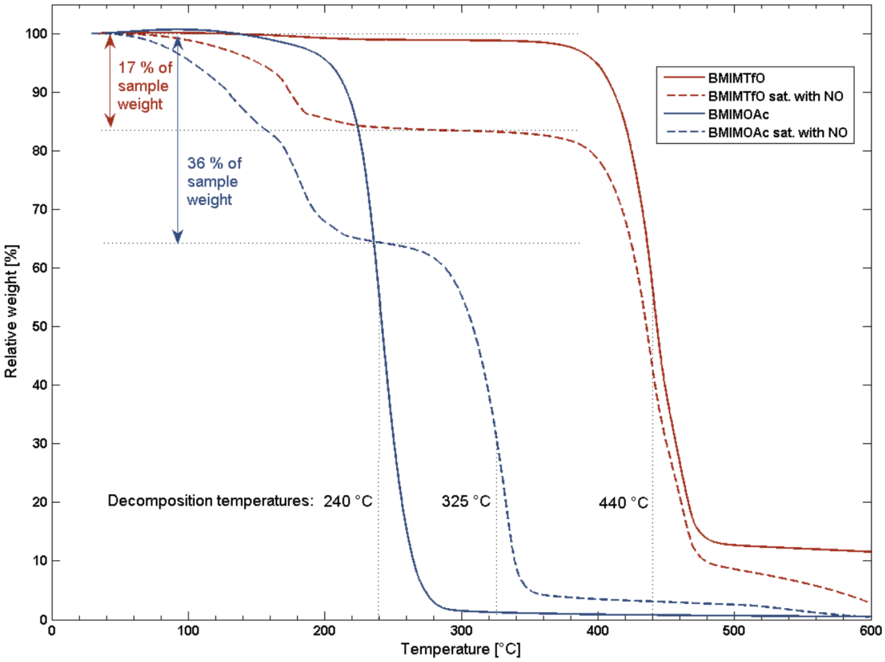

Figure S7: Thermogravimetric analysis (TGA) of bulk [BMIM][CH_3COO] and [BMIM][CF_3SO_3] after saturation with NO with traces of water and O_2.

TGA was recorded at a temperature ramp of 10 ℃/min of [BMIM][CH_3COO] (blue) and [BMIM][CF_3SO_3] (red, also written as [BMIM][OTf]) before (solid lines) and after (dashed lines) saturation with NO. The thermal stability of [BMIM][CH_3COO] increases significantly after absorption and oxidation of NO, resulting in a stability similar to that of [BMIM][NO_3]. The first loss of weight is thought to be due to desorption of HNO_3. The thermal stability of [BMIM][CF_3SO_3] remains unchanged after absorption and oxidation of NO, the only difference being the initial desorption of HNO_3. For [BMIM][CF_3SO_3], the initial weight loss corresponds to a molar ratio (HNO_3 : IL) of 1:2 instead of 1:1 as for [BMIM][CH_3COO].

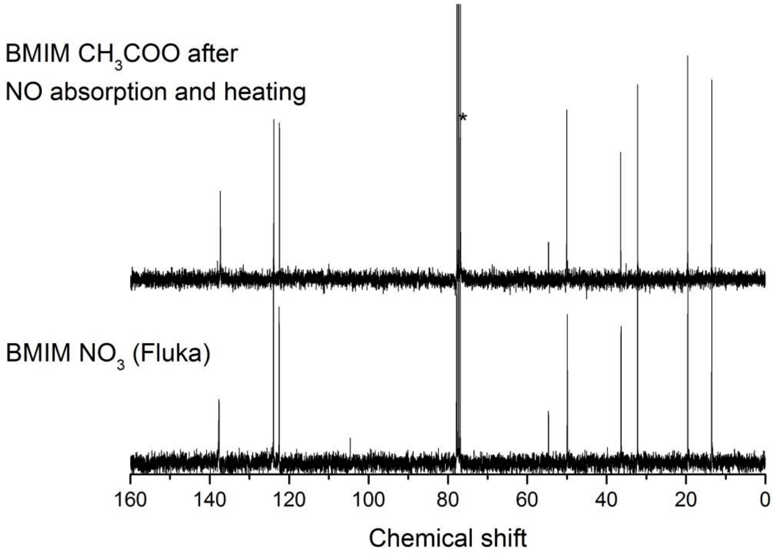

Figure S8: ^{13}C-NMR in CDCl$_3$ of [BMIM][CH$_3$COO] after one absorption desorption cycle compared with commercial [BMIM][NO$_3$].

^{13}C-NMR in CDCl$_3$ of bulk [BMIM][CH$_3$COO] after absorption of NO with traces of water and O$_2$ present, followed by static desorption at 120 ^{o}C (top). The spectrum is almost identical to a reference [BMIM][NO$_3$] spectrum (bottom); furthermore, all peaks assignable to acetate are absent. Asterisks denote solvent peaks.

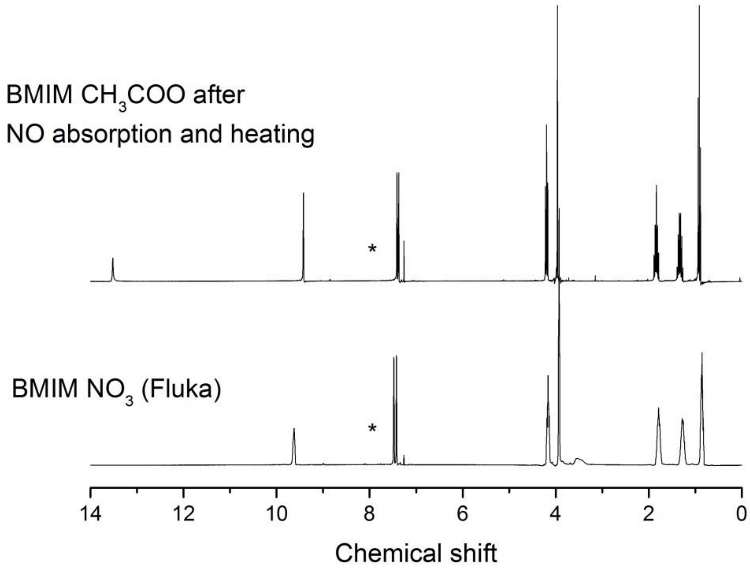

Figure S9: ^1H- NMR in $CDCl_3$ of [BMIM][CH_3COO] after one absorption desorption cycle compared with commercial [BMIM][NO_3].

^1H-NMR in $CDCl_3$ of [BMIM][CH_3COO] after absorption of NO with traces of water and O_2 present, followed by static desorption at 120 °C (top). The spectrum is almost identical to a reference [BMIM][NO_3] spectrum (bottom), apart from a strongly acidic proton (13.6 ppm) and a small shift of the peak of the aromatic H atom (~9.5 ppm). No chemical shifts assignable to acetate are present in the spectrum. The relative integration of the spectrum is not reliable for the acidic proton due to partial phase separation of the IL from the $CDCl_3$ in the top spectrum. Asterisks denote solvent peaks.

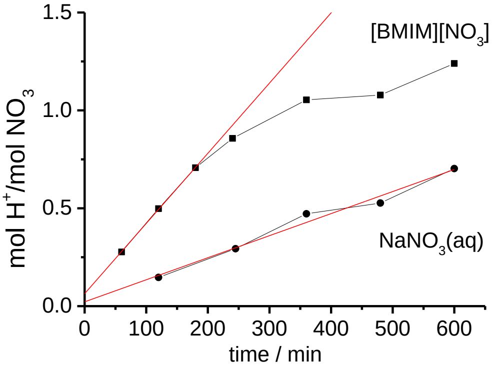

Figure S10: Comparison of absorption and oxidation of NO in bulk [BMIM][NO$_3$] (squares) and in 6 M NaNO$_3$ (circles).

A gas flow of 5 % v/v NO, 10 % v/v O_2 and 1.4 % v/v H_2O was bubbled through 3 mL of either [BMIM][NO$_3$] or 6 M NaNO$_3$. The reactions were stopped after the indicated time intervals, diluted with water and titrated with 0.10 M NaOH. The results are given as the molar amount of acidic protons divided by the amount of nitrate in the absorber before the reaction. The linear fit of all results for the aqueous solution and for the 0.5, 1 and 1.5 h data for the IL solution are shown. At longer times the conversion is slower for the IL as the solution goes to saturation. The ratio between the slopes of the two lines is 2.9.

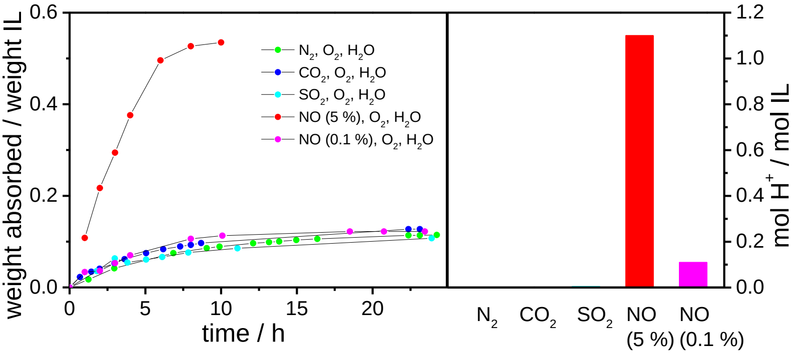

Figure S11: Comparison of accumulation in bulk [BMIM][NO$_3$] of inert gas, CO$_2$, SO$_2$ and NO.

A gas flow (40 mL/min) of 10 % v/v O$_2$ and 1.4 % v/v H$_2$O mixed with either N$_2$ (green), CO$_2$ (50 % v/v, blue), SO$_2$ (1% v/v, cyan) or NO (5 % v/v, red or 0.1 % v/v magenta) was bubbled through 1 g of initially dry [BMIM][NO$_3$]. The change in weight is given in the left graph and the content of acidic protons found by titration with 0.1 M NaOH at the end of the measurement is shown in the right graph. The end of the measurement was after 24 h for N$_2$, CO$_2$ and SO$_2$, after 10 h for NO (5 %) and after 36 h for NO (0.1 %).

Around 0.1 g of water was absorbed in the IL for all experiments. For CO$_2$ and SO$_2$ the interaction with the IL is a weak physisorption and for N$_2$ and CO$_2$ no acidity is detected. For SO$_2$ the solution is acidic but the molar equivalence point is only 0.004 relative to the IL. For NO (5 %) the oxidation to HNO$_3$ takes place and the solution is saturated after around 6 hours. For the low concentration of NO the saturation is slower since so little NO is added. The generated acidic protons correspond to ~15 % of the NO in the volume of the gas that had been bubbled through the IL over the 36 hours of the experiment.

Table S1: Individual reactions involved in the oxidation of NO to HNO_3 in [BMIM][NO_3].

The coefficients are given so that the total reaction equals $4\,NO + 3\,O_2 + 2\,H_2O \rightarrow 4\,HNO_3$.

Reaction	Reaction coefficient
$NO + NO_3^- \rightleftharpoons N_2O_4^-$	6
$N_2O_4^- \rightleftharpoons NO_2 + NO_2^-$	6
$2\,NO_2 \rightleftharpoons N_2O_4$	4
$N_2O_4 + H_2O \rightleftharpoons NO_3^- + HNO_2 + H^+$	4
$H^+ + NO_2^- \rightleftharpoons HNO_2$	6
$2\,HNO_2 \rightleftharpoons (HNO_2)_2$	5
$(HNO_2)_2 + O_2 \longrightarrow 2\,NO_3^- + 2\,H^+$	3
$(HNO_2)_2 \longrightarrow H_2O + NO_2 + NO$	2
$H^+ + NO_3^- \rightleftharpoons HNO_3$	4

References

[1] Kunov-Kruse, A. J.; Riisager, A.; Saravanamurugan, S.; Berg, R. W.; Kristensen, S. B.; Fehrmann, R. *Green Chem.* **2013**, *15* (10), 2843.

C.3 Absorption of Flue-Gas Components by Ionic Liquids

H. Kolding, P. Thomassen, S. Mossin, S. KegnÃęs, A. Riisager, J. Rogez, G. Mikaelian, and R. Fehrmann
Electrochemical Society Transactions, **2014**, 64, 97-108

Absorption of Flue-Gas Components by Ionic Liquids

H. Kolding[a], P. Thomassen[a], S. Mossin[a], S. Kegnæs[a], A. Riisager[a], J. Rogez[b],
G. Mikaelian[b], and R. Fehrmann[a]

[a]Centre for Catalysis and Sustainable Chemistry, Department of Chemistry, Technical University of Denmark, DK-2800 Kgs. Lyngby, Denmark
[b]TECSEN, UMR6122, CNRS-Université Paul Cezanne, Aix-Marseille III, France

Gas separation by ionic liquids (ILs) is a promising new research field with several potential applications of industrial interest. Thus cleaning of industrial off gases seems to be attractive by use of ILs and Supported Ionic Liquid Phase (SILP) materials. The potential of selected ILs for absorption of NO_X, CO_2 and SO_2 are demonstrated and the possible mechanism of absorption described on the molecular level. Special focus regards the interaction of the ILs with water vapor, which is an important feature in envisaged application of flue gas cleaning in power plants, waste incineration plants, cement and glass factories as well as on board ships.

Introduction

A major concern in relation to atmospheric pollution and climate changes is emission of acidic gases such as NO_X, SO_X and CO_X from combustion of fossil fuels in, e.g. power plants. Accordingly, these gases have to be effectively removed from flue gases. Presently this is mainly achieved by relatively energy intensive and resource demanding technologies via selective catalytic reduction (SCR) of NO_X with ammonia, SO_2 wet-scrubbing by lime obtaining gypsum and CO_2 wet-scrubbing with organic amines obtaining carbamates. The latter leads to particular concern about, e.g. intensive energy requirements for desorption, corrosion of steel pipes and pumps, CO_2 absorption capacity and thermal decomposition of the amine.

In this work we demonstrate how ionic liquids (ILs) can be applied as selective, high-capacity absorbents of environmentally problematic flue gases like, e.g. SO_2, NO/NO_2 and CO_2. Reversible absorption has been obtained for several different ILs at different temperatures and flue gas compositions. The structures of ILs are well-ordered even in the liquid state with regular cavities which can host selected solute species depending on the IL ion composition. This makes the materials promising for selective, reversible absorption of gaseous pollutants in, e.g. power plant flue gases and other industrial off-gases (1,2). Furthermore, different porous, high surface area carriers like mesoporous silica and titania have been applied as supports for the ionic liquids to obtain Supported Ionic Liquid-Phase (SILP) absorber materials, Figure 1. These materials benefit from low mass transport resistance of the often highly viscous ILs by the distribution of the liquid as a thin film (or small droplets) on the surface of highly porous carrier materials which enable fast absorption/desorption rates of the particular gas exposed to the SILP absorber (3).

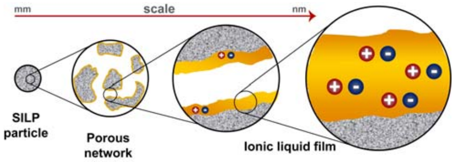

Figure 1. Principle of SILP materials.

Experimental

Materials

Synthesis of 1-butyl-3-methylimidazolium nitrate [BMIm]NO_3. 1-butyl-3-methylimidazolium nitrate was prepared using commercially available [BMIm]Cl (Fluka, >99%). The anion was exchanged by dissolving the [BMIm]Cl in water and adding a solution of silver nitrate in water to precipitate AgCl. Just below equivalent amounts of $AgNO_3$ was used to avoid silver pollution in the IL. After mixing, the solution was left overnight to ensure complete precipitation. The solution was then filtered (repeated 6 times) after gently heating to aid clotting of the precipitate. Finally, the water was removed under reduced pressure (10 mbar, 40°C) followed by heating under high vacuum resulting in clear viscous [BMIm]NO_3. The water content of the IL was measured by Karl Fisher titration to be 1.1%.

Synthesis of 1,1,3,3-tetramethylguanidinium chloride [TMGH]Cl. The 1,1,3,3-tetramethylguanidinium chloride was prepared by direct neutralization of an ethanolic (99.9%, Aldrich) solution of TMG (99%, Aldrich) with hydrochloric acid (37%, Aldrich) (4). To an ice-bath cooled stirred solution of TMG (11.5 g, 0.10 mol) in ethanol (100 mL) concentrated hydrochloric acid (0.10 mol) was carefully added. Caution: neutralization of base with a strong acid is highly exothermic. After continuous stirring (25 °C, 24 h), the solvent was removed under reduced pressure with heating at 70°C followed by heating under high vacuum. The product was recrystallized in ethanol.

Synthesis of tetrahexylammonium prolinate [N6666][Pro]. 40 wt% aqueous solution of tetrahexylammonium hydroxide, [N6666]OH (13.92 g, 15 mmol, Sigma-Aldrich) and L-proline (1.89 g, 16 mmol, Sigma-Aldrich) was mixed and the solution stirred overnight at room temperature to ensure full deprotonation of the amino acid. Most of the water was removed under reduced pressure (10 mbar, 40 °C), and excess amino acid removed from the product by filtration after addition of cold acetonitrile (10 mL) and immersion into an ice bath for 1 h. Finally, the solvent was evaporated under reduced pressure to obtain the IL. The NMR and FT-IR spectra confirmed the identity of the ionic liquid. The purity of the IL was estimated by integration of visible impurities in the ^{1}H NMR spectrum. Yield > 99 %. Purity > 99 mol %.

Preparation of SILP absorbers. The SILP absorbers were prepared using fractioned (180-355 µm) silica, anatase and carbon support materials. The pore volume and specific area of the support materials were determined from nitrogen physisorption by BET measurements on a Micromeritics ASAP 2020 pore analyser after out gassing the samples in vacuum at 200 °C prior to measurement (see Table I).

TABLE I. Characteristics of the SILP support materials.

Support material	Type	Surface Area (m^2/g)	Pore Volume (cm^3/g)
Carbon	Black Pearl 1400 (Cabot)	580	0.71
Anatase	ST 31119 (Saint-Gobain)	150	0.38
Silica	SS 611138 (Saint-Gobain)	251	0.93
Silica	Gel-90 (Fluka)	257	0.93

NO SILP absorbers were prepared by suspending support material in an excess of solvent (methanol for anatase and silica, dichloromethane for carbon) and then adding [BMIm]NO_3 corresponding to a pore volume filling degree of 25-30% to the mixture. After stirring the solvent was removed using a rotary evaporator. The evaporation was performed at slightly reduced pressure and ambient temperature in order to give the best possible distribution of IL on the surface of the support. In the case of silica (Saint-Gobain), two type of SILP absorbers were prepared; one with the fractioned silica as is and one with fractioned silica that had been calcined at 500 °C for 20 h and cooled to room temperature in a desiccator.

SO_2 SILP-absorbers were made in a similar way as the NO SILP absorbers by wet impregnation by an ethanolic solution of [TMGH]Cl on SiO_2 (Fluka). In the investigation only the absorption optimized SILP of 20 wt% was used.

Gas absorption methods

NO absorption: NO removal with SILP-absorbers was performed using a fixed-bed reactor system with about 3 g SILP absorber as outlined previously (5). A simulated flue gas containing 0.2 vol% NO (AGA) and 16 vol% O_2 in N_2 with and without ~2 vol% water was adjusted by Bronkhorst mass-flow controllers to a total flow of 50 ml/min and passed through the reactor interacting with all of the material. The reaction was followed by gas phase UV-Vis (Lambda 11 UV/Vis spectrophotometer) with a gas cuvette of path length 10 cm downstream of the reactor. The NO removal could be followed by integration of the characteristic lines from NO (227 nm) in the spectrum and comparison to the spectrum of the bypass flow. NO_2 and N_2O_5 were observable as a broad, slightly asymmetrical band at approximately 218 nm (NO_2) and a broad, symmetrical band centered at around 191 nm (N_2O_5). The amounts of these gases could not be quantified reliably by the same method.

SO_2 absorption: The measurements on the SO_2 SILP-absorbers were performed in a similar setup as used for the NO absorption studies (see above) using about 4 g of absorber and a dry or wet gas flow of 100 ml/min 3% SO_2 in N_2 (Air Liquide). The SO_2 concentration in the carrier stream was determined by UV-Vis (JACS V570 UV/Vis/NIR spectrophotometer).

CO_2 absorption: Absorption of CO_2 in different amino acid-based ILs was performed at 1 bar CO_2 at room temperature with 1.0-1.2 g ILs in bubble reactors by monitoring the mass increase on an analytic balance (Sartorius CPA324S, accuracy ±0.0001 g) at regular intervals.

Thermal methods

Enthalpy of fusion and heat capacity: Enthalpy of fusion (ΔH_{fus}) and heat capacity (C_p) were measured for SO_2 absorption with a DSC 111 SETARAM calorimeter. The temperature of the thermostat was measured by the resistance of a suitable Pt resistor, which was calibrated by the melting points of standards. All around the reference and the sample cylindrical cells were placed thermopiles of Tian-Calvet type, which consists of many thermocouples connected in series. At a given temperature, the voltage difference between the two thermopiles is proportional to the differential heat flux through the walls of the reference and the sample cells. By recording the thermogram the enthalpy of reaction or transformation can be measured. For an ideal instrument of perfect thermal symmetry, the differential heat flux is zero under constant temperature or dynamic changing temperature conditions. Asymmetries may arise from several effects: Static effects due to the ineluctable asymmetry in the cells and sensors and their location, which translate into a stationary flux recorded at any given temperature. The data processing must take the corrections of asymmetric heat flows into account.

C_p was measured by the step method which consists in programing the temperature and measuring differential heat fluxes between reference and sample cells. At each step the integration of the differential heat flux divided by the temperature step gives the value of C_p. First a blank experiment using empty sample containers was performed. Then, at the same temperature and time conditions a known mass of sample was added in the sample container and a similar run achieved. Calibration with a standard NBS-Al_2O_3 sample finished the measurement. An inaccuracy generally less than 5% is expected forenthalpy and C_p measurements.

Heat of gas absorption: The integral or partial enthalpies of dissolution of gases in liquids or solids (ΔH_{diss}) can be measured by direct reaction calorimetry. In an ambient temperature Tian-Calvet calorimeter, the sorbent was placed in a special glass cell containing a device for flowing a gas or a mixture of gases. The applied calorimeter was of classical design with thermopiles as described above, but including hundreds of thermocouples. The heat flux sensitive volume was 14 cm^3. The calorimeter with special characteristics of high sensibility (70 µW/µV) and very high stability (less than ± 20µW over several days) was used in isothermal mode up to 80 °C in a temperature controlled room at 19.5 ± 0.1 °C. The gas flow was controlled by Brooks mass-flow meters calibrated for SO_2 and Ar, respectively, at a sufficiently low flow not disturbing the heat flow of the calorimeter.

Results and Discussion

NO absorption

Recently, it has been found that NO can be absorbed and oxidized to nitric acid (HNO_3) in several ILs according to equation [1] (6,7).

$$4\ NO + 3\ O_2 + 2\ H_2O \rightarrow 4\ HNO_3 \qquad [1]$$

Water is needed in the reaction but it is also possible that water can inhibit the uptake of NO. It is most probable that the anion of the IL activates the otherwise unreactive NO molecule by nucleophilic attack. Extensive hydrogen bonding is expected to take place when water is dissolved in the IL, possibly weakening the basicity and the nucleophilic strength of the anion. The identity of the cation of the IL does not seem to play any significant role for the rate nor the capacity (6). In analogous measurements with SILP materials containing other IL anions (results not shown) a different initial rate of uptake was found.

The initial absorption capacity (interpreted as the UV-silent time) of a SILP material consisting of $[BMIm]NO_3$ on anatase was determined at water:NO molar ratios of 1:1 and 10:1 in the gas corresponding to 2:1 and 20:1 in stoichiometric terms according to equation [1] (Figure 2). The initial uptake appeared to be largely independent of the water concentration, and no apparent inhibition was found when increasing the water content of the simulated flue gas. At steady state a small but significant decrease in NO_2 content in the effluent flue gas was observed. This is likely caused by a larger fraction of the NO_2 molecules reacting with water according to equation 2.

$$2NO_2 + H_2O \rightarrow HNO_3 + HNO_2 \qquad [2]$$

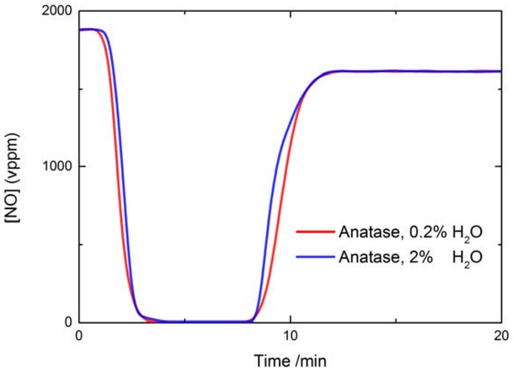

Figure 2. Concentration of NO measured downstream of the absorber for an anatase SILP with a water:NO molar ratio of 1:1 (0.2 % water) and 10:1 (2 % water).

The absorption reaction was also investigated with lower than stoichiometric amounts of water and examples of resulting spectra after breakthrough are shown in Figure 3 for a carbon and a (uncalcined) silica based SILP, respectively. The broad absorption band seen in Figure 3 is interpreted as N_2O_5. It is usually observed in the absorption spectra when the water content of the flue gas is low. The amount of N_2O_5 increased significantly when applying more hydrophobic supports (e.g. carbon) for the SILP absorber. The formation of N_2O_5 under dry conditions is suggested to be facilitated by ionization of N_2O_4 to NO_2^+ and NO_2^- in the IL (6). The formed NO_2^+ can undergo further reaction with NO_3^- from the IL to form N_2O_5 observed in the gas phase downstream of the absorber. When water is present both the N_2O_4 and the N_2O_5 dissolved in the IL reacts with water, leading to formation of HNO_3 which accumulates in the IL due to the formation of strong symmetric hydrogen bonds with the nitrate anion.

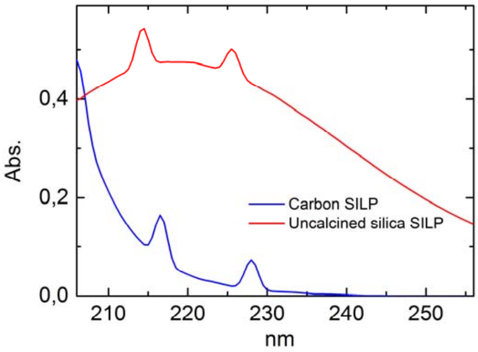

Figure 3. Post-breakthrough spectral data at sub-stoichiometric amounts of water, for two different SILP formulations.

<u>SO_2 absorption</u>

Figure 4 shows the results of the absorption measurements of 0.15 % of SO_2 in dry N_2 and with 2 % water vapour at 30 °C for a SiO_2 based SILP absorber with 20 wt% [TMGH]Cl. The figure shows the amount of SO_2 (mmol) detected in the gas stream after the absorber as a function of time. In the experiment the gas stream was initially bypassing the absorber and directed to the detector and after 10 min the gas flow was led to the reactor with the absorber material. From Figure 4 it is seen that the concentration of SO_2 in the gas stream dramatically drops after the gas flow was shifted from the bypass to the reactor with the absorbent. It is also seen that when the saturation of the investigated material with SO_2 is completed, the concentration of SO_2 in the outlet gas began to increase. After ca. 80 min of the reaction the concentration of SO_2 in the outlet gas was identical to the concentration of SO_2 in the inlet gas.

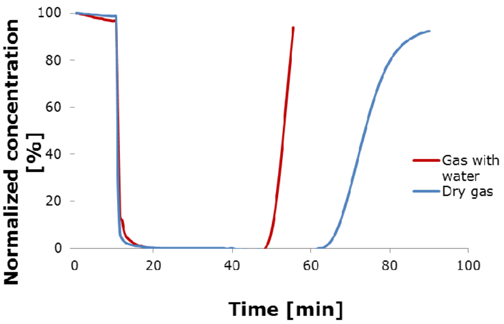

Figure 4. SO_2-absorption by 20 wt% [TMGH]Cl-SiO_2 SILP absorber in dry 0.15 % SO_2/N_2 and this gas saturated with water (3 %) until breakthrough.

The total absorption capacity for SO_2 (1500 ppm in N_2) for the 20 wt% [TMGH]Cl-SiO_2 SILP absorber at the given conditions is determined by integration of the area of absorption within the curve from 10 to ca. 80 min to be 0.05 mole fraction SO_2 in the IL for the dry gas and reduced by ca. 35% in the wet gas. The absorber material was tested by absorption and desorption of SO_2 up to 10 times in the dry gas without any significant changes in the absorption capacity as shown in our previous work (5).

Based on a X-ray investigation of crystals obtained of the SO_2 adduct [TMGH]Cl·SO_2, we previously suggested strong interaction between Lewis basic chloride ions and the Lewis acidic SO_2 molecules to account for the high absorption affinity of the salt (4). With water present in the gas the capacity is significantly reduced probably due to competition between water molecules and SO_2 regarding coordination to Cl^-. This scenario will be further elucidated by ongoing Raman spectroscopic investigations. However, thermal investigations allowed providing insight about the energy of these interactions in dry and wet gases.

Thermal investigations of SO_2 and H_2O absorption

The DSC investigations were performed on samples of 60-80 mg of [TMGH]Cl loaded in a dry box into aluminium capsules and sealed airtight by pressing an aluminium lid into the capsule using a Ni-joint. The thermogram (DTA) was run in the range 26-225 °C at a rate of 1 °C/min. The thermogram exhibited one endothermic peak corresponding to the fusion of [TMGH]Cl at 205 °C in good accordance with the previously reported value of 208-209 °C (4).

The heat of fusion (ΔH_{fus}) of [TMGH]Cl was found to be 22.5 kJ/mol. There is no value in the literature to compare with as far as we know. The measured heat capacities (C_p) varied in the range 200-300 J/mol·K for the solid state, expressed by the polynomium $191 + 0.645 \cdot T$ in the temperature range 26-176 °C, and is equal to 420 J/mol·K within the experimental error for the liquid state in the short interval 206-225 °C.

In Figure 5 the thermograms obtained on [TMGH]Cl at 25 °C in the calorimeter under a flow of dry SO_2 gas and humid gas (2.3% H_2O in SO_2) at 1 bar total pressure are shown. The absorption of dry SO_2 gas lead to a strong exothermic effect, which by integration after calibration by heat pulses from an electrical resistance in contact with the experimental cell, gives a value of 90.35 kJ/mol for the heat of absorption of [TMGH]Cl. By weighing of the solid sample after the experiment the mole ratio of SO_2:[TMGH]Cl in the solid in the cell was found to be 1.15. These values were found to be 74.66 kJ/mol and 1.19 at 50 °C and 9.62 kJ/mol and 0.40 at 84 °C, respectively, indicating an increasingly weaker bonding of SO_2 by increasing temperature.

The absorption of humid SO_2 gas in [TMGH]Cl at 25 °C leads to an exothermic peak as well, but with a heat of absorption of 145.73 kJ/mol. The kinetics of the absorption process was obviously different for the two experiments being very slow in the humid gas only obtaining equilibrium after several days, while the dry gas absorption process was much faster taking only a few hours to reach equilibrium, as realized by blow up of the tail end of the thermograms (not shown). A marked difference was that the final product after humid gas exposure was a liquid, while it was a solid up to around 85 °C in dry gas where it starts to melt incongruently under 1 bar dry SO_2. This solid is presumably the adduct compound TMGH]Cl·SO_2, which structure has been described recently (4).

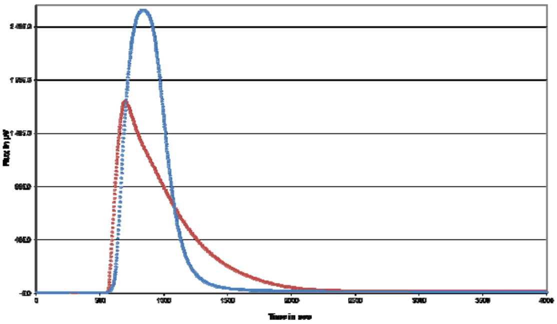

Figure 5. Thermograms (selected time period) of 1 mmol [TMGH]Cl in dry SO_2 (blue) and in humid SO_2 with 2.3 % H_2O vapor (red) at 25 °C with gas flow of 5.0 ml/min.

The absorption process in the humid gas comprised two components: A fast exothermic coordination of SO_2 to the solid TMGH]Cl followed by a slower uptake and less exothermic absorption of H_2O eventually leading to fusion of the mixture. The quantification of the equilibrium mole ratio SO_2:[TMGH]Cl in the humid gas at equilibrium is in progress. Desorption by a flow of dry Ar through the cell at 25-50 °C is a slow process leading to almost the same enthalpy as for the absorption, but slightly lower indicating that it was difficult to completely remove the absorbed components. However, successive absorption of SO_2 appeared completely reversible in this temperature range. From previous measurements on SILP absorbers (3) it is obvious that fast and reversible desorption can be performed by raising the temperature to 120 °C in a flow of, e.g. N_2 or air.

In a separate experiment at 25 °C with a flow of Ar and 2.3 % H_2O vapour, again a rather fast exothermic absorption of water by [TMGH]Cl was observed followed by a very slow further absorption of water reaching equilibrium only after several days. Again the solid was transformed to a liquid. Here the weight increase corresponded to a molar ratio H_2O:[TMGH]Cl of 4.42 and a heat of absorption of 289 kJ/mol [TMGH]Cl or 65.3 kJ/mol H_2O. This latter value is significantly higher than the heat of vaporization of water of 43.9 kJ/mol also at 25 °C. This indicates a much stronger interaction of the H_2O molecules with the ions in the formed IL, than in pure water at the same conditions. Further progress on the thermal measurements is expected in the near future.

CO_2 absorption

Previous results from our group for CO_2 absorption by amino acid-based ILs show a super-stoichiometric uptake of CO_2 (8). The effect of water on the ILs ability to take up water is explored here. Water content seems to play an important role for CO_2 absorption by amino acid-based ILs. Not only does it lower the ILs viscosity, but it also seems to have a large positive effect on the CO_2 absorption stoichiometry and -rate. This can be seen for the IL [N6666][Pro] in Table II and Figure 6.

TABLE II. Effect of water on CO_2 absorption capacity in neat [N6666][Pro] IL at room temperature.

Entry	Ionic liquid	Water content (qualitative assessment)	CO_2 absorption stoichiometry (mol CO_2/mol IL)
1	[N6666][Pro]	Wet[a]	0.71
2	[N6666][Pro]	Dried[b]	0.38
3	[N6666][Pro]	Very dry[c]	0.93

[a] Dried at 15 mbar for 1 h. Probably 5-10 % water. [b]Dried at 1 mbar for 24 h. Probably 1-2 % water. [c] Dried at 1 mbar for 24 h followed by three freeze-pump-thaw cycles. Water content measured to be < 0.01 % by Karl-Fischer.

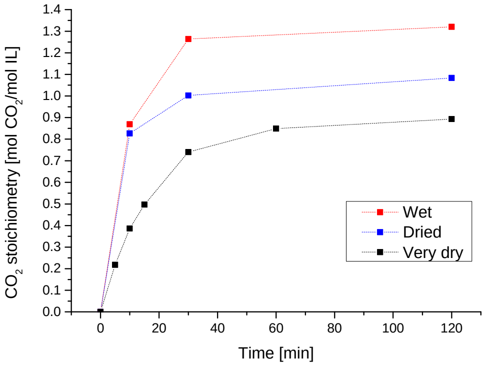

Figure 6. CO_2 absorption capacity in [N6666][Pro] at room temperature as a function of time with varying degrees of IL dryness (see Table II).

In the experiment, all mass at time zero was assumed to be IL and the absorption stoichiometries have been calculated accordingly, despite that a significant percentage of the wet sample was water. Surprisingly, a higher water content was not only associated with a higher CO_2 uptake stoichiometry, but seems to be a prerequisite for the previously reported super stoichiometric CO_2 uptake (8). The solubility of CO_2 in pure water at 25 °C and 1 atm is only $6 \cdot 10^{-4}$ mol per mol of H_2O (9). Hence, this low value cannot account for the added CO_2 absorption, but the water content in the IL is most likely responsible for the super stoichiometric CO_2 uptake.

CO_2 absorption in the samples was measured by mass increase, but it can be hard to correct for a possible loss of weight from evaporation of water. Therefore, an experiment was devised in which the CO_2 absorption of the very dry sample was compared to that of a sample absorbing from a gas stream that had been pre-saturated with water by passing the gas through a wash bottle with water at room temperature. Absorption from both wet CO_2 and wet Ar gas was followed, and it is assumed that the water content in the gas streams were identical. This can be seen from Figure 7. The sample in the wet Ar stream did not - strictly speaking - take up CO_2, but as “stoichiometry” scales linearly with weight it allowed directly comparison of the samples.

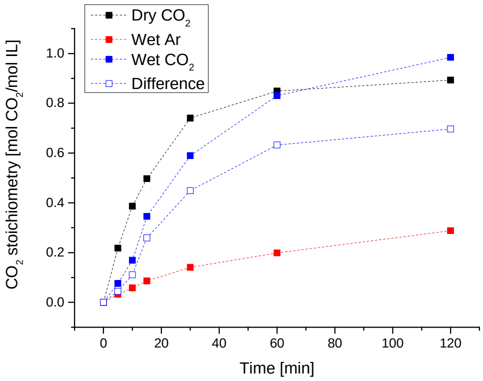

Figure 7. Uptake of CO_2 by dry [N6666][Pro] at room temperature during absorption in dry CO_2 (black), in wet Ar (red) and in wet CO_2 (blue, full), as well as in wet CO_2 corrected for mass increase in wet Ar (blue, open).

The mass of the sample in wet CO_2 did not increase more rapidly than the sample in dry CO_2. This is in agreement with experiments performed with 1,1,3,3-tetramethyl-guanidinium imidazolate [TMGH][Im], where presence of water slowed down the CO_2 absorption (10). A first impulse would be that the IL at first is “busy” taking up water, and it only gains absorption momentum later, which is in agreement with a minimum amount of water being needed for rapid uptake of CO_2.

Figure 8. Absorption stages in dry [N6666][Pro]. The IL is initially transparent (left) but a turbid phase appeared during absorption (right).

A possible explanation for the difference in absorption stoichiometry and rate in the presence of pre-absorbed water (Table II and Figure 7), is possibly that water facilitate a different mechanism for uptake of CO_2 that is not available in a dry gas stream. This is supported by the qualitative assessment of the ILs upon CO_2 absorption. During absorption, a turbid phase appeared in the dried and very dry samples after absorbing 1.00 and 0.38 equivalents, respectively (see Figure 8). This turbid phase did not appear during absorption in the wet sample. This suggests that pre-absorbed water has a highly positive influence on CO_2 absorption in amino acid-based ILs. For some reason, concerted absorption of water and CO_2 did not see this positive effect – possible because water was not absorbed sufficiently fast.

Conclusions

The presented results demonstrate that NO/NO_2, SO_2 and CO_2 can be absorbed by ILs through different mechanisms of absorption. Furthermore, impregnation of porous solids to make Supported Ionic Liquid-Phase (SILP) absorbers leads to solid materials with good absorption/desorption dynamics. However, water plays a significant role for the absorption processes and the absorption capacities regarding the different gases and the investigated ILs.

Unlike separation of other acidic gases (e.g. SO_2 and CO_2) using ILs, NO absorption and oxidation in IL-based materials is less dependent on the nature of the anion. It is also less affected by the presence of large amounts of water in the gas flow. Water is necessary to provide the final product - nitric acid - but the reaction can also proceed under relatively dry conditions. In this case, the products are more dominated by the anhydrous oxidation products N_2O_4 and N_2O_5. The observation that a large excess of water is not detrimental to the removal of NO is a big advantage for deNOx applications, since most flue gases contain large quantities of water. Furthermore, the hydrated conditions might hinder or slow down possible accumulation and poisoning of the NO absorbers by other acidic gases. Regarding absorption of SO_2 and CO_2 initially the presence of water is similarly not a drawback. It may even enhance the kinetics of absorption until saturation, but further uptake of water may lead to increasingly substitution of the absorbed molecules, thus decreasing the overall capacity for the flue-gas absorption.

The absorption/desorption process may be performed by SILP materials shaped in honey comb structures as the traditional SCR $deNO_X$ catalyst used in power plants today, leading to optimized gas diffusion and low pressure drop of the passing flue gas. Installed as a traditional rotating heat exchanger it will facilitate desorption by elevation of the temperature in a smaller side channel and make it possible to desorb the gases in concentrated form.

Acknowledgments

Energinet.dk, DONG Energy A/S, Vattenfall A/S, LAB S.A. Lyon, France and the Danish Maritime Fund are greatly acknowledged for financial support.

References

1. J. Huang, A. Riisager, P. Wasserscheid and R. Fehrmann, *Chem. Commun.*, 4027 (2006).
2. W. Wu, B. Han, H. Gao, Z. Liu, T. Jiang and J. Huang, *Angew. Chem. Int. Ed.*, **43**,

2415 (2004).

3. S. Shunmugavel, S. Kegnæs, J. Due-Hansen, T. A. Gretasdottir, A. Riisager and R. Fehrmann, *ECS Trans.*, **3**, 49 (2007).
4. R.W. Berg, P. Harris, A. Riisager and R. Fehrmann, *J. Phys. Chem.* A, **117**, 11364 (2013).
5. P. Thomassen, A.J. Kunov-Kruse, S. Mossin, H. Kolding, S. Kegnæs, A. Riisager and R. Fehrmann, *ECS Trans.*, **50**, 433 (2012).
6. S. Mossin, A.J. Kunov-Kruse, P. Thomassen, A. Riisager and R. Fehrmann, submitted.
7. A. Riisager, A. J. Kunov-Kruse, S. Mossin and R. Fehrmann, Patent Application *EP11191127.7* (2011).
8. H. Kolding, A. Riisager and R. Fehrmann, *Sci. China Chem.*, **55**, 1648 (2012).
9. J.J. Carroll, J.D. Slupsky and A.E. Mather, *J. Phys. Chem. Ref. Data*, **20**, 1201 (1991).
10. X. Lei, Y. Xu, L. Zhu and X. Wang, *RSC Adv.*, **4**, 7052 (2014).

C.4 Selective Reversible Absorption of the Industrial Off-Gas Components CO_2 and NO_x by Ionic Liquids

P. Kaas-Larsen, P. Thomassen, L. Schill, S. Mossin, A. Riisager, and R. Fehrmann

Electrochemical Society Transactions, **2016**, 75, 3-16

ECS Transactions, 75 (15) 3-16 (2016)
10.1149/07515.0003ecst ©The Electrochemical Society

Selective Reversible Absorption of the Industrial Off-Gas Components CO_2 and NO_X by Ionic Liquids

P. K. Kaas-Larsen, P. Thomassen, L. Schill, S. Mossin, A. Riisager, and R. Fehrmann

Centre for Catalysis and Sustainable Chemistry, Department of Chemistry, Technical University of Denmark, DK-2800 Kgs. Lyngby, Denmark

Ionic liquids are promising new materials for climate and pollution control by selective absorption of CO_2 and NO_x in industrial off-gases. In addition practical cleaning of industrial off gases seems to be attractive by use of ionic liquids distributed on the surface of porous, high surface area carriers in the form of so-called Supported Ionic Liquid Phase (SILP) materials. The potential of selected ionic liquids for absorption of CO_2 and NO_x are demonstrated and the possible interference of other gases influencing the stability and absorption capacity of the ionic liquids are investigated as well.

Introduction

Atmospheric pollution and climate changes is now recognized to be severely influenced by emission of acidic gases such as NO_X, SO_X and CO_X from combustion of fossil fuels in, e.g. power plants, cement factories and ships. Accordingly, these gases have to be effectively removed from flue gases. Presently this is mainly achieved by relatively energy intensive and resource demanding technologies via selective catalytic reduction (SCR) of NO_X with ammonia, SO_2 wet-scrubbing by lime obtaining gypsum and CO_2 wet-scrubbing with organic amines. The latter leads to particular concern about, e.g. intensive energy requirements for desorption, corrosion of steel pipes and pumps, CO_2 absorption capacity and thermal decomposition of the amine.

The structures of ionic liquids (ILs) are well-ordered even in the liquid state with regular cavities which can host selected solute species depending on the IL ion composition. This makes the materials promising for selective, reversible absorption of gaseous pollutants in, e.g. industrial off-gases (1,2).

In this work we demonstrate how more environmental friendly ILs as amino acid based ones can be applied as selective, high-capacity absorbents of CO_2, exemplified by a tetraalkylphosphonium prolinate IL. In the context of CO_2 removal, ILs are considered environmentally friendly because they are not emitted to the environment due to their negligible vapor pressure. In addition, an imidazolium nitrate IL is also investigated regarding absorption of NO. Only few publications deal with possible interferences of other flue gas components with the IL absorbers. Thus we here also investigate the interaction of the selected ionic liquids with SO_2, CO_2, NO and air. Furthermore, different porous, high surface area carriers like mesoporous silica has been applied as supports for the ionic liquids to obtain Supported Ionic Liquid-Phase (SILP) absorber materials, Figure 1. These materials benefit from low mass transport resistance of the often very viscous ILs by the distribution of the liquid as a thin film (or small droplets) on the surface of the highly porous carrier materials enabling fast absorption/desorption rates of the particular gas to be removed by the SILP absorber (3).

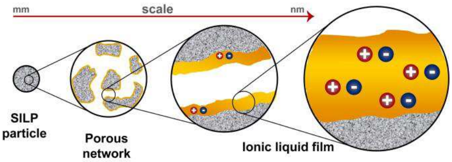

Figure 1. Principle of SILP materials.

Experimental

Materials

Synthesis of tetrabutyl phosphonium prolinate ([P4444][Pro]): 23.5 g of tetrabutylphosphonium bromide (Sigma-Aldrich, >98 %) (69.3 mmol) were dissolved in 65mL water and added to a beaker containing 105 g Amberlite IRN-78 (Sigma-Aldrich). The solution was left over night at room temperature under continuous stirring. XRF analysis indicated 98.7 % exchange of bromide. Additional 110 g Amberlite IRN-78 was added to the solution and left stirring for 20 h at room temperature. XRF analysis indicated 99.4 % exchange of bromine. The resin was decanted from the solution, and rinsed with 130 mL water to ensure minimal loss of tetrabutylphosphonium hydroxide. 7.747 g L-proline (Sigma-Aldrich, > 99 %) (67.5 mmol) were added to the solution and left stirring for 6 days at room temperature, until an aqueous solution containing roughly 50 wt% of [P_{4444}][Pro] was obtained (55 mL). NMR and dynamic TGA analysis confirmed the identity of the ionic liquid.

Synthesis of SiO_2 extrudates (monoliths): Cylindrical, small-scale monolithic samples were obtained by extrusion. De-ionized water, silica gel 60 (Merck) and sepiolite (Sigma Aldrich) were thoroughly mixed. The resulting paste was subsequently extruded, using a 5 mL syringe with an orifice of 2 mm, and left drying over night at room temperature followed by drying at 100 °C for 3 h. Calcination was carried at with a heating ramp of 96 °C/h to 500 °C and a dwelling time of 5 h. Two batches of extrudates were prepared. E-batch-1 contained 65 wt. % and e-batch-2 45 wt. % of sepiolite. The pore volume of the extrudates was determined by measuring the weight difference of a sample before and after saturation with water. The density was determined by measuring the weight of a known amount of extrudate plus water to yield 10 mL in a measuring jug. All measurements were carried out three times. Pore volumes of 0.970 ± 0.017 mL/g and 1.479 ± 0.107 mL/g and densities of 0.610 ± 0.038 g/mL and 0.476 ± 0.017 g/mL were measured for e-batch-1 and e-batch-2, respectively.

Preparation of SILP materials: The cylindrical monoliths were broken down into pieces sized (length) roughly 1-2 cm. These pieces were dipped into the aqueous solution containing roughly 50 wt. % of $[P_{4444}]$[Pro] until no more air bubbles appeared (max. 5 min) followed by placement on a paper towel for about 30 s in order to avoid formation of a thick IL film on the outside of the monoliths. The obtained SILP materials were dried over night at room temperature followed by 30 min at 80 °C under atmospheric conditions prior to CO_2 absorption studies. The IL loading was determined by measuring the weight of the monoliths dried at 80 °C before and after impregnation with $[P_{4444}]$[Pro]. Two portions of SILP material are based on e-batch-1 and are denoted s1-batch-1 and s2-batch-1. The respective IL loadings are 32.1 and 33.9 wt. %. One SILP material is based on e-batch-2 and is denoted s1-batch-2 and has an IL loading of 46.3 wt. %.

Characterization

Nuclear magnetic resonance (NMR): ^{1}H and ^{13}C NMR experiments on [P4444][Pro] dissolved in D_2O were carried out on a Varian Mercury 400 MHz instrument. Both the neat IL and IL extracted from monoliths were analyzed before and after long term exposure to 80 °C (atmospheric conditions).

Attenuated Total Reflectance – Fourier Transform Infrared Spectroscopy (ATR-FTIR): ATR-FTIR was performed on a Bruker Alpha FTIR spectrometer with a diamond plate. All spectra were recorded with a 4 cm^{-1} resolution with fresh background (taken before each experiment). There is no purge gas, but the Bruker software (OPUS) was used for atmospheric suppression.

Thermogravimetric analysis (TGA): Dynamic TGA experiments were conducted on a Mettler Toledo (TGA/DSC1 STARe System) instrument. In a typical experiment, about 20 mg of sample were heated from room temperature to 400 °C at a rate of 10 °C/min under a N_2 flow (50 mL/min). Long term stability under atmospheric conditions at 80 °C of the neat IL and SILPs was measured by placing the samples in a static oven. The samples were periodically taken out of the oven and weighed manually on an OHAUS Explorer Pro balance.

X-ray fluorescence (XRF): XRF measurements were carried out on a PANanalytical®εpsilon 3-XL wavelength dispersive X-ray fluorescence spectrometer. The bromide content of tetrabutylphosphonium hydroxide was determined by comparing the ratio of the Br to P signal to the one measured on tetrabutylphosphonium bromide. The relative P content in SILPs during long term exposure to 80 °C was determined by following the signal ratios of P/Mg, P/Si and P/Ca.

Gas absorption methods

CO_2 absorption: CO_2 absorption measurements were performed on a test-rig as shown in Figure 1. About 1.5 g of dried (80 °C) SILP material was loaded in a horizontally aligned tubular quartz reactor (inner diameter = 1.0 cm). 10 vol. % CO_2 in N_2 at a flow rate of 50 mL/min was passed through the bypass until a stable signal was obtained by the Quantek Model 906 CO_2 analyzer. Then the CO_2 flow was passed through the reactor loaded with SILP material. The amount of absorbed CO_2 was determined by integrating the difference of the signals obtained through the bypass and the loaded reactor. The volume of the empty reactor and of the tubing was determined by running a measurement with an unloaded reactor, and was taken into account when calculating the amount of CO_2 absorbed by the SILPs. All absorption measurements were conducted at room temperature. The measurements at t = 0 h correspond to the fresh samples after 30 min drying at 80 °C (water removal).

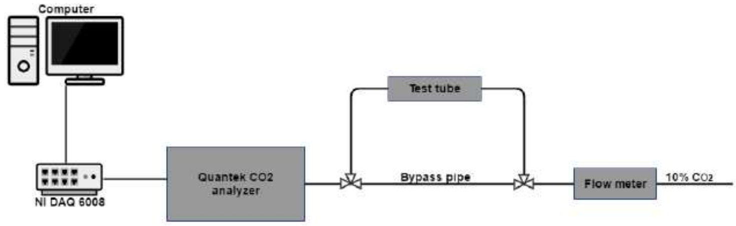

Figure 1. Schematic of the test-rig used for CO_2 absorption measurements.

NO and mixed gas absorption in bulk IL: All absorptions were carried out by passing the gas slowly through a sintered glass frit into the bulk ILs (~1 g). The gas uptake was followed gravimetrically during absorption. After absorption, part of the saturated IL was taken out and titrated with a 0.010M NaOH solution to determine the amount of H^+ formed during absorption. Another part of the saturated IL sample was regenerated by heating to 120 °C for 2 h while bubbling a dry, inert gas through (Ar or N_2). ATR-FTIR data was obtained before experiments, after absorption and after regeneration. It was not possible to obtain spectral data during the absorption.

Results and Discussion

CO_2 capacities of SILPs

Figure 2 shows the CO_2 capacities of the three SILP materials as a function of time spent at 80 °C. Samples s1-batch-1 and s2-batch-1 have in common that their exposure to 80 °C was only interrupted by the CO_2 capacity measurements. The heat treatment of sample s1-batch-2 was divided into periods of 30 min with periods of 15 min at room temperature in between. This was done to mimic the temperature and moisture content fluctuations which the IL would experience in a rotating wheel absorber. Capacity measurements using pure monolith (without IL) showed that the contributions from sepiolite and silica are negligible.

The initial CO_2 capacities of all three samples are between 0.9 and 0.95 moles of CO_2 per mole of $[P_{4444}][Pro]$. Recently 0.88 ± 0.11 moles of CO_2 per mole of IL was reported for absorption into pure $[P_{4444}][Pro]$ (4). The CO_2 capacities of all three samples decrease strongly during exposure to 80 °C. The capacity loss of s1-batch-2 seems to be slightly higher than the ones of s1-batch-1 and s2-batch-2, at least during the first 24 h of exposure. If this is due to the fact that s1-batch-2 differs both in terms IL loading and sepiolite content or due to the interruptions to the heat treatment is unclear at present. Samples s1-batch-1 and s2-batch-2 loose 50 % of their capacities in less than 100 h and no leveling-off is observed during the period investigated. This level of capacity loss is unacceptable in light of the expected life time of months to years.

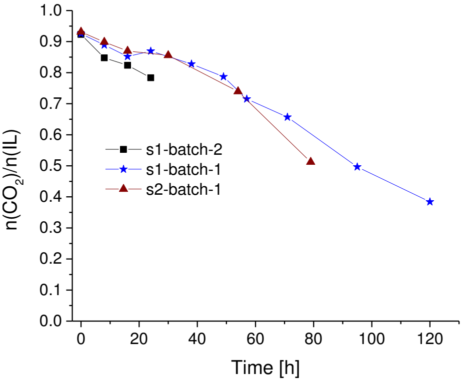

Figure 2. Moles of CO_2 absorbed per mole of initially present [P_{4444}][Pro] as a function of total dwelling time at 80 °C under atmospheric conditions.

Such rapid and pronounced capacity losses have not been reported before, at least to the best of our knowledge. This might be because most studies on CO_2 desorption are performed in the absence of oxygen and moisture (5,6). Therefore we have conducted corresponding stability studies both under a flow of dry and wet Ar and under a flow of nearly dry air. The addition of water to Ar was done by bubbling the stream through a water reservoir at room temperature. The dried air was obtained by passing it first through a cold trap at 0 °C followed by a $CaSO_4$ filter. The SILP was kept in the tubular quartz reactor used for absorption measurements which in turn was placed into a tubular oven heated to 80 °C.

Figure 3 shows that exposure to both dry and wet Ar at 80 °C does not reduce the CO_2 capacity. However, exposure to (almost) dry air for 44 h causes a relative capacity loss of about 20 %, which is similar to the loss observed in the presence of moisture, see Figure 2.

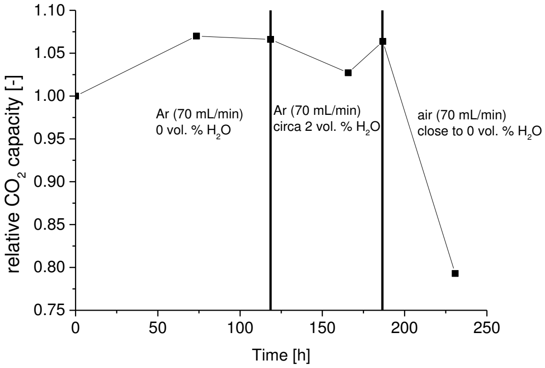

Figure 3. Relative CO_2 capacity as a function of dwelling time at 80 °C under several atmospheres as stated in the diagram.

Weight loss of SILPs

The relative weight loss of the IL component in the SILPs exposed to 80 °C (atmospheric conditions) is much lower than the corresponding loss in CO_2 capacity. For example, s1-batch-1 loses less than 10 % of the IL weight after 100 h while it loses about 50 % of its CO_2 capacity. This is a clear indication that the capacity loss is not caused by simple evaporation of [P_{4444}][Pro]. The neat IL loses weight at a significantly lower rate than the SILPs do. This might be due to a lower surface area per volume of IL.

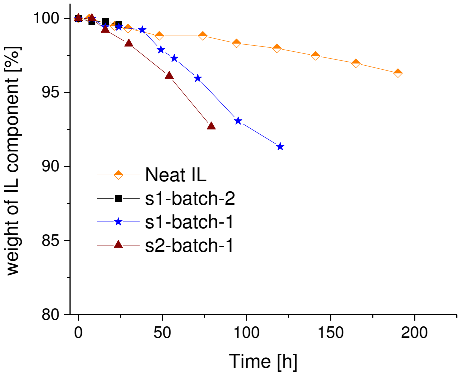

Figure 4. Relative weight of [P_{4444}][Pro] as a function of total dwelling time at 80 °C under atmospheric conditions.

Characterization of SILPs

XRF analysis of SILPs exposed to 80 °C in air revealed that the signal ratios of P/Mg, P/Si and P/Ca do not decrease over time, while both the CO_2 capacity and the mass of $[P_{4444}]$[Pro] decrease continuously. Hence, simple evaporation of the IL can be ruled out as a cause for weight- and CO_2 capacity loss.

The ^{1}H NMR spectra reveal that heat treatment causes the signals assigned to prolinate ($\delta \approx 1.8$; 2.3; 3.3; 3.8 and 4.2 ppm) to decrease relative to the ones assigned to tetrabutylphosphonium ($\delta \approx 0.9$; 1.5 and 3.0 ppm). This indicates that the anion is less stable than the cation. The ^{13}C NMR spectra of the heat treated IL show a strongly reduced (neat IL) or almost vanished (SILP derived IL) signal at 180 ppm which is typically assigned to the carboxylate carbon. The group of Altarawneh (7) has investigated the unimolecular decomposition of proline using density functional theory (DFT) calculations and concluded that decarboxylation is associated with the lowest energy barrier. Modeling of the reaction at 500 K (1 bar) showed that decarboxylation is the second most important initial reaction channel. The anion signal reducing effect of heat is more pronounced in the case of the SILP in spite of a shorter exposure period. This reflects the lower rate of mass loss of the neat IL as shown in Figure 4.

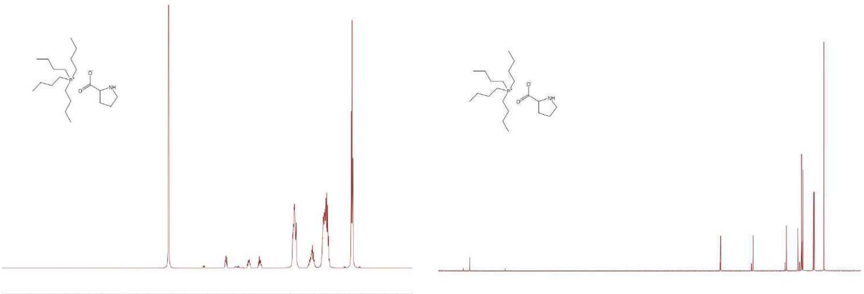

a) ^{1}H NMR of neat, fresh $[P_{4444}]$[Pro]

b) ^{13}C NMR of neat, fresh $[P_{4444}]$[Pro]

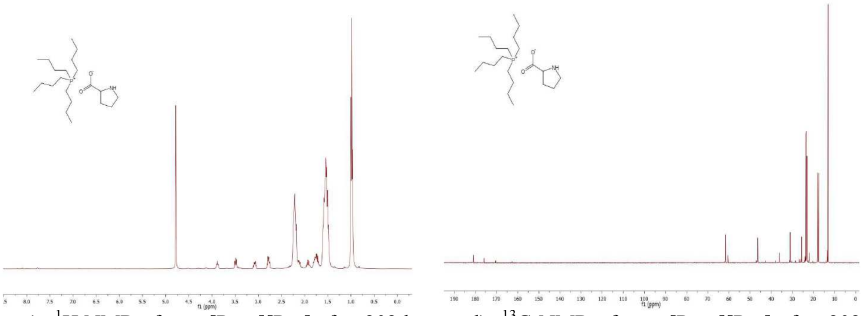

c) ^{1}H NMR of neat $[P_{4444}]$[Pro] after 202 h

d) ^{13}C NMR of neat $[P_{4444}]$[Pro] after 202 at 80 °C h at 80 °C

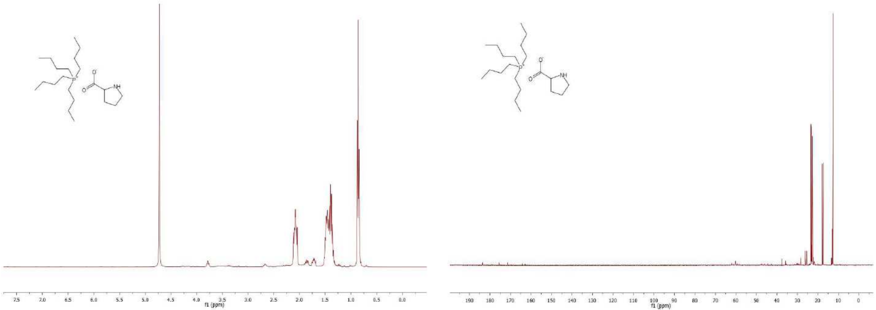

e) ^{1}H NMR of $[P_{4444}]$[Pro] extracted from SILP after 176 h at 80 °C

f) ^{13}C NMR of $[P_{4444}]$[Pro] extracted from SILP after 176 h at 80 °C

Figure 5. NMR spectra of fresh and heat treated neat $[P_{4444}]$[Pro] and $[P_{4444}]$[Pro] extracted from heat treated SILP. Solvent = D_2O. Atmosphere during heat-treatment = air.

ATR-FTIR spectra of neat IL before and after 117 h of exposure to 80 °C were measured in order to confirm and quantify the removal of the carbonyl group. The ratio of the peak heights of the carbonyl group (circa 1570 cm^{-1}) to the one of the cation (circa 2970 cm^{-1}) was chosen as a gauge for the relative concentration of the carbonyl group. 117 h of heat exposure caused this ratio to decease by 21.1 %. This translates into a mass loss of about 2.5 % assuming that decarboxylation is the only cause of mass loss (after drying). This value agrees reasonably well with the measured weight loss, see figure 4.

At present it is not clear to us which anion replaces prolinate but this will probably be investigated in the near future.

Selectivity of gas absorption in ILs

Different ILs have shown to absorb SO_2 and CO_2. It is often reported that water is a likely inhibitor and this has been investigated for several materials (8). Even oxygen can have an influence as described above. Several other possible inhibitors that would also be present in a flue gas have not been considered. There is the possibility of strongly limiting the applicability of IL absorbers if the interactions between the IL and the gas phase are not selective enough. To our knowledge, ILs targeting CO_2 or SO_2 have not been tested for cross absorption of other relevant species, e.g. there are no reports of ILs active in CO_2 absorption being tested for SO_2 and NO absorption. Industrial flue gasses are complex mixtures, and understanding the selectivity and behavior of potential IL absorbers is vital for overcoming the hurdles associated with the practical application of these methods.

It has previously been shown that a broad range of ILs can absorb and oxidize NO to HNO_3 in the presence of water and oxygen at low temperatures (8-10). The best performing IL has nitrate as the anion. Other anions such as chloride and acetate will be turned into the corresponding acid. Volatile acids will be driven out, effectively turning the IL into the corresponding nitrate IL during absorption of NO.

As described in (10) and outlined below H_2O, CO_2 and SO_2 do not interact to any significant extent with nitrate based ILs that are specifically targeting NO in off gasses and thus the reactivity can be said to be quite selective towards NO. On the other hand our studies have revealed a potential problem for CO_2 absorbers, since the interaction with NO and subsequent oxidation to HNO_3 will generate acidic protons in the IL and will drive out the weakest acid thus changing the properties and the selectivity of the IL. Even gas streams that are quite dilute in NO will eventually accumulate enough HNO_3 to deteriorate the CO_2 capacity of the IL.

Properties of nitrate based ILs

Pure NO diluted in inert gas does not interact to any significant extent with the IL (10). If O_2 and H_2O are both present NO is oxidized to HNO_3 in a 2nd order process, which is fast enough to follow even at low temperatures. The HNO_3 is retained in the IL until it is released by increasing the temperature to above 80 °C. Full desorption occurs just above 120 °C, corresponding to the highest boiling azeotrope of water and HNO_3. The capacity for ILs with nitrate anions in the bulk phase at low temperatures is around 1:1 given as molar ratio (HNO_3:IL). The IL is stable under these conditions and several hundreds of absorption/desorption cycles have been performed on [BMIM][NO_3] supported in a SILP formulation without any sign of capacity loss (9). The reaction has been proposed to be second order in NO, which is in good accordance with the results in (9,10). This is also similar to what is reported in aqueous solutions for NO oxidation to HNO_3 (11,12).

The interaction of NO, CO_2 and SO_2 with bulk [BMIM][NO_3] was recently investigated. The gas mixtures were bubbled through the IL in a simple setup and were followed gravimetrically. In addition, titrimetric analysis of the generated acidic protons was performed after the experiment was stopped. Water and oxygen was present in the gas. The IL was dried carefully prior to starting each of the experiments in order to have a common, reproducible starting point. The flow rate, the water and oxygen concentrations were kept constant in all 5 experiments. The results are shown in Table 1 (10).

Table 1: Absorption of gasses in initially dry [BMIM][NO_3] determined gravimetrically and by titration with 0.1 M NaOH. Adapted from ref. (10).

Experiment no.:	**1**	**2**	**3**	**4**	**5**
CO_2	-	50%	-	-	-
SO_2	-	-	1%	-	-
NO	-	-	-	5%	0.1%
O_2	10%	10%	10%	10%	10%
H_2O	1.4%	1.4%	1.4%	1.4%	1.4%
Absorption Time	24h	24h	24h	8h	36h

Weight increase (g/g IL)	0.10	0.11	0.09	0.53	0.11
Weight increase (g/mole IL)*	20	22	18	107	22
Mol H^+/mole IL	0	0	0.004	1.10	0.11

* *M*([BMIM][NO_3]) = 201.1 g/mol

In experiments 1 and 2, the gravimetric increase is solely due to uptake of water since no acidity was detected when the IL interacts with H_2O + O_2 + CO_2 or only with H_2O + O_2. A very small amount of acid was detected in experiment 3 when H_2O + O_2 + SO_2 are passed through the IL but it was not detectable on the weight increase. Experiment 4 show a drastic increase in weight of the liquid phase after interaction with NO. Experiment 5 shows only a modest weight increase, comparable to the blank experiment, but titration reveal that the reaction had also taken place here. Thus even at low NO concentrations, there is a significant uptake of NO in the IL. The experiment was stopped after 36 h to be comparable with the others but absorption was still ongoing. The generated acidic protons correspond to 15 % of the NO in the highly diluted gas having reacted. Based on these experiments, we have concluded that [BMIM][NO_3] is selective in the absorption and oxidation of NOx species.

Stability of [P_{4444}][Pro] when subjected to NO, air and water

Previous work on NO oxidation and absorption in ILs have shown that after an absorption/desorption cycle, the anion of the IL has been exchanged to nitrate when starting with ILs with the anions chloride, acetate and bromide. This was not the case for triflate ([CF_3SO_3]$^-$) based ILs, since triflate is a too weak base to be protonated by nitric acid. Prolinate, [Pro]$^-$, contains a carboxylate group which is similar to acetate in base strength and it was anticipated that a similar reaction could take place.

In order to investigate this, [P_{4444}][Pro] was subjected to the same conditions that [BMIM][NO_3] was subjected to during the previous experiments for NO absorption (experiment 4 in Table 1.) The experiment was monitored gravimetrically for 8 h and the development is shown in Figure 6. Several physical changes to the IL were observed during absorption; within a few minutes, the color of the IL changed from colorless to yellow. Within the first hour white sedimentation started to form both in the IL but also as a solid film on the gas outlet, causing the IL to appear opaque. After a while, the liquid became clear and yellow again, and finally the white film on the gas outlet slowly disappeared as well.

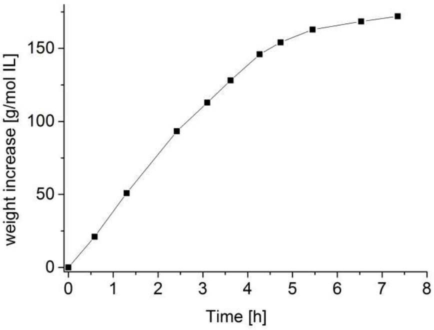

Figure 6. Change in weight with time when a gas mixture containing 5% NO, 10% O_2, 1.4% H_2O and balance N_2 is bubbled through 1 g of dry $[P_{4444}]$[Pro] at room temperature. The weight change is given as g per mole of IL ($M([P_{4444}][Pro]) = 373.6$ g/mol) in order to be comparable with the data for [BMIM]$[NO_3]$ in Table 1.

From the gravimetric data, it is seen that a significant amount of NO has reacted and has been caught in $[P_{4444}]$[Pro] during the experiment. The overall profile of the curve corresponds well with what has been reported previously for nitrate based ILs. The total weight increase at saturation is significantly higher for $[P_{4444}]$[Pro] when compared with the mole of IL: 172 g is found per mole $[P_{4444}]$[Pro] whereas it was 107 g per mole [BMIM]$[NO_3]$. If compared on a weight of IL basis the numbers are very similar (0.46 g/g IL for $[P_{4444}]$[Pro] and 0.53 g/g IL for [BMIM]$[NO_3]$). The ratio of water to HNO_3 to other products cannot be determined just from the weight increase.

Titration of the solution with NaOH after absorption in the IL for 450 min revealed that 1.7 mole of H^+ had accumulated per mole of IL. This is significantly higher than the 1.1 mole H^+/mole IL observed at saturation for [BMIM]$[NO_3]$ (10).

In order to identify the changes in the IL, ATR-FTIR spectra were measured before absorption and after saturation. The data are shown in Figure 7. After saturation a portion of the IL was heated to 120 °C and bubbled through with nitrogen a few times. This is sufficient to remove nitric acid and water from the IL. The ATR-FTIR spectrum of the resulting IL is also given in Figure 7.

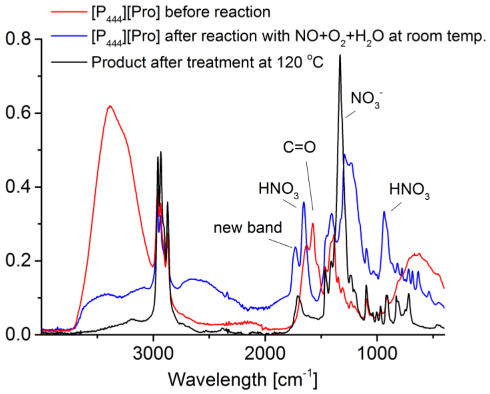

Figure 7. ATR-FTIR spectra obtained for $[P_{4444}][Pro]$ before and after exposure to NO + O_2 + H_2O at room temperature as well as after subsequent regeneration at 120 °C.

From Figure 7 it can be seen that a drastic change in the composition of the liquid has taken place. The intense band centered at 3350 cm^{-1} consists of O-H and N-H stretch vibrations. This band is diminished and has shifted to several broader bands between 2600 and 3600 cm^{-1} after exposure, probably since the water dissolved in the IL has been partially consumed and the NH group has been protonated. The signature bands for HNO_3 at 940 and 1660 cm^{-1} are also observed. The sharp C-H bands around 2900 cm^{-1} are assigned to the alkyl chains in $[P_{4444}]^+$. They are unchanged after exposure indicating that the cation does not partake in the reaction. The band assigned to C=O stretch for prolinate at 1570 cm^{-1} has disappeared after the reaction.

After desorption the nitric acid bands disappear completely. All O-H and N-H bands are also gone which indicates that the prolinate anion did not survive the treatment. A new intense band at 1340 cm^{-1} is signature of the symmetric nitrate anion. There is one significant band around 1725 cm^{-1} which has not yet been assigned. This band was not present before the exposure but can be found after exposure and also after desorption. It is not recognized from previous experiments with $[BMIM][NO_3]$. This wavelength correspond to C=C or C=N and we suggest that it is likely a fragment of the prolinate anion formed after elimination of CO_2.

Clearly the $[P_{4444}][Pro]$ IL reacts just as willingly with NO in the presence of O_2 and H_2O as the previously investigated $[BMIM][NO_3]$ did. The cation is not destroyed during absorption and desorption. The anion has reacted - probably decomposing by decarboxylation already at low temperatures - as HNO_3 accumulates in the IL. The possible cyclic amine remaining is expected to increase the absorption of HNO_3, since additional acid might be retained in the liquid by protonating the amine. Indeed an even higher amount of acidic protons were found by titration. After heating to 120 °C the HNO_3 has desorbed and the IL has been transformed into a nitrate based IL. By analogy with $[BMIM][NO_3]$ the new nitrate based IL is not expected to have any activity towards absorption of CO_2.

The investigation reveals that NO interacts prominently with amino acid based ILs and that the result is destruction of the IL for CO_2 absorption applications. Even low concentrations of NO present may accumulate over time and it is therefore recommended only to apply this technology for off gasses that does not contain the combination of NO, O_2 and water. Since [P_{4444}][Pro] is already showing some decomposition in O_2 containing gas streams this will not pose a further restriction on the applicability of the technology. It is also shown how IL anions with amine acid functional groups can increase the capacity for NO in the first absorption step per mole IL, but that the extra capacity will not survive regeneration conditions.

Conclusions

Long term treatment of [P_{4444}][Pro] based SILPs at 80 °C causes severe CO_2 capacity losses (about 50 % in 100 h). NMR analysis revealed that heat treatment most probably causes decarboxylation and possibly other forms of degradation of the prolinate anion while the cation remains largely intact. This can cause huge capacity reductions, because the anion is the major CO_2 capturing entity. However, CO_2 capacity losses were not observed after exposure to 80 °C in Ar. Moisture, irrespective of the presence or absence of oxygen, has no effect on the rate of CO_2 capacity loss. Preliminary stability studies on [N_{66614}][Pro] and [N_{66614}][Lys] show similar trends and suggest that decarboxylation of the amino acid anion could be a general problem. This will be investigated further in the near future.

The probable need for an inert environment during CO_2 desorption does, at present, not rule out the viability of the SILP based CO_2 capture technology, but it nevertheless introduces a new constraint. Also interference of NO in oxygen and water containing gases may cause transformation of the amino acid anion to nitrate leading to an inactive CO_2 absorber also limiting the possible applications. On the contrary the NO absorbing ionic liquid [BMIM][NO_3] seems not to suffer from negative interferences with other gases like SO_2, CO_2 or water possibly present in the NO containing flue gas.

Acknowledgments

Energinet.dk, Denmark is greatly acknowledged for financial support of this work through the PSO project no. 12096.

References

1. J. Huang, A. Riisager, P. Wasserscheid and R. Fehrmann, *Chem. Commun.*, 4027 (2006).
2. W. Wu, B. Han, H. Gao, Z. Liu, T. Jiang and J. Huang, *Angew. Chem. Int. Ed.*, **43**, 2415 (2004).
3. S. Shunmugavel, S. Kegnæs, J. Due-Hansen, T. A. Gretasdottir, A. Riisager and R. Fehrmann, *ECS Trans.*, **3**, 49 (2007).

4. Q. Yang, Z. Wang, Z. Bao, Z. Zhang, Y. Yang, Q. Ren, H. Xing and S. Dai, *ChemSusChem,* **8**, 806 (2016).
5. C. Wang, X. Luo, H. Luo, D.E. Jiang, H. Li and S. Dai, *Angew. Chem. Int. Ed.*, **50**, 4918 (2011).
6. H. Kolding, *PhD thesis "Catalysis and selective gas absorption in ionic liquids"*, Technical University of Denmark (2015).
7. S. Rawadieh, I. Altarawneh, H.B. Alteyat and M. Altarawneh, *Comp. Theor. Chem.*, **1018**, 45 (2013).
8. H. Kolding, P. Thomassen, S. Mossin, S. Kegnæs, A. Riisager, J. Rogez, G. Mikaelian and R. Fehrmann, *ECS Trans.***,** **64**, 97 (2014).
9. P. Thomassen, A. Riisager, A.J. Kunov-Kruse, S. Mossin, H. Kolding, S. Kegnæs and R. Fehrmann, *ECS Trans.*, **50**, 433 (2012).
10. A.J. Kunov-Kruse, P.L. Thomassen, A. Riisager, S. Mossin and R. Fehrmann, *Chem. Eur. J.*, in press (2016).
11. P.C. Ford, D.A. Wink and D.M. Stanbury, *FEBS Lett.*, **326**, 1 (1993).
12. M. Thiemann, E. Scheibler and K.W. Wiegand, *Ullmann's Encycl. Ind. Chem.*, **24**, 177 (2012).

Appendix D

Unpublished Work

D.1 Methanol Promoted Low Temperature Oxidation of NO

P. W. Jakobsen, S. Mossin* and Rasmus Fehrmann*
Unpublished Work (Patent Restrictions), **2017**

Methanol promoted low temperature oxidation of NO

Peter W. Jakobsen[a], Susanne Mossin[a]* and Rasmus Fehrmann[a]*

Department of Chemistry, Technical University of Denmark

Abstract: We present a novel catalyst for low temperature (30 – 120 °C) oxidation of nitric oxide by air. A porous material in conjunction with methanol and water catalyzes the oxidation in continuous flow. The conversion of NO is significantly increased by impregnating the material with the ionic liquid 1-butyl-3-methylimidazolium nitrate, [BMIM][NO_3]. At 100% relative humidity the activity for NO oxidation is several orders of magnitude higher than reported for other porous materials and slightly higher than the best reaction rates reported by state-of-the-art NO oxidation catalysts under dry conditions. NO conversion of 40% is reported at 30 °C with a high flow rate (space velocity: 96,000 h^{-1}), low NO concentration (500 ppm), trace amounts of methanol (17 ppm), and a relative humidity of 100%. The promotor methanol achieves a turn over number of up to 30 before finally being oxidized to CO_2. A low-temperature method for oxidation of NO to NO_2 in wet flue gasses allow using fast selective catalytic reduction (SCR) technology for NO_x removal in a tail-end configuration at low temperature.

Harmful effects caused by anthropogenic NO_x-emissions are well documented[1,2]. NO_x gasses are known to have a negative effect on human health[3], on the ozone layer[4] and to cause acid rain. SCR is a well-established method for removing NO_x from flue gasses from combustion of fossil-based fuels. SCR is often not a viable option in processes where the fuels are not fossil-based, due to deactivation of the catalyst[5]. One of the main problems is deactivation of the traditional vanadium based SCR catalyst by alkali metal containing aerosols in the flue gas from combustion of biomass[6,7]

A possible solution to the deactivation is to move the SCR reactor to the tail-end position, in which the temperature of the flue gas is significantly lower (~80 °C), while the relative humidity of the gas is close to 100%. Most commonly used SCR catalysts operate at temperatures above 300 °C[8]. Consequently, much effort is currently being put into the development of new, low-temperature SCR catalysts[9–12]. Current best technologies have improved low temperature activity (200 °C) but lower N_2 selectivity compared to the regular SCR catalysts[13,14].

When the flue gas contains an equimolar mix of NO and NO_2, conditions commonly referred to as “fast SCR”[15,16], existing SCR catalysts have improved activity and selectivity[15,16] and can be successfully applied at lower temperatures. A viable method for oxidation of NO to NO_2 in the presence of water will allow existing SCR technology to be applied in the tail-end position without costly reheating of the gas stream.

There are several reports of siliceous zeolites[17,18], ion-exchanged zeolites[19] and carbonaceous materials[20,21] being able to perform oxidation of NO at low temperatures. The reaction occurs in the micro pores of the materials and is hindered by competitive absorption of both water and NO_2[22], especially at low temperatures[18–20,23]. Very recently, Ghafari and Atkinson, reported oxidation of NO to NO_2 over a crosslinked polymer catalyst, reaching conversions upwards of 35% in the presence of water. These results were obtained at space velocities around 2500 h^{-1} (estimated from provided data) and with NO concentrations around 1000 ppm[24].

Here we present a novel method for oxidizing NO to NO_2, HNO_2 and HNO_3 at low temperatures in continuous flow. The oxidant is dioxygen and the catalyst is a porous silica material impregnated with the ionic liquid 1-butyl-3-methylimidazolium nitrate, [BMIM][NO_3], to obtain a supported ionic liquid phase (SILP) catalyst. The reaction is promoted by water and small amounts of methanol added in the gas phase before the catalyst.

Results and discussion

The reaction proceeds over several silica materials. The hollow sphere-SILP (HS-SILP) material shown in Scheme 1 showed significantly higher conversions and was used for further investigations.

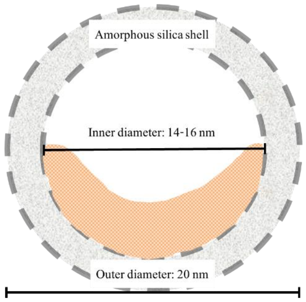

Scheme 1: Illustration of the HS-SILP catalyst at a pore-filling degree of 30 %.

NO conversions at steady state for different methanol to NO ratios are shown in Figure 1, the effect of varying alcohols and catalysts materials in Figure 2 and the effect of temperature is shown in Figure 3.

A NO conversion slightly below 50 % is optimal for SCR, since a surplus of NO_2 decreases the reaction rate considerably[27,28]. The highlighted point in Figure 1 correspond to a conversion of NO of 46 % at a partial pressure of methanol of 80 ppm (ratio of 1:38 compared to NO) and a TON of methanol of 17. For an even lower methanol content of 40 ppm (1:75) conversion was 40 % and TON was 30. It is also seen that the NO conversion decreases when the MeOH:NO ratio becomes higher than 1:8.

---

[a] Ph.D. P. W. Jakobsen, Assoc. Prof. S. Mossin*, Prof. R. Fehrmann*
Department of Chemistry
Technical University of Denmark
Kemitorvet 207, DK-2800, Kgs. Lyngby
Denmark
E-mail: slmo@kemi.dtu.dk, rf@kemi.dtu.dk

Supporting information for this article is given via a link at the end of the document.((Please delete this text if not appropriate))

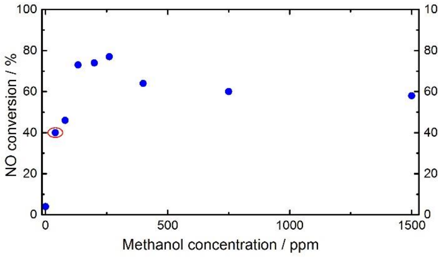

Figure 1. Steady state NO conversions at varying methanol concentrations for a HS-SILP exposed to a gas containing 3000 ppm NO, 12% O_2 and balance N_2 at 100% relative humidity (RH) with a space velocity (GHSV) of 15,000h^{-1}, at 30 ºC. The highlighted point corresponds to methanol:NO = 1:38.

With a methanol concentration of 240 ppm (MeOH:NO = 1:12.5) the exit gas was collected at steady state and investigated by high resolution FTIR. It was found that all methanol had been oxidized to CO_2 and that no N_2O was detectable in the gas, see Figure S2.

Figure 2 shows that methanol is more efficient than the longer chain alcohols. Further screening of alcohols can be found in Figure S3.

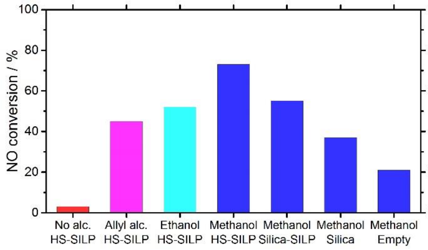

Figure 2. Steady-state NO conversions over different catalysts at 30 ºC with different alcohols added to the flue gas stream. 3000 ppm NO, 130 ppm alcohol (1:23), 12% O_2 and balance N_2, at 100% RH with a GHSV of 15,000 h^{-1}.

The NO conversion increases significantly when a porous materials is used and even further when the material is impregnated with the ionic liquid., see Figure 2.

Methanol clearly acts as a promoter for the oxidation since the NO conversion in this setup is 3 % in the absence of methanol and up to 78 % with methanol. At a NO partial pressure of 3000 ppm a considerable effect is seen even in the empty reactor, see Figure 2. The promoting effect of methanol is suggested to be due to activation of dioxygen by carbon-based radicals generated in the NO_x assisted oxidative degradation of methanol. One such radical is the methanal radical, CHO. The resulting oxygenated radical species proceed to oxidize NO to NO_2. This is completely analogous to the accepted scenario for smog formation. There, however, the radical initiators are generated by cleaving of gas phase HNO_2 into NO and OH radicals by UV light. The resulting highly reactive hydroxyl radical in turn induce the generation of more persistent radicals of small organic molecules [29,30]. In order to eliminate the influence of UV light in this study the setup was wrapped in aluminum foil. The presence of this cover did not influence the conversion of NO and we suggest that another path to the carbon based radicals is relevant here. HNO_2 can be observed in the exit gas and is believed to be the origin of the initiating radicals also in the dark. The initiation reaction is suggested to occur in the liquid covered porous surfaces where methanol is dissolved and a build-up of reactive HNO_2 takes place due to the interaction between nitrate, NO and water [vores ref]. The product NO_2 reacts with water present in the gas and generates HNO_2 and HNO_3 that has a tendency to condense on all surfaces. It is therefore important to wait several hours for the setup to equilibrate in order to be able to close the nitrogen balance. HNO_2 and HNO_3 will decompose to NO, NO_2 and water at temperatures above 120 °C and will therefore not pose a problem for SCR applications. For absorber technologies based on basic materials HNO_2 and HNO_3 are preferable over NO_2[ref].

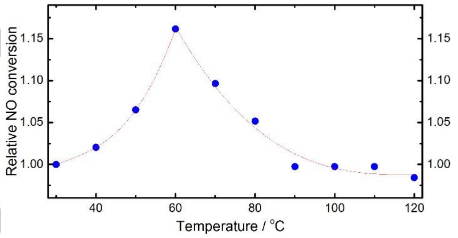

Figure 3: Steady state NO conversion for a HS-SILP at temperatures ranging from 30 ºC to 120 ºC given relative to the conversion observed at 30 ºC. 2000 ppm NO, 800 ppm methanol (1:2.5), 12% O_2, 4% H_2O and balance N_2, GHSV of 15,000 h^{-1}.

Previous literature on ambient temperature NO oxidation report an increased rate with decreasing temperature, i.e. a negative apparent activation energy[17–19,21], which is consistent with homogenous phase oxidation[17]. As shown in Figure 3, a temperature optimum is observed around 60 ºC, albeit with a rather low impact on the conversion. This temperature optimum may be caused by competing limitations such as radical formation at low temperature and gas-solubility in the IL at higher temperatures. This effect is similar to what has been reported previously for absorption and oxidation of NO in ILs[31].

In order to test this method for common NO_x abatement applications, the setup was pushed to high flow rates per g of catalyst and low NO content: NO: 500 ppm, methanol: 17 ppm, 100% RH, 30 ºC and a space velocity of 96,000 h^{-1}. The contribution from autoxidation becomes negligible at these NO concentrations. The NO conversion under these conditions was found to be an impressive 40%.

In conclusion, we have presented a novel method for low temperature oxidation of NO by using methanol as a promoter. To the best of our knowledge this is the only reported low-temperature oxidation method utilizing methanol. When comparing results obtained under wet conditions, the presented method shows reaction rates several orders of magnitude higher than found in the recent literature[24].

Experimental Section

The SILP was prepared by impregnating hollow-sphere silica (HS)[25,26] or silica gel 100 (Fluka) with [BMIM][NO_3] (Io-Li-Tec, >98.5%) dissolved in methanol and drying by rotary evaporation at decreased pressure for 2 h at 60 °C. The materials were further dried at 120 °C for 12 h and stored in a desiccator until used. The final material contained 0.33 g IL per g HS corresponding to a pore-filling degree of 30 %. 0.8 g of the SILP material was placed on a glas frit in a vertical glas tube (Ø = 10 mm) and thermostated at 30 °C. The material was exposed to a gas stream containing NO (500-3000 ppm), O_2 (14-20%), H_2O (2-4%) and balance N_2 at temperatures ranging from 30-120 ºC in a continuous flow setup using GE50A mass flow controllers from MKS instruments, with total gas flow rates of 100-200 NmL/min. Gas bottles were supplied by AGA: 1 % NO in He and pressurized air. A methanol/water solution (0-4 wt %) was injected into the gas stream prior to contact with the catalyst bed through a KDS 100 Legacy infusion pump at flow rates between 0.2 and 0.4 mL/h, a schematic overview is found in Figure S1. The exit gas stream was continuously monitored by gas phase UV-Vis spectroscopy and the NO partial pressure was determined by comparing the area of the 204 nm NO band, obtained through spectral deconvolution, to a reference curve constructed by feeding NO gas at different partial pressures to a stream bypassing the setup. The setup was allowed to equilibrate for several hours; steady state was considered to have been achieved when there was no change in the NO partial pressure of the exit gas for 1.5 hours.

Keywords: NO oxidation • NO_x removal • Ionic Liquids • Flue gas • Radical reaction

(1) Chang, S. G.; Liu, D. K. *Nature* **1990**, *343*, 151.
(2) Pham K., E.; Chang G., S. *Nature* **1994**, *369*, 139–141.
(3) Kanchongkittiphon, W.; Mendell, M. J.; Gaffin, J. M.; Wang, G.; Phipatanakul, W. *Environ. Health Perspect.* **2015**, *123*, 6–20.
(4) W. L. Chameides, P. S. Kasibhatla, J. Yienger, H. L. I. *Science (80-.).* **1994**, *264*, 74–77.
(5) Nicosia, D.; Czekaj, I.; Kroecher, O. *Appl. Catal. B Environ.* **2008**, *77*, 228–236.
(6) Sander, B. *Biomass and Bioenergy* **1997**, *12*, 177–183.
(7) Zheng, Y.; Jensen, A. D.; Johnsson, J. E.; Thøgersen, J. R. *Appl. Catal. B Environ.* **2008**, *83*, 186–194.
(8) Busca, G.; Lietti, L.; Ramis, G.; Berti, F. *Appl. Catal. B Environ.* **1998**, *18*, 1–36.
(9) Qi, G.; Yang, R. T. *J. Catal.* **2003**, *217*, 434–441.
(10) Reddy, P.; Ettireddy, N.; Mamedov, S. *Appl. Catal. B Environ.* **2007**, *76*, 123–134.
(11) Thirupathi, B.; Smirniotis, P. G. *J. Catal.* **2012**, *288*, 74–83.
(12) Peña, D. A.; Uphade, B. S.; Reddy, E. P.; Smirniotis, P. G. *J. Phys. Chem. B* **2004**, 9927–9936.
(13) Yang, S.; Qi, F.; Xiong, S.; Dang, H.; Liao, Y. *Appl. Catal. B Environ.* **2016**, *181*, 570–580.
(14) Casapu, M.; Kroecher, O.; Elsener, M. *Appl. Catal. B Environ.* **2009**, *88*, 413–419.
(15) Koebel, M.; Elsener, M.; Madia, G. *Ind. Eng. Chem. Res.* **2001**, *40*, 52–59.
(16) Koebel, M.; Madia, G.; Elsener, M. *Catal. Today* **2002**, *73*, 239–247.
(17) Artioli, N.; Lobo, R. F.; Iglesia, E. *J. Phys. Chem. C* **2013**, *117*, 20666–20674.
(18) Zhang, Z.; Atkinson, J. D.; Jiang, B.; Rood, M. J.; Yan, Z. *Appl. Catal. B Environ.* **2015**, *163*, 573–583.
(19) Loiland, J. A.; Lobo, R. F. *J. Catal.* **2014**, *311*, 412–423.
(20) Mochida, I.; Kawabuchi, Y.; Kawano, S.; Matsumura, Y.; Yoshikawa, M. *Fuel* **1997**, *76*, 543–548.
(21) Zhang, Z.; Atkinson, J. D.; Jiang, B.; Rood, M. J.; Yan, Z. *Appl. Catal. B Environ.* **2014**, *149*, 573–581.
(22) Kircher, O.; Hougen, O. A. *AIChE J.* **1957**, *3*, 331–335.
(23) Guo, Z.; Xie, Y.; Hong, I.; Kim, J. *Energy Convers. Manag.* **2001**, *42*, 2005–2018.
(24) Ghafari, M.; Atkinson, J. D. *Environ. Sci. Technol.* **2016**, *50*, 5189–5196.
(25) Qiao, Z.; Huo, Q.; Chi, M.; Veith, G. M.; Binder, A. J.; Dai, S. *Adv. Mater.* **2012**, *24*, 6017–6021.
(26) Qiao, Z.-A.; Zhang, P.; Chai, S.-H.; Veith, G. M.; Gallega, N. C.; Kidder, M.; Dai, S. *J. Am. Chem. Soc.* **2014**, *136*, 11260–11263.
(27) Madia, G.; Koebel, M.; Elsener, M.; Wokaun, A. *Ind. Eng. Chem. Res.* **2002**, *41*, 4008–4015.
(28) Grossale, A.; Nova, I.; Tronconi, E.; Chatterjee, D.; Weibel, M. *J. Catal.* **2008**, *63*, 492–531.
(29) Niki, H.; Maker, P. D.; Savage, C. M.; Breitenbach, L. P. *J. Phys. Chem.* **1978**, *82*, 135–137.
(30) Fox, D. L. .; Kamens, R.; Jeffries, H. E. . *Science (80-.).* **1975**, *188*, 1113–1114.
(31) Kunov-kruse, A. J.; Thomassen, P. L.; Riisager, A.; Mossin, S.; Fehrmann, R. *Chem. - A Eur. J.* **2016**, *22*, 11745–11755.

Entry for the Table of Contents (Please choose one layout)

Layout 1:

COMMUNICATION

Text for Table of Contents

((Insert TOC Graphic here))

*Author(s), Corresponding Author(s)**

Page No. – Page No.

Title

Layout 2:

COMMUNICATION

((Insert TOC Graphic here))

*Author(s), Corresponding Author(s)**

Page No. – Page No.

Title

Text for Table of Contents

Supporting Information for

Methanol promoted low temperature oxidation of NO

Peter W. Jakobsen[a], Susanne Mossin[a]* and Rasmus Fehrmann[a]*

[a]Centre for Catalysis and Sustainable Chemistry, Department of Chemistry, Building 207,

Technical University of Denmark, DK-2800 Kgs. Lyngby, Denmark

*slmo@kemi.dtu.dk, rf@kemi.dtu.dk

Content:

Figure S1: Experimental setup used in continuous flow experiments.

Figure S2: In-situ ATR-FTIR absorption spectra of NO absorption in [BMIM][NO$_3$].

Figure S3: In-situ ATR-FTIR absorption spectra of NO absorption and oxidation in [BMMIM][NO$_3$].

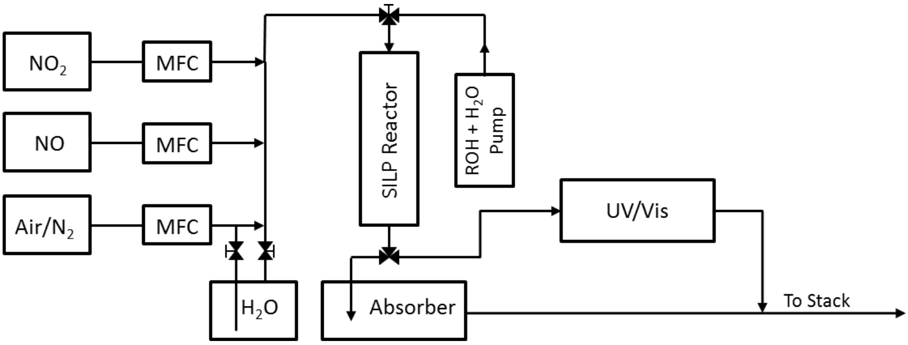

Figure S1: Schematic overview of experimental setup.

The setup depicted allows for mixing of the predetermined water/alcohol solution into the gaseous phase prior to leading the flue gas into the reactor. The bottom of the reactor was fitted with a 3-way valve. One exit led directly to a frit placed in a strong NaOH solution, the other led to the gas cuvette in the UV/Vis spectrometer. The gas was led through the basic solution during startup, prior to reaching steady-state, both to reduce exposure time for the UV/Vis and avoid corrosion, but also to circumvent condensation issues which were observed at high conversions. After 2.5-3 hours, the gas was led through the spectrometer, where 15 spectra were obtained from 200-600 nm with 0.02 nm resolution. The reaction was considered to be steady state when ten consecutive spectra were identical, corresponding more than one hour of on-stream measurements.

In all cases where the alcohol concentration was changed, the pumping system and top of the reactor were removed. The top of the reactor was cleaned and put back in place and the SILP reactor was exposed to a gas mixture containing 3000 ppm NO, 14% O_2 *and balance* N_2*, while the NO conversion was monitored. When no excess conversion compared to bypass was observed, the new alcohol solution was administered to the system and the system was allowed to equilibrate again for several hours. Same procedure was followed when testing different alcohols.*

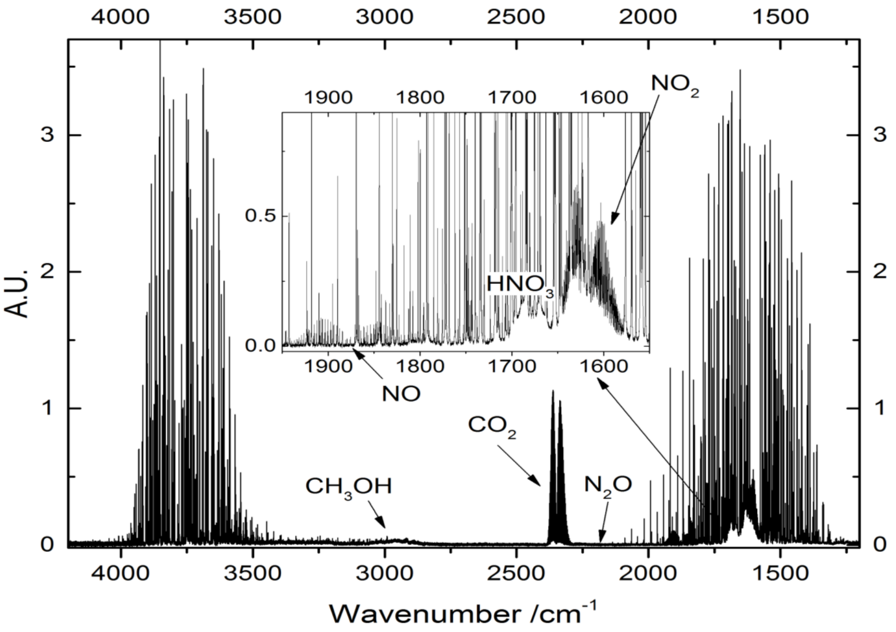

Figure S2: High resolution gas phase FTIR spectra of the effluent gas.

High resolution FTIR gas phase spectrum of steady-state effluent gas from the reactor. Experimental conditions: 3,000 ppm NO, 240 ppm methanol, 12% O_2, 4% H_2O and balance N_2, GHSV = 15,000 h^{-1} at 30 °C. The relevant area for NO_x species has been magnified and is shown together with the full spectrum. Relevant band centres have been marked. N_2O and methanol are not found in the spectrum.

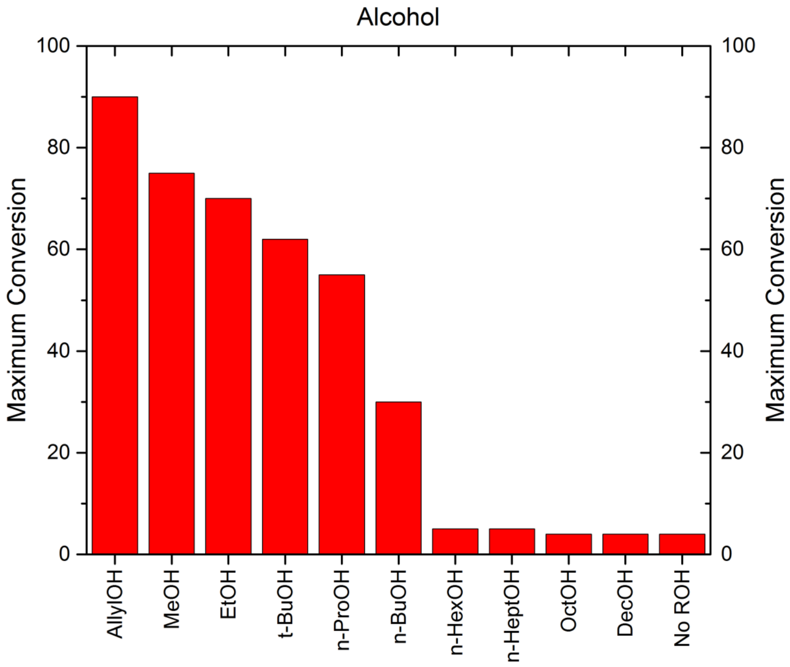

Figure S3: Column plot of maximum conversion during screening of different alcohols.

Maximum obtained NO conversion over after adding three drops of alcoh ol to the SILP (30% v/v [BMIM][NO$_3$*] on silica gel 100) reactor and then exposing it to a simulated flue gas containing 2000 ppm NO, 1.5%* H_2O*, 16%* O_2*, balance N2, GHSV = 4500h*$^{-1}$*. In all cases, maximum conversion was obtained within the first 10 minutes.*